

NSTX-U FY2017 Year End Report

J. Menard and the NSTX-U Team

September 15, 2017 – Version 8

Table of contents

• Executive Summary of NSTX-U Year-End Report	2
○ Notable Outcomes	2
○ Facility and Diagnostics	2
○ Research Milestones	2
○ Additional Research Highlights: Boundary, Core, and Scenarios	6
• Performance of FY2017 Notable Outcomes	13
• Facility and Diagnostics	14
• Research Results	27
FY2017 Research Milestones:	
○ R(17-1): Simulation-based projection of divertor heat flux footprint for NSTX-U	27
○ R(17-2): Advanced divertor operating scenario modeling for NSTX-U	32
○ R(17-3): Identify, mitigate, and develop correction strategies for intrinsic error field sources in NSTX-U	38
○ R(17-4): Assess high-frequency Alfvén Eigenmode stability & associated transport	63
○ R(17-5): Analysis & modelling of current ramp-up dynamics in NSTX & NSTX-U	67
• Additional Research Highlights:	
I. Boundary Science	88
A. Pedestal Structure and Control	88
B. Divertor and Scrape-Off-Layer	91
C. Materials and Plasma Facing Components	100
II. Core Science	111
A. Macroscopic Stability	111
B. Transport and Turbulence	139
C. Energetic Particles	153
III. Integrated Scenarios	159
A. Solenoid-Free Start-up and Ramp-up	160
B. Wave Heating and Current Drive	169
C. Advanced Scenarios and Control	180
• NSTX-U FY2017 publications, invited talks, seminars, major awards, hosted meetings, external leadership (PPPL only), and collaborator institutions	186

Executive Summary of NSTX-U Year-End Report for FY2017

- **Executive Summary for FY2017 Notable Outcomes**

- *Notable 1 - Objective 2.1: “Complete an extensive extent-of-condition review of NSTX-U to identify all design, construction, and operational issues. Prepare a corrective action plan (CAP) to include cost, schedule, scope, and technical specifications of actions. Provide an interim progress report by March 31, 2017, and complete the CAP review and send the final report to DOE by September 30, 2017.”*

- Twelve Design Verification and Validation Reviews (DVVRs) were conducted by external and internal scientists and engineers and focused on identifying issues associated with both the design of the systems and whether the as-built components will meet the design requirements to support experimental operation.
- An external review panel reviewed the DVVR assessments in two separate reviews and provided an independent analysis of the proposed corrective action and issued an additional set of high-level recommendations. The panel made significant recommendations on four high-level programmatic decisions regarding the inner poloidal field coils, limitations to the required bake-out temperature needed for conditioning of the vacuum vessel, divertor and wall protection tiles, and coaxial helicity injection.
- A detailed Corrective Action Plan (CAP), Conceptual Design Review (CDR), and an independent Cost and Schedule Review (CSR) have been completed.

- **Executive Summary for Facility and Diagnostics**

- **Facility and Diagnostic Milestones**

- Diagnostic Milestone D(17-1): Complete installation and preliminary commissioning of the pulse burst laser system. The Pulse Burst Laser System was completed and the system operated to verify proper performance at the specified laser pulse repetition rates and energy per pulse. This milestone is complete.

- **Executive Summary of Research Results – FY17 Milestones**

- *R(17-1): Simulation-based projection of divertor heat flux footprint for NSTX-U*

- XGC1 simulations of projected NSTX-U 1MA and 2MA scenarios have been carried out to investigate the projected heat-flux width as a function of plasma current. The results indicate that the 2MA projected scenario has SOL widths that are significantly larger than the Eich-Goldston scaling. Further, there are (preliminary) indications that enhanced electron turbulence is a potential cause of this heat-flux spreading. This result has potentially important implications for the projected peak heat flux for NSTX-U at 2MA and for ITER which is also projected via XGC1 simulations to have wider SOL widths than the Eich-Goldston scaling due to enhanced SOL turbulence.

➤ *R(17-2): Advanced divertor operating scenario modeling for NSTX-U*

- Models of advanced divertors in NSTX-U, including snowflake and X-divertor configurations, have been developed using the EMC3-EIRENE code. The impact of 3D fields on the advanced divertors has been previously studied. These simulations enabled studies of the 3D fields on neutrals distribution and core fueling in the advanced divertors: core fueling may be reduced due to a reduced number of edge higher-energy neutral particles with applied 3D fields.
- Detailed studies of plasma response to the externally applied $n = 3$ magnetic perturbations in the snowflake divertor configuration was investigated using the two-fluid resistive magnetohydrodynamic code M3D-C1. The modeling enabled predictions of magnetic field lobe structure in the divertor.
- A new numerical mesh generation code Gingred has been developed to enable grid generation for arbitrary snowflake divertor configurations. The snowflake-minus and snowflake-plus grids generated for NSTX-U parameters were used in the multi-fluid code UEDGE simulations to study radiation and transport in snowflake divertors.

➤ *R(17-3): Identify, mitigate, and develop correction strategies for intrinsic error field sources in NSTX-U*

NSTX-U operation was observed to be strongly affected by the presence of non-axisymmetric magnetic field errors. Here we document metrology data obtained after the FY16 NSTX-U operational campaign, and use that data to estimate the magnitude of field errors from the TF center stack bundle, the PF5 coils, and the OH coils. The plasma response to these field errors is also calculated using IPEC/GPEC and M3D-C1. Then, reinstallation strategies for mitigating the TF and PF5 error field sources are considered. Finally, efforts to improve 3D magnetic field sensor compensations in support of dynamic error field correction are detailed. In summary,

- The field error introduced by misalignment of the TF center stack bundle is between 5 and 10 G in the scenarios considered here. This significantly exceeds the limit of 1 G of 2/1 resonant field prescribed by the NSTX Center Stack Upgrade General Requirements Document (GRD) [R17-3-1], and also exceeds the maximum 2/1 resonant field that can be produced by the NSTX-U RWM coils (~6 G).
- By all metrics considered, the $n = 1$ error fields from the OH coil and PF5 are subdominant to that from the TF. This is true despite the relatively weak coupling between the TF error field and the plasma, because of the large magnitude of the TF error field. The 2/1 resonant error field from the OH coil is found to especially small, at less than 1 G with 24 kA of OH current.
- The resonant current due to TF error is comparable to that produced by 1 kA in the NSTX-U RWM coils, and the optimum correction to the TF error field is found to vary as the q profile and plasma shape evolves. These findings are consistent with experimental evidence that the optimum error field correction evolves during the current ramp, and suggest that a robust correction algorithm with the present TF error field source would need to depend on the (time-dependent) current profile.
- The error field due to the horizontal shift of the TF rod at the midplane couples more strongly to the plasma than does that from the tilt of the TF rod with respect to the vertical.

From the metrology data obtained after the initial NSTX-U campaign, the horizontal shift was ~5 mm, while the tilt was ~1.2 mrad.

- NTV from the TF and PF5 error may be significant in high-beta discharges. The PF5 error field will likely be able to be canceled by the RWM coils, but the TF error will not. To ensure that the NTV torque from the TF error can be adequately compensated by the neutral beams, the TF NTV should be reduced by an order of magnitude. This requires a factor-of-three reduction in the TF error field.
- The maximum perturbation to the pitch angle at the divertor targets due to the TF error field alone may approach 0.5° , with the largest perturbations on the vertical targets. These perturbations, while significant, are not presently believed to be large enough to merit concern.
- We recommend re-aligning the TF rod to reduce these field errors by at least a factor of three. Modeling indicates that this will reduce the resonant plasma response to levels that fall below the locking threshold scaling even in the absence of EFC, and will reduce the NTV torque to levels that can be reliably compensated by neutral beams. This reduction in error field can be achieved by re-aligning the center of the TF rod with a minimum accuracy of 2 mm.

➤ *R(17-4): Assess high-frequency Alfvén Eigenmode stability and associated transport*

The expanded parameter range achievable on NSTX-U with the 2nd NB line has provided insight into the fast ion phase space regions that are relevant for destabilization of high frequency Alfvénic modes (CAE/GAE).

- Experiments have shown that small amounts of beam ions with high pitch-angle values (pitch~1) injected by the new, more tangential beamlines can suppress strongly counter-propagating Global Alfvén Eigenmodes (GAEs).
- The non-linear HYM code was used to perform a quantitative analysis of these results, and simulations predict both the frequencies and instability of the GAE prior to, and suppression of the GAE after, the injection of high pitch-angle beam ions.
- HYM simulations further indicate strong energetic particle modifications to the ideal-GAE properties. These modifications depend primarily on the injection velocity for both co- and counter-propagating GAEs through the Doppler shifted cyclotron resonance condition.
- A new method of analyzing reflectometer measurements to determine the internal amplitude and structure of Compressional Alfvén Eigenmodes (CAE) and GAE density perturbations has been developed.
- A database on the instability threshold for CAEs and GAEs has been developed. A clear correlation emerges between the total power in the instabilities and the injected neutral beam power. A correlation between mode number and frequency appears to confirm the importance of the parallel resonance condition to destabilize the modes.

- Measurements from the high-k diagnostic potentially show evidence of coupling between CAEs and Kinetic Alfvén Waves (KAW), a process predicted in recent simulations by the HYM code.
- *R(17-5): Analysis and modeling of current ramp-up dynamics in NSTX and NSTX-U*
- The highest performance H-mode scenarios on NSTX and NSTX-U are enabled by achieving broad current and pressure profiles and large elongation ($\kappa > 2$) via an L-H transition early in the ramp up phase.
 - A database of NSTX and NSTX-U discharges demonstrates that the maximum elongation versus I_i operation space for the two devices is similar for $I_i \geq 0.8$ despite the increased aspect ratio of NSTX-U.
 - A corresponding database was created of vertical disruption events (VDEs) on NSTX and NSTX-U using an automated VDE search algorithm. The limit to the elongation by VDEs was more restrictive on NSTX-U than NSTX. Thus, NSTX-U achieved a similar elongation to NSTX by operating closer to the VDE stability boundary.
 - Calculation of the open-loop VDE growth rate found that NSTX-U achieved stable operation at larger VDE open-loop growth rates compared to NSTX due to improvements to the active vertical position controller. This is consistent with achieving stable operation closer to the vertical stability limit.
 - The elongation at the time of diverting was restricted ($\kappa < 2$) in NSTX-U operations by the occurrence of vertical oscillations (“the bobble”) as the discharge transitioned to a diverted shape.
 - Potential sources of the initial vertical motion are a mismatch at the time of transitioning between control algorithms, and a poor convergence of rtEFIT. An overshoot in the inner gap size exacerbates the vertical position oscillations by increasing the vertical growth rate.
 - Operational and scenario development improvements were identified that would reduce the probability of the deleterious oscillations. These include the removal of an algorithm transition within ISOFLUX at the time of diverting, improved rtEFIT reconstructions using multi-threading of the real-time calculation, an inner gap control algorithm that reduces overshoot and diverting with finite δ_{sep} .
 - A database of L-H transitions was created with a corresponding database of L-mode and dithering discharges with $P_{\text{NBI}} > 3$ MW. A set of four criteria for the database was developed that excluded all of the L-mode times from the database. The criterion informs the target conditions for triggering the L-H transition during ramp-up.
 - The lowest I_i discharges ($I_i \leq 0.55$) on NSTX-U were susceptible to fast disruptions after the L-H transition. MHD stability calculations of the ramp-up phase indicates the discharges were ideally stable and moving away from the no-wall stability boundary at the time of the disruption. Subsequent analysis indicated that the fast disruption was initiated by an H-L transition that was most likely driven by changes to the equilibrium due to vertical position oscillations.

Executive Summary for Additional Research Highlights

Boundary Science

➤ Summary of Research Highlights for Pedestal Structure and Control

- ELM stability analysis was performed using NIMROD on NSTX lithiated discharges to show that, in addition to the stabilizing effect due to the profile modifications, the enhanced η plays a key role in explaining the mechanism behind the complete ELM suppression in lithium-conditioned.
- Additional analysis has been performed on a database of EP-H modes to further understand this attractive scenario to be exploited on NSTX-U. The detailed analysis supports the hypothesis that the local ion collisionality is a criterion for the bifurcation into EP H-mode.

➤ Summary of Research Highlights for Divertor and Scrape-off Layer

- Further analysis of NSTX Gas Puff Imaging database revealed significant variations of 2D radial vs. poloidal cross-correlation functions of edge plasma turbulence. Possible causes for may include the misalignment of the GPI view with the local B field line, the magnetic shear of field lines in the edge, the poloidal flow shear of the turbulence, blob-hole correlations, and the neutral density 'shadowing' effect in GPI.
- Results from Gas Puff Imaging diagnostics on NSTX and Alcator C-mod tokamaks have been summarized in an invited review paper.
- A synthetic diagnostic based on neutral densities modeled by the neutral transport code DEGAS 2 in combination with time varying, 3D plasma simulations produced by the full-f edge gyrokinetic code XGC1 have been developed to analyze NSTX Gas Puff Imaging edge turbulence data.
- Divertor fluctuations were studied in NSTX-U L-mode plasmas using fast filtered cameras. Statistical analyses of near-separatrix filaments revealed divertor filament characteristics, such as correlation lengths, autocorrelation times, and probability distribution functions. Poloidal velocities were inferred to be 1 km/s for both inner and outer leg filaments. Motion was generally upward (towards X-point) in both legs, and no radial propagation was observed for outer leg filaments.
- Additional analysis of divertor heat flux profiles in the NSTX double-null configurations showed that the deposited heat flux profiles broadened as magnetic balance approached a perfect double null. The parallel heat flux profiles mapped to the outer midplane showed that the scrape-off layer width had no trend, while the scrape-off layer S parameter was systematically lower in the double null configurations as compared to lower single null configurations.
- EMC3-EIRENE modeling of coherence imaging diagnostic on MAST confirmed field aligned flows in the scrape-off layer with a direction away from the site of neutral puffing. This work was done in support of modeling of density control with 3D fields in future high performance NSTX-U discharges.

- Plasma response was successfully incorporated into 3D edge modeling of divertor fueling and exhaust using the EMC3-EIRENE code.
- Significant code developing and modeling was carried out in order to simulate snowflake divertor configurations for NSTX-U. With a new grid generation code Gingred and a multi-fluid edge transport code UEDGE it was possible to simulate radiation and plasma transport in snowflake-plus and snowflake-minus divertor configurations.

➤ **Summary of Research Highlights for Materials and Plasma Facing Components**

- Advanced computational simulations have been conducted examining the dynamics of the complex NSTX-U plasma-facing components including boron, carbon, oxygen, lithium, and deuterium. These simulations describe erosion and fuel retention processes at the atomic scale of the graphite PFCs once boron and lithium conditioning methods, and subsequent plasma bombardment, have altered the chemistry of the surface. These simulations are some of the first steps toward predictive simulations of the NSTX-U accounting for dynamically changing chemistry of the surfaces.
- Exposures of lithiated tungsten surfaces have been conducted to begin understanding the chemical interactions that may be present with future PFC materials. The effects of deuterium and helium bombardment on lithiated tungsten have been examined in both low-flux and high-flux experiments showing helium bombardment reduces the chemical indicators of hydrogen retention in the lithium coatings.
- Surface science computational and laboratory experiments are being incorporated into whole-device models of the NSTX-U in an attempt to understand integrated diagnostic signals from filterscopes or from the MAPP diagnostic. Evolution of boron and oxygen signals is qualitatively replicated by simulations of the NSTX-U L-mode plasmas in these simulations.
- The Plasma-Facing Components Requirements Working Group (PFCR-WG) has been formed to coordinate physics and engineering activities for the NSTX-U recovery project. The working group has coordinated input from the NSTX-U topical science groups as well as PPPL design engineers to develop refined physics requirements to maximize scientific flexibility of the NSTX-U while minimizing risks to future operations.

Core Science

➤ Summary of Research Highlights for Macroscopic Stability

- The Disruption Event Characterization and Forecasting (DECAF) code was expanded to analyze data from the TCV tokamak, including real-time MHD analysis signals. The presence of a mode and likelihood of its m/n numbers can be tracked, as well as the mode frequency, although a low frequency limitation does not yet allow tracking modes to the locking point in TCV.
- A module was written for the DECAF code that generalizes magnetic spectrogram analysis of MHD modes. This new portable code, written in Python, discriminates the toroidal mode number of instabilities and can track each mode as a DECAF event, monitoring the evolution of the mode through bifurcation and locking points. This is a critical new capability to allow disruption event characterization for general tokamak databases.
- DECAF analysis of NSTX-U plasmas also continued, including statistics on warning levels for tracking sawtooth timing and analysis of discharges reaching the Greenwald density limit, both of which had not been performed previously on NSTX data.
- Development of a fast time response electromagnetic disruption mitigation system continues, and this NSTX-U scale system has been operated and the most important parameters, the system response time and the attained velocities, have been verified.
- Efforts to generate an ITPA halo current rotation database in order to provide guidance to ITER have been completed. The resulting database, which now includes data from DIII-D, C-Mod, AUG, NSTX, and JET, is used to develop scalings of the halo current rotation duration and frequency. These scalings indicate that substantial halo current rotation below 20 Hz is possible in ITER such that dynamic amplification of halo current forces could occur during unmitigated disruptions. Additionally, halo current data from the center-stack of NSTX-U has been analyzed to provide guidance to the Recovery Project regarding the amplitude and toroidal peaking of center-stack halo currents.
- A review report on error field correction criteria for ITER has been successfully delivered to ITER organization through ITPA MHD and MDC-19 joint activities. The report addresses 3 critical charge questions, suggesting the retirement of vacuum 3-mode criterion but identifying research area to understand multi-mode resonant coupling and non-resonant error field effects. Collaboration on COMPASS using its unique high-field-side control coils showed decoupling between core and edge resonances as shown in NSTX-U TF (See R17-3), and collaboration with KSTAR using 3 rows of internal coils provided important data for quantifying remnant error field effects on transport.
- Collaborative experiments have been conducted in DIII-D to assess the scaling of the n=2 mode locking threshold with parameters such as the toroidal magnetic field and the applied field resonance spectrum. Locking was achieved with three different 3D coil configurations (i.e., resonance spectra), which indicates that n=2 error field correction is possible with outboard midplane coils as in NSTX-U. The toroidal field scaling, on the other hand, shows a strong negative dependence in the n=2 locking threshold with increasing B_T . This behavior has implications for both NSTX-U operations at 1T and for the n=2 error field correction strategy in

ITER.

- The NTV offset rotation profile, V_0^{NTV} , was directly measured and studied in the KSTAR tokamak that has shown for the first time strong, controlled rotation in the co- I_p direction at high electron temperature. Past experiments and associated theory have only considered that the NTV offset rotation can occur in the direction opposite to the plasma current. The new result is expected from generalized NTV theory that allows for electron and ion torques. Rotation in the plasma outer region exceeded 12 krad/s, quite significant compared to projections for ITER of approximately 2 krad/s in the pedestal region. Also, the V_0^{NTV} rotation profile shear is 15 times greater than measured in the intrinsic rotation profile (without 3D field). Experiments at higher T_e produced the strong co-rotation and rotation shear while higher density and lower T_e reduced these characteristics.
- The success of validating 3D MHD spectroscopy in DIII-D experiments extended the capability of external coils to qualitatively detect plasma stability. The method greatly helps to better understand underlying 3D MHD physics and the role of each eigenmode in RMP-ELM suppression. Therefore, this achievement also suggests the importance of installing NCC in NSTX-U experiments.
- Observations of core $n=1$ mode instability from the initial NSTX-U campaign have been analyzed and compared with NSTX data. This is done in part to test predictions that the change in aspect ratio would cause NSTX-U to exhibit a reduction in the stabilizing effect of field line curvature against tearing mode instability. The newly developed RDCON linear resistive stability code is employed to determine the classical stability of NSTX and NSTX-U discharges, for comparison with observations. The SXRFIT code for internal mode structure determination using soft X-ray cameras has been improved to include additional diagnostics and physics effects as well as improved algorithms. Mode identification is a key step in experimental stability analysis.
- The first benchmark of effort in full toroidal geometry has been carried out between RDCON and PEST3, with a good quantitative agreement. This work greatly improves the confidence of using RDCON and PEST3 in stability analysis of experimental data. Moreover, RDCON achieves better convergence than PEST3 in high-beta plasmas, which will be critical to NSTX-U applications. With this achievement, the work implementing RDCON into TRANSP to provide for NTM simulation has commenced.

➤ **Summary of Research Highlights for Transport and Turbulence**

- A series of L-mode discharges was run in NSTX-U to be used as a basis for validating gyrokinetic predictions at low beta and low aspect ratio. Gyrokinetic simulations showed that electrostatic ITG modes are unstable at low wavenumber, but with growth rates in the mid-plasma region that are smaller than the ExB shearing rates. This indicates that the ion transport is near neoclassical, and it is the electron channel that dominates transport in this region.
- ITG transport can be more important farther out, as indicated by the gyrokinetic simulations and turbulence measurements from the BES diagnostic. Microtearing modes may also be important in the outer regions of the plasma, according to the simulation results. BES measurements indicate that two modes may be unstable simultaneously in the outer plasma region, one propagating in the electron direction and one in the ion direction, consistent with the simulation results.

- Two approaches to developing a high-k scattering system synthetic diagnostic in the GYRO code for assessing Electron Temperature Gradient (ETG) modes have been developed in collaboration with an MIT graduate student. Considerable effort has gone into validating both methods using non-linear GYRO simulations of the CYCLONE Base Case.
- Non-linear global GTS simulations including self-consistent turbulent and neoclassical dynamics have been applied to NSTX H-mode discharges in which the density gradient-driven DTEM turbulence is unstable. It was found that the neoclassical bootstrap current is affected strongly by the DTEM turbulence, influencing both the magnitude and profile of the current density.
- Progress has been made on updating the Startsev-Lee scheme to include toroidal electromagnetic effects in the GTS code to simulate tearing and microtearing modes, as well as the transition between ITG and kinetic ballooning modes. While most of the initial work was done in circular geometry, recent developments have been made to handle generalized geometry, and preliminary validation studies have started.
- The XGC1 code has been updated to include electromagnetic effects in one of three ways, and the code has been used to study the stability of the NSTX/NSTX-U edge plasmas. The XGC1 results show how the strong toroidicity at low aspect ratio can distort the finite beta tearing parity modes and also predicts the transition from ITG to KBM modes at a beta value that is consistent with that inferred from linear GYRO simulations.
- Two transport-related experiments were carried out on DIII-D under the umbrella of the dedicated NSTX-U campaign on that device. The first was titled “Study of collisionality dependence of ion- and electron-scale turbulence in advanced inductive hybrid scenario with ST-relevant q_0 ” and the second was titled “Validating electromagnetic effects in high performance plasmas”. Both experiments addressed topics related to NSTX-U transport research thrusts.
- The results of the perturbative momentum transport experiment performed in MAST to investigate the momentum pinch in L-mode plasmas was recently published. The work showed that a very weak momentum pinch is predicted in ST L-mode plasmas, and this agrees with the results inferred from the experiment.

➤ **Summary of Research Highlights for Energetic Particles**

- Initial NSTX-U operations with the 2nd more tangential NB line in FY-16 have substantially increased the parameter space for EP research.
- Suppression of high-frequency Global Alfvén eigenmodes (GAEs) with tangential NBI has been documented. Experimental results have been compared with GAE theory. Extensive comparison with predictions from the HYM code has started, showing good agreement between theory and experiments.
- Characterization of CAEs, Global AEs (GAEs) and Ion Cyclotron Emission (ICE) has expanded beyond the parameters space previously achievable on NSTX.

- Destabilization of counter-propagating toroidal Alfvén eigenmodes (TAEs) have been observed. TRANSP simulations augmented with a reduced EP transport model (kick model) compare well with the experiment in terms of toroidal mode number, frequency and timing of destabilization of the unstable modes.
- Stationary, 2-sec long L-mode discharges with sawteeth have been achieved on NSTX-U. Improvements to existing sawtooth models in TRANSP are being explored for a cross-machine validation of sawtooth effects on EP transport.
- Improved analysis techniques have been developed for EP-related diagnostics, including reflectometers and FIDA systems.

Integrated Scenarios

➤ **Summary of Research Highlights for Solenoid-Free Start-up and Ramp-up**

- New collaborative experiments on the QUEST facility in Japan were carried out. In experiments led by researchers from the University of Washington and PPPL, up to 48 kA of plasma current was generated using Coaxial Helicity Injection. In separate collaborations by PPPL researchers, up to 85kA of plasma current was generated using 230kW of 28GHz ECH/EBS power.
- Predictive TRANSP free-boundary transport simulations were used to study the dependence of the non-inductive current drive fraction on applied toroidal field and high-harmonic fast-wave heating and current-drive power in $I_p \leq 300$ kA NSTX-U discharges. Results from the TORIC full wave spectral code indicate full non-inductive current drive is possible for toroidal fields above 0.75T and coupled RF powers above 2-2.5MW.

➤ **Summary of Research Highlights for Wave Heating and Current Drive**

- The RF group has repaired and refurbished the HHFW detection circuits for antenna voltages, currents and phase, and has advanced installation of several HHFW diagnostics.
- The full-wave simulation TORIC has been extended to include the effects of arbitrary ion distribution functions on the wave propagation and absorption, and the extended code has been applied to NBI-driven discharges on NSTX.
- The full wave code AORSA has been used to extend helicon simulations to include the SOL. These simulations show the existence of another mode in the SOL that can perhaps cause significant SOL losses at high SOL densities.
- Collaborations with QUEST continues with modeling of EC and EBW and experiments in EC-assisted start-up and EBW current drive.
- The two-dimensional full-wave code FW2D was adapted to tokamak geometry to incorporate a more realistic vessel boundary into studies of SOL losses of HHFW power. The vessel boundary is found to significantly affect the FW propagation in the SOL.

- The RF-SciDAC project was awarded funds for the next 5 years.
- Annulus resonances are modes found in a cylindrical model that could potentially explain the SOL of HHFW power. We evaluated their impact on the three-dimensional wave-field reconstructions and have found cases where over half of the wave power is trapped in the edge.
- Experiments aimed at studying the fundamental properties rectification and its detection were conducted on the Large Plasma Device (LAPD) at the University of California Los Angeles. Particular attention was paid toward the distinction of rectified current versus rectified voltage in support of findings on NSTX.
- Experiments were conducted on EAST to study the interaction between ICRF heating and the SOL plasma. The floating potential of divertor probes increases significantly if the probes connect magnetically to the antennas and decrease otherwise; this change is suppressed with midplane gas puffing.

➤ **Summary of Research Highlights for Advanced Scenarios and Control**

- The description of the conducting structures of NSTX-U has been included in the TokSys Modeling Framework for developing and testing real-time control on NSTX-U. Simulated magnetic measurements are in good agreement with field-only tests.
- A collaboration on startup and ramp-up development was initiated with MAST-U. The first activities included applying the LRDFIT code to evaluate direct induction startup on MAST and MAST-U and compare to NSTX and NSTX-U results.
- An experiment on DIII-D demonstrated a new feedback algorithm that leverages the real-time beam voltage and perveance control to provide simultaneous feedback on the plasma power, torque, energy and rotation. The feedback system builds on the control design approach developed for NSTX-U.

Performance of FY2017 Notable Outcomes:

Notable 1 - Objective 2.1: *FES: Complete an extensive extent-of-condition review of NSTX-U to identify all design, construction, and operational issues. Prepare a corrective action plan (CAP) to include cost, schedule, scope, and technical specifications of actions. Provide an interim progress report by March 31, 2017, and complete the CAP review and send the final report to DOE by September 30, 2017.*

Notable Report:

The National Spherical Torus eXperiment –Upgrade (NSTX-U) has a critical and unique role in the US fusion science program to:

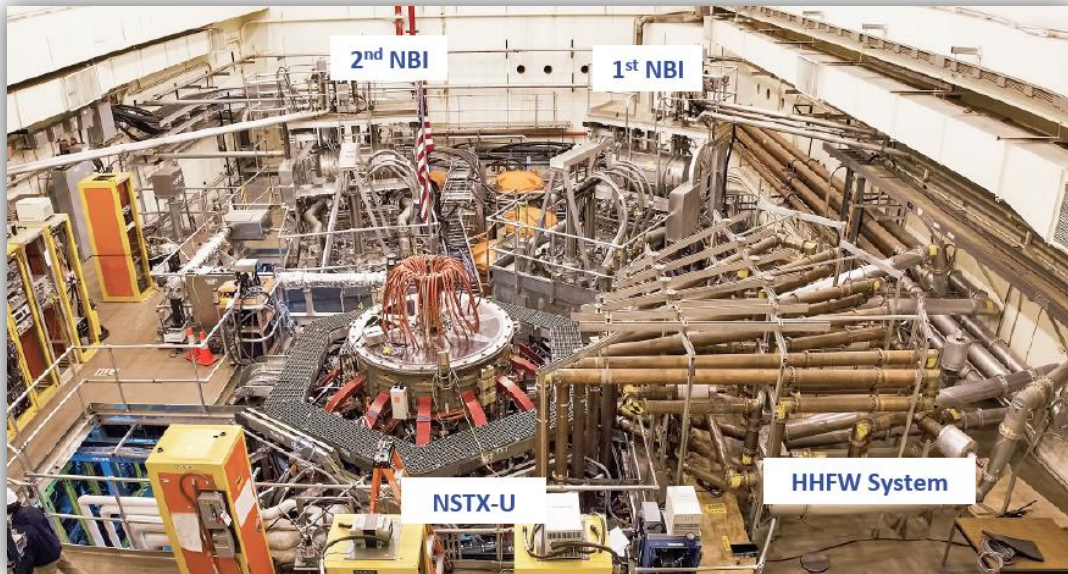
- Explore unique parameter regimes to advance predictive capability - for ITER and beyond
- Develop solutions for the plasma materials interaction challenge
- Advance the understanding of the ST configuration for the next generation fusion devices

To study these important scientific issues, the NSTX device underwent a major upgrade to replace the central magnet composed of inner toroidal field conductors and central solenoid as well as to add a second neutral beamline. These upgrades enable an increase in the toroidal field, plasma current, heating power, and pulse length. On September 25, 2015, the Department of Energy completed its review of the upgrade project and approved project completion. Afterwards, testing continued on NSTX-U and operation of plasma experiments began.

The NSTX-U device experienced a series of technical problems; the most recent of which was the failure of one of the poloidal magnetic field coils, which rendered the device inoperable and in need of significant repair. The causes of these problems are attributed to technical, operational, and procedural issues. As a result of these incidents, the Laboratory performed a very comprehensive analysis of all of the systems on NSTX-U. Through an integrated system's analysis approach, this process identified which actions need to be taken to form a corrective action plan to ensure reliable and predictable operation. Twelve Design Verification and Validation Reviews (DVVRs) were conducted by external and internal scientists and engineers that focused on identifying issues associated with both the design of the systems and whether the as-built components will meet the design requirements to support experimental operation. In addition, an external review panel, chaired by Tom Todd from the UKAEA (retired) reviewed the DVVR assessments in two separate reviews and provided an independent analysis of the proposed corrective action and issued an additional set of high-level recommendations. The panel was composed of scientists and engineers from the US and the international community identified and made significant recommendations on four high-level programmatic decisions regarding the inner poloidal field coils, limitations to the required bakeout temperature needed for conditioning of the vacuum vessel, divertor and wall protection tiles and coaxial helicity injection.

At the request of DOE/FES and as part of the Notable deliverable, PPPL is also providing cost and schedule estimates to facilitate out-year budget planning. The technical Conceptual Design Review (CDR) and an independent Cost and Schedule Review (CSR) have been completed. The CAP, CDR, and CSR reports and/or URLs are available upon request.

NSTX-U FY2017 Year End Report: Facility and Diagnostics



Aerial view of the NSTX-U Test Cell showing Neutral Beam Injection (NBI) and High-Harmonic Fast Wave (HHFW) heating systems in the background.

Much of FY2017 was dedicated to responding to Notable 1 - Objective 2.1: FES: “Complete an extensive extent-of-condition review of NSTX-U” (as described in the previous section) with a mission to bring NSTX-U to full performance with high reliability. Nevertheless, important non-Recovery NSTX-U facility and diagnostic activities were also carried out in FY2017 as described below.

Facility and Diagnostic Milestones for FY2017

Facility Milestone F(17-1): Complete installation and preliminary commissioning of the pulse burst laser system. (September 2017)

Description: The purpose of the pulse burst laser system (PBLS) is to measure the electron density and temperature evolution of edge and core transient plasma phenomena using bursts of high-repetition-rate Thomson scattering. The PBLS is designed to provide a steady state 30 Hz repetition rate, in addition to two modes of burst operation: a) a slow burst mode at 1 kHz repetition rate for 50 ms, and b) a fast burst mode at 10 kHz for 5 ms. The PBLS has been characterized in the laboratory and will be installed on NSTX-U during FY2017. The PBLS system will undergo preliminary commissioning in the absence of plasma. This commissioning consists of energizing the laser power supplies and flashing the flashlamps of the laser head.

Report: Installation of the PBLS was completed in FY2017. The laser power supplies were installed on the ground floor of the NSTX-U gallery, adjacent to the Test Cell, as shown in Figure F17-7-1. The PBLS laser head was installed on a supporting cradle

mounted to the wall in the mezzanine in the gallery area (above the power supplies) where the existing Thomson Scattering lasers are located. The installed laser head is shown in Figure 2. Initial testing of the power supplies was performed to verify proper operation prior to connection to the PBLS laser head. The cabling between the power supplies and the laser head was then completed. The installed PBLS laser was successfully operated in August 2017. The laser pulse repetition rate and energy per pulse were measured in three operating regimes to verify operation of the installed system, completing Facility Milestone F(17-1). The achieved parameters were: 1) 1.5 J/pulse at 30 Hz repetition rate; 1.5 J/pulse at 1 kHz; and 1.6 J/pulse at 10 kHz. Prior to resumption of NSTX-U operation, the PBLS laser beam will be combined with the beams from the two existing Thomson scattering lasers and the system will be aligned and calibrated in preparation for experimental operation.



Fig. F17-1-1: Installed PBLS power supplies.



Figure F17-1-2: Installed PBLS laser head.

Upward Evaporator System Development

On NSTX, lithium was used for conditioning plasma-facing components (PFCs) to improve discharge performance. Two lithium evaporators (LITERs) were mounted on the upper dome of the vacuum vessel to deposit a lithium coating on the lower divertor region. To increase PFC coverage with lithium, an upward lithium evaporator (ULITER) has been designed. [Dang Cai, Robert Kaita, and Richard Majeski, SOFE-2017] A schematic of the ULITER is shown in Figure FD-1. The lithium is contained in a porous evaporator, which can be preloaded and readily replaced under argon. The evaporator fits around a heating element for temperature control that allows adjusting the evaporation rate. The test configuration in Figure FD-1 also includes a rotary feedthrough for turning the porous evaporator, and a “drip tray” to catch any liquid lithium that might fall as the temperature is increased.

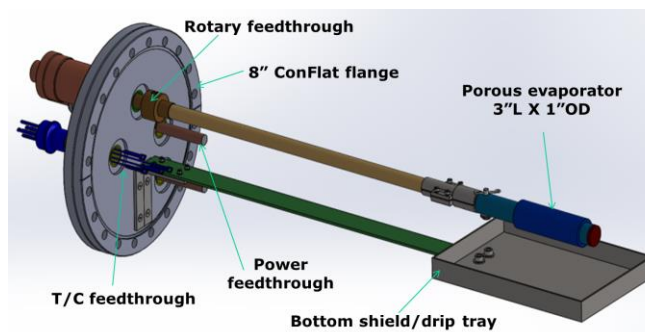


Fig. FD-1. ULITER schematic showing lithium filled porous evaporator at end of rotatable shaft. Test apparatus includes “drip tray” to catch any liquid lithium that might fall from porous evaporator.

The thermal mass of the ULITER is significantly lower compared to the LITER, and the heating element is more closely coupled to the lithium reservoir. Because of the long heating and cooling times for the LITERs, they had to be kept at temperature even when evaporation into the vacuum chamber was not desired. This is no longer a requirement with the ULITER due to its faster thermal response, and should result in more efficient lithium usage.

The porous evaporator is intended to be a commercially-available 3” long, 1” OD and 0.75” ID porous SS 316 tube. A major unknown was its lithium capacity, so fill tests were performed with stainless steel tube samples of various porosities. The tests were conducted in an argon-filled glovebox with O₂, H₂O and N₂ levels controlled to be less than 1 PPM at room temperature, using the apparatus shown in Fig. FD-2.



Fig. FD-2: Apparatus showing porous evaporator sample suspended over lithium pool in container with band heater

They indicate that regardless of porosity, 100% of the expected lithium fill percentage is achieved at a liquid lithium pool temperature of 500C. It was also observed that no lithium dripping occurred when the samples were raised above the lithium pool. The next step is to assemble the apparatus in Fig. FD-1, and measure the distribution of the lithium evaporated into a test chamber.

Electromagnetic Particle Injector (EPI) – Providing a rapid response for the onset of disruptions in ITER is an important issue. A novel system termed the Electromagnetic Particle Injector (EPI), based on the rail-gun concept, was proposed to address this challenge. The system consists of a 1m long rail gun powered by a 20mF, 2kV capacitor bank. The capacitor bank parameters are essentially the same as that used for the transient CHI experiments on NSTX. The EPI is fully electromagnetic, with no mechanical moving parts, which ensures high reliability even after being in “standby” for long periods. In addition to responding on the required fast time scale, its performance is projected to substantially improve when operated in the presence of a high magnetic field. The system is also suitable for installation in close proximity to the reactor vessel. We have now operated this NSTX-U-scale system and have been able to verify the most important parameters, i. e., the system response time and the attained velocities. The performance is consistent with the model calculations, giving confidence that larger systems can be built to attain the target goals. The results from the operation of the EPI were presented at the 2016 IAEA Fusion Energy Conference. [see more details in the MHD section.]

Far-infrared Interferometer/Polarimeter

The purpose of the Far-infrared Interferometer/Polarimeter (FIReTIP) is to provide time-integrated measurements of the line-averaged plasma density [E. R. Scott, et al., RST 2016]. The FIReTIP system is a heterodyne interferometer, which requires two beams of differing frequencies to determine the sign of the phase difference between the beam that passes through the plasma and the reference beam. The FIReTIP layout is shown in Fig. FD-3.

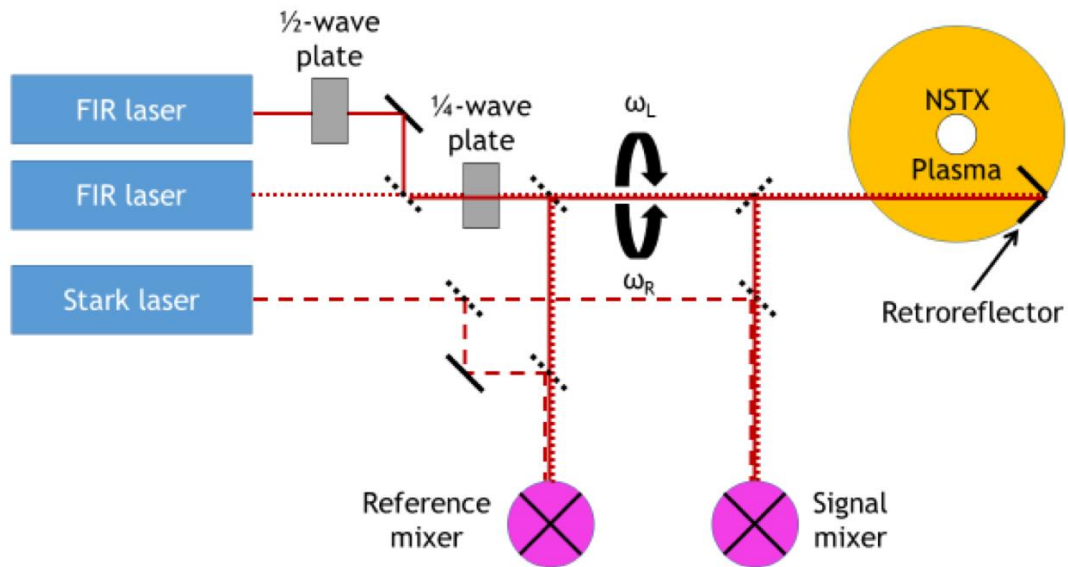


Fig. FD-3: Layout showing basic components of FIREtIP system. The Faraday rotation angle can be determined from difference in the phase shifts introduced with the $\frac{1}{2}$ -wave and $\frac{1}{4}$ wave plates, and hence the parallel component of the magnetic field.

There are three 118.8 μm methanol lasers in the FIREtIP system. The laser wavelength was chosen to reduce the effects of plasma refraction, and the large Stark splitting of the 118.8 μm methanol line. By applying an external electric field, a 5 MHz shift in the lasing frequency could be obtained.



Fig. FD-4 a) Enclosure for FIREtIP lasers (left) and b) waveguide in NSTX-U Test Cell (right).

In FY17, all three FIREtIP lasers were installed in an enclosure outside of the NSTX-U Test Cell (Fig. FD-4a). The mounting of the waveguide for the laser beams was also completed from the laser enclosure to the NSTX-U vacuum vessel (Fig. FD-4b). To minimize the space required for the reference waveguide, the tubes were installed in a folded geometry to match the path for the beam that passes through the plasma.

Densities obtained with FIRETIP can be affected by spurious phase shifts from any difference between the reference beam path and the distance traveled by the beam that passes through the plasma. This means that measurements are sensitive to vibrations that affect the beam, and they must be compensated for if FIRETIP is to be used for real time density feedback control.

One approach to vibration compensation is to use adaptive filtering. An example is the Kalman filter. The first step involves the prediction of the state of the system based on its prior state, using a state-space model of the system. The second step involves an update of the state of the system, based on the predicted state and a measurement taken of the system, with weighting that favors higher certainty. By iterating the steps, the process reduces the effects of unwanted disturbances to the system. Because only previously calculated states and uncertainty matrices and present measurements are involved, the algorithm is amenable to real time application.

The Kalman filter approach was tested for the FIRETIP system. The corner cube retroreflector was identified as a component that was sensitive to vibrations (Fig. FD-5a). The state-space model was obtained by striking the vacuum vessel with a brass hammer (Fig. FD-5b). While it was not practical to hit the retroreflector, a midplane port cover outside the NSTX-U vacuum vessel was chosen as a location that would result in a similar response.

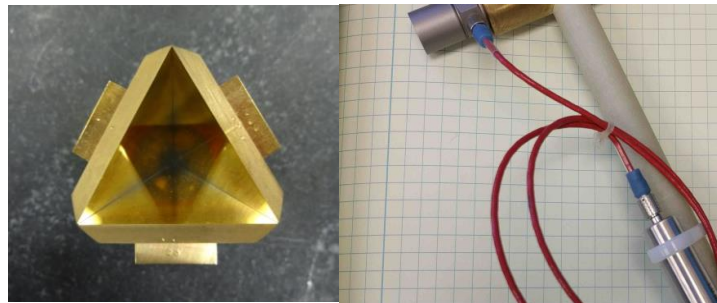


Fig. FD-5 a) Retroreflector located on midplane inside NSTX-U vacuum vessel (left) and b) brass hammer used to get system response for state-space model.

The measured and modeled response is shown in Fig. FD-6. The state-space model was then used in an application of the Kalman filter to simulated data. The uppermost trace in Fig. FD-7 represents the line-averaged density during the current ramp phase in NSTX-U, with noise that included a sinusoidal component added. The lower traces are the densities without noise and after the application of the Kalman filter. The similarity of the curves reflects the effectiveness of the Kalman filter in noise reduction. [E. R. Scott, Ph. D. Thesis, Department of Mechanical and Aerospace Engineering, University of California at Davis (2017)].

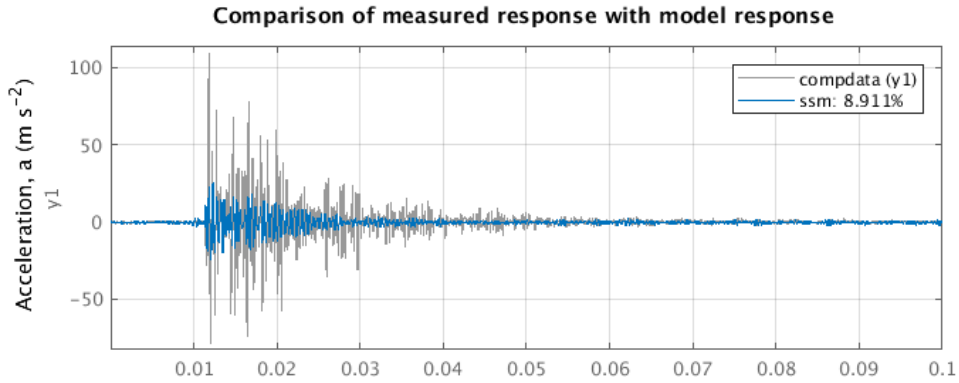


Fig. FD-6: Comparison of measured (gray trace) and modeled response (blue trace) for response of NSTX-U vacuum vessel to impulse on midplane.

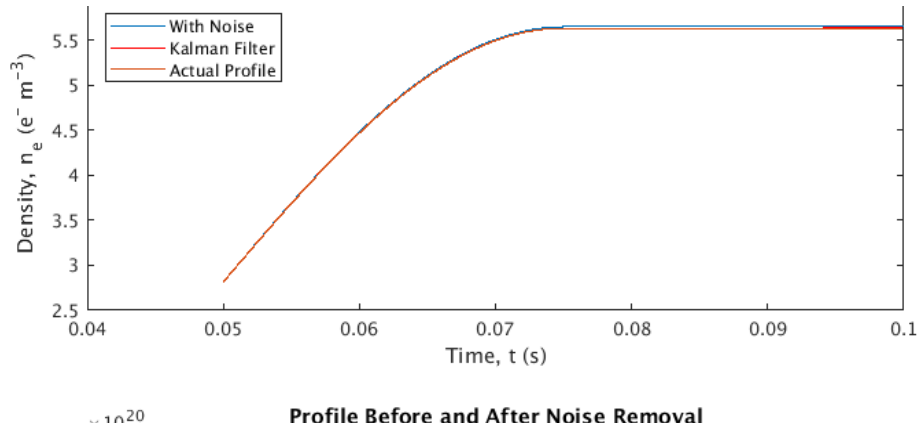


Fig. FD-7: Simulated data with upper curve showing line-averaged density during plasma current ramp up in NSTX-U with noise added. Similarity of lower curves shows effectiveness of Kalman filter in noise removal.)

High-k Scattering System

The high-k scattering system is intended to investigate electron thermal transport through the observation of turbulent fluctuations by the coherent scattering of electromagnetic waves. The high-k system on NSTX was designed to resolve the radial component of the fluctuation wave vector by detecting the scattering in the plasma midplane. In contrast, the NSTX-U high-k system will measure the poloidal component of the fluctuation wave vector with an array of detectors with a poloidal view of the plasma. The geometry is shown in Fig. FD-8.

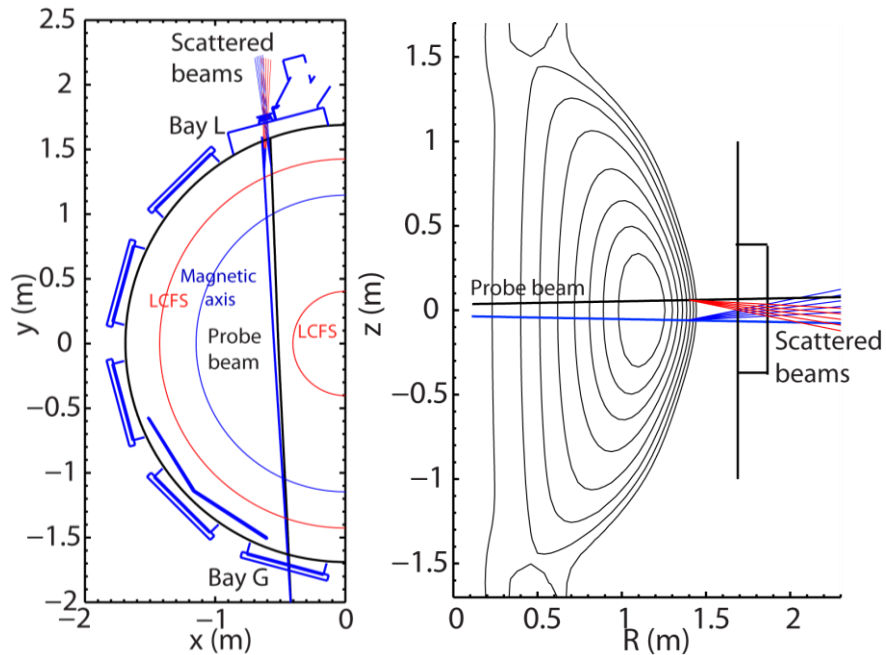


Fig. FD-8. Midplane plan view (left) and poloidal elevation (right) of high- k scattering system on NSTX-U. The probe beam enters the vacuum vessel at Bay G and leaves at Bay L. The scattered beams are detected with an array of mixers in the poloidal plane.

A successful final design review for the NSTX-U high- k scattering system was held on May 12, 2017. The first major element consists of the lasers that are the required to create the probe beam. An Edinburgh Instruments PL-G CO₂ laser is used to optically pump a far infrared formic acid laser, which produces the 88 mW probe beam at 693 GHz (432 mm). These lasers are presently at the University of California at Davis, and will share the laser enclosure described in the FIRE TIP section.

The probe beam will be transmitted from the laser enclosure to the NSTX-U vacuum vessel through about 20 meters of corrugated overmoded waveguide. The waveguide sections have been fabricated and are ready for installation. Since much of the high- k waveguide run follows the same path as the FIRE TIP waveguides, they share common supports.

The scattered beams pass through a rectangular port on Bay L. A special window made of fused silica was purchased to minimize transmission losses. A receiver carriage was also designed fit within the tight space constraints. It includes a five-axis mechanism that allows position adjustment of the mixer arrays for detecting the scattered beams. The Bay L port cover and a model of the receiver carriage are shown in Fig. FD-9.

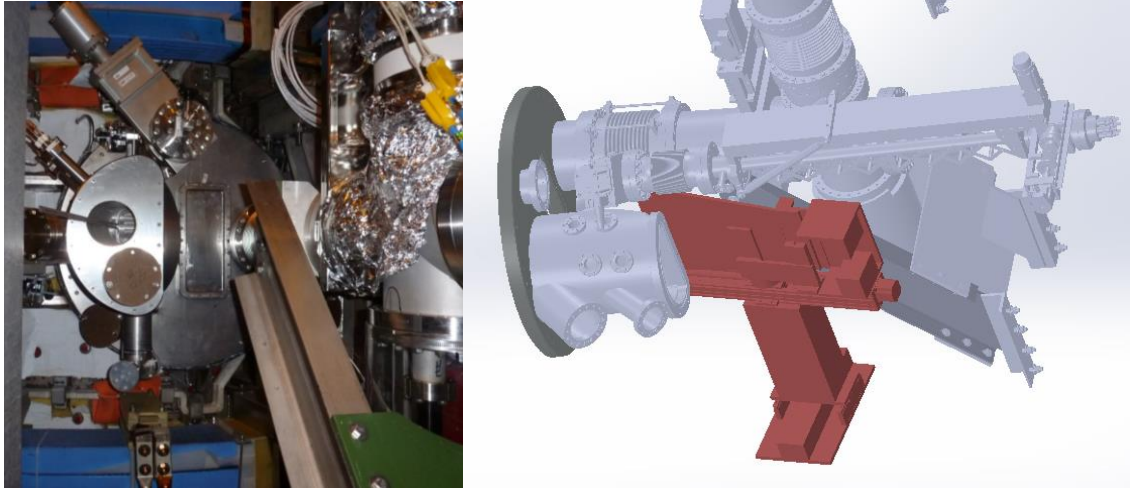


Fig. FD-9: Bay L port cover (left) and model of receiver carriage for high-k scattering system (right).

Multi-Energy Soft X-ray Diagnostic - The upgrades to the Multi-Energy Soft X-ray diagnostic amplifier electronics have been completed, with delivery expected in Fall 2017 by the Johns Hopkins University team. The upgrades are intended to reduce the impact of the NSTX-U environmental noise, specifically the noise from the Switching Power Amplifiers (SPAs) that energize the magnetic coils. As such, a reconfiguration of the pre-amplifier and second stage amplifiers will allow a continuous shield from the diagnostic to the machine. Additionally, 5-pole Butterworth 350kHz noise filters have been added on the input stage of the second stage amplifiers to attenuate the ~800kHz SPA noise. Finally, the second stage output has been converted to a true differential output to reduce the noise pickup over the cabling to the digitizer rack. After delivery, these electronics will be bench-tested, and then tested on one or more tokamak experiments (e.g. EAST, J-TEXT, LTX) in preparation for eventual deployment on NSTX-U when it restarts operation. This time window will also allow additional iterative design improvements as needed.

Transmission Grating Imaging Spectrometer – The JHU group has completed the design and has started construction of the Radiation-hardened Transmission Grating Imaging Spectrometer. The previous TGIS used a direct detection CCD camera as the imaging sensor, which will become incompatible with the higher neutron fluence in NSTX-U. Therefore, this detector will be replaced with a combination of a phosphor plate, MCP imaging intensifier, and fiber optic imaging bundle that will transport the TGIS measurement to a high sensitivity ProEM Princeton Instruments camera inside of a radiation shield box. Currently, the design of the MCP flange is being finalized with Proxitronix and delivery and final assembly is expected early 2018.

Neural Network Analyses for X-ray Diagnostics - The JHU group has continued development of its machine learning Neural Network algorithms that are designed to extract complex information out of simple X-ray diagnostic measurements. Fast temperature profiles using ME-SXR measurements have already been demonstrated, and the technique is now being extended to extract fast radiated power measurements from AXUV diode arrays. This technique relies on the

use of slower foil-based bolometer diagnostics to train the Neural Networks with the raw AXUV signals, along with auxiliary information, such as VUV spectroscopy data, as inputs. Once the Neural Networks have been trained, the AXUV diagnostics can then provide accurate and fast ($>10\text{kHz}$) measurements of radiated power. This novel technique is one way to overcome the non-linearity of the AXUV response and overall inaccuracy when it comes to total radiated power. This technique is being developed using data from the Alcator C-mod experiment, and will be applied to the ME-SXR AXUV diode system on NSTX-U by using the vertically adjacent foil bolometers. Figure FD-10 shows results from the uncorrected AXUV and Neural Network output compared to foil bolometry using C-Mod data.

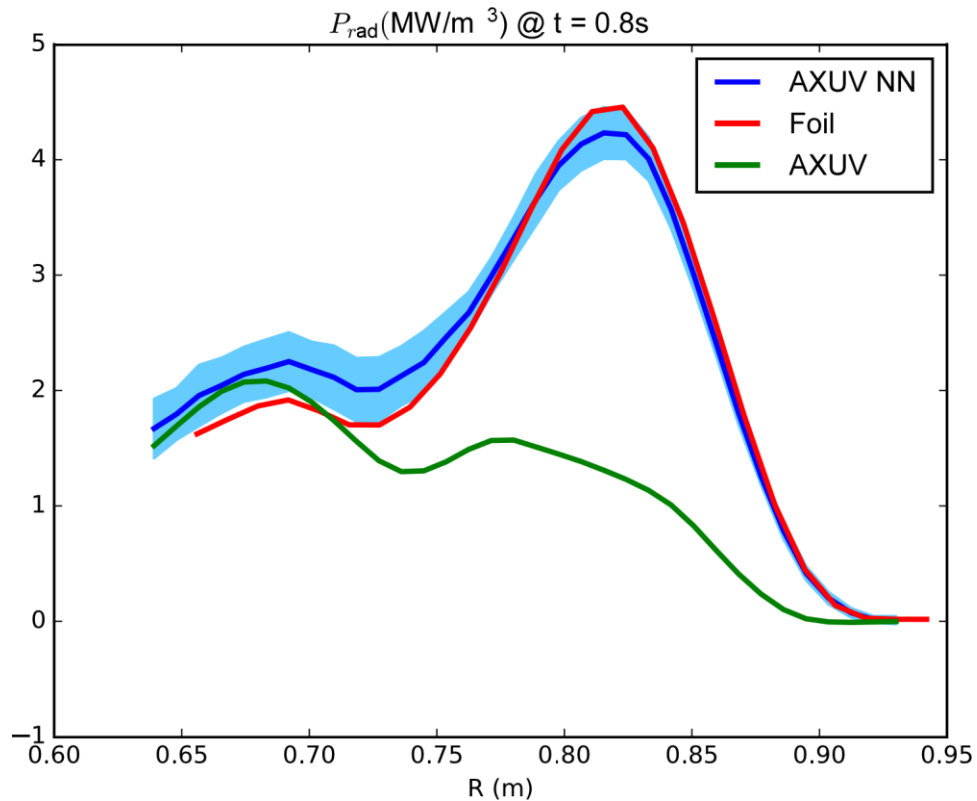


Fig. FD-10: C-Mod Radiated power profile from Neural Network trained with foil bolometers using AXUV diodes and spectroscopy as inputs (blue) compared to uncorrected AXUV (green) and baseline foil bolometer measurements (red)

Multi-Energy Soft X-Ray Imaging Diagnostic (ME-SXRI) – The NSTX-U multi-energy soft x-ray imaging diagnostic system (ME-SXRI) is being prepared for installation on the MST and DIII-D devices. A successful CDR was conducted in August 2017 for the ME-SXRI system for MST. For the DIII-D ME-SXRI system, the physics validation review will be conducted in the near future. A new computational tool for ME-SXRI was developed that can be used to calculate how many x-ray photons will impinge on the new multi-energy cameras to be installed on MST and DIII-D as well as NSTX-U. This capability can be also applied to other tokamaks, including ones in Japan.

Doppler backscattering and cross-polarization scattering systems for NSTX-U - The UCLA team successfully tested the high frequency Doppler backscattering (DBS) system on the DIII-D tokamak. This four-channel DBS system was designed to go onto NSTX-U at the Bay J mid-plane. Construction and lab tests of this system were successful and UCLA was in the final planning stages to install the system on NSTX-U. This installation was delayed due to the NSTX-U recovery effort. After consultation with DOE-OFES and NSTX-U management, it was decided to install the system on the DIII-D tokamak for testing and physics use during the NSTX-U recovery period (Figure FD-11).

DBS is a scattering method that measures local intermediate to high wavenumber density fluctuations (\tilde{n}) and turbulence flow as well as lower frequency MHD type disturbances such as GAMS, EHOs, etc. After the NSTX-U recovery is completed, UCLA will install the four-channel DBS system on NSTX-U, followed by installation of a cross-polarization scattering system (CPS). CPS is a new method that measures local, internal magnetic fluctuations \tilde{B} using a sensitive scattering technique. Both measurements are expected to contribute strongly to the NSTX-U science program.

In addition to the foregoing, the UCLA eight-channel V-band reflectometer system was also temporarily transferred to DIII-D to support DOE-sponsored research there (see Fig. FD-11). This was also after discussions with both DOE and NSTX-U. This system was operated for both DBS as well as multi-channel fluctuation reflectometry. Both systems have performed very well, with the high frequency DBS system passing all plasma tests. They have added significantly to the science program at DIII-D, and also to the ‘NSTX-U National Experimental Campaign on DIII-D’. These systems were also utilized by UCLA graduate student Ms. Shawn Tang, who led a DIII-D experiment as part of the ‘NSTX-U National Experimental Campaign on DIII-D’.

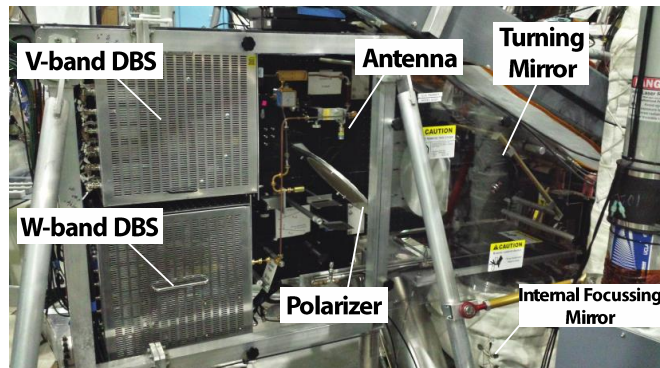


Figure FD-11: Modular Doppler backscattering systems (V and W-band) from the UCLA–NSTX-U collaboration project. Installation at the DIII-D tokamak is shown. The tokamak vessel is to the right in this photo. The systems have produced interesting and useful data in the short time they have been at DIII-D.

Graduate student Yusuke Iida from the University of Tokyo completed his visit to PPPL under Dr. Shigeyuki Kubota of UCLA. Iida learned to run beam tracing and 2-D full-wave (FWR2D) codes for studying microwave beam propagation and scattering in toroidal plasmas. Target magnetic equilibria from the University of Tokyo's TST-2 device were also used. These tools will assist the researcher in his graduate research, which involves installing and operating a microwave imaging reflectometer on the TST-2 device for density fluctuation measurements.

Motional Stark Effect – Collisionally Induced Fluorescence (MSE-CIF) – Operation of the MSE-LIF system during the FY16 run revealed some issues that hinder reliability and maintainability of the diagnostic neutral beam (DNB) and diode laser systems. Nova Photonics is in the process of designing and implementing improvements to the MSE-LIF system. Specifically, a design for improvements to the hydrogen gas delivery system passed a final design review, and modifications are currently being implemented. These changes are focused on improving control of neutralization in the DNB. In addition, R&D toward fiber coupling the diode laser is underway, with the goal of moving the laser system outside of the harsh environment of the NSTX-U Test Cell. Finally, maintenance on monitoring and support systems for the DNB is being conducted, and these systems are being reviewed to identify potential improvements.

New Main-Chamber and Divertor Resistive Bolometers – To enhance a variety of NSTX-U boundary physics and core transport research, improvements in the radiated power measurements were planned for the next operational period, led by Oak Ridge National Laboratory collaborators. Modifications to the divertor resistive bolometers fielded on NSTX and a new 24-channel mid-plane array of core resistive bolometers were originally planned and designed in FY16. This continued into FY17, completing designs of new pinhole cameras as well as completing fabrication and bench-top fit-checks of new assemblies, shown below. A summary of status and plans for NSTX-U radiated power diagnostics was given at APS-DPP 2016. In FY17, procurement was completed of new sensors to equip the mid-plane system, as well as two 24-channel D-tAcq BOLO8BLF systems for signal conditioning and digitization. These are new units, designed by D-tAcq in partnership with CCFE and Durham University in the UK. The latter sent staff to PPPL to assist CODAS in integrating units into MDSPlus and work with NSTX-U physicists to demonstrate the accuracy intra-shot calibration capability. An additional interface box to convert the ODU plugs from the resistive bolometer to the RJ45 input used by the BOLO8BLF was designed, built and tested by the PPPL electronics group. As shown in Figures FD-12 and FD-13, internal reflections would create systematic errors. The compatibility of a new stainless steel blackening process, MIL-DTL-13924D, was investigated for use on NSTX-U. While this process had been used successfully for decades on Alcator C-Mod, the higher bake temperature and compatibility with lithium deposition made further qualification necessary. Neither was demonstrated to be a problem, and testing for the lithium was done in collaboration with Dr. Andruczyk's group at University of Illinois. This method is being considered as a solution to replace Aerodag in NSTX-U, identified as important for the NSTX-U Recovery Project Diagnostic scope and also being considered for LTX- β . The Bay-G mid-plane bolometer camera shares flange space with The Johns Hopkins University ME-SXR system. Design modifications to the flange and ME-SXR components to incorporate bolometry were completed as part of this scope.

Attempts to field resistive bolometry on NSTX were unsuccessful due to sensor damage during bake and the new divertor pinhole cameras have been redesigned with improved thermal handling. Benchtop testing is planned to demonstrate cooling and investigate the diagnostics

response to transient cooling failure. ORNL has established a measurement and testing laboratory space at PPPL to accomplish this, as well as purchased a recirculating chiller to compare compressed air versus water cooling, an open DVVR CHIT. While the original FY16 planning had the bolometers to be completed by mid FY17, this was delayed due to overlapping Cognizant Engineering and Physics resources needed on the Recovery Project. In FY18, final thermal testing and blackening will be completed and the bolometers stored. Fabrication of new ME-SXR components on the Bay-G Midplane flange will also be completed. Radiation measurements are expected to be important for early post-Recovery NSTX-U commissioning operations and ORNL staff engaged in the Recovery Project will adapt bolometer systems to evolving needs of NSTX-U.



Figure FD-12: Bench-top test fit of the new 24-channel Bay-G Mid-plane bolometer pinhole camera. Inset shows the internal collimator design.

Figure FD-13: Bench-top test fit of new divertor pinhole cameras for Bay-J Upper (top) and Bay-I Bottom (lower). Inset shows the Bay-I Lower sensor cooling block with and without the new heat shield.

Energetic Particle Diagnostics - Fabrication of the Florida International University’s Fusion Products Diagnostic (FPD) probe head containing the six detector modules has been completed including a test assembly (Figure FD-14). Major parts of the support structure of the thermionic probe drive have been fabricated as well. All parts except for the probe head are placed in storage and will be used in the final installation at the end of the NSTX-U recovery outage. The probe head in the mean-time will be used for test measurements at MAST. For the UC Irvine’s Solid-State Neutral Particle Analyzer (SSNPA) diagnostic hardware improvement, new trans-impedance amplifiers and voltage amplifiers for the SSNPA diagnostic are redesigned. They will be tested on MAST-U in FY18 prior to the final installation on NSTX-U at the end of the recovery outage. The improvements will further increase signal-to-noise ratio and enable measurements of fast ion density fluctuation up to 150 kHz.

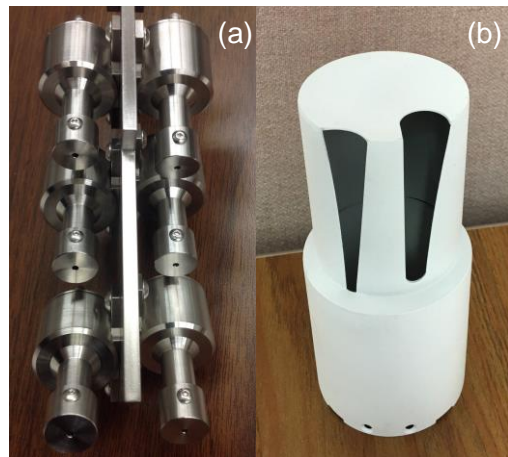


Figure FD-14: (a) FPD detector modules mounted on central support plate. (b) Heat Shield (BN covered).

NSTX-U FY2017 Year End Report: Research Results

In FY2017, the NSTX-U research team contributed experimental data and analysis in support of the 2017 DOE Joint milestone:

“Conduct research to examine the effect of configuration on operating space for dissipative divertors. Handling plasma power and particle exhaust in the divertor region is a critical issue for future burning plasma devices, including ITER. The very narrow edge power exhaust channel projected for tokamak devices that operate at high poloidal magnetic field is of particular concern. Increased and controlled divertor radiation, coupled with optimization of the divertor configuration, are envisioned as the leading approaches to reducing peak heat flux on the divertor targets and increasing the operating window for dissipative divertors. Data obtained from DIII-D and NSTX-U and archived from Alcator C-Mod will be used to assess the impact of edge magnetic configurations and divertor geometries on dissipative regimes, as well as their effect on the width of the power exhaust channel, thus providing essential data to test and validate leading boundary plasma models.

The NSTX-U research contributions to the 2017 Joint Milestone are described in a separate report, and the NSTX-U contributions to *“Conduct research to examine the effect of configuration on operating space for dissipative divertors”* are summarized above.

Summary descriptions of the results of research milestones are provided below. Descriptions of additional selected research highlights are also provided in subsequent sections.

Research Milestone R(17-1): Simulation-based projection of divertor heat flux footprint for NSTX-U (Completed September 2017)

Milestone Description: Understanding the underlying physical mechanisms that contribute to the scrape-off layer (SOL) power flux width, λ_q , is of utmost importance for future tokamaks such as ITER and FNSF. The 2016 FES Joint Theory Milestone (JTM) carried out extensive modeling to predict λ_q under attached divertor conditions. XGC modeling reproduced the observed trends in present day tokamaks where λ_q is found to be nearly inversely proportional to the midplane poloidal field, i.e. $\lambda_q \propto B_{pol}^{-1.19}$. The XGC SOL widths were influenced by both the magnetic drift of warm ions across the separatrix and by the cross-field $E \times B$ drift heat-flux width from the edge turbulence. However, only a limited NSTX dataset was included in the 2016 JTM. Here we will extend simulations of a plasma current scan for NSTX to evaluate the SOL width and edge turbulence under a wider range of conditions and to evaluate the magnitudes of the turbulent $E \times B$ and ion drift effects in XGC. Building on the NSTX results and modeling, XGC simulations will be extended to predict λ_q for a high-current 2 MA NSTX-U discharge using a set of assumptions to project the expected midplane profiles.

Milestone R(17-1) Report:

Understanding the underlying physical mechanisms that contribute to the scrape-off layer (SOL) power flux width, λ_q , is of utmost importance for future tokamaks such as ITER and FNSF. The 2016 Theory/Simulation Joint Research Target (JRT) carried out extensive modeling to predict λ_q under attached single-null divertor conditions. First-principles-based XGC modeling reproduced the observed trends in present day tokamaks where λ_q is found to be proportional to the Eich-scaling $B_{pol}^{-1.19}$ and is dominated by the magnetic drift of warm ions across the separatrix, with the cross-field electron heat-flux width from the edge turbulence being narrower while the particle-flux footprint is the same. However, a NSTX-U relevant plasma-shape case was not included in the NSTX data base of the JRT research. We enhance the plasma current scan by including an NSTX-U relevant plasma-shape in the NSTX data, and carry out simulations to predict λ_q for a 2 MA NSTX-U model discharge.

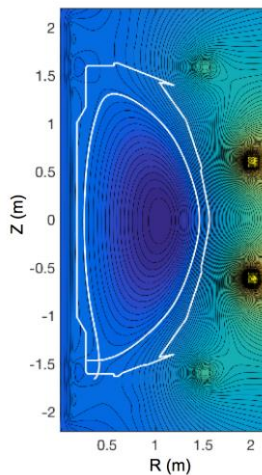


Figure R17-1-1: Magnetic equilibrium contours of NSTX shot #139047

Most of the NSTX-U operation is expected to be in high triangularity shape for better plasma performance. Hence, both of the divertor legs will be located at the inboard side (inboard divertor). To be relevant to this NSTX-U plasma, we picked an NSTX shot #139047 ($B_{p,mid}=0.25T$, Heat input=3.8MW), which has single lower divertor configuration with the inner separatrix leg on the lowest vertical tile and the outer leg on the far inboard horizontal tile, as can be seen in Fig. R17-1-1. The single divertor configuration is chosen here for consistency with other studies performed by XGC, including an ITER model plasma. Figure R17-1-1 shows the magnetic equilibrium and Fig. R17-1-2 depicts the NSTX #139047 input profiles, as imported from experimental measurement data (blue line), together with the XGC-evolved profiles at the end of the simulation (red line) when λ_q is approximately saturated. The short time simulations have generated turbulence in the edge plasma only, evolving the edge plasma profiles to some degree.

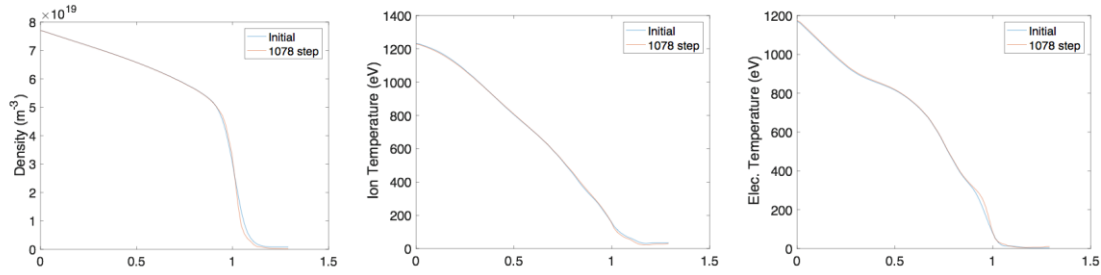


Figure R17-1-2: (left) Electron density, (middle) ion temperature, and (right) electron temperature profiles for the NSTX baseline plasma #139047. Blue lines represent the input profiles from experimental measurements, and red lines are the XGC evolved profiles when the heat-flux footprint is approximately saturated.

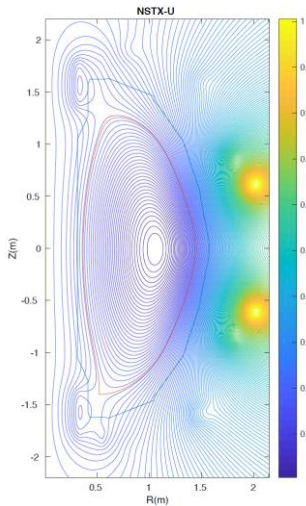


Figure R17-1-3: NSTX-U magnetic equilibrium

The above NSTX baseline plasma profiles have then been projected to 2MA NSTX-U, while keeping similar q -profile and β_N , and about 17% lower Greenwald density at pedestal top ($n_{ped}/n_G=0.5$). Figure R17-1-3 depicts the magnetic equilibrium of the 2MA NSTX-U model plasma, showing a similar divertor magnetic structure as in Figure R17-1-1. Fig. R17-1-4 shows the input plasma profiles (blue line) and the XGC-evolved profiles (red lines).

Simulation results for the NSTX baseline case ($B_{pol,MP}=0.25T$) and the NSTX-U 2MA case ($B_{pol,MP}=0.58T$) are added, marked as dark upside-down triangles, to the 2016 Theory/Simulation Milestone Target results. It can be seen that the NSTX baseline λ_q is ~ 1.3 times greater than the Eich scaling value, but still sits around the upper error limit from the Eich regression. However, λ_q for the NSTX-U 2MA case is ~ 2.3 times greater, which is significantly outside of the Eich regression error bar. As a matter of fact, the NSTX-U case with $B_{pol,MP}=0.58T$ yields only about 30% lower λ_q value than the NSTX case with $B_{pol,MP}=0.25T$ while the Eich scaling implies the reduction would have been be $\sim 62\%$. Most of the reduction in λ_q from NSTX to NSTX-U is from the e-folding length alone (see Figure R17-1-5).

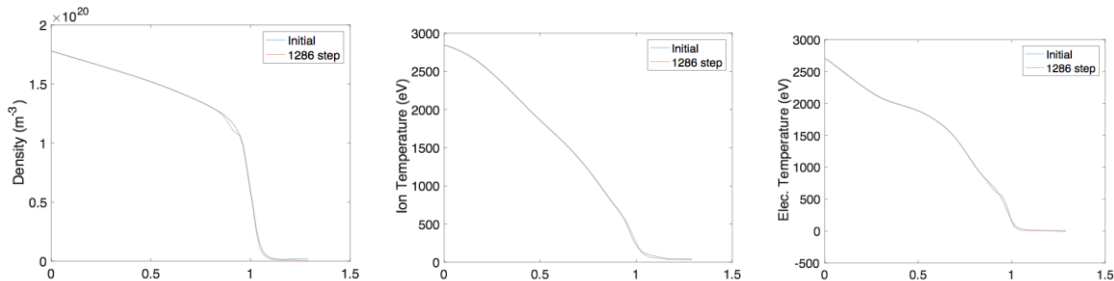


Fig. 4. (left) electron density, (middle) ion temperature, and (right) electron temperature profiles for the NSTX-U 2MA model plasma. Blue lines represent the input profiles from experimental measurements, and red lines are the XGC evolved profiles when the heat-flux footprint is approximately saturated.

The cause of such larger λ_q values can be pointed to two possibilities. If we inspect the NSTX inboard-divertor case only, we could attribute the 1.3-times greater λ_q than the Eich value to the

weaker spread of downward Grad-B driven neoclassical ion orbit into the private flux region (hence smaller S value, as can be seen in the left plot in Figure R17-1-5).

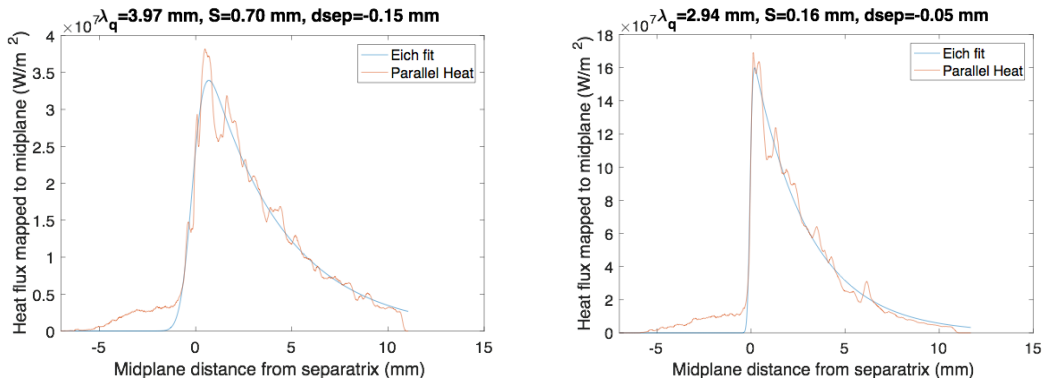


Fig. R17-1-5. Divertor heat-flux footprints for (left) the baseline NSTX case and (right) model NSTX-U 2MA case.

However, if we inspect the NSTX-U case together with the NSTX case, it can be seen that the neoclassical ion orbit spread into the private flux region alone cannot explain such a large λ_q for the NSTX-U case. It is true that about two-times greater magnetic field strength is reducing the S-value further to a negligible level, the S-value is already too small in the NSTX case to affect λ_q much. For reference, the inner-leg has about 50% heat-load than the outer-leg for both NSTX and NSTX-U cases. λ_q at inner-inner leg is about 2/3 of the outer leg value for both cases.

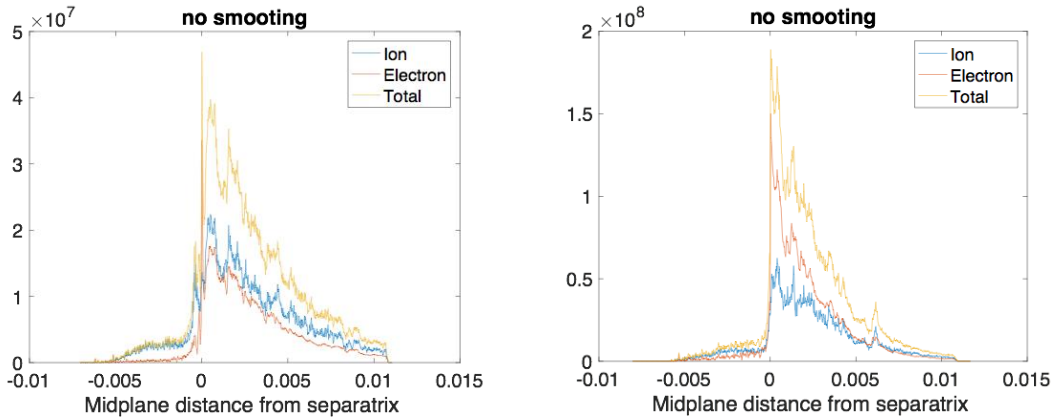


Figure R17-1-6: Electron and ion contribution to the total parallel heat-flux to the outer-leg divertor plates in Watt/m² for (left) NSTX and (right) NSTX-U. Electron contribution from turbulence is higher than the ion contribution from neoclassical orbit physics in the NSTX-U case.

The second possibility is the stronger neoclassical or turbulence contribution to the e-folding length in the inner-divertor geometry. It can be easily seen that the increased angle of the outer-leg magnetic field line with respect to the vertical Grad-B direction could increase the ion orbit spread away from the outer strike point and the e-folding length. However, the fact that the B_{pol} is more than twice stronger in the NSTX-U case than in the NSTX case may not allow the neoclassical ion Grad-B drift effect to be totally responsible for the large λ_q behavior. A stronger turbulence spread effect is a possibility. As a matter of fact, if we investigate the ion and electron

contribution to λ_q , as shown in Figure R17-1-6, there is evidence that the turbulence spread can be a strong candidate to the enhanced λ_q in the inboard divertor, higher B geometry. Unlike in the outboard divertor geometry cases studied previously in the 2016 JRT, the electron contribution (which is mostly from turbulence) is comparable to the ion contribution (which is mostly from neoclassical orbits) in the inboard-divertor NSTX case. At higher B_{pol} in the NSTX-U case, the electron contribution becomes significantly higher than the ion contribution, indicative of the enhanced role of turbulence in the divertor heat-flux footprint.

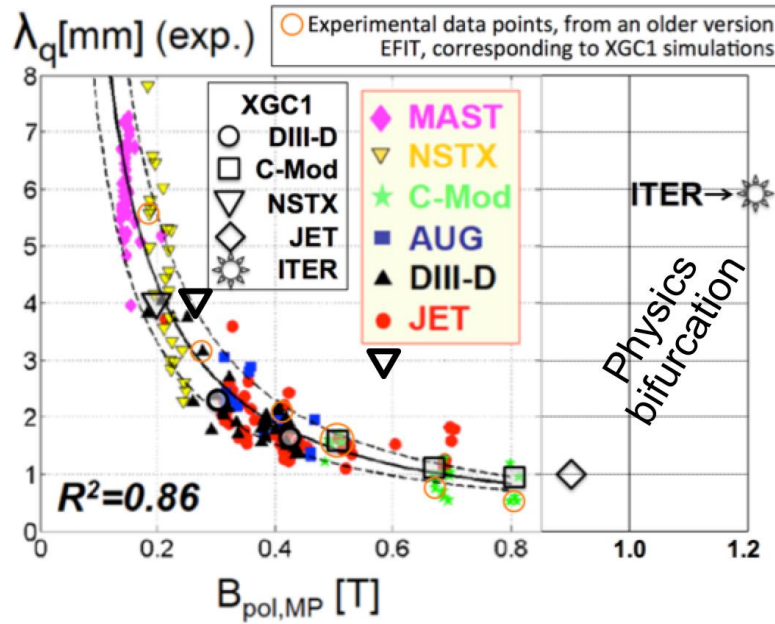


Figure R17-1-7: Simulation results for the NSTX baseline case ($B_{p,mid}=0.25T$) and the NSTX 2MA case ($B_{p,mid}=0.25T$) are added, as dark upside-down triangles, to the 2016 Theory/Simulation Milestone Target results.

This could be an important physics to be studied further, since it may have a connection to the enhanced role of turbulence and increased λ_q found in the ITER model plasma as indicated in Figure R17-1-7. This physics could have a critical impact on the high-triangularity operation of ITER plasma.

Research Milestone R(17-2): Advanced divertor operating scenario modeling for NSTX-U
(Completed September 2017)

Milestone Description: Divertor power exhaust is a critical issue for ITER and next-step tokamaks, and advanced magnetic divertor configurations are being developed and tested to provide candidate solutions for high heat flux and excessive material erosion expected in future facilities. NSTX-U will enable access to a number of advanced divertor configurations including snowflake and X-divertors thanks to a flexible set of divertor poloidal field coils. A range of scrape-off-layer (SOL) widths and high parallel heat fluxes expected in NSTX-U with $I_p = 1\text{-}2\text{ MA}$, $P_{NBI} = 6\text{-}12\text{ MW}$ will enable critical tests of the underlying physics of advanced divertor configurations. To guide the experiments, modeling of advanced divertor scenarios and transport will be performed. Divertor radiation and heat fluxes as functions of current, input power, density, and seeded impurities will be studied. Predictive free-boundary codes including ISOLVER and CORSICA will be used to study the operational space of advanced divertor configurations under various solenoid and poloidal field coil current states. The recently developed GINGRED code will be utilized for numerical grid generation for divertor configurations with multiple X-points. Transport and radiation in these advanced divertor configurations will be modeled using SOLPS and UEDGE multi-fluid two-dimensional transport codes and will include studies of the effects of poloidal variation of transport coefficients. The impact of 3D fields on advanced divertor configurations will also be studied using M3D-C1 and EMC3-EIRENE codes to understand how small non-axisymmetric perturbation fields may change plasma parameters inside the separatrix and in the divertor. This research will provide a significant step in advanced divertor concept development for NSTX-U and future conventional and spherical tokamaks.

Milestone R(17-2) Report:

EMC3-EIRENE simulations

As part of these ongoing modeling efforts, further EMC3-EIRENE simulations were conducted on a tilted symmetric snowflake minus configuration that was modeled as part of [R-17-2-1]. This new work focused on the impact that 3D fields have on the core fueling by neutrals in an advanced divertor scenario. EMC3-EIRENE simulations used different external core fueling rates (analogous to NBI fueling) and different recycling coefficients to achieve a range of fueling scenarios that could be characterized by the total fueling by diffusive neutrals ionized by the simulated edge plasma. The number of these diffusive neutrals that penetrated to the inner boundary of the simulation, were ionized, and then reintroduced self consistently as “core region fueling”—in addition to NBI fueling—can then be compared between axisymmetric and 3D field cases. It is found that the application of 3D fields led to a dramatic reduction in core fueling from recycling, as seen in Figure R-17-2-1. This reduction in core fueling was in addition to the severe plasma density pump-out that was observed in these simulations.

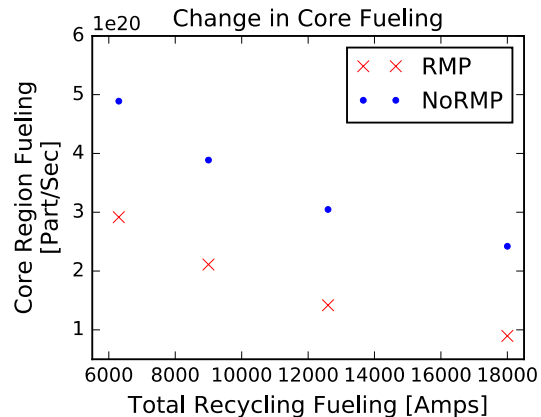


Figure R17-2-1: The core fueling as a result of diffusive neutrals in EMC3-EIRENE simulations of NSTX-U across a number of fueling scenarios with and without 3D fields.

The cause of this reduction in core fueling via-diffusive neutrals is believed to be related to the change in the neutral particle energy distribution function in the plasma edge region ($0.5 < \varphi < 1.0$) shown in Figure R-17-2-2. With the 3D fields, the population of high energy neutrals is degraded, and these high energy neutrals are then unavailable to penetrate deeply into the plasma. This reduction in core fueling then contributes to the plasma density pump-out. These simulations used a vacuum approximation of the RMP field strength which may be over-predicting this phenomena, and ongoing work (described in BPR-DSOL-2.b) will utilize plasma response modeling, with EMC3-EIRENE simulations, and experimental data from MAST to further bound the density control impacts of this effect.

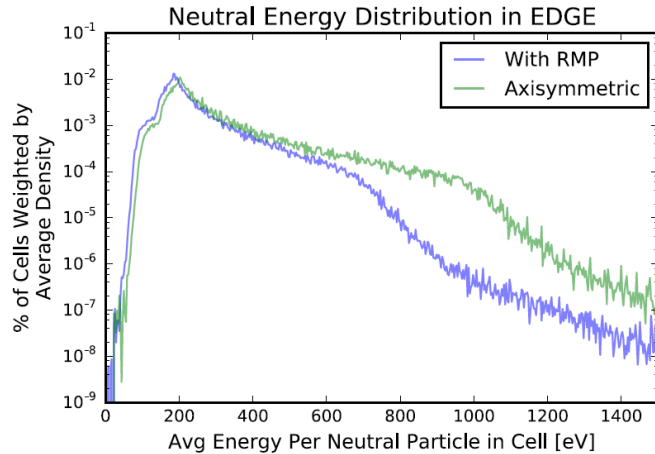


Figure R17-2-2: Neutral energy distribution function in the plasma edge ($0.5 < \varphi < 1.0$) of EMC3-EIRENE simulations with and without RMPs applied for the 18000 Amp recycling fueling case. Application of RMPs degrades the high energy tail of neutrals.

M3D-C¹ simulations of the plasma response to RMPs in NSTX-U single-null and snowflake divertor configurations [R17-2-2]

The ELM control coils and the snowflake (SF) divertor configuration are two potential solutions proposed to solve two separate outstanding issues on the path towards self-sustained burning plasma operations. These two solutions have been tested separately in several machines worldwide but, in a reactor, these two solutions would have to operate simultaneously. It is, therefore, important to investigate the compatibility between these two solutions and to identify possible conflicts that could prevent them of operating simultaneously. In this work, the effect of externally applied $n = 3$ magnetic perturbations on the snowflake divertor configuration is investigated using the two-fluid resistive magnetohydrodynamic code M3D-C¹ to estimate the single- and two-fluid plasma responses. The single-fluid calculations show a significant reduction of the resonant tearing components with respect to the vacuum approach calculations for both SN and SF configurations. In the two-fluid calculations, the tearing components are significantly reduced in the plasma edge and significantly amplified in the region of low electron fluid rotation perpendicular to the magnetic field. The differences between the single- and two-fluid plasma responses are mainly caused by the different screening mechanism of these two plasma models. While the screening of resonant magnetic perturbations (RMPs) in the single-fluid model is caused by the $\mathbf{E} \times \mathbf{B}$ rotation, the screening of RMPs in the two-fluid model is caused by the local electron fluid velocity perpendicular to the magnetic field. In this work, the NSTX-U midplane resistive wall mode, error field correction coils were used to apply the $n = 3$ perturbations to the plasmas and no significant differences between the SN and SF plasma responses is found.

To evaluate the effect of the magnetic perturbations on the structure of the magnetic lobes, the manifolds in both SN and SF configurations were calculated using the field line tracing code TRIP3D-MAFOT. A comparison between the size of the magnetic lobes and the amplitude of the kink and tearing components from the single- and two-fluid plasma responses suggests that the size of the magnetic lobes is more sensitive to the resonant than to the non-RMPs. The results also show that, independent of the plasma response model used, the SF has more and longer magnetic lobes than those in the SN configuration. This increase in number and size of the lobes comes from an interplay between the conservation of the magnetic flux through the lobes and the lower poloidal magnetic field in the null-point region of the SF configuration that causes a stronger compression of the lobes towards the null-point and a stretching of the lobes in the null-point region. The intersection of these longer and additional magnetic lobes with the divertor plates are expected to cause more striations in the particle and heat flux target profiles leading to a larger wetted area and smaller peak heat fluxes onto the plasma facing components.

Developing two-dimensional divertor transport and radiation modeling capability for snowflake divertor configurations

The two-dimensional multi-fluid codes presently in use do not have the capability to generate numerical grids for snowflake divertor configurations with multiple nulls. An exception is the three-dimensional code EMC3-EIRENE [R-17-2-3, R-17-2-4], however, it has a simplified trace impurity model and does not include recombination processes, which are critical for detachment physics. Transport models typically used are also simplified and do not attempt to include fast convection in the high β_p region, a key theoretically predicted snowflake divertor property. The UEDGE code has been extensively used to model snowflake configurations: snowflake-minus experiments in NSTX [R-17-2-5, R-17-2-5, R-17-2-7], NSTX Upgrade snowflake-minus divertor with neon and argon seeding and cryopumping [R-17-2-8, R-17-2-9], the spherical tokamak based fusion nuclear science facility divertor with nitrogen seeding [R-17-2-9], and snowflake-plus configurations for a fusion development facility device [R-17-2-10, R-17-2-10]. This modeling generally showed that increased plasma-wetted area and connection length, as well as increased radiated power loss fraction in the snowflake divertor led to divertor detachment either at a lower density, or at a lower impurity seeding fraction, as compared to the standard divertor.

Previous modeling of NSTX-U snowflake divertor configurations focused on two aspects: equilibria simulations with various coil sets and transport modeling with multi-fluid code UEDGE [R-17-2-8, R-17-2-9]. The initial NSTX-U snowflake simulations had several limitations. First, the coil sets and plasma-facing component geometry were projected from the planned NSTX-U design. Since the designs of the divertor coils and plasma facing components are still developing, the focus of the current work was shifted to the UEDGE transport model, in particular, to improve the UEDGE capabilities and results. Previous UEDGE snowflake transport model developed for NSTX-U [R-17-2-8, R-17-2-9] was limited to the snowflake-minus configuration only. The model was also simplified, as it only included the fixed fraction carbon model. The current work has extended the UEDGE simulations to a variety of snowflake configuration grids, and used the charge-state resolved impurity (carbon) model for more accurate radiation distribution simulations. This work is summarized below.

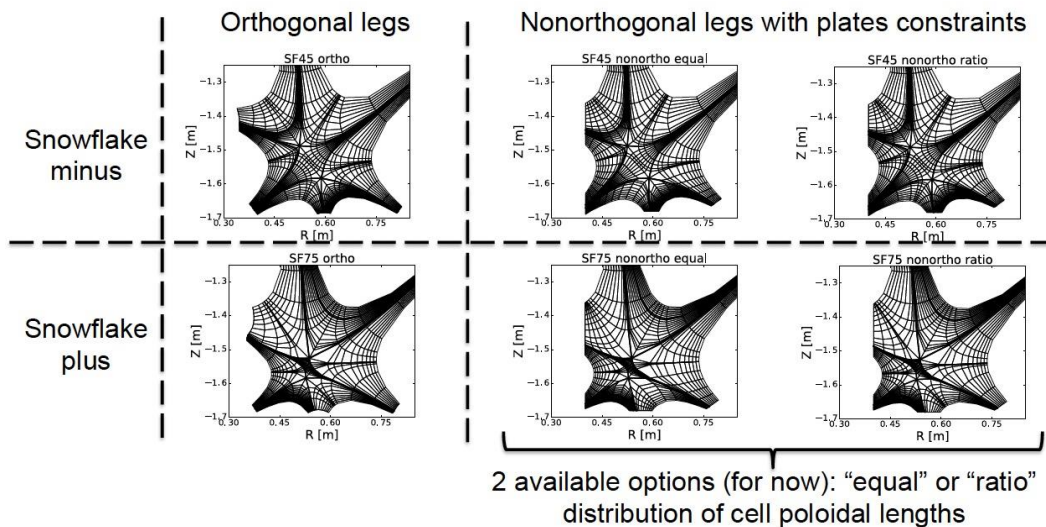


Figure R17-2-3 Examples of snowflake divertor numerical grids generated for NSTX-U using Gingred.

A new grid generator for UEDGE, Gingred, has been developed [R-17-2-12]. The code is written in IDL and can produce a numerical grid for an arbitrary magnetic geometry that includes two poloidal magnetic field nulls. The code uses reliable built-in IDL routines such as those for root finding and biquadratic interpolation of poloidal magnetic flux. The code also includes an interactive debugging capability, as well as a manual refinement capability with a graphical user interface. For the first time, numerical grids for further two-dimensional transport simulations have been produced for a number of snowflake divertor configuration (snowflake-plus, snowflake-minus), as shown in Figure R17-2-3. One important capability is the use of grids that are non-orthogonal with respect to divertor target plates. This capability will affect realistic plasma-surface-interaction models for deuterium recycling and impurity (carbon and lithium) sputtering that will be used in future work.

Several UEDGE models were developed for four configurations: the standard divertor, the snowflake-minus with short and long divertor legs, and the snowflake-plus. Numerical grids for these configurations (generated by Gingred) are shown in Figure R17-2-4. The model included deuterium ions and neutrals, as well as either the fixed carbon fraction (5%) model or the charge state resolved carbon model with physical and chemical carbon sputtering from the walls and the divertor plates. NSTX-like poloidally-constant transport coefficients were used: particle diffusion $D = 0.5 \text{ m}^2/\text{s}$, heat conduction $k_e = k_i = 1.5 \text{ m}^2/\text{s}$. The boundary conditions included high-recycling wall and divertor plates.

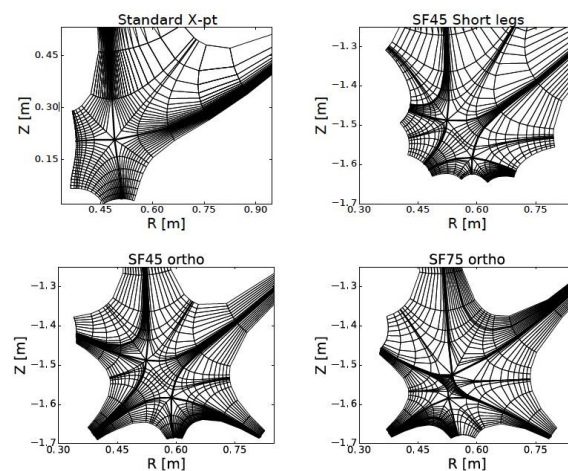


Figure R17-2-4: Numerical grids for four cases that are used for transport model comparisons in UEDGE.

Preliminary results are summarized as follows:

- Total radiation distributions have been compared between the snowflake configurations with the simplified fixed carbon fraction model, as shown in Figure R17-2-5. The Snowflake-minus configuration with Short legs shows higher total radiation between the X-points as compares to that with the longer legs. The snowflake-plus showed the trend to detach more likely in comparison with snowflake-minus configurations.

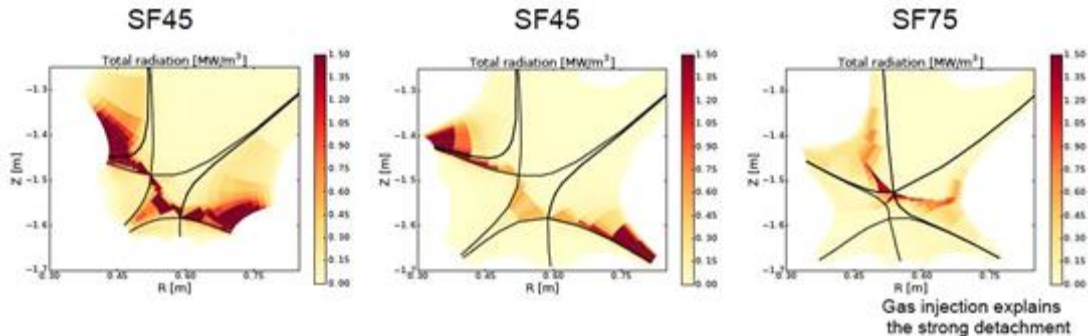


Figure R17-2-5: Total radiation distribution in the short-leg snowflake-minus, long-leg snowflake minus, and the snowflake-plus, using the fixed carbon fraction impurity model.

- An effect of increased plasma heating power was investigated using snowflake-minus divertor configuration. The power at the core-boundary interface was varied from 4 to 7.5 MW. The charge-state resolved carbon model was used. The modeling showed that carbon ion distributions changes with power, enabling to visualize radiation fronts in snowflake divertor legs and strike points using carbon radiation (Figure R17-2-6). Total radiation fronts are dominated by C 2+ radiation in the 4 MW case, and both C 2+ and C 3+ radiation in the 7.5 MW case.

On-going work is focusing on developing parametric scans of power and density in order to make consistent comparisons of the standard divertor and snowflake divertor configurations. Future work will encompass radially and poloidally dependent transport coefficients in order to simulate the snowflake region convection.

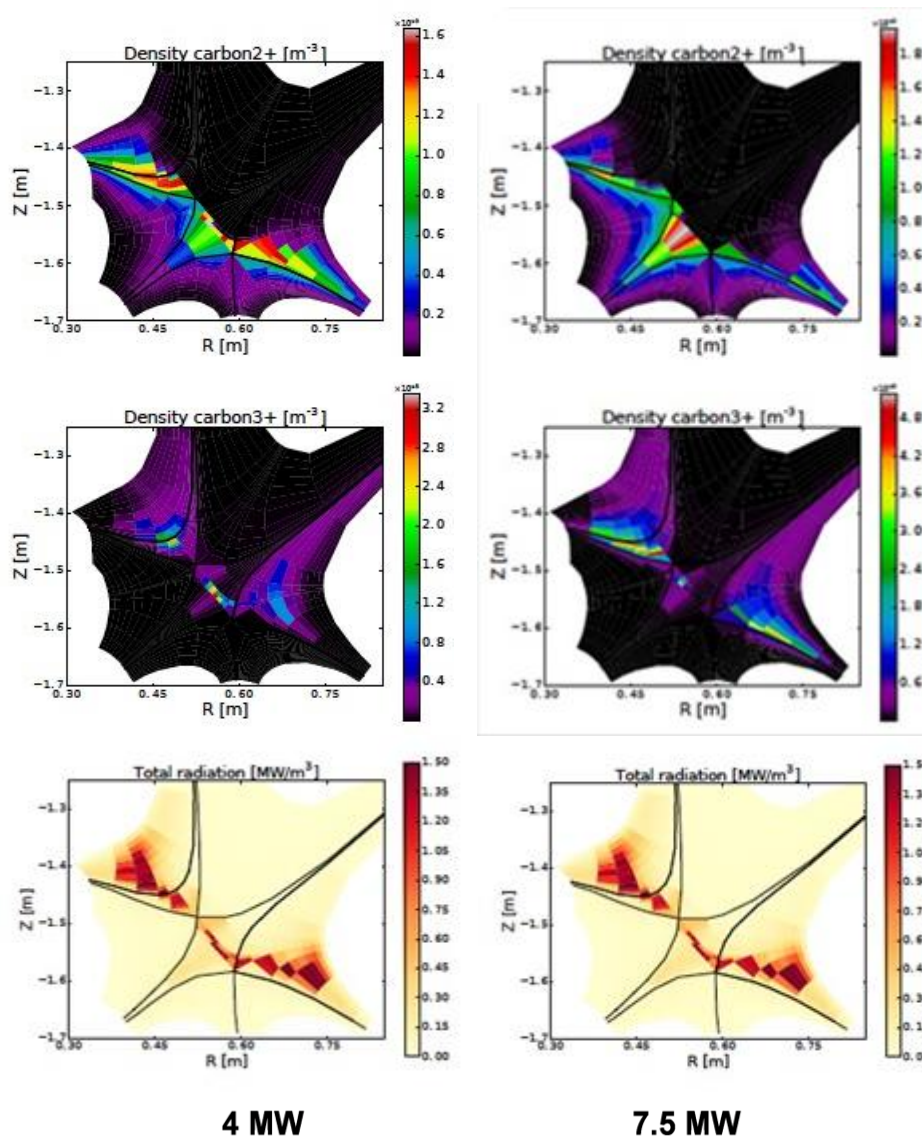


Figure R17-2-6: Distributions of C 2+ and C 3+ densities and total plasma radiation in the snowflake-minus divertor at 4 MW and 7.5 MW power.

References

- [R-17-2-1] H. Frerichs, et al Phys. of Plasmas 23, 062517 (2016).
- [R-17-2-2] G. P. Canal et. al., Nuclear Fusion **57** (2017) 076007.
- [R-17-2-3] Lunt T et al 2014 Plasma Phys. Control. Fusion 56 035009
- [R-17-2-4] Lunt T et al 2016 Plasma Phys. Control. Fusion 58 045027
- [R-17-2-5] Soukhanovskii V et al 2012 Phys. Plasmas 19 082504
- [R-17-2-6] Meier E et al 2015 J. Nucl. Mater. 463 1200
- [R-17-2-7] Meier E, et al., 2014 Contrib. Plasma Phys. 54 454
- [R-17-2-8] Soukhanovskii V A et al 2016 IEEE Trans. Plasma Sci. 44 3445
- [R-17-2-9] Meier E, et al., 2015 Nucl. Fusion 55 086002
- [R-17-2-10] Umansky M V, et al., 2009 Nucl. Fusion 49 075005
- [R-17-2-11] Umansky M, et al., 2010 Contrib. Plasma Phys. 50 350
- [R-17-2-12] O. Izacard and M.V. Umansky, “Gingred, a universal grid generator for arbitrary magnetic geometry”, submitted to Comm. Comput. Phys., 2016

Research Milestone R(17-3): Identify, mitigate, and develop correction strategies for intrinsic error field sources in NSTX-U (**Completed September 2017**)

Milestone Description: A key aspect of achieving high performance in magnetic confinement fusion devices is the successful identification, mitigation, and correction of intrinsic error field sources. During the initial NSTX-U research campaign, error field correction (EFC) experiments revealed strong intrinsic error field effects. In L-mode scenarios, these included the near-universal locking of the $q=2$ surface and a time-dependence in the optimum phase of the applied $n=1$ EFC. In H-mode scenarios, error field effects may have impeded early-time H-mode access and limited flat-top performance. As such, it is imperative to identify and develop correction strategies for the intrinsic error field sources in NSTX-U. Activities to support this milestone will include conducting in situ coil metrology to generate as-built coil shape models that can be used to inform numerical modeling of intrinsic error field effects. The results of these numerical modeling efforts will be compared to experimental results from the initial NSTX-U campaign in order to identify the key error field sources. Once the error field sources are identified, strategies for mitigating these sources will be developed (for example, realigning the toroidal field bundle within the center-stack casing). For error field sources that cannot be mitigated, strategies for correcting the remaining error fields during plasma operations will be developed (for example, determining optimum pre-programmed $n=1$ EFC phases and amplitudes). Finally, the calibration procedures for the 3D magnetic field sensors will be improved so that real-time dynamic $n=1$ EFC can be used during the plasma current ramp in the event that the unmitigated error field sources are difficult to correct with pre-programmed EFC. These various activities will ensure that NSTX-U is optimally positioned to access high performance plasma operations at the outset of the next research campaign.

Milestone R(17-3) Report:

In FY17, substantial progress has been made toward identifying and understanding the dominant error field sources in NSTX-U. A series of metrology campaigns were conducted to assess the as-built shapes of both the main vertical field coils (PF5 upper and lower) and the OH and TF center rod. These metrology results are combined here with numerical modeling from the IPEC [R17-3-4] and M3D-C1 [R17-3-5] codes in order to understand the experimental results obtained during the FY16 NSTX-U commissioning campaign. The numerical modeling indicates that a misalignment of the TF center rod was the dominant error field source during the FY16 campaign. The TF misalignment produces a high-field-side error field that is found to elicit an equilibrium-dependent plasma response that is difficult to correct with standard externally applied magnetic perturbations. These findings, which are consistent with the experimental observations from the FY16 campaign, indicate that the TF center rod should be realigned to a tolerance of 2 mm with respect to the vertical axis of NSTX-U. This tolerance is based on numerical modeling of both the resonant error fields/currents and the neoclassical toroidal viscosity that the misaligned TF center rod produces. Strategies for achieving this tolerance upon reinstallation are presented. While the TF center rod was the dominant error field source in NSTX-U, the PF5 main vertical field coils are also found to have misalignments, both radial and vertical, that must be addressed. Finally, efforts to improve the calibration of 3D magnetic sensors using data from both NSTX-U and DIII-D are summarized. These efforts are expected to improve the real-time dynamic error field correction capabilities of both DIII-D and NSTX-U.

Section R17-3-1: Error field correction results from the FY16 NSTX-U campaign

The bulk of the error field correction results from the FY16 NSTX-U commissioning campaign were previously reported in the FY16 year-end report. As such, we only briefly review them here in order to provide context and motivation for the metrology and numerical modeling results that follow. Experimental data obtained during the FY16 campaign on NSTX-U show clear signatures of the impact of error fields. In particular, it has been observed that most L-mode discharges on NSTX-U do not rotate outside of the $q = 2$ surface. This strongly implies the existence of a locked 2/1 field. Attempts to avoid or unlock this mode using the existing RWM coil capabilities on NSTX-U were not successful.

One of the key observations regarding error field correction in the FY16 campaign is that the optimum error field correction (EFC) was found to change with the plasma equilibrium [R17-3-2, R17-3-3]. For example, the optimum EFC phase is different by $\sim 45^\circ$ in the flattop of ohmic versus beam-heated L-mode discharges. More strikingly, a scan of the applied EFC phase during the ramp-up of beam-heated L-mode discharges reveals a marked change in the optimum error field correction from the ramp-up phase to the flattop (see Fig. R17-3-1). *We note that a version of Fig. R17-3-1 was included in the FY16 year-end report; it is reprinted here to motivate the new metrology and numerical modeling results that follow.*

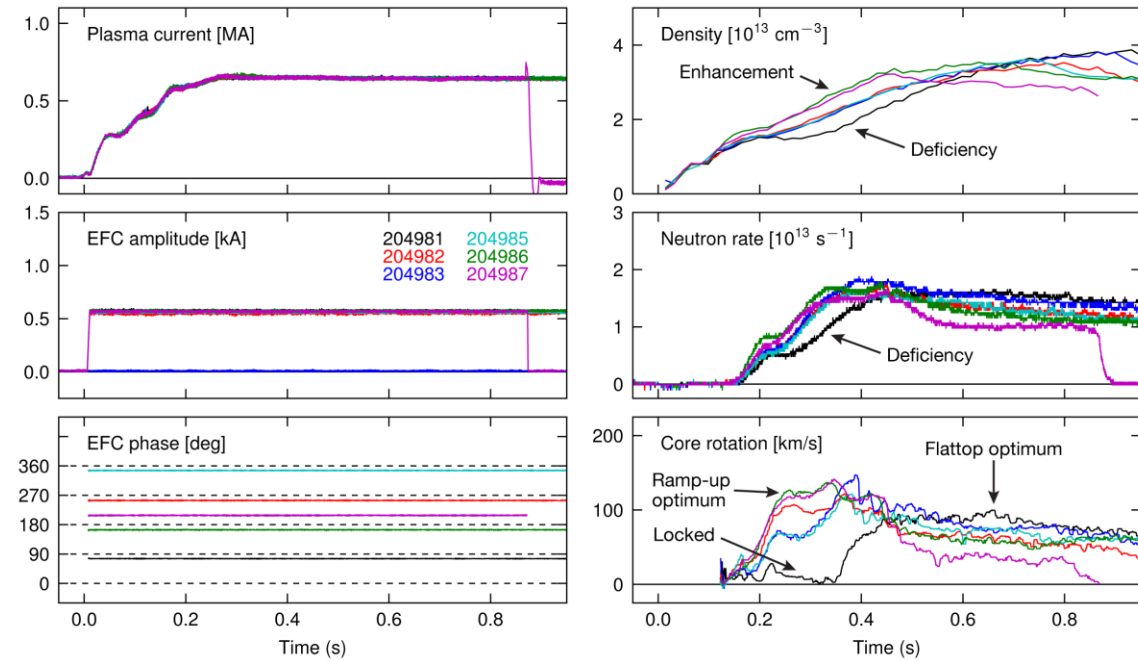


Figure R17-3-1: Scan of early-time externally applied error field correction (EFC) in 1 MW L-mode discharges in NSTX-U. The applied EFC current waveform is simply a square wave starting shortly after $t = 0$. The amplitude of the EFC is 600 A (1.2 kA-turns) in all cases, while the phase is varied from shot to shot. In the three panels on the right, and in particular in the panel showing core rotation at the bottom right, a phase dependence of the plasma response is clearly visible (see the text for further details).

Figure R17-3-1 shows the results of a scan of early-time error field correction (EFC) in 1 MW L-mode discharges in NSTX-U. In each case, a square EFC waveform of 600 A (1.2 kA-turns) is applied shortly after $t = 0$. The phase of this applied EFC waveform is varied from shot to shot.

From flattop compass scans (not shown), the optimum EFC phase in the flattop is found to be $\phi = 80^\circ$. In the $\phi = 80^\circ$ case in Fig. R17-3-1 (204981, black), however, the core rotation is locked until $t \sim 0.350$ s, indicating that the optimum flattop EFC is not the same as the optimum early-time correction. In contrast, the $\phi = 200^\circ$ case in Fig. R17-3-1 (204987, magenta) shows high early rotation ($t < 0.400$ s), but poor flattop rotation ($t > 0.400$ s). From these data, we infer that the optimum correction phase rotates from $\phi = 200^\circ$ early in time to $\phi = 80^\circ$ in the flattop. This phase rotation constitutes a time (and/or scenario) dependent error field that would require a sophisticated EFC algorithm to correct. The results of this ramp-up EFC scan will be compared to numerical modeling of the NSTX-U error field sources in Section R17-3-4.

Section R17-3-2: *In situ* metrology of the PF5 and OH/TF coils

In FY17, *in situ* metrology was carried out to develop coil shape models for two likely error field sources: the PF5 vertical field coils and the OH/TF center rod. This metrology included: (1) ROMER Arm measurements of the outer vessel wall and the center-stack casing that serves as a basis for orienting the PF5 coils and the TF center rod to a standardized coordinate system; (2) FARO Laser Tracker measurements was employed to measure the relative positions of the inboard vertical divertor targets (IBDV) and the faces of the flags on the TF center rod; and (3) ruler-based measurements of the distance between the PF5 coils and the vessel. The results of these measurements are presented below.

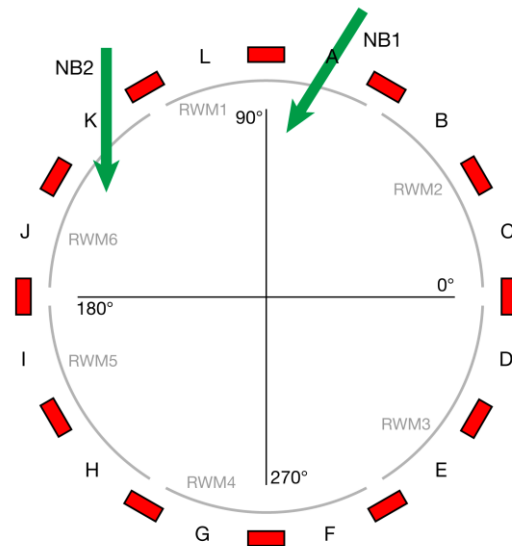


Figure R17-3-2: Schematic illustrating the toroidal angle used in this document.

Throughout this document we use a coordinate system in which the toroidal angle is defined to increase counter-clockwise looking down on the vessel from above with $\phi = 0^\circ$ pointing East between ports C and D (see Fig. R17-3-2).

Section R17-3-2.1: Metrology of the vacuum vessel and the PF5 coils

In this section, we report measurements of the vacuum vessel and the PF5 coils that are used to develop coil shape models for both the radial and vertical profiles of the PF5 upper and lower coils as a function of the toroidal angle. These profiles provide a basis for numerical modeling of the error fields generated by the PF5 coils, which is reported in Sections R17-3-3 and R17-3-4.

The PF5 coils have a nominal major radius of $R \sim 2$ m and nominal heights of $Z \sim \pm 60$ cm. The goal of the metrology reported here is to assess the deviations from these nominal values as a function of toroidal angle. First, the radial field profiles of the PF5 coils are assembled from precision measurements of the vacuum vessel wall ($R_{VV} \sim 1.7$ m) combined with ruler measurements of the spacing between the vessel wall and the PF5 coils. The precision vessel wall measurements are obtained with a ROMER Arm, which is a coordinate measuring machine that

can be placed inside the NSTX-U vacuum vessel. Once installed, it is aligned to a standardized outer vessel coordinate system using permanent monuments located on the inner wall of the outer vacuum vessel. In FY17, with the passive plates removed from NSTX-U, the ROMER arm was used to acquire detailed measurements of the interior outer vacuum vessel wall at the approximate locations of the PF5 upper and lower coils. These measurements trace out two rings of points at a height of $Z \sim \pm 57$ cm (see Fig. R17-3-3). The thickness of the stainless steel wall (5/8") is added to the ROMER Arm measurements such that the average wall radius of $R_{VV} \sim 1.7$ m represents the outer surface of the wall. The solid lines, which are $n=1-6$ fits to the ROMER arm data, reveal that the upper and lower vessel shapes are very similar. The fits indicate the presence of strong $n=1$ and $n=6$ components, the latter of which has not been previously resolved.

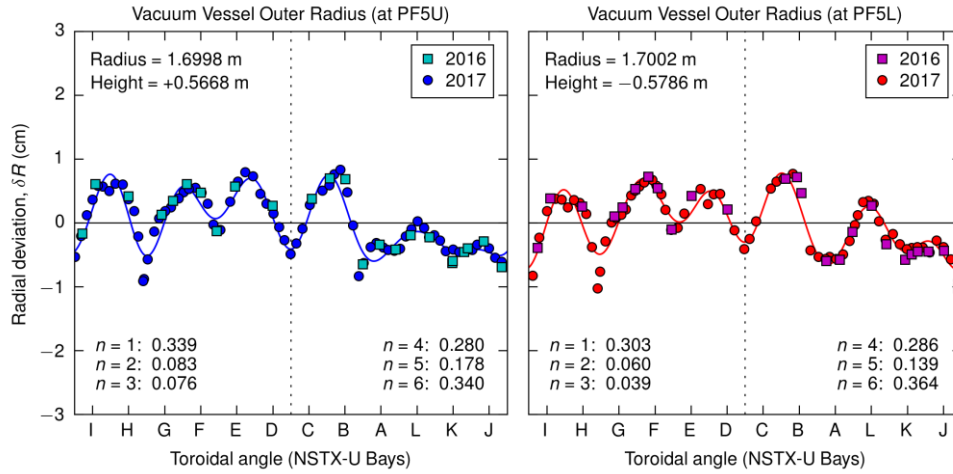


Figure R17-3-3: Upper and lower vacuum vessel shapes as obtained from the ROMER Arm measurements. The shape profile on the left is for the upper circle of VV, while the shape profile on the right is for the lower circle of VV points. The solid lines in each plot represent $n=1-6$ fits to the measurements. The measured shape of the upper and lower vessel is similar, and large $n=1$ and $n=6$ components are detected.

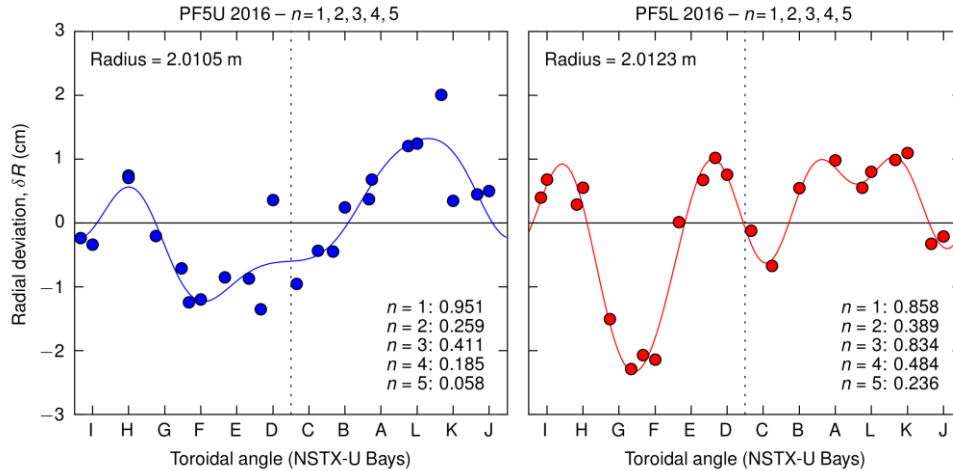


Figure R17-3-4: PF5 coil shape measurements for the upper coil (PF5U) and the lower coil (PF5L). These measurements combine the vessel shape model in Figure R17-3-3 with ruler-based measurements of the distance between the coils and the outer vessel wall. The solid lines in each panel represent $n=1-5$ fits to the data.

The distance between the vessel and the coils was obtained with ruler-based measurements. These data are combined with vacuum vessel measurements in Figure R17-3-3 to generate PF5 radial profiles shown in Fig. R17-3-4. The left panel represents the upper coil (PF5U), while the right panel represents the lower coil (PF5L). It is found that the total coil shape variations in Fig. R17-3-4 are larger than the vessel shape variations in Fig. R17-3-3. In Fig. R17-3-4, the solid lines represent $n=1-5$ fits to measurement points. The quantitative results of these fits are summarized in Table R17-3-1 and show that there are large $n=1$ and $n=3$ components in the PF5 coils.

		$n=1$	$n=2$	$n=3$
PF5U	Amplitude, δR	9.51 mm	2.59 mm	4.11 mm
	Phase, ϕ	126°	164°	324°
PF5L	Amplitude, δR	8.58 mm	3.89 mm	8.34 mm
	Phase, ϕ	92°	343°	269°

Table R17-3-1: Amplitudes and phases of the non-axisymmetric components of the PF5 upper and lower coils.

With the radial profiles of the PF5 coils in hand, we now turn to measurements of their vertical profiles. These measurements have not previously been attempted and therefore constitute new information not previously available on NSTX or NSTX-U.

The vertical profiles of the PF5 coils are of interest for assessing any tilt in the PF5 coils that may serve to distort the plane of reference for the tilt of the TF center rod, which will be addressed in the next section. For the PF5 vertical profile measurements, the FARO Laser Tracker, which is another coordinate measurement machine, is placed at the midplane of the interior of the NSTX-U vessel. When aligned at the midplane, the laser tracker can project its beam through open midplane ports to provide a vessel coordinate point of reference outside the machine at multiple toroidal angles. Using this laser tracker project technique in combination with a customized framing square, the vertical height of the PF5 upper and lower coils was measured

at eight toroidal locations. The framing square is referenced to gravity using a precision inclinometer. As such, the various vertical height measurements can then be transformed into vessel coordinates. The resulting vertical PF5 profiles are shown in Fig. R17-3-5. While the PF5L

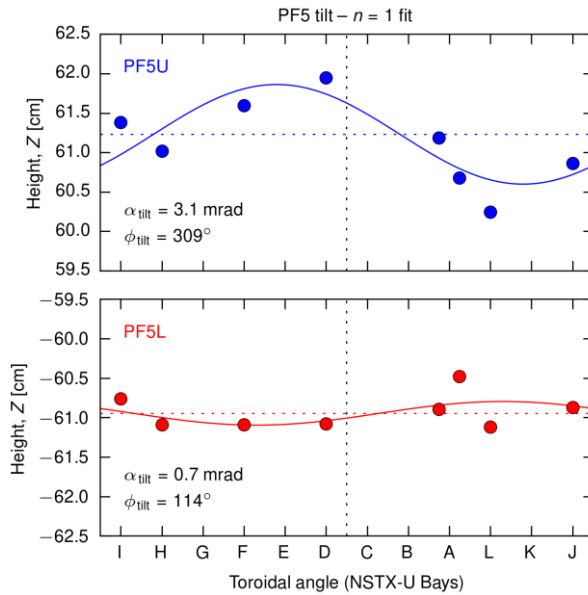


Figure R17-3-5: Measurements of the vertical profiles of the PF5 upper and lower coils. While the PF5L coil is reasonably well aligned to the horizontal plane of the vessel, the PF5U coil has a 3 mrad tilt toward Bay K.

coil is reasonably well aligned to the horizontal plane of the vessel, the PF5U coil has a 3 mrad tilt toward Bay K that may be mitigated with a careful re-shimming of the PF5U supports.

Section R17-3-2.2: Metrology of the OH/TF center rod

The major potential sources of error fields from the TF rod misalignments are from tilts or horizontal shifts of the TF center with respect to the horizontal plane of the poloidal field coils. The procedure for determining the shift and tilt of the TF center rod consists of combining inboard vertical divertor target (IBDV) ROMER Arm measurements with data from a dedicated metrology run conducted after the center-stack assembly was removed from the machine.

Once the NSTX-U center-stack assembly was removed from the machine in November 2016, the FARO laser tracker was employed to measure the relative positions of (1) the inboard vertical divertor targets; and (2) the faces of the flags on the TF center rod. The TF center rod orientation in the ROMER Arm coordinate system was determined by using IBDV measurements that were acquired before the center-stack assembly was removed to transform the Laser Tracker measurements into ROMER Arm coordinates. The resulting position of the upper and lower TF flag faces in ROMER Arm coordinates defines the absolute shift and tilt of the TF center rod.

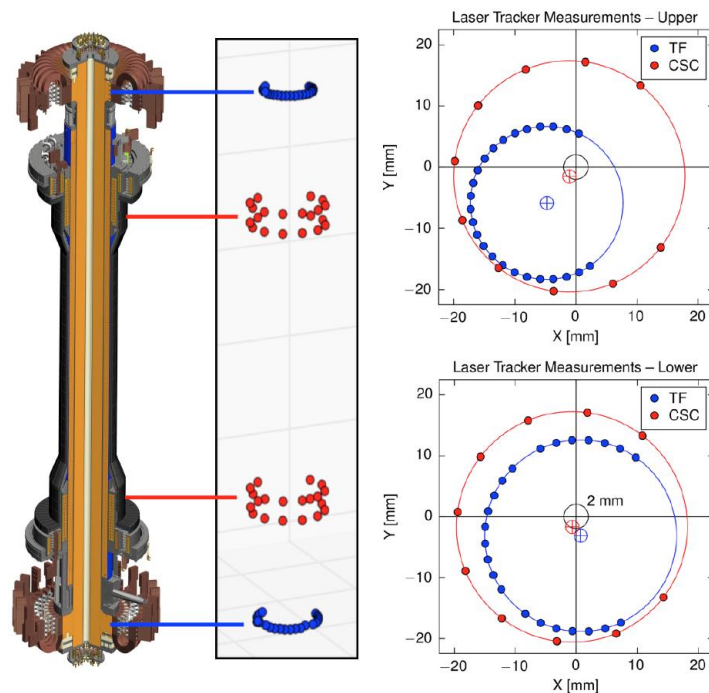


Figure R17-3-6: Measurements of the shift and tilt of the center-stack casing (from the IBDV targets) and the TF center rod (from the TF flag faces). The left panel shows a schematic of the locations of the four measurement circles. The top right panel represents the upper TF flag faces and IBDV target, while the bottom right panel represents the lower TF flag faces and IBDV target. The measurement points in each of the four measurement circles have been multiplied by a factor of 0.05 so that the various millimeter-scale shifts are visible to the reader. The numerical values for the shifts and tilts obtained from these data are listed in the Table R17-3-2.

Figure R17-3-6 shows the resulting X-Y positions of the TF flag faces and the IBDV targets once they have been transformed into the ROMER arm system. In the two panels on the right side of the figure, the data points in each of the four measurement circles have been multiplied by a factor of 0.05 so that the various millimeter-scale shifts are visible to the reader. First, it is clear that the IBDV targets (and therefore the center-stack casing) have a slight shift toward the southwest (red cross-hairs, $\delta R \sim 1.8$ mm at $\phi \sim 242^\circ$). Since the amplitude and direction of the shift is consistent at the top and bottom of the center-stack casing, the tilt of the casing is very small ($\alpha \sim 0.15$ mrad at $\phi \sim 156^\circ$).

For the TF flag faces, on the other hand, both a large shift and a large tilt are apparent in the data. First, the aggregate TF center rod shift is nearly 5 mm, again toward the southwest ($\delta R \sim 4.9$ mm at $\phi \sim 246^\circ$). The corresponding TF center rod tilt is an order of magnitude larger than the center-stack casing tilt ($\alpha \sim 1.15$ mrad at $\phi \sim 206^\circ$). The large TF center rod shift and tilt relative to the center-stack casing indicate that the TF center rod is not well centered within the casing. The various shift and tilt numbers are summarized in Table R17-3-2. The [X,Y,Z] coordinates that are used for the CS casing and TF center rod coil shape models are listed in Table R17-3-3.

	Shift		Tilt	
	Amplitude, δR	Phase, ϕ	Tilt angle, α	Phase, ϕ
CS casing	1.8 mm	242°	0.15 mrad	156°
TF center rod	4.9 mm	246°	1.15 mrad	206°

Table R17-3-2: Shift and tilt amplitudes and phases for the center-stack (CS) casing and the TF center rod. The phase of the tilt in the right-most column represents direction of the tilt of the top of the CS casing or the TF center rod. Note that the shift and tilt of the TF center rod are much larger than the shift and tilt of the CS casing, indicating that the TF center rod is poorly aligned within the casing.

		X [mm]	Y [mm]	Z [m]
CS casing	Top	-1.07	-1.53	+1.439
	Bottom	-0.68	-1.70	-1.439
TF center rod	Top	-4.76	-5.84	+2.671
	Bottom	+0.74	-3.14	-2.668

Table R17-3-3: Numerical coordinates at the top and bottom of the CS casing and the TF center rod. The coordinates for the TF center rod are used as the input to IPEC and M3D-C1 for numerical modeling of the error field effects of the TF tilt.

Section R17-3-2.3: The straightness of the OH/TF bundle

A second Laser Tracker metrology run was conducted in Jan. 2017 after the center-stack casing was separated from the OH/TF bundle to determine if the bundle is curved or bowed. A ring around the exterior of the OH bundle was measured at seven positions along its vertical length. The centers of the seven measured rings are fitted to a line, and deviations from that line are used to estimate the deviation of the OH bundle from straight. The root mean square error of the best-

fit line is RMSE ~ 0.4 mm, which indicates that any bow in the OH bundle is at the sub-millimeter scale.

The accuracy of the OH bundle measurements is likely limited to ~ 0.5 mm given that the epoxy on the exterior of the OH bundle is itself non-uniform. Furthermore, the straightness of the TF bundle is not directly represented by the straightness of the OH bundle. Regardless, the fact that the OH bundle is quite straight builds some confidence that the TF bundle might also be straight.

Section R-17-3-3: Evaluation of Error Fields

The asymmetries measured in the TF rod and PF5 coils will produce non-axisymmetric magnetic fields that will couple to the plasma and drive it to a new equilibrium. The distribution of the $n = 1$ magnetic field by the TF and PF5 error field models is shown in Fig. R17-3-7, which shows the field normal to the boundary surface of plasma. TF error generates $m = 1$ dominant structure everywhere but also contains significant higher $m > 1$ in straight-field line coordinates.

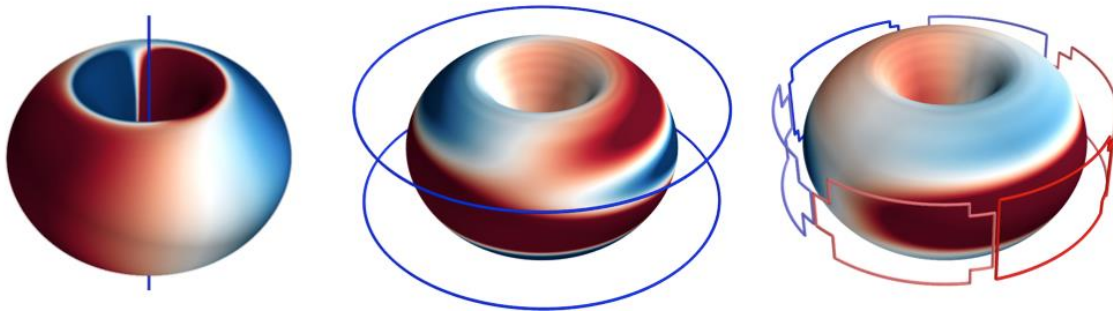


Figure R17-3-7: δB_n distribution due to the TF coil misalignment (left) and the PF5 non-circularity (middle), and due to the $n=1$ RWM coil currents neglecting the response of the plasma (right), on the plasma boundary of NSTX-U 204077.00307. The colors illustrate the relative amplitudes of the field (+red, -blue).

The Fourier spectrum of the component of the error field normal to the equilibrium (axisymmetric) magnetic surfaces often provides good guidance to understand the impact the error field will have on the plasma, especially when it is measured as a normal flux:

$$\delta B_{m/n}(\psi) = \frac{1}{A} \iint \frac{\delta \mathbf{B} \cdot \nabla \psi}{\mathbf{B}_0 \cdot \nabla \theta} e^{i(m\theta - n\phi)}$$

where A is the surface area of the axisymmetric surface with poloidal flux ψ . It is important to include plasma response when evaluating $\delta \mathbf{B} \cdot \nabla \psi$ when assessing the impact of the error field; this is done in the next section. In this section, we present the spectrum of the error fields in the absence of plasma response (the “vacuum fields”). Comparison of vacuum fields was also used to verify the error field models of IPEC and M3D-C1.

The field errors due to the magnetic coils is proportional to the current in the coils, but is also influenced by the plasma shape. For example, the TF coil field error at a given major radius R increases in magnitude with Z , and therefore the error field experienced by the plasma will

increase with the elongation. In order to illustrate the error field spectrum expected over a range of conditions, $B_{mn}(\psi)$ from the TF and PF5 error fields is plotted in Fig. R17-3-8 for three NSTX-U equilibria:

1. 204077.00307: an EFIT01 reconstruction of NSTX-U discharge 204077 at $t = 307$ ms, when $q_0 > 1$. This is an L-mode plasma with $BT = -0.63$ T, $IP = 0.65$ MA, and $\kappa = 1.78$.
2. 204077.00697: an EFIT01 reconstruction of NSTX-U discharge 204077 at $t = 697$ ms, during the IP flattop and with $q_0 < 1$. This is an L-mode plasma with $BT = -0.63$ T, $IP = 0.65$ MA, and $\kappa = 1.68$.
3. 142301: a model NSTX-U H-mode equilibrium based on the profiles from an NSTX discharge, with $IP = 1.5$ MA, $BT = -0.9$ T, and $\kappa = 2.25$.

The 2/1 resonant component of the applied “vacuum” field from the PF5 coils is found to be roughly 1 G in L-mode cases and 2 G in the H-mode case. The vacuum 2/1 field from TF error is considerably larger (5–10 G) and significantly exceeds the design tolerance of 1 G. As shown in Fig. R17-3-9, this error field arises dominantly from horizontal shift of the TF center rod.

The vacuum error field from the OH shift and tilt for 204077.00697 is shown in Fig. R17-3-10. In this case, the OH current was approximately 3.5 kA. The 2/1 component is found to be less than 0.1 G here, which implies that the 2/1 component would be <1 G even in the maximal 24 kA case. Given that this is strongly subdominant to the PF5, TF, and RWM error fields, we do not consider the OH error field in depth in this report.

An assessment of the effect of the error fields will be overly pessimistic when considering the vacuum fields alone, since the TF error field spectrum is not expected to couple well to the modes of the plasma response that contribute to mode locking. (For example, a horizontal shift of both the TF and PF5 coils in the same direction would result in a large vacuum error field in this analysis, but the only effect on the plasma would be to shift its axis of symmetry.) An accurate assessment of the effects of these error fields requires calculating the plasma response. This is considered in the following section.

One implication from the vacuum field calculations is that the TF resonant error can be as large as what RWM coil can drive with the maximum level of current (~ 3 kA), as shown in Fig. R17-3-11. We note that this is apparently inconsistent with two observations: first, that the maximum $n = 1$ RWM coil current that NSTX-U (and NSTX) plasma can tolerate without a disruption is evidently less than 2 kA; and second, that the empirically optimized corrections from various compass scans indicate RWM coil currents less than 1 kA. On the other hand, the empirically optimized corrections were never successful in unlocking 2/1 and edge islands. This is probably not because the optimal correction current exceeds the limit of the power supply, but may be because of the dynamic change of the optimal correction phase (and current) as implied by plasma response modeling.

It is important to note that the error field calculations in this section (Section R17-3-3) and the plasma response modeling in the next section (Section R17-3-4) use a PF5 coil shape model that

includes only the radial profiles and not the vertical profiles reported in Section R17-3-2. Furthermore, the radial profiles that are used are slightly different than those reported in Section R17-3-2 because the latest vacuum vessel data shown in Fig. R17-3-3 was not acquired until August 2017.

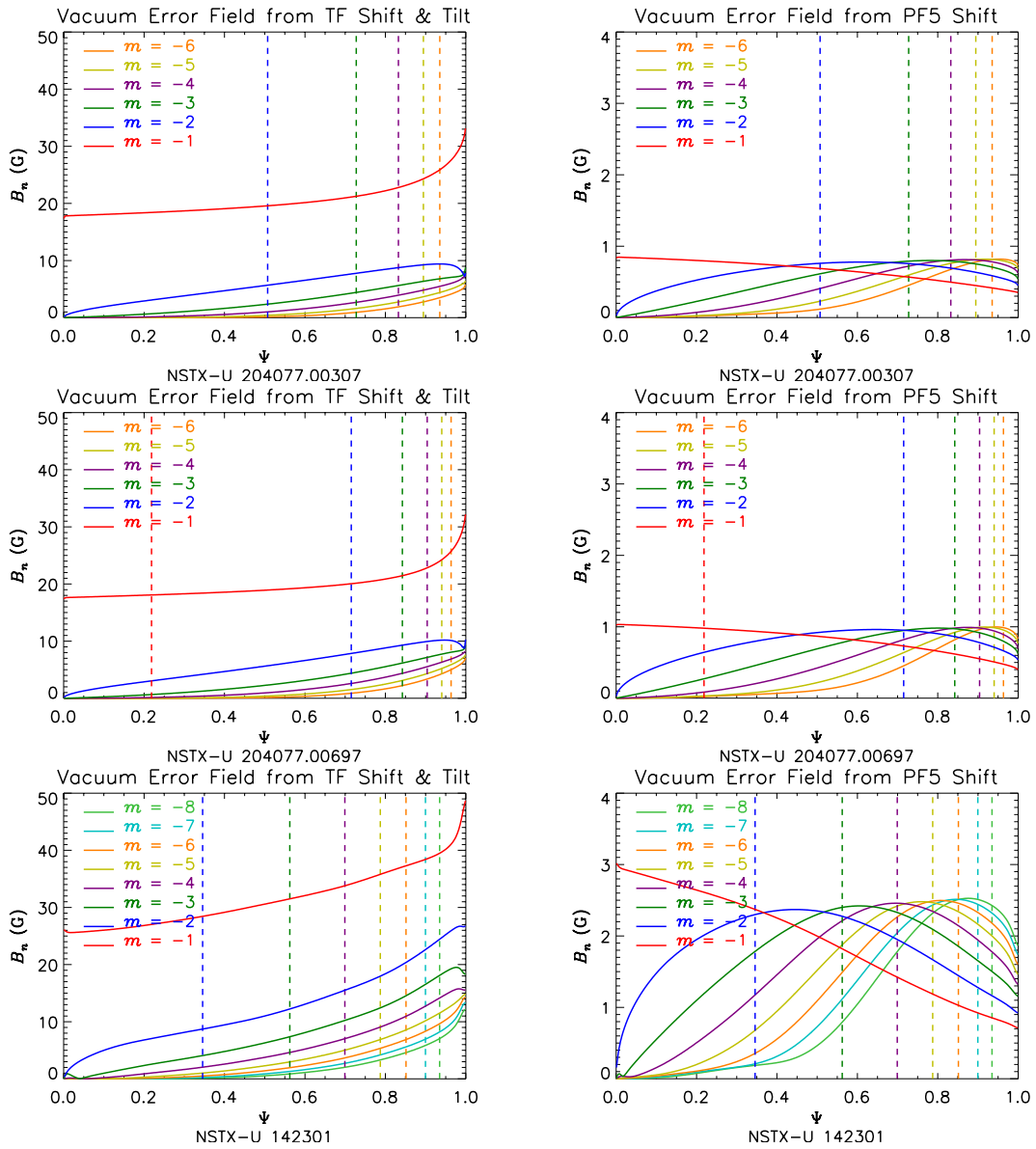


Figure R17-3-8: $\delta B_{m/1}$ due to the tilt and shift of the TF coil (left) and the shifts of the PF5 coils (right) neglecting the response of the plasma, in NSTX-U 204077.00307 (top), 204077.00697 (middle), and 142301 (bottom). Vertical dashed lines represent the radial location of the associated mode-rational surfaces.

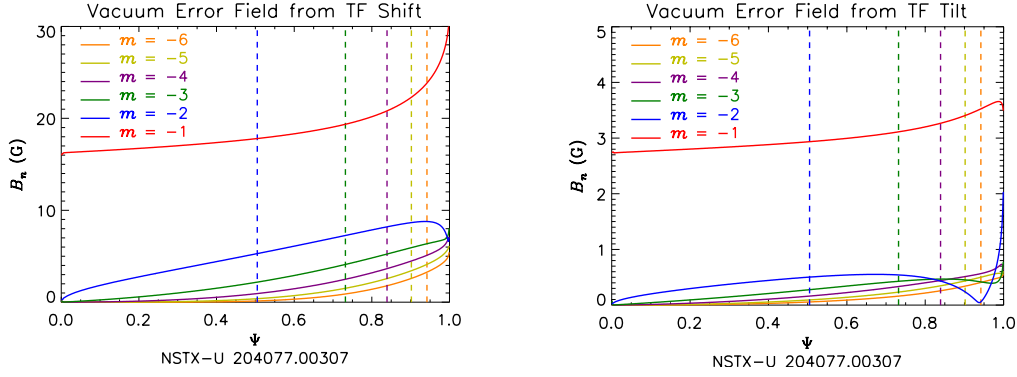


Figure R17-3-9: The separate contributions to the $n = 1$ error field of the horizontal shift (left) and tilt (right) of the TF bundle in NSTX-U 204077.00307.

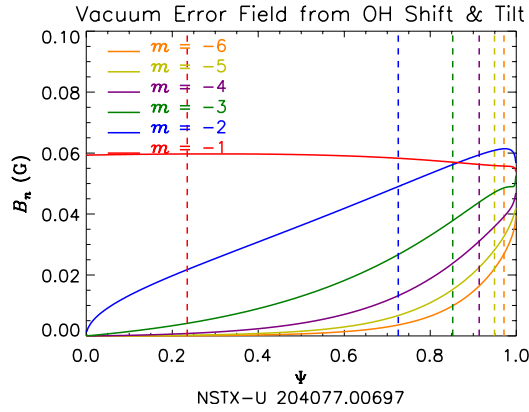


Figure R17-3-10: The vacuum error field from the OH shift and tilt for NSTX-U 204077.00697. The OH current was approximately -3.5 kA at this time.

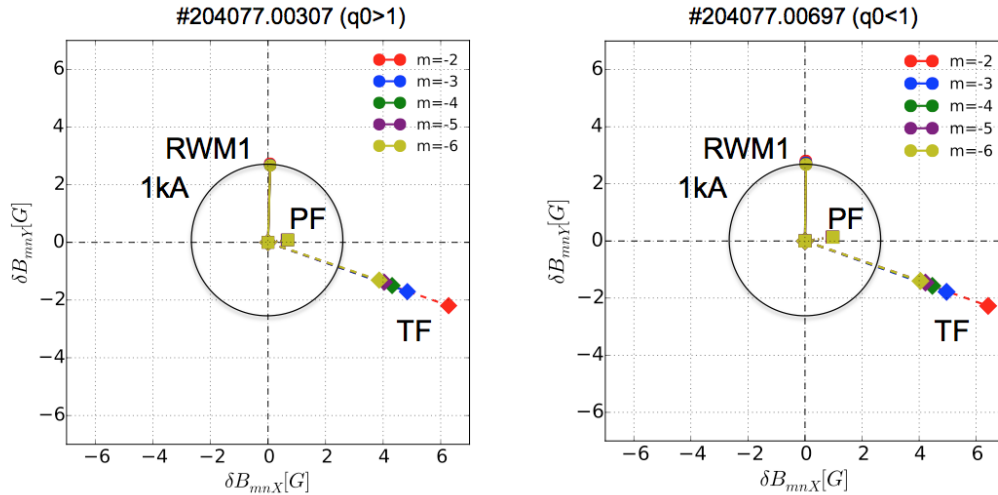


Figure R17-3-11: The amplitudes and phases of the $n=1$ vacuum resonant field due to TF/PF5 error and RWM 1kA for NSTX-U 204077.00307 (left) and 204077.00697 (right). The circle indicates the amplitude of error correctable by RWM 1kA, and TF error clearly exceeds it and requires 2-3kA for correction.

Section R17-3-4: Plasma Response to Error Fields

To assess the resonant interaction of the plasma with the applied fields, linear plasma response modeling was performed using IPEC and M3D-C1. The plasma tends to amplify the external kink-type structure by generating perturbed currents as the response to an externally applied field, as illustrated in Fig. R17-3-12.

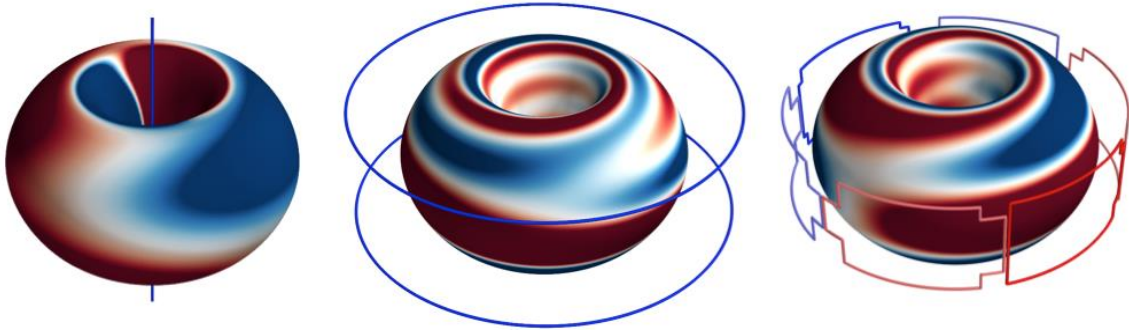


Figure R17-3-12: δB_n distribution due to the TF coil misalignment (left) and the PF5 non-circularity (middle), and due to the $n=1$ RWM coil currents including ideal plasma response, on the plasma boundary of NSTX-U 204077.00307. The colors illustrate the relative amplitudes of the field (+red, -blue). Compared to Figure R17-3-7, the helical structure aligned with the external kink is strongly pronounced.

The resonant components of the $\delta B_{m/n}(\psi)$ profiles that are established with this response represent a coordinate-independent indication of the size of linear islands in the perturbed equilibrium. The resonant shielding currents that arise in the response can be used to give an indication of the tearing response of the plasma, which correlates to mode locking.

IPEC Calculations

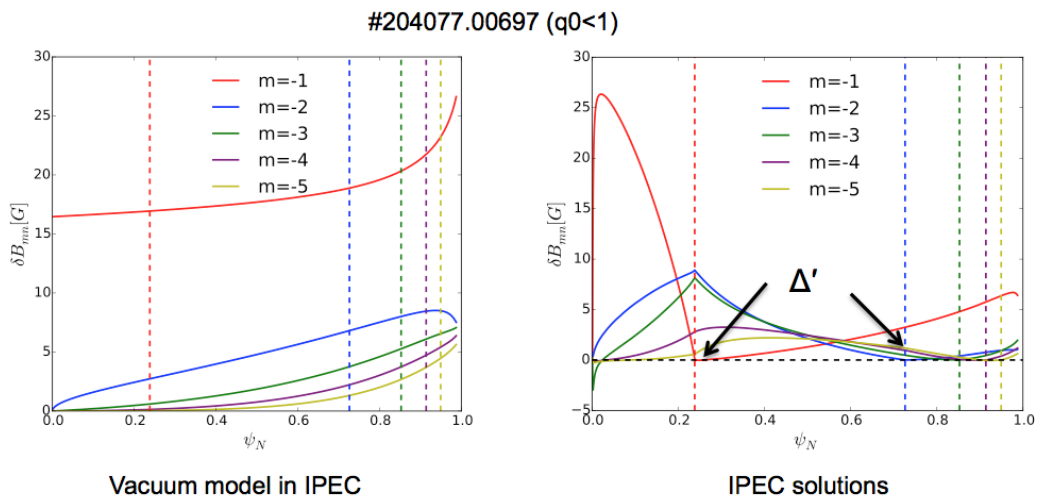


Figure R17-3-13: Comparison of $\delta B_{m/1}$ profiles due to the TF coil misalignment in vacuum (left) and in IPEC (right). The resonant component for each resonant surface is completely suppressed in IPEC, but the resulting discontinuity (indicated as Δ') is used to measure the potentials driving magnetic islands.

IPEC measures the potential to drive magnetic islands using an external Δ' , which is defined by the slope change of the $\delta B_{m/n}(\psi)$ across the rational surface as illustrated in Figure R17-3-13. The slope change of the normal magnetic field physically implies the resonant shielding current δj_{\parallel} suppressing islands before the onset of locking or tearing. The IPEC resonant field is defined as the field that would arise if this shielding current is fully dissipated, that is, simply by $\delta j_{\parallel} \hat{b} = \nabla \times \delta B$, since this is a convenient measure, especially for comparison to vacuum resonant field.

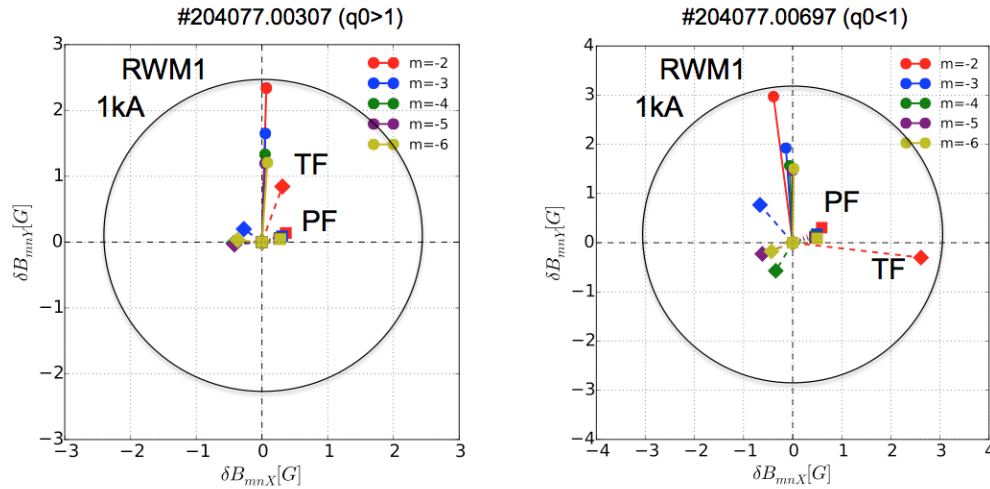


Figure R17-3-14: The amplitudes and phases of the $n=1$ IPEC resonant field due to TF/PF5 error and RWM 1kA for NSTX-U 204077.00307 (left) and 204077.00697 (right). The circle indicates the amplitude of error correctable by RWM 1kA. One can see that the TF error can be corrected with an RWM coil current that is less than or comparable to 1 kA. Also note that the toroidal phase of the TF resonant field changes with the rational surfaces and target equilibria that are used.

The resonant field estimated by this method that includes plasma response shows substantially weaker coupling of TF error field than PF5 or RWM field, as can be seen in Fig. R17-3-14 compared to Fig. R17-3-13. The key aspects observed in IPEC solutions are (I) TF error field is now smaller or comparable to RWM field with 1kA due to the weak coupling, but (II) TF error field is still the dominant source of error field despite the weak coupling, and furthermore (III) the toroidal phase of TF error field exhibits significant variations depending on the rational surfaces and target equilibria. This variation of the toroidal phase is not seen for PF5 error and RWM field, which are almost fixed and even similar to the phase predicted by vacuum superposition.

IPEC simulations are found to be consistent with the empirically determined optimum for early-phase in L-mode discharge evolution, as shown in Fig. R17-3-15. This agreement achieved with plasma response modeling suggests that the TF and PF5 error fields identified by new metrology are likely the major sources of asymmetry found in the compass scan and thereby the confinement degradation in general if no correction is introduced. The simulations however are not successful in explaining the changes of the empirical correction phase for flattop-phase in Ohmic and L-mode discharges. A plausible explanation for this partial matching is that the flattop-phase was almost always accompanied by 2/1 and edge islands and thus not in the regime IPEC can properly describe. Note that IPEC is a valid approximation only when magnetic islands are strongly suppressed before the onset of locking or tearing.

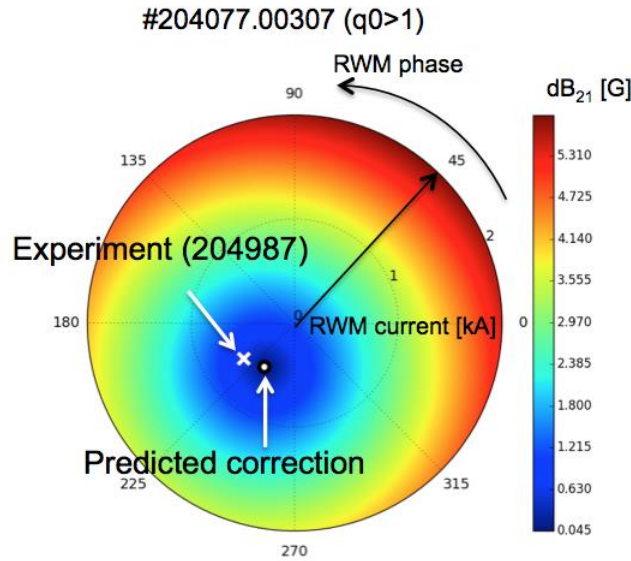


Figure R17-3-15: Comparison of the empirically determined optimal correction to numerically predicted one by plasma response modeling in terms of RWM coil current and phase, in early-phase of a L-mode discharge. This good agreement is however not found for error field correction in flattop-phase.

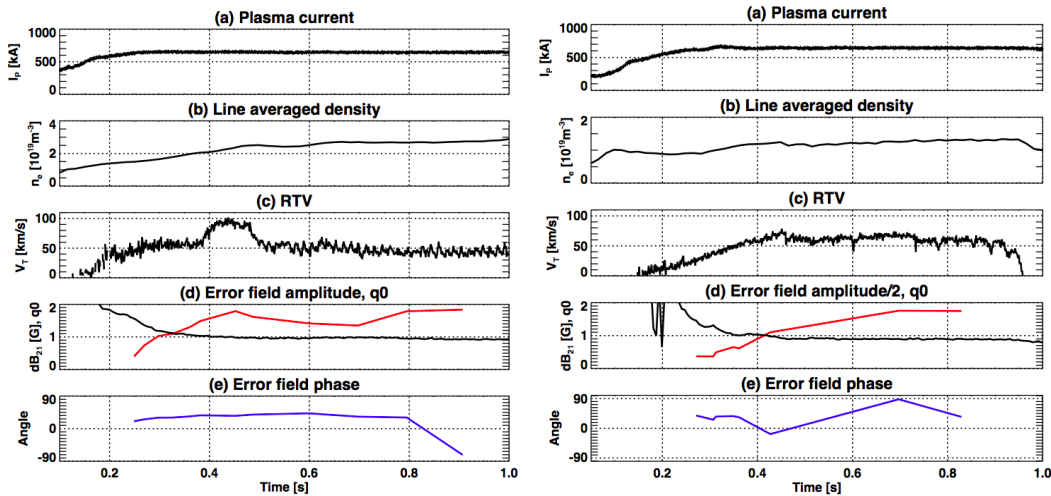


Figure R17-3-16: Traces of experimental parameters for NSTX-U discharges 204939 (left) and 204077 (right). IPEC calculations of the error field amplitude are plotted in red over the q_0 traces, and IPEC calculations of the error field phase are plotted in blue in the bottom panel.

Another important question to be addressed is why the empirical correction for early-phase could not successfully prevent 2/1 locked islands from occurring in the experiments. The key aspect (III) described above might serve as a clue: the toroidal phase for optimal correction can vary in time due to the plasma response to the TF error field, and thus a static correction field is likely to be significantly misaligned at some time during early evolution. The amplitude of the total error field can be strong enough to hit the locking threshold if not properly compensated. Fig. R17-3-16 shows the evolution of the error field amplitude and phase for two NSTX-U discharges, 204939, a high-density L-mode discharge, and 204077, a low-density L-mode discharge as examples.

The estimated threshold value of $\delta B_{2/1}$ for mode locking based on a NSTX scaling law [R17-3-6] is roughly 1.8 G in the high-density case and 0.6 G in the low-density case. IPEC calculates that $\delta B_{2/1}$ meets the threshold in the high-density case and exceeds these values in the low-density case. The traces also show that the error field phase, when taking the plasma response into account, may change significantly over the duration of the discharge. Again this phase shift is largely due to the changing response to the TF error field, and is not typically observed in response to other sources of error fields.

The aggregate findings of the IPEC modeling presented in this section suggest that the TF rod is indeed the most important error field source in NSTX-U. In particular, the time varying plasma response to the TF error field makes it very difficult to develop a correction scheme that keeps the error field below the locking threshold throughout the current ramp. Alternatively, by mechanically correcting the TF misalignment by least by a factor of 2–3, the TF error fields would be below the locking threshold at these densities, even without external error field correction.

M3D-C1 Calculations

M3D-C1 calculations of plasma response were calculated for three equilibria: 204077.00307, a reconstruction of an L-mode NSTX-U discharge at a time during the IP ramp when $q_0 > 1$; 204077.00697, a reconstruction of the same discharge during IP flattop when $q_0 < 1$; and 142301, a model H-mode NSTX-U equilibrium in which $q_0 > 1$. For this study, the single-fluid resistive model was used. In each case presented here, the angular rotation frequency was taken to have Mach number 0.05, giving roughly 15, 19, and 19 kHz at the magnetic axis in 204077.00307, 204077.00697, and 142301 respectively. Spitzer resistivity was used, with the electron temperature roughly 1.1, 1.8, and 1.7 keV in these three cases, respectively.

Unlike IPEC, M3D-C1 has not been validated against NSTX mode locking data, and therefore these results cannot be used to give a quantitative prediction of mode locking. However, by comparing the TF and PF5 response to that from the RWM coils, we may estimate whether and to what extent these error fields can be corrected using the RWM coils.

Two features of the plasma response are assessed here: $\delta B_{m/n}$ as defined above, and the similarly defined resonant components of the parallel perturbed current, $\delta J_{m/n}$. M3D-C1 uses a resistive extended-MHD model that calculates non-zero $\delta B_{m/n}$ directly. In contrast, IPEC calculates $\delta J_{m/n}$ directly and infers $\delta B_{m/n}$ from the perturbed currents, as described in the previous section. Therefore, we believe the resonant currents $\delta J_{m/n}$ give a more direct comparison with the IPEC results and a more accurate picture of the coupling of the error field to the plasma than do the perturbed linear fields $\delta B_{m/n}$.

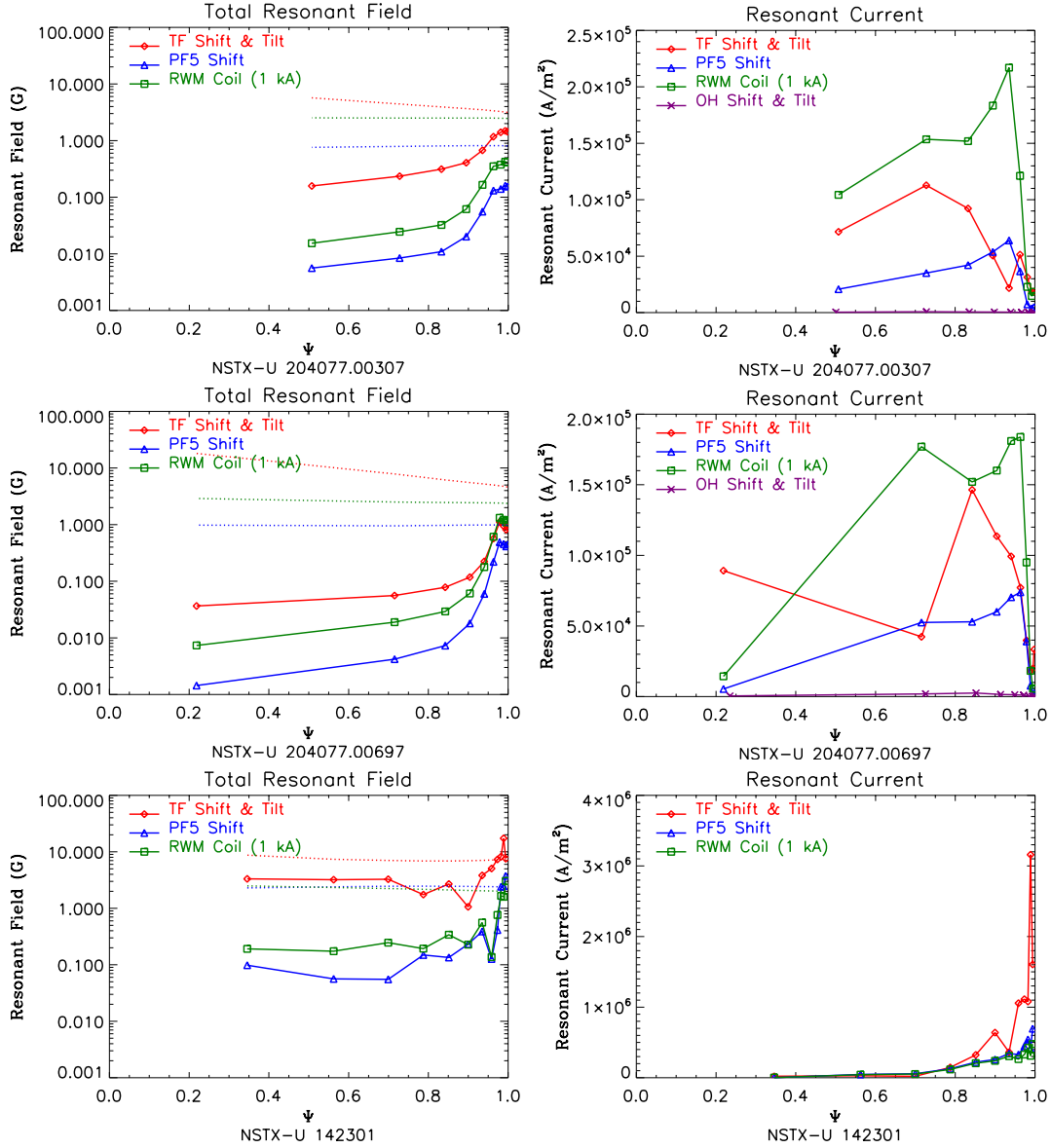


Figure R17-3-17: Left panels: The symbols linked by solid lines represent the total resonant field at each rational surface, for equilibria 204077.00307 (top left), 204077.00697 (middle left), and 142301 (bottom left). The dotted lines represent the vacuum resonant fields. Right Panels: the resonant currents for the three equilibria at each mode rational surface are plotted.

The resonant components of $\delta B_{m/n}$ and $\delta J_{m/n}$ from M3D-C1 are plotted in Fig. R17-3-17. For all equilibria, good screening is found in the core, where rotation is large. In the L-mode cases, both $\delta B_{m/n}$ due to the TF error fields are generally found to be larger than that due to the PF5 error field by a factor of $\sim 3-10$. Despite the fact that the TF error field is significantly larger than the field from the RWM coils powered at 1 kA, the resonant currents $\delta J_{m/n}$ in the plasma response to these two sources of error field are comparable. The resonant currents driven by the PF5 error are weaker than that driven by the RWM coils by a factor of 2–3. By all metrics, the error field from the OH coil is found to be more than an order of magnitude weaker than that from the other coils.

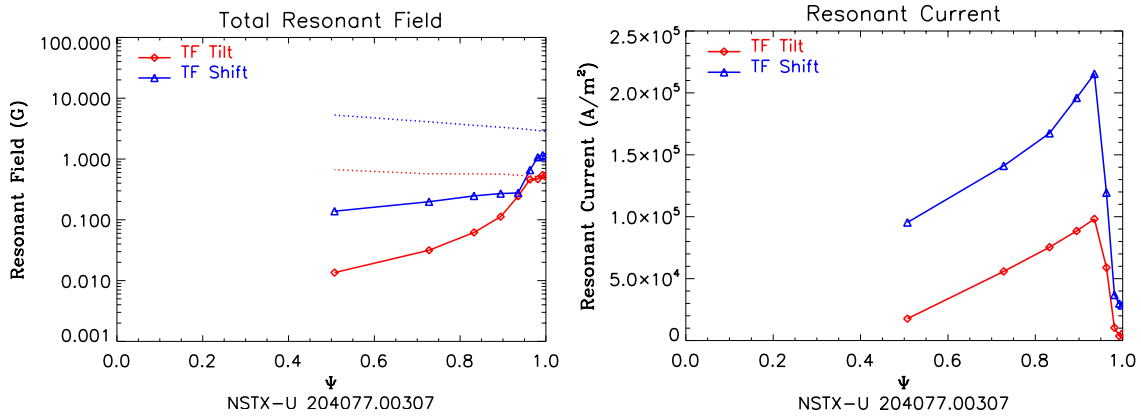


Figure R17-3-18: The resonant components of $\delta B_{m/n}$ (left) and $J_{m/n}$ due to the shift and tilt of the TF rod separately, including the response of the plasma. The dotted lines indicate the values of the applied $\delta B_{m/n}$.

The resonant components of $\delta B_{m/n}$ and $J_{m/n}$ due separately to the tilt and shift of the TF rod are shown in Fig. R17-3-18. M3D-C1 finds that both the applied error field and the plasma response to the TF shift is larger than those from the TF tilt.

Despite the substantial difference in the physical model used by M3D-C1 from that used by IPEC, the results are qualitatively consistent: despite its relatively weak coupling to the plasma, the TF error field is the dominant driver of plasma response currents, at levels comparable to the RWM coils powered at 1 kA.

Neoclassical Toroidal Viscosity

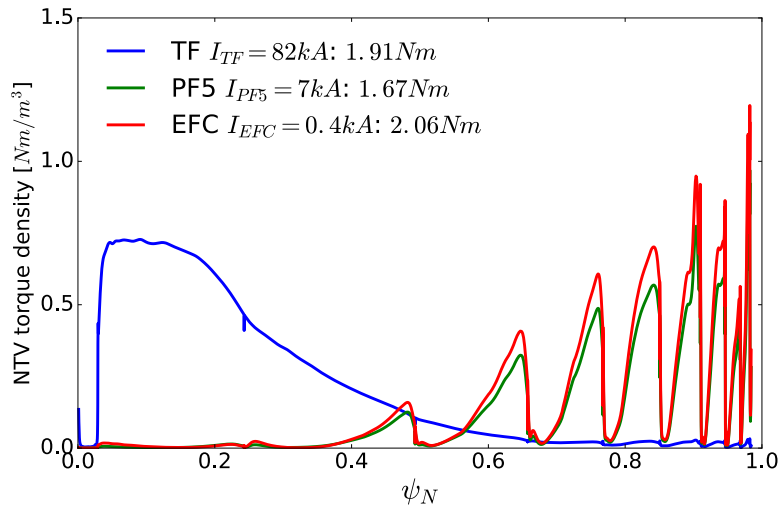


Figure R17-3-19: The NTV torque density caused by error fields from various sources in a high-beta NSTX-U model equilibrium, as calculated by GPEC.

Neoclassical toroidal viscosity was calculated using GPEC [R17-3-8] both for 204077.00307 and for a model H-mode discharge. This H-mode case is based on the 1.5 MA model equilibrium 142301 described above, but with pressure reduced by 20% to reduce β_N below the no-wall limit.

The NTV from all error field sources considered was found to be less than 0.1 Nm in 204077.00307, and therefore is not expected to significantly affect the performance of these discharges. In contrast, the NTV in the H-mode case, shown in Fig. R17-3-19, is found to be much larger—greater than 1 Nm from both the TF and PF5 error fields. The NTV from the TF error field is found to be core-localized, whereas the NTV from the PF5 and RWM coils were found to be more edge-localized and very similar in radial distribution. This suggests that the RWM coils should be effective in canceling the nonresonant PF5 error and minimizing the NTV from that source. It also suggests that the RWM coils will likely not be effective in canceling the non-resonant fields from the TF error, and significant NTV will arise from those uncorrected fields.

The relationship between NTV and locking has not been quantitatively explored. However, we expect that any deleterious effect of NTV torque should be able to be compensated by NBI provided that the NTV torque is significantly less than the torque imparted by a neutral beam, roughly 1 Nm. This suggests that the NTV torque from the TF error should be reduced by an order of magnitude, which entails a factor of ~ 3 reduction in the TF error field (since NTV scales quadratically with the error field).

Section R17-3-5: Effect on the magnetic pitch angle at divertor targets

In this section, we consider the effect of the TF error field on the magnetic pitch angle at the divertor targets, which may have implications for poloidal or toroidal localization of heat flux. Here we consider the model equilibrium NSTX-U 115313.00851_NfHz0+_0, which is a high-performance H-mode model equilibrium with IP=2 MA and BT=1 T.

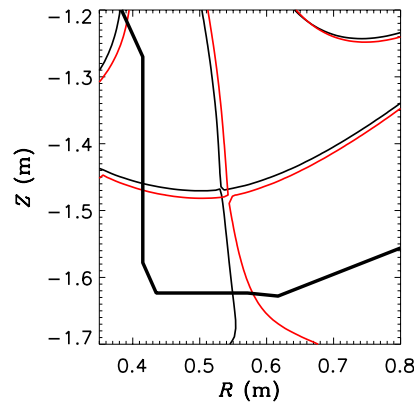


Figure R17-3-20: The magnetic geometry in the lower divertor region in the original LRDFIT g-file (black line) and for the recalculated M3D-C1 equilibrium (red line).

In order to get an accurate response calculation, M3D-C1 re-solves the Grad-Shafranov equation on its own computational mesh using the coil currents, pressure, and toroidal field profiles specified in the g-file produced by LRDFIT. Because details of this calculation differ from the

original LRDFIT calculation, including different methods for keeping the plasma correctly positioned and symmetry assumptions (M3D-C1 does not enforce up-down symmetry), the plasma boundary shape in the final M3D-C1 equilibrium can differ from the original LRDFIT equilibrium. This case, which features a significant flux expansion near the horizontal divertor target, is especially susceptible to shape differences. The shape of the M3D-C1 equilibrium and the original LRDFIT equilibrium near the lower divertor in this case is shown in figure R17-3-20.

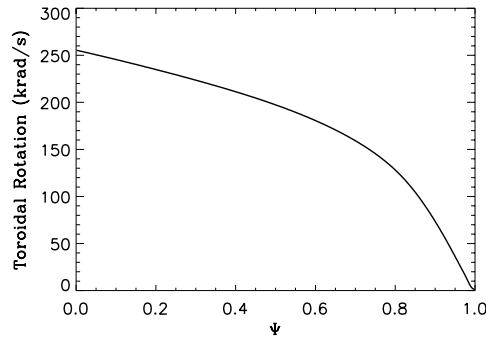


Figure R17-3-21: The equilibrium toroidal rotation profile assumed here.

Rotation plays a significant role in the plasma response calculated by the resistive MHD model. Therefore, an equilibrium rotation profile is included in this equilibrium. We assumed the toroidal ion rotation is proportional to the square-root of the pressure, with a central angular rotation frequency of approximately 250 krad/s (*c.f.* Fig. R17-3-21). In the single-fluid model considered here, the ion, electron, and $E \times B$ rotation profiles are equivalent. Equilibrium poloidal rotation is not considered.

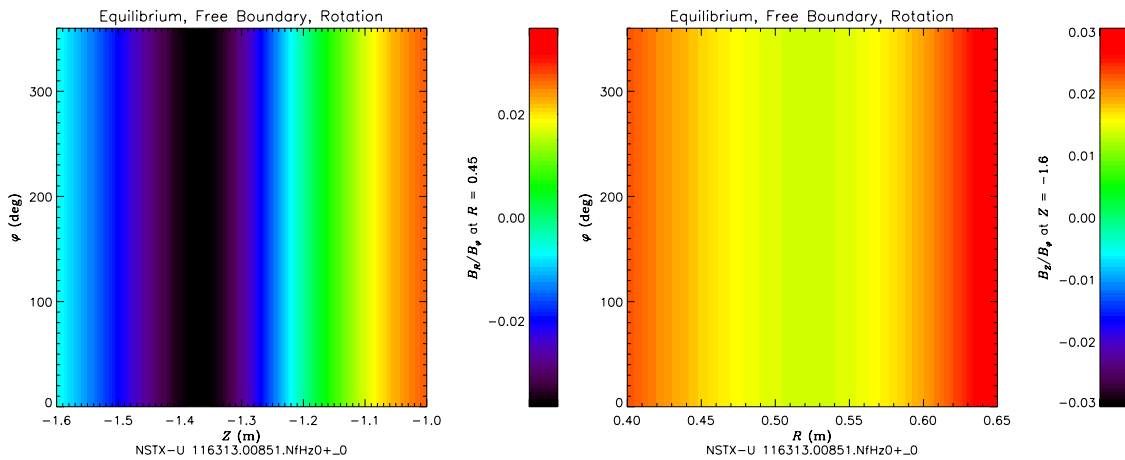


Figure R17-3-22: Equilibrium Field. The equilibrium values of B_R/B_ϕ at $R = 0.45$ m (left) and B_Z/B_ϕ at $Z = -1.6$ m (right) for the model equilibrium NSTX-U 11613.00851_NfHz0+_0. The inner divertor leg passes through $R = 0.45$ at $Z = -1.477$ m, and the outer divertor leg passes through $Z = -1.6$ m at $R = 0.569$ m.

The values of B_R/B_ϕ at $R = 0.45$ m (left) and B_Z/B_ϕ at $Z = -1.6$ m for the (axisymmetric) equilibrium are plotted in Fig. R17-3-22. Given that $B_\phi \gg B_R, B_Z$, these values are approximately the pitch angle (in radians) at which the magnetic field strikes the inner vertical target and lower horizontal target, respectively.

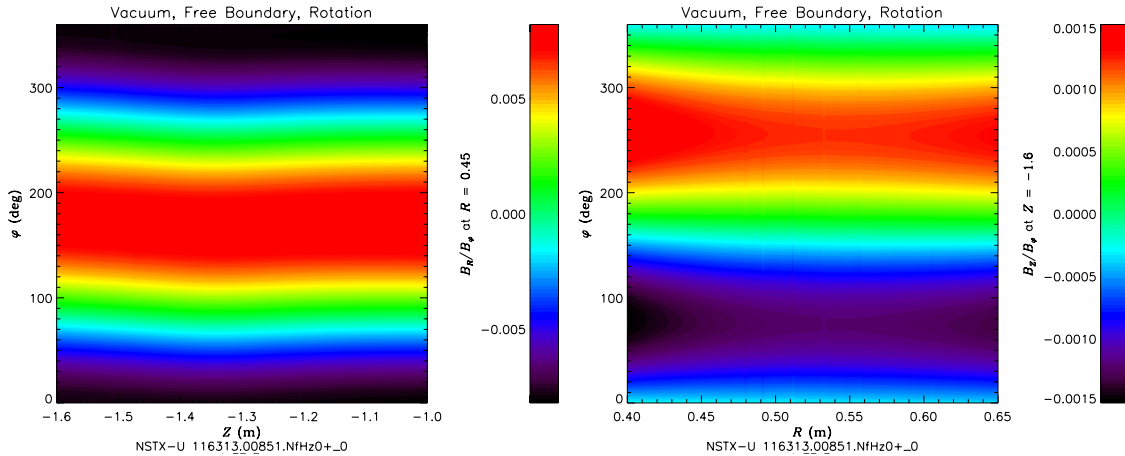


Figure R17-3-23: Vacuum Field. The values of $\delta B_R/B_\phi$ at $R = 0.45$ m (left) and $\delta B_Z/B_\phi$ at $Z = -1.6$ m (right) for the model equilibrium NSTX-U 11613.00851_NfHz0+_0, from the TF error field model in the absence of plasma response (i.e. the vacuum field). The inner divertor leg passes through $R = 0.45$ at $Z = -1.477$ m, and the outer divertor leg passes through $Z = -1.6$ m at $R = 0.569$ m.

The calculated perturbation to the pitch angle at $R = 0.45$ m (left) and $\delta B_Z/B_\phi$ at $Z = -1.6$ m due to the TF error field in the absence of the plasma response (i.e. the vacuum field) is shown in figure R17-3-23. At $R = 0.45$ and $Z = -1.6$, the maximum perturbed pitch angle is roughly 7.5 mrad (0.43°) and 1.5 mrad ($.09^\circ$), respectively.

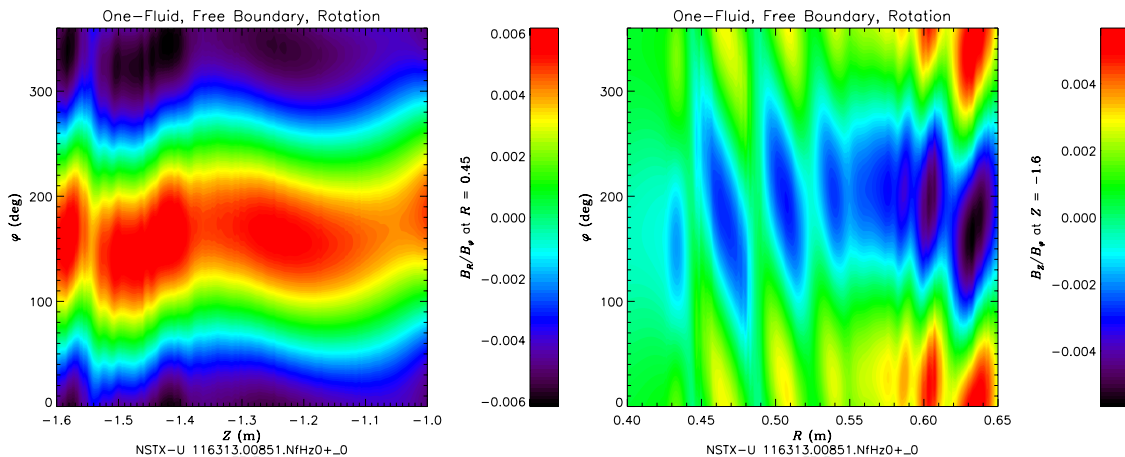


Figure R17-3-24: Total Field, Free-Boundary. The values of $\delta B_R/B_\phi$ at $R = 0.45$ m (left) and $\delta B_Z/B_\phi$ at $Z = -1.6$ m (right) for the model equilibrium NSTX-U 11613.00851_NfHz0+_0, from the TF error field, including the plasma response. The inner divertor leg passes through $R = 0.45$ at $Z = -1.477$ m, and the outer divertor leg passes through $Z = -1.6$ m at $R = 0.569$ m.

Total perturbed field (vacuum plus plasma response) calculated using the linear, one-fluid model in M3D-C1 with a “free” boundary is shown in Fig. R17-3-24. By “free” boundary it is meant that the computational domain boundary, at which superconducting boundary conditions are applied ($\mathbf{B} \cdot \hat{\mathbf{n}} = \text{const.}$), is outside the poloidal field coils; this gives a good approximation to the true free-boundary solution. Here, the pitch angle at $R = 0.45$ m is not significantly different from the vacuum case. However, the pitch angle at $Z = -1.6$ m is seen to develop striations, with the maximum perturbation to the pitch angle increasing to roughly 5 mrad (0.29°). The toroidal phase of the pitch angle perturbation also shifts relative to the vacuum field by roughly 90° .

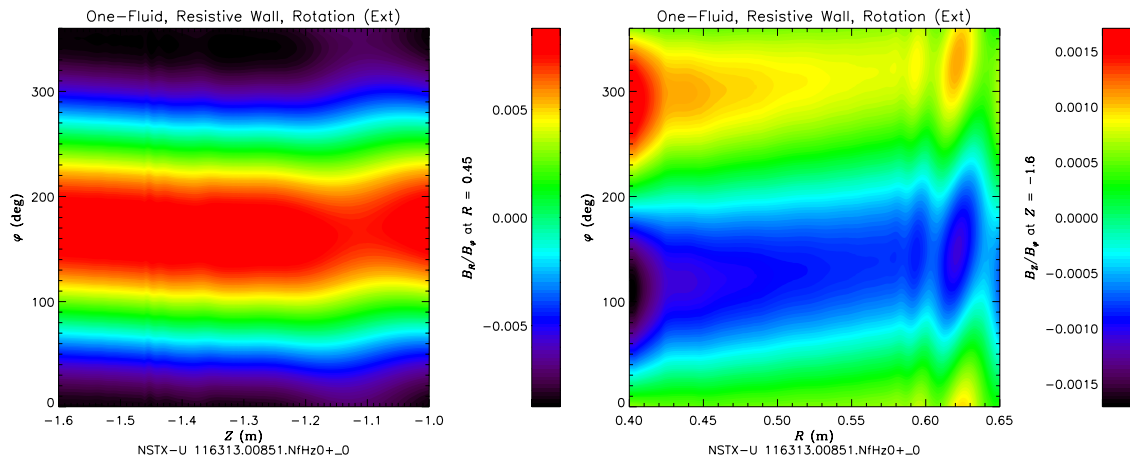


Figure R17-3-25: Total Field, Resistive Wall. The values of $\delta B_R/B_\phi$ at $R = 0.45$ m (left) and $\delta B_Z/B_\phi$ at $Z = -1.6$ m (right) for the model equilibrium NSTX-U 11613.00851_N/Hz0+_0, from the TF error field model, including the plasma response and the effect of a resistive wall. The inner divertor leg passes through $R = 0.45$ at $Z = -1.477$ m, and the outer divertor leg passes through $Z = -1.6$ at $R = 0.569$ m.

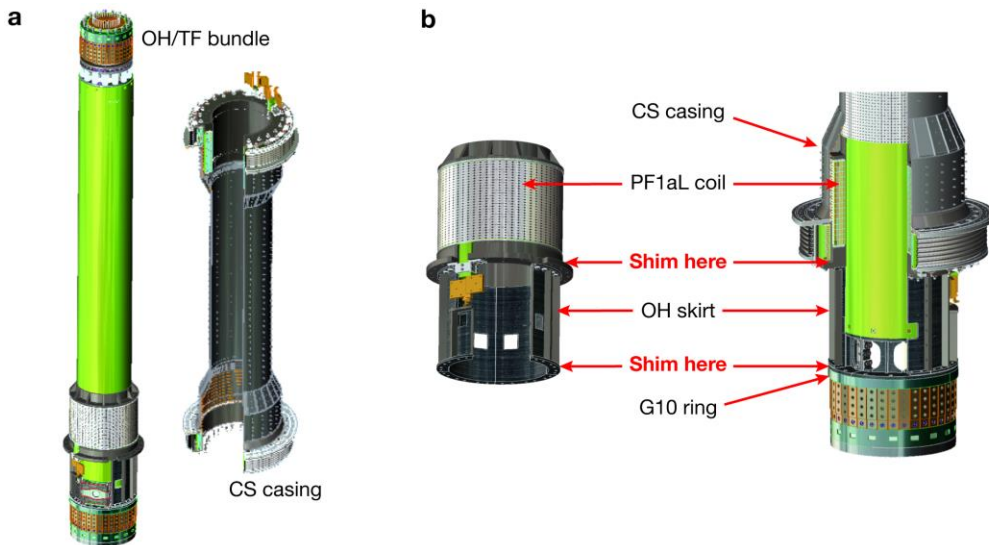
The free-boundary calculation may overestimate the plasma response by neglecting the fields due to eddy currents induced in surrounding conducting structures by the rotating plasma. Here we consider the effect of those currents by modeling the first wall as having resistivity $\eta_W = 1.9 \times 10^{-5} \Omega\text{m}$ and thickness $d = 2$ cm. This implies a wall time of $\tau_W = \mu_0 da/2\eta_W = 0.6$ ms, choosing $a = 1$ m. As in the free-boundary case, the perturbed pitch angle at $R = 0.45$ m is essentially unchanged from the vacuum field. However, the inclusion of the resistive wall causes the perturbed pitch angle at $Z = -1.6$ to resemble the vacuum field more closely than the free-boundary calculation. With the resistive wall, the maximum perturbation to the pitch angle at $Z = -1.6$ is roughly 1.5 mrad (the same as for the vacuum field), and the toroidal phase of the perturbation is smaller than in the free-boundary calculation.

Section R17-3-6: Mitigation and reinstallation strategies

The various metrology and numerical modeling results presented in Sections R17-3-2–R17-3-4 motivate the development of error field mitigation and reinstallation strategies that will physically

modify the positions of the magnetic field coils in NSTX-U in order to mitigate the error fields they produce. The primary mitigation strategy involves the realignment of the TF center rod.

Realigning the TF center rod is a multi-step procedure that first requires that the OH/TF bundle be re-centered within the center-stack casing. At present, the OH/TF bundle is separated from the center-stack casing (as in Fig. R17-3-26a). During reinstallation, the new PF1aL coil will be lowered over the OH/TF bundle, which provides the first opportunity to shim the alignment so that the coil is exactly centered on the bundle (see Fig. R17-3-26b). Next, the CS casing must be lowered over the OH/TF bundle. The point where the mating surface of the casing meets the top of the OH skirt provides a second opportunity to shim the alignment (again see Fig. R17-3-26b). It is important to note that both the PF1aL coil and the CS mating surface will be new as per the Recovery Project Corrective Action Plan. As such, consideration should be given to post-machining the various mating surfaces to promote good alignment between the various pieces. Even if the post-machining is imperfect, the shimming locations identified here provide two options for correct any misalignments between the OH/TF bundle and the CS casing. Finally, the OH/TF bundle metrology from Section R17-3-2.2 should be repeated upon reassembly to verify that the 2 mm alignment tolerance identified in Section R17-3-4 is met.



R17-3-26: (a) At present, the OH/TF bundle and the CS casing are separated from each other. This provides an opportunity to realign the casing with respect to the bundle during reassembly. (b) Two shimming locations, one between the PF1aL coil and the G10 ring and the other between the top of the OH skirt and the CS casing, are identified. These shimming locations provide flexibility in the event that the new PF1aL coil and CS mating surface do not produce a sufficiently centered alignment of the OH/TF bundle within the CS casing. We note that these CAD images are of the FY16 configuration such that some of the design details will be different as a result of redesigns during the recovery outage.

Once the OH/TF bundle has been aligned to the CS casing during reassembly, the combined center-stack assembly must be realigned in the machine. *In situ* metrology of the top and bottom flanges of the NSTX-U outer vessel (not shown) reveal that the flanges are aligned to the vessel coordinate system to within 0.5 mm. Thus, they should introduce minimal error during the reassembly process. The overall positioning of the center-stack assembly should be verified by

conducting *in situ* metrology of the IBDV targets to verify their position. In doing so, the absolute alignment of the OH/TF bundle can also be determined as in Section R17-3-2.2. If final adjustments are required, the radial tensioning rods that are being considered for load mitigation in the polar regions could be used to shift the top and bottom of the OH/TF bundle if needed. It is desirable to avoid this option, but it should be considered if the final OH/TF alignment is out of tolerance.

Another error field mitigation strategy that warrants consideration is the possible shimming of the PF5 coils to adjust their vertical alignment (i.e., their tilt). As shown in Fig. R17-3-5, the PF5 upper coil, in particular is tilted ~ 3 mrad toward Bay K. It may be possible to shim the individual vertical supports for this coil in order to mitigate this tilt. Given that the vertical position measurements of the PF5 coils were obtained in August 2017, modeling efforts to motivate this mitigation strategy are ongoing.

Section R17-3-7: Improved calibration of 3D magnetic field sensors for dynamic EFC

The final milestone task is to assess methods for improving the calibration of 3D magnetic field sensors. This is important from an error field correction perspective because dynamic error field correction algorithms can be activated earlier in the discharge if the calibration and compensation of the sensors can be improved to more effectively remove non-plasma-generated signals. As detailed in the FY16 year-end report, the NSTX real-time dynamic EFC algorithm was reconstituted for NSTX-U during the FY16 commissioning campaign. Substantial non-plasma-generated pickup was observed, however, during the ramp-up phase of the discharge. Had the campaign continued, this would have prevented the use of the dynamic EFC algorithm during the current ramp phase. To enable its use in the future, a collaboration has been initiated with DIII-D to improve the 3D magnetic sensor compensations in both the NSTX-U and DIII-D facilities.

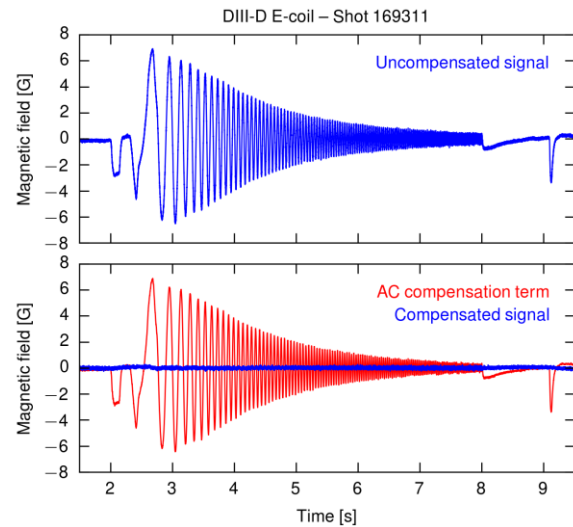


Figure R17-3-27: Sample ACPF compensation test shot from the DIII-D E-coil (the ohmic coil). The frequency of the E-coil oscillations is swept in order to provide maximum spectral content. Top panel: A sample uncompensated 3D magnetic field sensor signal (MPID66M020) showing magnetic field pickup from the E-coil oscillations. Bottom panel: The computed AC compensation term based on a layered low-pass filter approach along with the resulting compensated signal,

From the sensor data acquired during the FY16 NSTX-U campaign, it is clear that the main source of poor compensation is due to signals generated by swinging currents in poloidal field coils. Improving the compensation of these so-called ACPF signals require more spectral information about the signals that the poloidal field coils generate. As such, in FY17, single coil vacuum shots were designed and executed for all of the poloidal field coils in DIII-D (the E- and

F-coils). These vacuum shots provide the necessary foundation for compensating a broader spectral range of AC poloidal field signals. One such DIII-D test shot is shown in Fig. R17-3-27. Here the DIII-D E-coil (the ohmic coil) is oscillated in a frequency sweep from 1–100 Hz. A layered low-pass filter approach to generating sensor compensations, which is what is implemented both offline and in real-time on NSTX-U, is used to eliminate a broad range of spectral content from a sample 3D magnetic field sensor. A general framework to apply these layered low-pass filter techniques to both DIII-D and NSTX-U is nearing completion. These results motivate developing and executing similar calibration vacuum shots in NSTX-U in order to improve 3D magnetic field sensor compensations and to enable more effective use of dynamic error field correction.

Section R17-3-8: Conclusions

It is found that the dominant source of $n = 1$ field error among the sources considered is from the misalignment of the TF rod. This field error is dominantly $m = 1$, which is not expected to strongly couple to the plasma through resonant interaction (*i.e.* excitation of kink modes). However, the $m > 1$ contributions to the field error are large enough to be expected to have considerable impact on plasma performance. In particular, the $m/n = 2/1$ component of the field error is roughly $(\delta B/B) \sim 7 \text{ G} / 7000 \text{ G} = 10^{-3}$.

Vacuum field modeling, IPEC modeling, and M3D-C1 modeling all suggest that the $n = 1$ fields from the PF5 and OH errors are subdominant to that from the TF error, and that the error field from the PF5 can be well-corrected by the existing NSTX-U RWM coils. Error fields from eddy currents in the vacuum vessel and passive plates during I_p ramp-up were also calculated by Dr. Jim Bialek using VALEN (not presented here). The error fields from these currents were found to be below 1 G, and are therefore not presently considered as a likely source of the observed error fields.

Calculations of the plasma response with IPEC and M3D-C1 both find relatively weak coupling of the TF error field to the plasma. Plasma response calculations from both codes suggest that the resonant currents elicited by the TF error field are comparable to those elicited by the RWM coils powered at 1 kA, despite the significantly larger vacuum fields from the TF error. IPEC modeling also found good agreement between the predicted and measured optimal error field correction in the early phase of an NSTX-U discharge. NTV calculations using GPEC find that NTV may be significant for high-beta discharges, and may in fact rival the NBI torque input. While the NTV from the PF5 error is expected to be correctable by the RWM coils, the NTV from the TF error is not. Reducing the TF error by a factor of three would reduce the associated NTV to a level that could be reliably compensated by NBI.

M3D-C1 calculations of a high-beta model NSTX-U equilibrium find that the maximum perturbation to the pitch angle due to the TF error field alone (without plasma response) at the vertical and horizontal divertor targets is roughly 7.5 mrad (0.43°) and 1.5 mrad (.09°), respectively. The plasma response is generally found to increase the maximum perturbation to the pitch angle, especially at the horizontal target. However, when the effect of the resistive wall

is included, the primary effect of the plasma response appears to be a toroidal phase shift of the perturbed field, with the maximum perturbed pitch angle remaining comparable to the vacuum field. This lack of amplification from the plasma response is likely due to the non-resonant nature of the TF error field. The calculated perturbations to the pitch angle, while significant, are not presently believed to be large enough to merit concern. Calculations of the heat flux in the perturbed magnetic geometry are planned to help quantify the potential risk.

Despite the comparable couplings of the RWM coils and TF coils to the plasma, experiments were not successful in preventing 2/1 locking using the RWM coils. IPEC calculations show that the optimal correction phase and amplitude changes as the plasma current density profile. This suggests that while EFC with the existing RWM coils may be possible, it would likely require a time-dependent correction algorithm that will be sensitive to plasma parameters (*e.g.* current density profile). This requirement could pose a significant challenge to reliable operation of NSTX-U.

These results motivate realigning the TF rod in such a way as to reduce the error field by at least factor of three from its present configuration, which we expect to reduce the resonant error fields to levels that will not exceed the locked-mode threshold scaling in the absence of RWM correction. This could be done by leaving the bottom of the TF bundle pinned to its present location and realigning the top of the TF bundle center to within 4 mm of $(x, y) = (0, 3)$ mm; or by realigning both the top and bottom of the TF bundle to within 2 mm of $(x, y) = (0, 0)$. From the modeling, it appears that the most crucial parameter in the realignment is the point at which the TF bundle passes through $Z = 0$. Presently this is roughly 5 mm from the machine axis of symmetry; it should be reduced to less than 2 mm.

References

- [R17-3-1] “NSTX Center Stack Upgrade General Requirements Document.” PPPL Technical Report NSTX_CSU-RQMTS-GRD Rev 5. URL: http://nstx-upgrade.pppl.gov/Engineering/Overall_Project_Information/GRD/CSU_Rev5/NSTX-RQMT-GRD-120614_MO_JEM.pdf. June 14, 2012.
- [R17-3-2] C. E. Myers, et al. “Initial error field correction studies in the National Spherical Torus Experiment Upgrade,” *Bull. Am. Phys. Soc.* **61**, GO6.00002 (2016).
- [R17-3-3] C. E. Myers, et al. in preparation (2017).
- [R17-3-4] J.-K. Park, et al. *Phys. Plasmas* **14**, 052110 (2007)
- [R17-3-5] N. M. Ferraro, *Phys. Plasmas* **19**, 056105 (2012)
- [R17-3-6] J.-K. Park et al. *Nucl. Fusion* **52**, 023004 (2012)
- [R17-3-7] M.J. Lanctot, et al. *Phys. Plasmas* **17**, 030701 (2010)
- [R17-3-8] J.-K. Park, et al., *Phys. Plasmas* **24**, 032505 (2017)

Research Milestone R(17-4): Assess high-frequency Alfvén Eigenmode stability and associated transport (Completed September 2017)

Milestone Description: Experiments and modeling on NSTX have indicated the potential of Compressional and Global Alfvén Eigenmodes (CAE/GAE) to induce both fast-ion redistribution/loss and enhanced electron thermal transport. More flexible NBI heating capabilities in NSTX Upgrade (NSTX-U) enable more comprehensive studies of CAE/GAE physics and support a goal of assessing CAE/GAE stability as a function of the injected NBI source mix. Initial results from the FY-2016 run campaign have already shown a clear dependence of GAE behavior on NBI from specific sources. For example, complete GAE suppression has been observed when a small fraction of NB power from the new 2nd NBI line is added to the total power. Simulations with the HYM code will be used to investigate these initial NSTX-U results and to predict expected CAE/GAE behavior on NSTX-U as the experimental heating power, plasma current, and toroidal field are increased up to their nominal maximum values. Further validation of HYM will be pursued through comparison with experiments from NSTX/NSTX-U and planned experiments from the DIII-D National Campaign. In parallel with CAE/GAE studies, an initial assessment of Ion Cyclotron Emission (ICE) observations from NSTX-U will be performed to characterize the distinctive features of ICE versus sub-ion-cyclotron frequency AEs. For example, ICE features observed on NSTX-U appear different than those observed on conventional tokamaks in that NSTX-U ICE originates near half-radius, i.e. not near the plasma edge. These observations can provide insight into theoretical models of ICE, which are crucial for the potential exploitation of ICE as a confined fast ion diagnostic for ITER. The main goals for ICE studies are: (i) to assess possible correlations with fast ion properties such as the radial profile and the energy dependence of the distribution function, and (ii) to identify which improvements to existing codes (e.g. HYM) are required to properly model ICE.

Milestone R(17-4) Report:

The expanded parameter range achievable on NSTX-U with the 2nd NB line has provided insight into the fast ion phase space regions that are relevant for destabilization of high frequency Alfvénic modes (CAE/GAE). For example, early results during the FY-16 Run have shown that small amounts of beam ions with high pitch-angle values (pitch ~ 1) can strongly suppress the counter-propagating Global Alfvén Eigenmodes (GAE) [R17-4-1], see Fig. R17-4-1. A

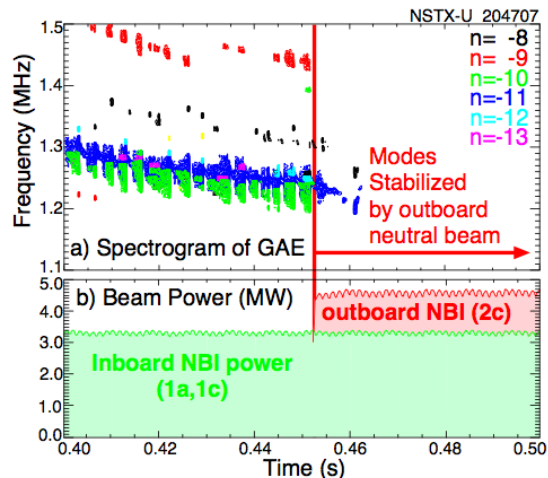


Figure R17-4-1: (a) Spectrum of magnetic fluctuations showing GAE stabilization after turn on of one of the 2nd NBI lines. (b) Waveforms of injected NB power.

quantitative analysis of this data with the HYM stability code predicts both the frequencies and instability of the GAE prior to - and suppression of the GAE after - the injection of high pitch-angle beam ions. Simulations with the HYM code find unstable GAE with $n=-7$ through -12 (Fig. R17-4-2) using plasma equilibrium parameters and the fast-ion distribution function calculated at 0.44s, and that the modes are stable using an analytic fit to the beam ion distribution parameters at 0.47s, consistent with experiment. The linear growth rates at 0.44s for the modes are shown in Fig. R17-4-2a, with the fastest growing modes being $n=-9$, -10 , and -11 (negative values here denote that the GAEs were counter-rotating) in good agreement with the experimental measurements. The mode frequencies are shown in Fig. R17-4-2b (red curve). Experimental estimates of the drive and damping rates for the GAE can be made from the growth and decay rates of the GAE bursts, Fig. R17-4-2c. For comparison to the simulation results, experimental growth rates are normalized to the ion cyclotron frequency providing $\gamma_{\text{growth}}/\omega_{\text{ci}} \approx 0.3\%$ and $\gamma_{\text{drive}}/\omega_{\text{ci}} \approx 0.5\%$. Those values appear to be lower than what predicted by the HYM code. However, the agreement in unstable mode numbers and mode frequencies between theory and experiment in these initial results represents a strong validation of the HYM code physics, providing confidence in the use of HYM to predict stability of plasmas on ITER.

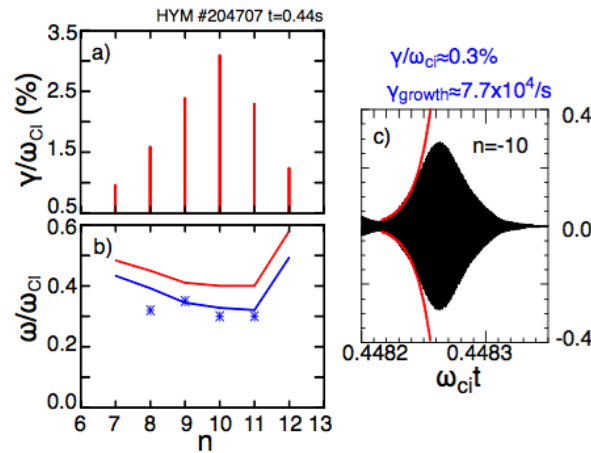


Figure R17-4-2: (a) Growth rate and (b) frequency of unstable GAEs from HYM simulations. Symbols refer to the experimental data. The blue line takes into account Doppler shift corrections to the mode frequency. (c) Estimate of the growth rate from the experiment.

HYM simulations in low-aspect ratio, NSTX-like conditions also reveal strong energetic particle modifications to GAE properties [R17-4-2]. Key parameters defining the fast ion distribution function – such as the normalized injection velocity $v_0/v_{\text{Alfvén}}$ and central pitch – are varied in order to study their influence on the characteristics of the excited modes. It is found that the frequency of the most unstable mode changes significantly and continuously with beam parameters, depending most substantially on $v_0/v_{\text{Alfvén}}$. This unexpected result is present for both co- and counter-propagating GAEs, which are driven by Doppler-shifted cyclotron resonances. Large changes in frequency without clear corresponding changes in mode structure could indicate the existence of a new energetic particle mode, i.e. an “energetic-particle-modified GAE” (or EP-GAE). Additional simulations conducted for a fixed MHD equilibrium have demonstrated that the GAE frequency shift cannot be simply explained by the equilibrium changes due to energetic

particle effects. These results call into question the description by ideal MHD theory of sub-cyclotron Alfvénic modes as GAEs, and open a new line of future research.

Besides the HYM code, the linear eigenmode solver CAE3B [R17-4-3][R17-4-4] can be used to simulate a Hall-MHD plasma with realistic geometry, allowing predictions of CAE frequency and structure based on experimental plasmas parameter. CAE3B results can be compared with experimentally observed modes, e.g. in NSTX plasmas, in order to validate the physics model of CAE3B and better understand CAEs. For example, comparisons between CAE3B and NSTX discharge #130335 show that low- n (e.g. $n=-3$) simulated eigenmodes occur with frequencies and frequency rates-of-change similar the experimentally observed modes. High- n (i.e. $|n|>5$) simulations, however, do not match experimentally observed modes in either frequency or frequency rate-of-change. These results suggest that the low- n modes are in fact CAEs and that high- n modes are instead probably global Alfvén eigenmodes (GAEs). CAE3B simulations may thus complement and improve existing methods of eigenmode identification.

On the experimental side, new results on measurements of the internal amplitude and structure of CAE and GAE density perturbations in NSTX have been submitted to the journal Nuclear Fusion [17-4-5]. These measurements are being compared with the CAEs and GAEs mode structure from simulations by the HYM code. The results will be presented in an invited talk at the 15th IAEA Technical Meeting on Energetic Particles in Magnetic Confinement Systems (Princeton, NJ, Sep. 2017).

A previous database on scaling laws and instability threshold for CAEs and GAEs [R17-4-6] has been expanded for a broad range of parameters in NSTX/NSTX-U configuration. The database is expected to provide information on the physics controlling the instabilities, as well as on their role in causing enhanced thermal transport. The expanded database includes 195 discharges (mostly H-mode plasmas) with plasma current in the range 0.3-1.3MA, toroidal field 2.7-5.3kG and up to 6MW of injected NB power. Mode properties (frequency, toroidal mode number, amplitude) are computed for 50ms time intervals and correlated with properties of the thermal plasma and NB injection. A clear correlation emerges between total power in the instabilities and the injected NB power. Also, the correlation between mode number and frequency appears to confirm the importance of the parallel resonance condition to destabilize the modes. Other results are more difficult to interpret. For instance, the dependence of mode power vs. injected NB power and electron temperature (Fig. R17-4-3) is difficult to untangle unambiguously. Work is in progress to implement multi-regression analysis technique to unfold single dependencies from complicated multi-parameter correlations from the experimental data

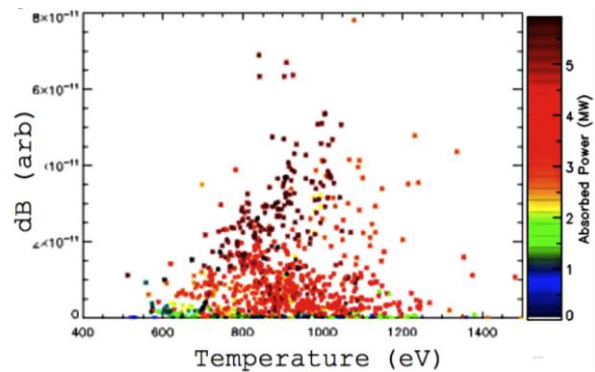


Figure R17-4-3: Experimental data on power in high-frequency Alfvénic instabilities vs. injected NB power and electron temperature.

[R17-4-7]. Additional results from the study of the improved database with respect to thermal electron transport are discussed in the Turbulence & Transport TSG Research Highlights.

To gain further information on the damping processes of CAE modes, measurements from the high-k diagnostic in NSTX potentially show evidence of coupling between CAEs and kinetic Alfvén waves (KAW) in NSTX, a process predicted in recently published simulations by the HYM code [R17-4-8][R17-4-9]. UCLA undergraduate student Zhi Deng will present the measurements at the 59th Annual Meeting of the APS Division of Plasma Physics (Milwaukee, WI, Oct. 2017).

Work on high-frequency Alfvénic modes is conducted in collaboration with other facilities, and in particular with DIII-D. UCLA graduate student Shawn Tang participated in the NSTX-U/DIII-D Collaborative Research National Campaign on behalf of NSTX-U, leading an experiment in July 2017 to investigate the dependence of CAE and coherent ion cyclotron emission (ICE) stability and spectral characteristics on beam velocity and injection angle in DIII-D. The experiment was very successful. UCLA millimeter-wave diagnostics on loan to DIII-D from NSTX-U were able to obtain valuable measurements of CAE internal amplitude during this experiment. S. Tang will present the results in a talk at the 15th IAEA Technical Meeting on Energetic Particles in Magnetic Confinement Systems (Princeton, NJ, Sep. 2017).

References

- [R17-4-1] Fredrickson, E. D. et al, Phys. Rev. Lett. 118, 265001 (2017).
- [R17-4-2] Lestz, J. B. et al, Phys. Plasmas (submitted 2017).
- [R17-4-3] Smith, H. M. et al, Plasma Phys. Control. Fusion 51, 075001 (2009).
- [R17-4-4] Smith, H. M. et al, Plasma Phys. Control. Fusion 59, 035007 (2017).
- [R17-4-5] Fredrickson, E. D. et al, Nucl. Fusion 54, 093007 (2014).
- [R17-4-6] Crocker, N. A. et al, Nucl. Fusion (submitted 2017).
- [R17-4-7] Tang, S. et al, plenary talk at TTF meeting (Williamsburg, VA - 2017).
- [R17-4-8] Belova, E. et al, Phys. Rev. Lett. 114, 015001 (2015).
- [R17-4-9] Belova, E. et al, Phys. Plasmas 24, 043505 (2017).

Research Milestone R(17-5): Analysis and modelling of current ramp-up dynamics in NSTX and NSTX-U (Completed September 2017)

Milestone Description: Steady-state, high-beta, and high-confinement conditions are required in future ST devices such as an FNSF or Pilot Plant. A major research goal of NSTX-U is to generate the physics basis for the achievement of such conditions by accessing high toroidal field (0.8-1T) and plasma current (1.6-2.0MA). This milestone aims to accelerate the realization of high plasma current exceeding NSTX levels ($I_p > 1.3$ MA) when plasma operations resume on NSTX-U. Realizing such target plasma conditions requires operating at sufficiently high elongation in order to operate below MHD stability limits. Scenarios that have achieved suitable elongation on NSTX and NSTX-U utilized an L-H transition early in the I_p ramp-up phase in order to obtain low internal inductance (l_i) throughout the discharge, which is conducive to maintaining vertical stability at high elongation. The details of the ramp-up phase, encompassing the transition from a limited to diverted shape, the L-H transition, and the rapid rise in the plasma current, have a large influence on the scenario current and pressure limits. The limits to the achievable elongation realized on NSTX-U will be evaluated, with new attention to the limits during the ramp-up phase, and compared to NSTX. In particular, the growth rate of vertical instabilities will be studied by evaluating the elongation limits realized on NSTX-U during the ramp-up phase, especially at the time of diverting. The dependence of the L-H transition on plasma parameters such as density, plasma shape, and plasma current on NSTX-U will be evaluated in order to generate a threshold criterion for simulations. Further, kink and tearing stability analysis of the ramp-up phase of the experimental and simulated discharges will be initiated to improve understanding of the global MHD stability limits of the current ramp-up phase.

Milestone R(17-5) Report:

Section R17-5-1: Introduction and Motivation

A critical component for achieving high-performance H-mode discharges on NSTX was the achievement of a broad current profile (i.e. lower l_i) and pressure profile during the I_p flattop. The broad current profiles increased the achievable elongation and average triangularity (δ) in the flattop phase [R17-5-1]. This is beneficial since the increased shaping acts to increase the I_p limit imposed by edge stability limits. A broad pressure profile enables stable operation at higher global β_N . Consequently, more heating power can be injected while remaining below global β_N limits, which is beneficial for inducing regular ELMs needed to flush impurities from the plasma core and maintain operation at reduced l_i by slowing diffusion of current toward the plasma core.

Experiments on NSTX established that transitioning to a diverted shape and entering H-mode early in the I_p ramp-up phase enable the access to a broad current and pressure profile. The increased edge temperature and density gradients that occur in H-mode act to broaden the pressure profile and reduce the penetration of the edge current that drives the increase in l_i during the ramp-up phase. Initial operations in NSTX-U observed improved H-mode performance as the timing of diverting and the L-H transition moved earlier in the discharge. Figure 17-5-1 compares three NSTX-U discharges (blue, red and black) to a fiducial NSTX H-mode discharge (green). The vertical dashed lines show the timing of the L-H and H-L transitions. As the timing of the L-H transition is moved earlier (blue is latest, green is earliest) the internal inductance through the flattop phase (panel c) is reduced enabling stable operation at larger elongation (panel d). The stronger shaping enables stable operation at larger I_p (panel a) and heating power (panel b).

The NSTX-U discharges shown in figure 17-5-1 provide a picture of the progress in developing the H-mode scenario during the first ten-week campaign, and the direction the development was headed when operations ended. Discharges 202946 (blue), 203679 (red) and 204112 (black) occurred in the third, fifth and seventh week, respectively. The I_p ramp rate (panel a) was kept relatively the same during this development and was slower than on NSTX. The slower ramp rate was chosen to maintain a loop voltage (V_{loop}) similar to NSTX when the available heating power was low (blue traces for example), with plans to increase the ramp rate when more heating power was available (this activity was planned, but not started). The slower I_p ramp rate delayed the time when the neutral beam injection began compared to NSTX since the injection is delayed until I_p is sufficiently large. Consequently, moving the L-H transition timing earlier in future operations will require increasing the I_p ramp rate in order for the NBI heating timing to move earlier.

The evolution of the plasma shape during ramp-up also requires further optimization. Panel d shows that the elongation was lower than the NSTX fiducial. Discharges 202946 (blue) and 203679 (red) achieved an elongation in flattop close to the expected maximum permitted for vertical stability at the respective values of I_i ; however the elongation limits at $I_i < 0.7$ were not established. Thus, discharge 204112 (black) would have most likely been stable at larger elongation during flattop.

All of the NSTX-U discharges achieve an elongation during I_p ramp-up that is considerably lower than on NSTX. This was partly due to not yet exploring the limits, but also due to unique characteristics of NSTX-U. One unique characteristic is that strong toroidal eddy currents were induced in the crowns of the ohmic solenoid that ultimately limited the elongation ($\kappa < 1.8$) for the first 50 – 80 ms of the discharge in order to avoid the loss of vertical position control. These eddy currents are expected to be significantly lower when NSTX-U operations resume with a different choice of cooling tube material in this region. The second unique characteristic was the common observation of a “bobble” at the time of diverting. The cause of the “bobble” was unknown, but diverting with $\kappa < 2$ allowed the discharge to survive this event. Future operations will aim achieve a larger elongation during ramp-up to enable the discharge to divert earlier, which is beneficial for maintaining a broad current profile by reducing the neutral and impurity influx.

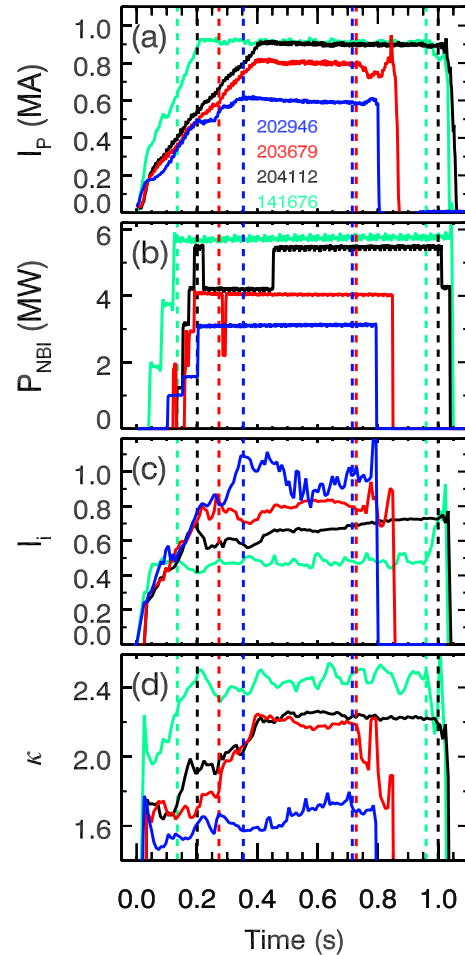


Figure 17-5-1 Comparison of 3 NSTX-U H-mode discharges (blue, red and black) demonstrating progress toward developing H-mode scenarios similar to NSTX (green). Vertical lines indicate L-H and H-L transitions.

The activities directed by this research milestone are aimed at accelerating the optimization of the H-mode ramp-up scenario when NSTX-U operations resume. Progress toward this optimization will drive the advancement toward satisfying a major research goal of NSTX-U Advanced Scenarios and Control topical science group: to generate the physics basis for the achievement of high toroidal field (0.8 – 1 T) and plasma current (1.6 - 2.0 MA). The five major elements of this milestone are: (1) comparison of the achieved elongation and internal inductance on NSTX-U to NSTX, with particular attention to the ramp-up phase, (2) determination of the limits to the elongation imposed by vertical stability (3) examination of the cause and mitigation of the “bobble” that limited the elongation at the time of diverting, (4) quantifying the target conditions for establishing a robust L-H transition early in the ramp-up, and (5) examination of the MHD stability properties of discharges near $l_i = 0.55$ that were difficult to reliably achieve. The progress made on these activities in FY17 increases the efficiency of H-mode scenario development in future NSTX-U operations.

Section R17-5-2: Achieved elongation and internal inductance for NSTX and NSTX-U

Figure R17-5-2 shows a plot of elongation versus internal inductance at the time of maximum stored energy in all plasma shots from both NSTX (red points) and NSTX-U (blue points). Typically, discharges with $l_i > 0.9$ are L-mode discharges, with the lower l_i range accessed via H-mode. The NSTX results span a large range of l_i ($0.4 < l_i < 1.2$) with the elongation typically limited to below 2 when $l_i > 0.75$. The achievable elongation increases toward $\kappa = 2.5$ as l_i decreases. L-mode discharges on NSTX-U achieved an internal inductance above 1.2 and are restricted to $\kappa < 1.8$, extending the trend that is evident in the high-internal-inductance NSTX data. H-mode discharges on NSTX-U operated with $l_i < 1.0$ and values of elongation similar to those obtained in the corresponding range in the NSTX data. This indicates that the elongation limits realized on NSTX-U were similar to those achieved on NSTX, now at higher aspect ratio. These results are promising and motivate pursuing scenarios that achieve $l_i < 0.6$ in order to achieve an elongation of κ up to 2.5.

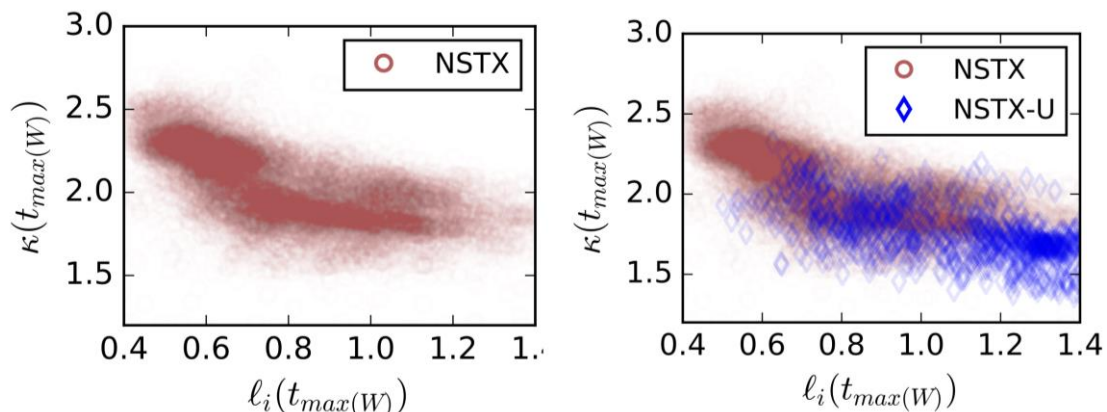


Figure R17-5-2: Elongation vs. internal inductance at the time of maximum stored energy for all plasma shots on NSTX and NSTX-U. NSTX-U achieved similar elongations to NSTX at higher aspect ratio.

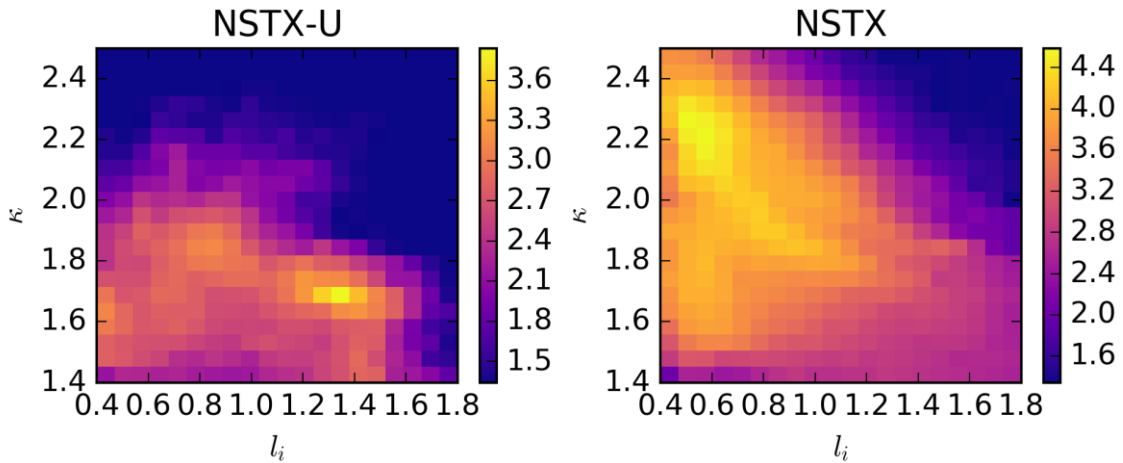


Figure R17-5-3: Log scale histogram of elongation vs. internal inductance of all EFIT01 equilibria. The histograms are heavily weighted toward the high- l_i L-mode fiducial on NSTX-U and the low- l_i H-mode fiducial on NSTX.

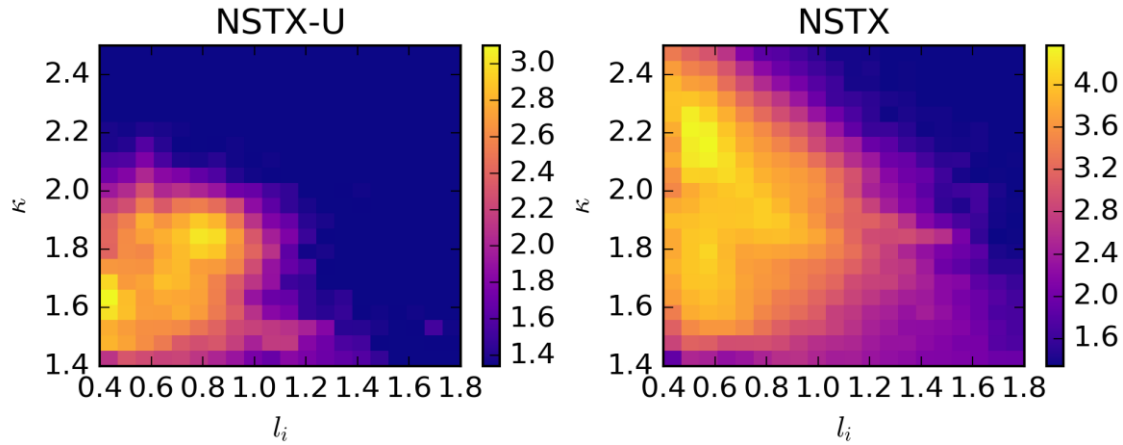


Figure R17-5-4: Log scale histogram of elongation vs. internal inductance of all EFIT01 slices for $t < 0.3s$ when l_i is typically less than one.

Histograms of all EFIT01 slices with plasma current above 200kA were generated for NSTX and NSTX-U in order to compare the elongation and internal inductance operating spaces in more detail. Since such histograms heavily weight frequently run discharges (like the daily fiducial discharge), the base 10 logarithm of the histograms are plotted to improve the visualization of the full operating space. Figure R17-5-3 shows the histograms of elongation versus internal inductance. The most frequent operating point on NSTX-U is around $\kappa = 1.7$ $l_i = 1.35$, corresponding to the L-mode daily fiducial used for many control and diagnostic commissioning activities. As the internal inductance decreases, the most commonly achieved elongation increases for $l_i > 0.8$. NSTX operated in a region approximately bounded by a negative sloping line, with the most common operating region occurring at $l_i < 0.6$ and $\kappa \approx 2.3$ (see NSTX H-mode fiducial in figure R17-5-1).

Figure R17-5-4 shows the same histograms with data restricted to the early part of the I_p ramp-up phase with $t < 0.3s$. The NSTX histogram is very similar to the full dataset, though the highest

values of internal inductance are less common, since internal inductance typically starts low and increases over time. The coincidence of the most common operating point in both the early and all-time plots indicates that NSTX often rapidly established the final operating point of the shot. NSTX-U, on the other hand, operated most frequently at low elongation early on, even in the favorable low internal inductance range. As discussed in section R17-5-1, the elongation early in the ramp-up phase was limited to $\kappa < 2$ due to issues with large eddy currents in the crowns of the ohmic solenoid and vertical oscillations that occurred during the transition to a diverted shape.

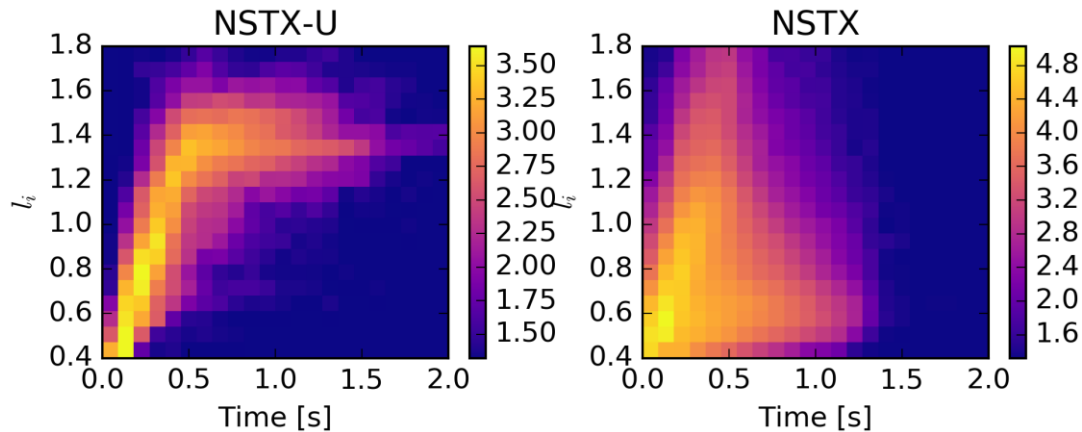


Figure R17-5-5: Log scale histogram of l_i vs. time for all EFIT01 slices. The rate of increase in l_i during ramp-up is similar for the two devices. The pulse length limit imposed by the available inductive V-s was achieved on NSTX for $l_i \geq 0.6$, while only for $l_i \geq 1.3$ on NSTX-U.

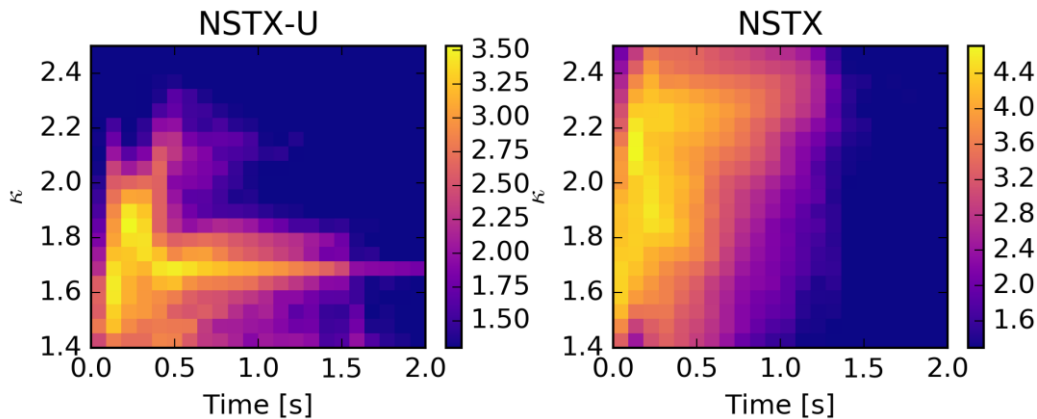


Figure R17-5-6: Log scale histogram of elongation vs. time for all EFIT01 slices.

Figure R17-5-5 shows histograms of internal inductance versus time for NSTX-U and NSTX. Both show a branch of common operation in which the internal inductance increases from 0.4 to 1.2 in the first 0.5s for L-mode discharges. On NSTX-U, this is the most common operating region, and after $t = 0.5$, the internal inductance reaches a steady value when sawtooth activity begins. The high- l_i L-mode discharges do not last as on NSTX due to the smaller available ohmic flux. A second common branch exists at low internal inductance corresponding to H-mode operation, which contains the longest duration shots on NSTX. Future H-mode operations on NSTX-U will achieve discharge lengths exceeding 2 s at $l_i < 1.2$ with 5 s discharges projected to be achieved with $l_i \sim 0.6$.

Figure R17-5-6 shows histograms of elongation versus time for NSTX-U and NSTX. For NSTX, high elongation ($\kappa \approx 2.1$) is established at $t = 0.15$ s followed by two common paths: the L-mode where elongation decreases and the shot length is typically less than 0.5s, and the H-mode scenarios in which elongation is maintained or increased and the shot length is longer. The H-mode scenario was more common on NSTX. The elongation achieved during ramp-up is lower in NSTX-U ($\kappa \approx 1.9$) and occurs later ($t = 0.25$ s). A steady elongation of 1.7 is commonly reached in the L-mode scenario and maintained as long as 2.0s. The H-mode scenario, which achieves $\kappa > 2$, was run less frequently and the longest H-mode discharges ran until 1.1s. Both NSTX-U and NSTX show a typical behavior of starting at low elongation and moving to higher elongation, however, NSTX begins at higher elongation, increases more rapidly, and commonly establishes elongation above 2.0 before $t=0.1$ s, whereas NSTX-U only infrequently exceeded $\kappa=2.0$ and, if so, this typically occurred around $t=0.15$ s and elongation was decreased afterwards.

The data presented in section 17-5-2 provide a quantitative comparison between commissioning operations on NSTX-U and the entirety of operations on NSTX. The maximum achieved elongation at matched I_i is similar between the two devices (figure R17-5-2), however most of the low- I_i operating space was not yet explored on NSTX-U when operations concluded. Low- I_i ($I_i < 1$) operation on NSTX-U should permit operations at larger κ (figure R17-5-3) and longer pulse lengths (figure R17-5-5), as demonstrated on NSTX.

Section R17-5-3: Vertical stability limits to elongation

The plasma elongation is ultimately limited by the loss of vertical stability, known as a vertical displacement event (VDE). It is important to determine whether the operational boundaries in κ presented in Section R17-5-2 are due to the VDE limit or if stable operation is permitted at larger κ . An automated VDE detection algorithm was developed and used to generate a database of times that VDEs were triggered on both NSTX and NSTX-U. The algorithm identifies the times that the quantity $z_p \frac{dz_p}{dt}$ exceeds a set of thresholds of increasing magnitude Z_0 through Z_5 , with Z_5 set to the level used in the real-time plasma control system to trigger shot termination. Intervals of stable control are identified by analyzing the rolling standard deviation of plasma motion, and the initial time of a VDE is taken to be the earliest time in a shot that $z_p \frac{dz_p}{dt}$ exceeds Z_0 without a subsequent recovery of stable control. The earliest time after this identified time that each of the other thresholds are crossed after this point are recorded. The database was populated with the phase of the shot at each of those times (ramp-up, flattop, shutdown), along with equilibrium parameters like elongation, internal inductance, etc., enabling filtering of the database based on common descriptors.

In order to examine the elongation limits imposed by vertical stability, VDEs that were due to large perturbations to the plasma by MHD activity (for example, locked modes) were removed from the database using an algorithm for detecting spikes in the plasma current that occurred in a time window of 100ms prior to reaching the vertical motion threshold Z_3 . Shots were also filtered out if the VDE duration, defined as $t(Z_4) - t(Z_1)$, was below a threshold of 5 ms since a fast VDE is typical of an MHD-induced disruption or an H-L transition.

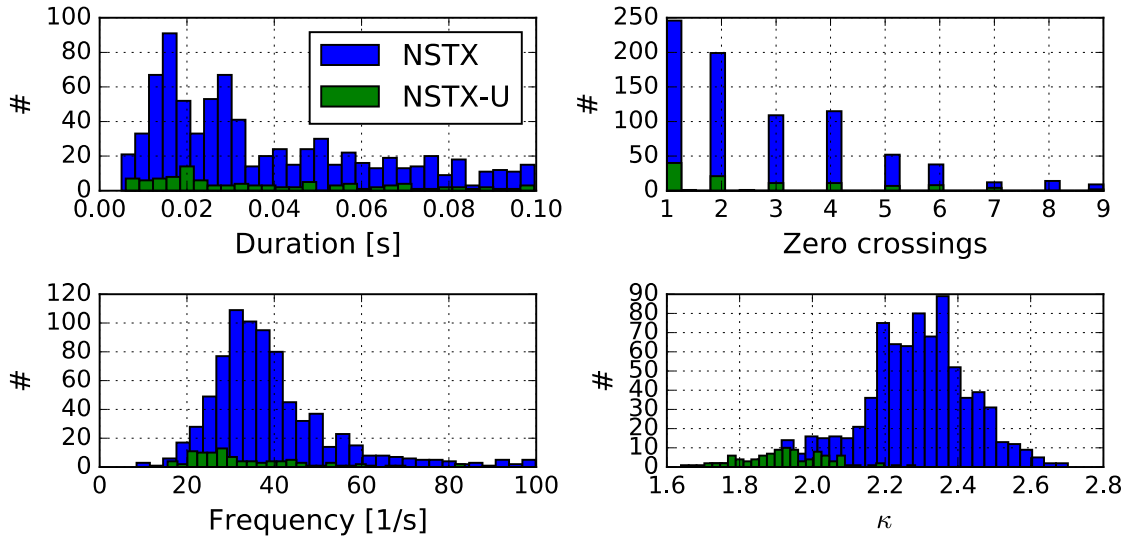


Figure R17-5-7: Histograms of VDE duration, number of zero crossings, oscillation frequency, and plasma elongation with $l_i < 1.0$, typical of H-mode operations and ramp-up.

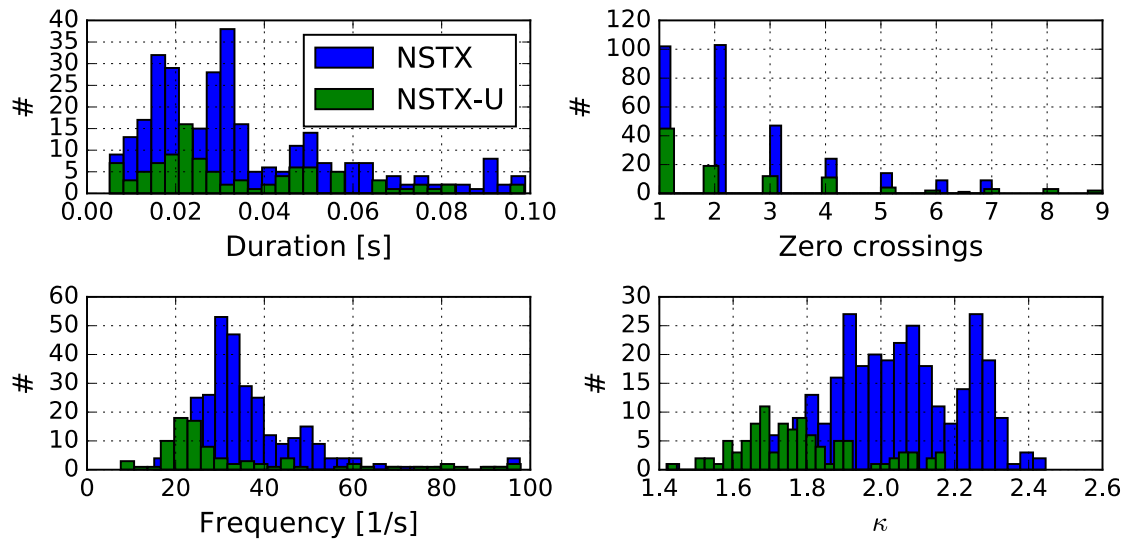


Figure R17-5-8: Histograms of VDE duration, number of zero crossings, oscillation frequency, elongation, internal inductance, and β_p for VDEs occurring at $l_i > 1.0$, typical of L-mode flattop or following an H-L transition.

Figure R17-5-7 shows histograms for identified VDEs that occurred at $l_i < 1.0$. VDEs in this range typically occurred in ramp-up or during H-mode operation, which enables low l_i to be maintained throughout the current flattop. Plotted quantities include the duration, the number of zero crossings in the vertical position, the oscillation frequency, and the elongation at the start of the VDE oscillations. The duration histogram shows multiple peaks, likely a result of VDEs completing different numbers of oscillations at roughly the same frequency before triggering a current quench. While the peaks in duration are at different locations, similar decreasing trends are seen for NSTX and NSTX-U in both duration and number of zero crossings. The frequency of oscillations is in general lower in NSTX-U compared to NSTX, possibly indicating either a change in the natural frequency of the system due to changes in the vessel and coils during the

upgrade, or a reduction in the effective proportional gain of the control system during shape control commissioning.

Figure R17-5-8 shows the same histograms for VDEs with $l_i > 1.0$ that is typical of L-mode operation. The duration, number of zero crossings, and oscillation frequency are similar to the VDEs at low internal inductance. The most significant result from figures R17-5-7 and R17-5-8 is that the frequency of the VDE oscillation is slower on NSTX-U than NSTX in both confinement states (L- and H-mode). Future calculations and operations will explore if further tuning of the active vertical feedback system on NSTX-U can stabilize conditions with slower oscillations and increase the peak in the VDE frequency to be closer to the NSTX result.

The VDE database can be used to compute the probability of VDEs occurring at a given operating point by dividing the counts of VDEs in each operating region by the number of EFIT01 slices in that bin (as calculated in Section R17-5-2). Results for all time ranges in the discharge are shown in Figure R17-5-9. Black regions indicate regions with less than 30 EFIT01

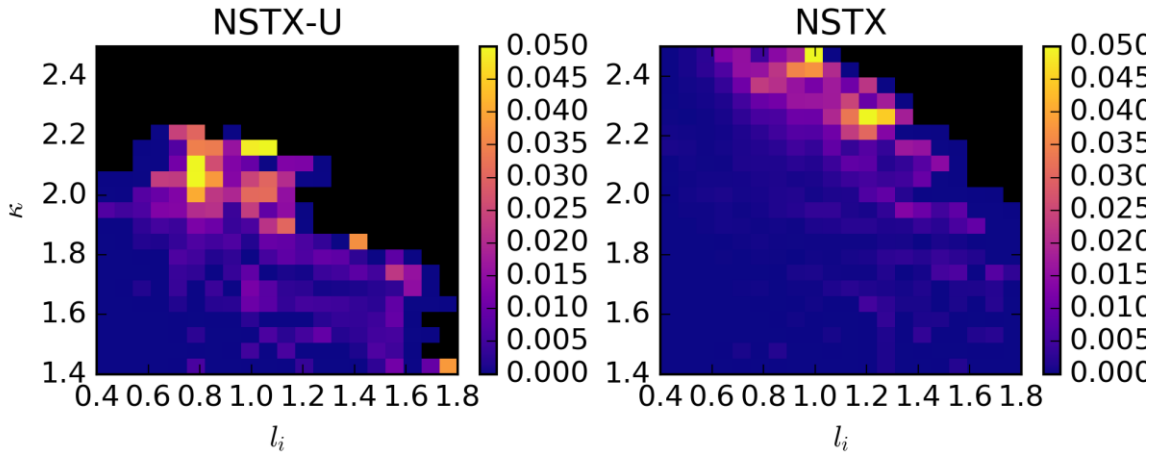


Figure R17-5-9: Probability of VDE as a function of elongation and internal inductance for all EFIT01 slices [#VDEs / #slices].

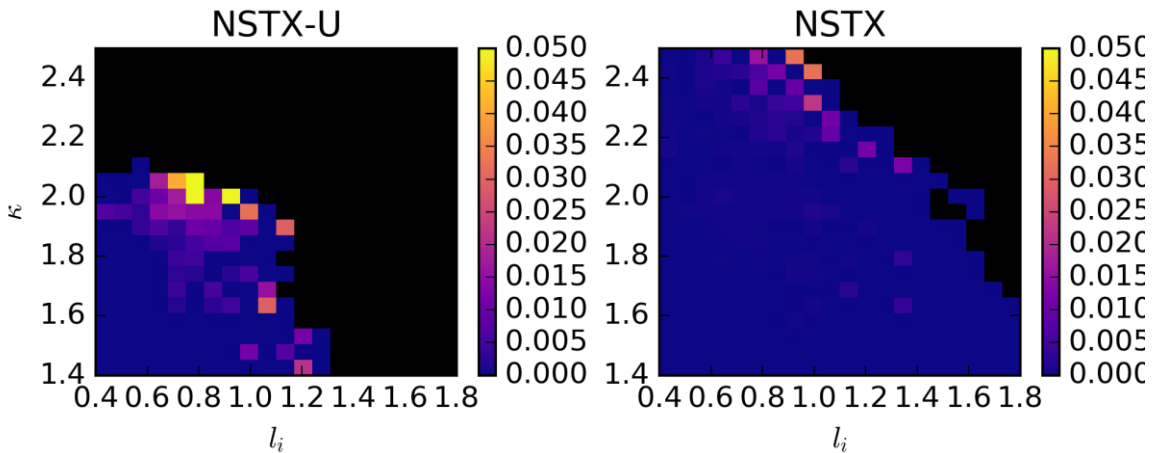


Figure R17-5-10: Probability of VDE as a function of elongation and internal inductance for $t < 0.3s$ [#VDEs / # slices].

slices. Both plots show increased probability of VDE along an approximately negatively sloping line such that there is higher probability of VDEs at higher elongation. Focusing on ramp-up ($t < 0.3$ s) in Figure R17-5-10 shows similar results though trends are not as clear since there are fewer data points.

These results indicate that the VDE stability limit to the elongation is more restrictive on NSTX-U than NSTX. This is consistent with the expected impact of operating at larger aspect ratio. However, other conditions of the plasma during NSTX-U startup can adversely impact the vertical stability, such as the presence of uncorrected error fields, large impurity content and an un-optimized vertical position control. These contributing factors were improving over the course of the ten-weeks of NSTX-U operation as illustrated by figure R17-5-11. The data points show the elongation versus internal inductance for NSTX-U discharges with VDEs that started in flattop and did not have I_p spikes during the initial part of the VDE. The left panel shows data at the initial VDE time, $t(Z_0)$, while the right panel shows the data at the time the vertical motion crossed the threshold Z_1 , $t(Z_1)$. The points are sized proportional to the product of β_p and the inverse aspect ratio ϵ , and are colored by shot number. The plot is an indication of the evolution of elongation limits during the campaign, reflecting advances in control, wall-conditions, and available beam power.

Early in the campaign (darker blue dots), VDEs occurred at low elongation, typically below 1.75, even for shots that had lower values of internal inductance and $\epsilon\beta_p$. Improved filtering of vertical control sensors and $n=1$ error field correction (light blue) resulted in VDEs occurring at higher values of elongation for a given internal inductance. In the 203700-204150 range of shots (green-yellow dots), higher values of $\epsilon\beta_p$ and lower values of internal inductance were often achieved as the availability of neutral beam heating exceeded 3 MW. These shots included several long pulse H-mode discharges, and typically had VDEs at much higher elongation. A period of L-mode development (orange points) illustrates the expansion of the VDE limit to κ at $l_i \sim 1.1$ compared to early campaign (dark blue) due to improvements in control and wall conditions. In the final two weeks of the campaign the elongation limit became more restrictive (red points) as the PF1A internal short began to introduce an error in the real-time interpretation of the magnetic signals.

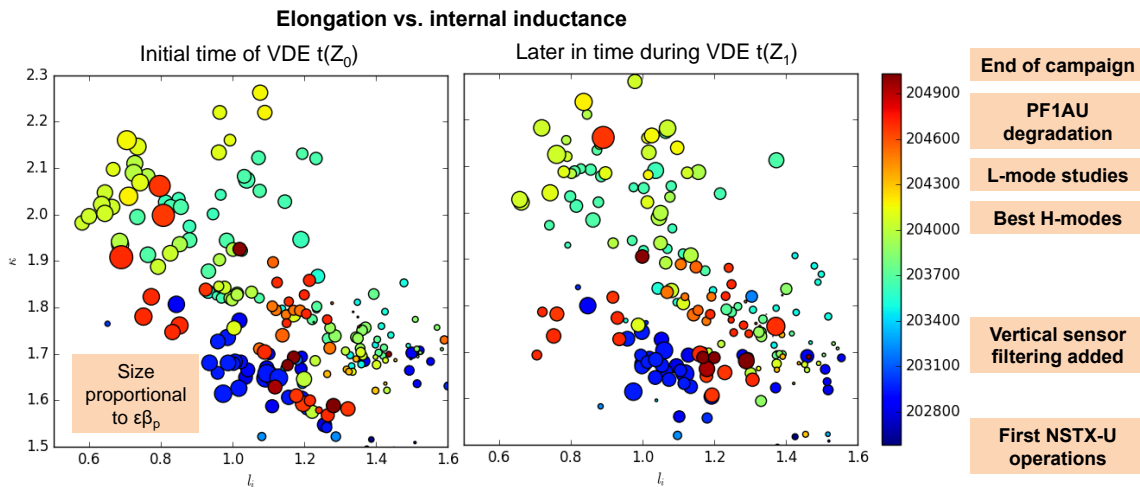


Figure R17-5-11: Elongation vs. internal inductance at the time of VDEs for NSTX-U illustrating the increase in the VDE limit as the campaign progressed.

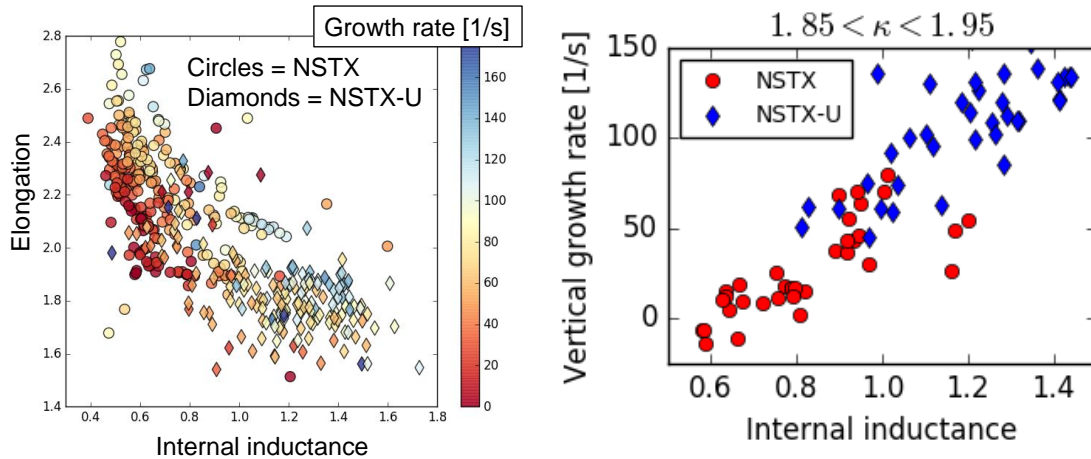


Figure R17-5-12: Growth rate at start of VDE for NSTX and NSTX-U.

Between $t(Z_0)$ and $t(Z_1)$ (left and right panels), shots typically show a shift toward higher internal inductance. Some shots in the left panel already appear at high internal inductance well above the elongation limit qualitatively defined by the other shots at the same internal inductance. The increase in internal inductance over time is likely a result of H-L back transitions leading to increases in internal inductance.

One metric for evaluating the optimization of the active feedback of the vertical position within the plasma control system (PCS) is to examine the open-loop growth rates of plasmas that begin a VDE. The ISOLVER free-boundary equilibrium code was upgraded in FY17 to enable calculation of open loop vertical instability growth rates. Larger growth rates imply a faster vertical motion if the active vertical position feedback within the plasma controls system was suddenly turned off. It is expected that the growth rate increases as the elongation approaches the VDE limit, and that the maximum achievable growth rate is related to the effectiveness of the active vertical control system.

The VDE database, including shots with I_p spikes and short duration VDEs, was down-selected to include only shots with VDEs occurring during the flattop phase, only NSTX shots after 141159 (~the last 1000 shots) and only NSTX-U shots after 203826. The left panel of figure R17-5-12 shows a scatter plot of elongation versus internal inductance at the start time of VDEs with points colored by the open loop growth rate of the vertical instability. NSTX-U shots are depicted with diamonds while NSTX shots are shown as circles. The right panel of figure R17-5-12 shows the vertical growth rate versus internal inductance for those points within the elongation range $1.85 < \kappa < 1.95$. The strong effect of internal inductance on the growth rate, which can be seen in the right panel, appears to be similar between NSTX and NSTX-U, though NSTX-U tends to have somewhat higher growth rates in the overlapping region and a slightly larger slope. While the NSTX shots occur at low internal inductance and have growth rates near or below $0s^{-1}$, the NSTX-U shots in the same elongation range have growth rates up to $150s^{-1}$, as high or higher than the largest growth rates calculated for high elongation NSTX cases. It is promising that NSTX-U was able to operate at growth rates at or above the largest NSTX growth rates, and the result implies that improvements to the active vertical control system allowed for operations at larger

open-loop growth rates, motivating continued work in this area. It is also promising that many of the NSTX-U points that overlap with NSTX points show similarly reduced growth rate at low internal inductance. There are however, a few large growth rate points in the NSTX-U dataset at internal inductance below 0.8, indicating the growth rate may be strongly dependent on other equilibrium parameters.

The conclusion derived from Sections R17-5-2 and R17-5-3 is that NSTX-U achieved a similar elongation to typical operations on NSTX at $I_i > 0.8$. However, at the achieved elongation, NSTX-U ran closer to the VDE stability limit than NSTX. This motivates the development of scenarios that achieve lower I_i as well as further optimization to the active vertical stability system to continue to expand the achievable elongation on NSTX-U. The results also provide guidance to optimizing the choice of equilibrium parameters to avoid operating at too high of an open loop growth rate when planning NSTX-U scenarios and optimizing ramp-up and ramp-down trajectories.

Section R17-5-4: Classification of vertical motion at the time of diverting on NSTX-U

One of the challenges encountered during development of H-mode scenarios on NSTX-U was the occurrence of vertical oscillations shortly after the time of diverting. These occasionally led to shot termination, motivating the restriction of maintaining $\kappa < 2$ until the oscillations were stabilized by the vertical position controller. The large plasma motion often coincided with the target H-mode transition time, and was thought to contribute to unreliable H-mode access.

To study these oscillations, identify the contributing factors, and determine ways to avoid them in the next campaign, a database of the behavior of the vertical velocity shortly before and after the time of diverting was generated. To help sort through the shots, a k -means clustering algorithm was applied to the database to identify shots with similar behavior. A few typical behaviors were identified from the clustering analysis, and three classes of practical interest to this study were chosen: which will be referred to as "bobbles", "dips", and "others". The most troublesome behavior was the so-called "bobble", which grew in magnitude for 2-3 cycles before either decaying away or triggering plasma termination (through either a disruption or automated controlled ramp-down). The "dip" was typified by a smaller motion with fewer oscillations, with dominantly downward motion of the plasma after the time of diverting. Typical examples of the bobble and dip behaviors, taken from shots 204152 and 204092, respectively, are shown in Figure R17-5-13. The "other" class was used as a container for shots with little to no oscillations or oscillations that did not

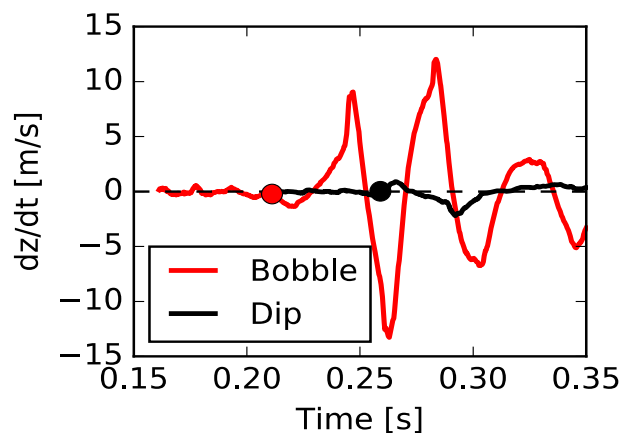


Figure R17-5-13: Typical behaviors of oscillations around the time of diverting (indicated by a dot).

match the two most common oscillating behaviors. A subset of NSTX-U shots was randomly selected, manually classified, and split into training and testing datasets. These datasets were then used to train and cross-validate a support vector classifier. The classifier was then used to classify the entire database of NSTX-U shots.

Figure R17-5-14 shows histograms of elongation, time of diverting, maximum vertical velocity, internal inductance, the ratio of lower divertor OII to D_γ , and the open loop vertical growth rate. Shots exhibiting the bobble typically diverted at higher elongation (averaging around $\kappa = 1.85$ with a cluster centered at $\kappa = 1.9$), though still far below the typical early elongation on NSTX. On average, the shots with bobbles diverted just after $t = 0.20$ s, with many clustered at 0.22s. The "dips" typically diverted later, averaging around $t = 0.23$ s with a mode around $t = 0.24$ s.

The "other" category shows two modes, with some shots diverting much earlier, around $t = 0.15$ s, and others diverting between the modes of the bobbles and dips. On average, the bobbles have

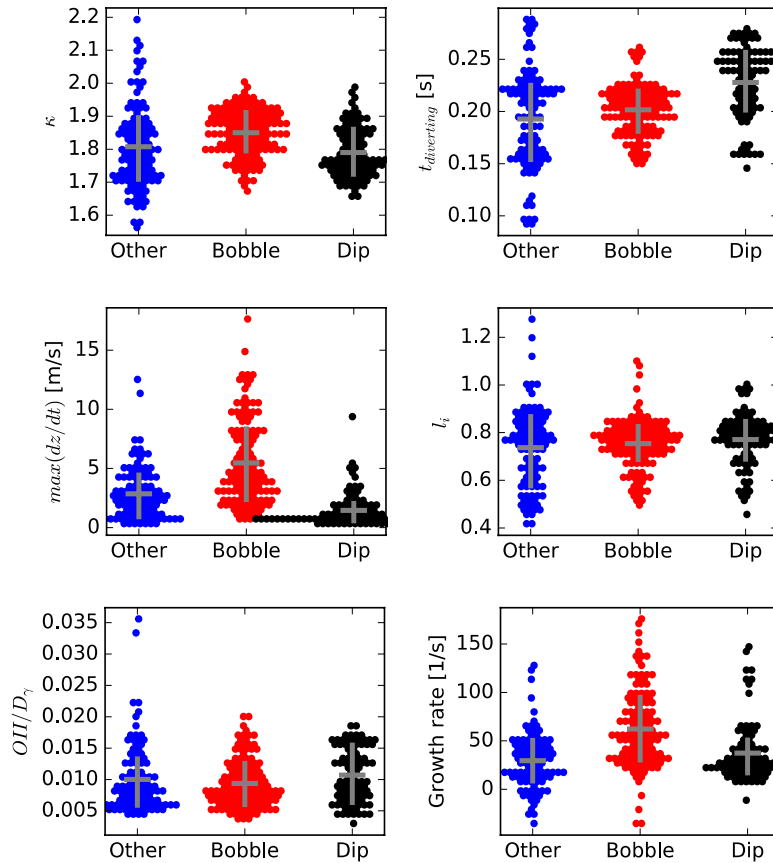


Figure R17-5-14: Histograms of elongation, time of diverting, maximum vertical velocity, internal inductance, ratio of lower divertor OII to D_γ , and open loop vertical growth rate for each of the classes of diverting behavior.

a much higher peak velocity, while the dips have the most consistently low peak velocity. This indicates that although there was vertical motion in these cases, it was not rapid, and was reproducible. The internal inductance exhibits trends similar to the time of diverting since internal inductance is essentially a linear function of time during the ramp-up. The open-loop vertical growth rate is on average highest among bobbles, however, the average and most common values are fairly low compared to the highest values calculated in Figure R17-5-12. There are many instances that occur at higher growth rates that would be expected to be near or beyond the maximum controllable growth rate. There is no obvious difference in the ratio of OII to D_γ , indicating that wall-conditions may not contribute strongly to the behavior of oscillations at diverting.

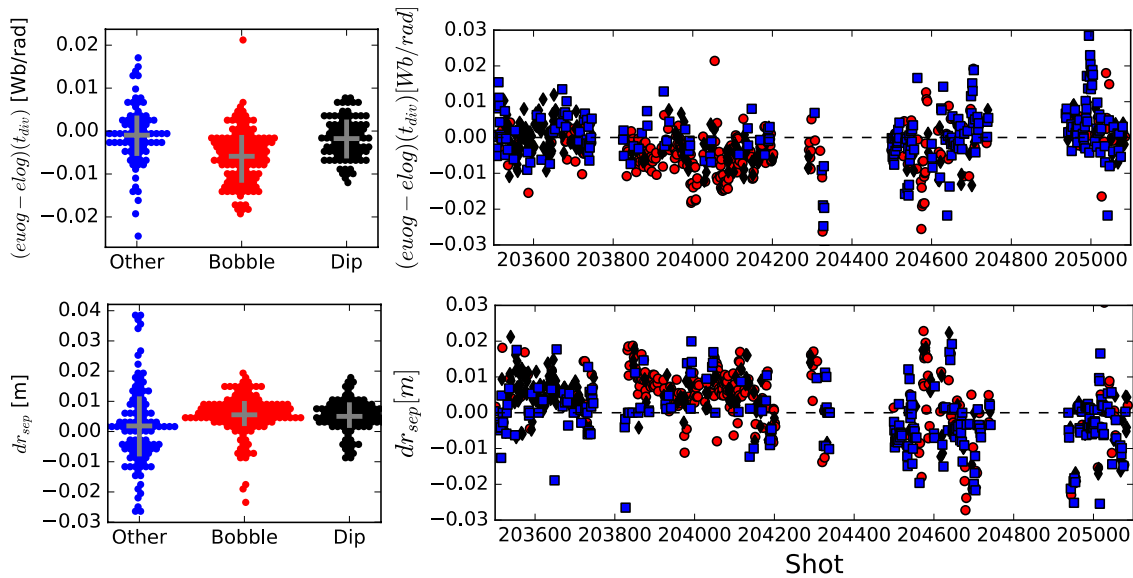


Figure R17-5-15: Histograms and run-time history of δr_{sep} and the difference between upper and lower outer gap control segment flux errors at the time of diverting for each class of behavior.

Figure R17-5-15 shows the histograms of δr_{sep} at the time of diverting for each class, as well as a scatter plot of δr_{sep} as a function of shot number, showing how the value and the distribution of each class of behavior evolved throughout the campaign. The same plots are shown for the difference between flux errors for the upper and lower outer gap control segments used in ISOFLUX (denoted $euog$ and $elog$ in the figure), which is the effective proxy for vertical position that is controlled when under ISOFLUX shape control. The histograms show the shots classified as “other” have a distribution around $\delta r_{sep}=0$, while the bobbles and dips have a positive value, corresponding to diverting with an upper biased shape. Shot numbers below 203800 typically exhibited dips with $\delta r_{sep} > 0$, but rarely exhibited bobbles. Shots between 203800 and 20420 that were classified as bobbles or dips typically occurred at $\delta r_{sep} > 0$, with bobbles having much higher frequency in this range. Later shots diverted with $\delta r_{sep} < 0$ more often than earlier shots, and had a higher frequency of “other” behaviors in this range. The histogram of the ISOFLUX upper/lower outer gap flux error differences at the time of diverting shows that for dips and shots in the “others” category, the difference is on average zero, while it is almost always negative in the case of bobbles. During shots prior to 203800,

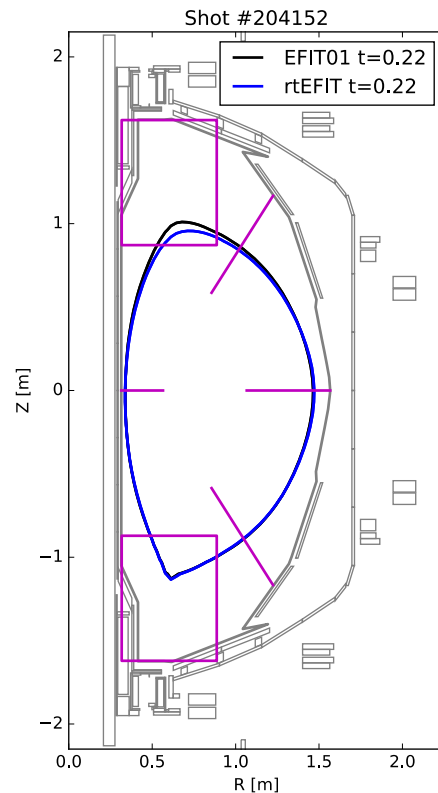


Figure R17-5-16: Comparison of rEFIT and EFIT01 boundaries just after the time of diverting for NSTX-U shot number 204152.

this difference was typically near zero and bobbles were infrequent. Between 203800 and 204600, this quantity was typically negative and bobbles were frequent, and after 204600 the difference returned to near zero and bobbles became less frequent, though they did not entirely disappear. The evolution of this difference throughout the campaign could be a result of mismatch between the achieved boundary and the target boundary across the transitions between the different shape control algorithms used during ramp-up. It was empirically observed during operations that improving matching across transitions made control more reliable.

It is also possible that the flux error differences were a result of real-time reconstruction convergence issues. Figure R17-5-16 compares the offline-reconstructed boundary (which iterates the Grad-Shafranov solution many times) to the boundary reconstructed in real-time (which only uses one iteration) for shot 204152, which was classified as a bobble. The comparison shows a difference in the upper part of the boundary just after the time of diverting that results in an effective downward shift of the measured plasma position. This could indicate poor convergence of the real-time boundary early in the shot due to rapid changes in the equilibrium, vessel currents, or corruption of measurements with 3D modes. Whether caused by error in the reconstructed boundary or too large discrepancies in target shape at the time of algorithm transition, the shape control algorithm would respond to try to correct the non-zero vertical position error, causing vertical motion around the time of diverting. This motion likely set off the observed oscillations.

Through the classification process, a range of similar shots was identified that contained a variety of behaviors: some exhibited a very small "dip", others exhibited very small oscillations at the time of diverting, and a few shots had typical bobbles. To assess the stability of these discharges during the time just after diverting, the vertical growth rate was calculated between 0.2s and 0.5s for each. The growth rates over time are shown in Figure R17-5-17. In the plot, diamonds indicate the time of diverting for shots that exhibited oscillations, while circles indicate the time of diverting for shots with little to no oscillation. Shots that oscillated started at higher growth rate, consistent with the histogram of growth rate at diverting time shown in Figure R17-5-14. Shortly after the time of diverting, the growth rate rapidly increases in all shots. For shots that exhibit significant oscillations, the growth rate approaches or exceeds 100s^{-1} and, at least for shots 204501 and 204507, the vertical oscillations appear to cause oscillations in the growth rate. While the elongation, shown in the second panel, also increases after diverting and later decreases, the

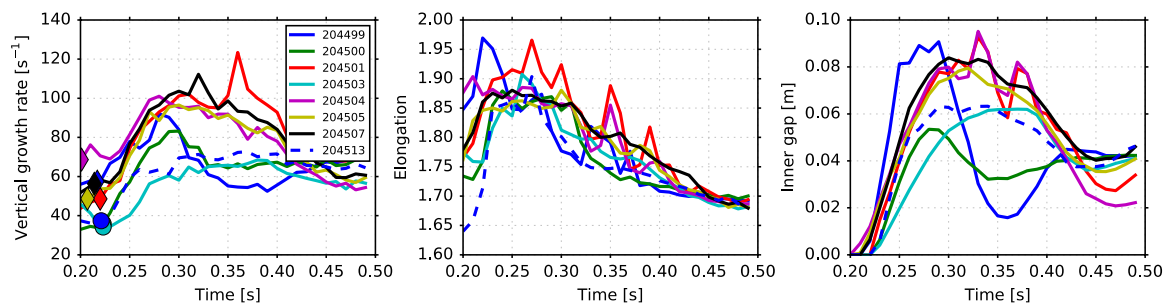


Figure R17-5-17: Vertical growth rate, elongation, and inner gap vs. time for a subset of shots exhibiting varied behavior at diverting time. Diamonds indicate the diverting time for shots with oscillations while circles indicate the diverting time for shots with small oscillations.

time evolution does not appear strongly correlated with the growth rate. The inner gap evolution, shown in the third panel, shows that the inner gap was typically formed rapidly and often exceeded the final value by several centimeters, especially in the case of shots with oscillations. The time evolution also appears to correlate more strongly with changes in vertical growth rate.

This is confirmed in Figure R17-5-18, which shows the vertical growth rate as a function of inner gap size for the shots considered. The shots are colored by elongation, showing that while there is not a strong elongation dependence, there is a nearly linear dependence of the vertical growth rate on the inner gap size, with a slope of approximately $5\text{s}^{-1}/\text{cm}$. This indicates that, at least for the equilibrium in these shots, the vertical stability is sensitive to the inner gap evolution. To avoid large increases in growth rate and decrease the likelihood of oscillations, a small inner gap should be targeted and significant overshoot should be avoided through more precise control. During these shots, the inner gap was only indirectly controlled through pre-programmed changes in other shaping parameters (mainly X-point locations), since there is no set of inboard shaping coils to dedicate to controlling this gap. With no feedback control on the gap evolution, shot-to-shot variation in wall-conditions and beam power availability caused variation in the time of diverting and sometimes caused the shot to fail to divert at all. Rapid pre-programmed shape changes were required to make diverting more reliable, however, this contributed to the rapid motion and overshoot evident in Figure R17-5-17. Near the end of the campaign, the shape control algorithm was upgraded to enable the targets for the shaping parameters that influence the inner gap to be adjusted in real-time based on the achieved inner gap. This algorithm was able to make diverting more reliable and will be used in the next campaign to precisely control the inner gap evolution.

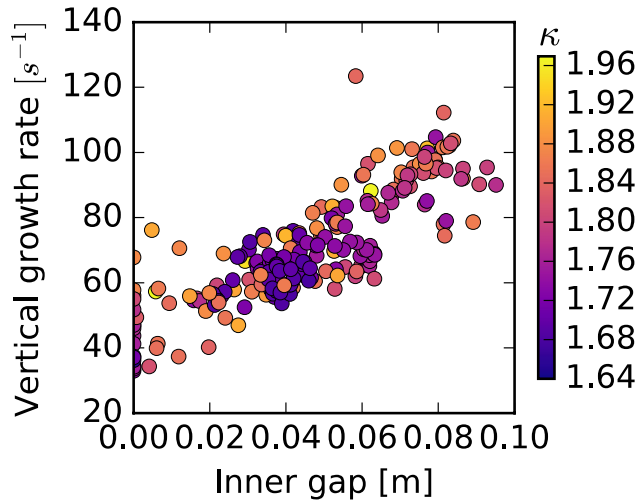


Figure R17-5-18: Vertical growth rate vs. inner gap size for $t < 0.5\text{s}$ in the shots considered. Points are colored by elongation.

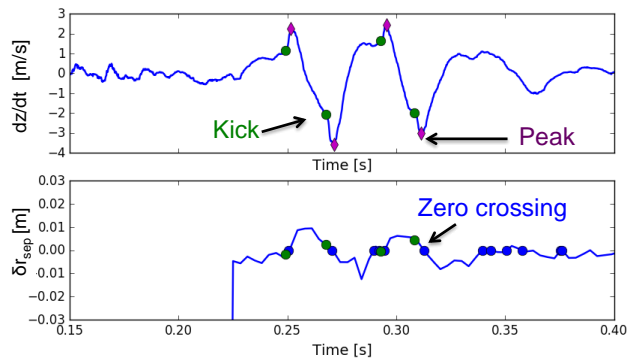


Figure R17-5-19: Typical behavior of 'kicks' in vertical velocity occurring near zero crossings in δr_{sep} .

One of the characteristics of the bobble is a sudden “kick” or increase in the speed of vertical motion (at least as estimated by the observer) that occurs near the time of crossing $\delta r_{sep} = 0$ that contributes to driving the vertical oscillations. In shots that survived through the oscillations, the size of the kicks and the oscillations decreased over time. In order to study the factors

contributing to the kick size, an algorithm for identifying spikes in vertical velocity near times of crossing the time of kicks. The algorithm was used to detect the location of kicks in the time interval $0.2s < t < 0.5s$ in shots that were identified as having bobbles with high probability using the bobble classification algorithm.

Figure R17-5-19 shows the vertical velocity during a typical bobble with identified kick start times and peak times indicated, as well as the evolution of δr_{sep} , showing that the kicks typically precede zero crossings. Figure R17-5-20 shows histograms of parameters associated with the kick occurrences. Kicks occurred most frequently when δr_{sep} and the vertical position are near zero, with a bias toward slightly positive values. The size of kicks has a broad distribution, but does not typically exceed 4m/s. Kicks occur most frequently between 0.2s and 0.3s

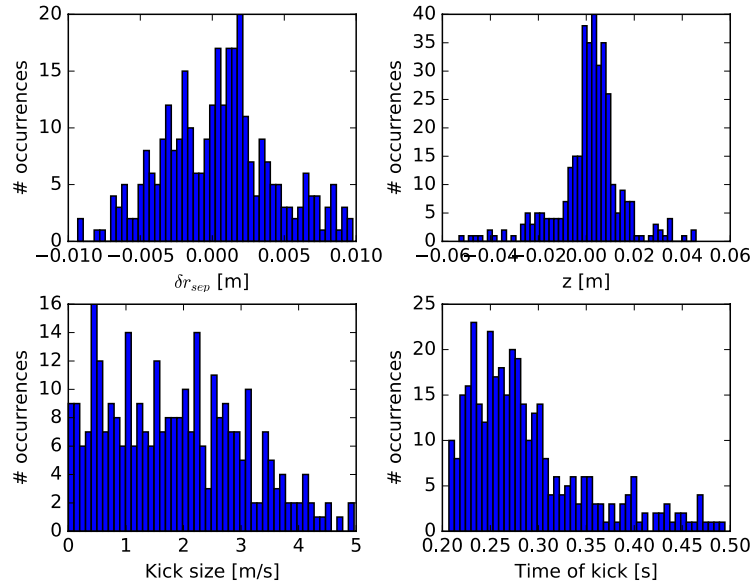


Figure R17-5-20: Histogram of δr_{sep} , vertical position, vertical speed, and time of identified kicks.

Vertical growth rates were also calculated for the start times of each identified kick. The relationship between kick size, vertical speed, growth rate, and internal inductance is depicted in Figure R17-5-21. The kick size appears to increase with the vertical speed at the time of the kick, with a stronger dependence at lower l_i as shown in the upper left panel. Plotting as a function of vertical growth rate (the upper right panel) shows that the largest kicks occur for growth rates above approximately $60 s^{-1}$. Plotting vertical growth rate at the time of kicks as a function of the identified kick time (lower left panel) shows that early on near the typical time of diverting, kicks only occur at high growth rates. There is a larger variation in growth rate of kicks between 0.22s and 0.28s, and growth rates are typically $60s^{-1}$ later in shots.

Kick sizes are therefore larger early on and much smaller after $t = 0.28s$. Plotting the growth rate as a function of l_i and coloring points by kick size (lower right panel) shows that for moderate growth rates (between $40s^{-1}$ and $80 s^{-1}$) large kicks occur at low l_i and kick size is reduced as l_i increases. This indicates that the sensitivity to kicks is equilibrium dependent. This likely contributed to the more frequent occurrence of “dips” instead of bobbles when diverting was delayed – the kick size was small since any δr_{sep} zero crossings only occurred later in time. The results motivate modeling efforts to identify equilibria that are less susceptible to large kicks. If a target equilibrium is susceptible to kicks, zero crossings will be avoided by biasing the plasma up or down, and large motion or high growth rates will be avoided. If kicks cannot be avoided, it may be possible to reduce the vertical control gains temporarily to avoid amplification of the motion. Modeling efforts in FY18 will be used to assess this approach.

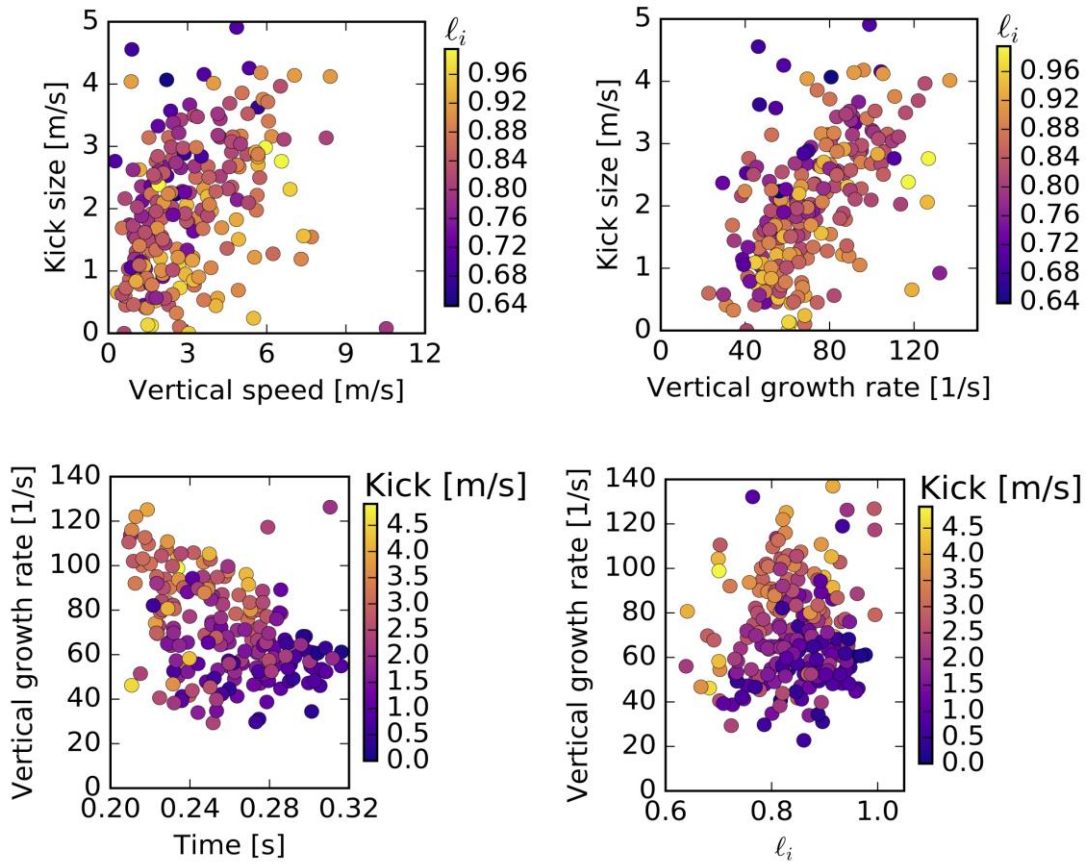


Figure R17-5-21: Dependence of kick size on vertical speed, growth rate, and internal inductance.

Section 17-5-5: Dependence of the L-H transition on plasma parameters

A database of diverted L- and H-mode discharges on NSTX-U was developed to examine the conditions that facilitated a robust and reliable L-H transition in the ramp-up phase of the discharge. H-mode was observed with heating powers as low as $P_{NBI} = 0.9$ MW during the I_p flattop, however larger heating power is typically required to trigger an H-mode transition at lower I_p . The database only includes times in the discharges with $P_{NBI} \geq 3$ MW that are diverted. The database includes 68 L-H transition times and 100 times when the discharge was in L-mode or dithered (brief entry and exit into H-mode) during the I_p ramp-up phase. Only L-mode times that occur 50 ms after a change in heating power are included in order to accommodate the beam slowing-down time.

The power required to trigger an L-H transition is often expressed in terms of the loss power: $P_{loss} = \eta P_{NBI} - dW/dt + P_{OH}$ where η is the NBI heating efficiency, P_{NBI} is the injected NBI power, dW/dt is the change in the stored energy and P_{OH} is the ohmic heating power. One available tool for calculating the heating efficiency is using interpretative TRANSP simulations of the beam absorption. For the purposes of this study, the between-shot TRANSP calculations (BEAST) were used to derive a reduced model for η to inform future predictive modeling efforts.

The reduced model was developed using a database of BEAST results for L-mode times. The simplified model assumes the beam slowing down time as well as the variation of the efficiency with I_p and line integrated density (nel) is the same for all six beams, while each beam has a unique efficiency coefficient:

$$\eta_{1A} = C_{1A} (I_p \text{ (MA)})^\alpha (\text{nel} (10^{19} \text{m}^{-2}))^\beta f(\tau) * P_{inj\ 1A}$$

$$\eta_{1B} = C_{1B} (I_p \text{ (MA)})^\alpha (\text{nel} (10^{19} \text{m}^{-2}))^\beta f(\tau) * P_{inj\ 1B}$$

....

In this model, $f(\tau)$ is an exponential function with time constant τ that is convolved with the neutral beam power versus time. The values for the best fit to the nine free parameters of the reduced model are shown in Table 17-5-1. It is important to consider that this reduced model does not contain information on the beam voltage and plasma profiles, which will impact the beam heating efficiency. Furthermore, certain beams (such as 1A) have very few data points to fit because they were not used often in operations. Nevertheless, the best-fit model reproduces reasonable parameters, with the heating efficiency is largest for the on-axis beams (2C, 2B and 1B) and improves with larger I_p and density. At typical values of I_p (0.5 MA) and n_{el} ($1.4 \times 10^{19} \text{m}^{-2}$), the beam heating efficiency (η) is nearly equal to the coefficient (C) for each individual beam.

Figure 17-5-22 shows the P_{loss} normalized to scaling factors for the plasma surface area (S) and toroidal field (B_T) derived from the ITPA P_{LH} database for all of the L- and H-mode points in the database. The data uses the reduced model definition of the beam heating efficiency and a dW/dt and P_{OH} derived from magnetics-only EFIT. The normalized P_{loss} is plotted versus line-averaged density. The solid lines indicate the scaling with n_{ebar} given by the ITPA database. The lowest line is the ITPA P_{loss} scaling, while the dashed and dotted lines are integer multipliers of this loss power scaling. The important point of this plot is that L-mode or dithering discharges can exist despite P_{loss} being many times larger than some H-mode discharges.

It is important to consider that the error bars on the calculation on P_{loss} are large (order 1 MW), mostly due to the uncertainty in dW/dt and, to a lesser extent, the neutral beam efficiency. Thus, the comparison with the ITPA scaling should be taken with a grain of salt. Careful quantification of the L-H power threshold will be conducted in future experiments on NSTX-U to compare to NSTX and the ITPA database.

Free parameter	Value
τ (slowing down time)	25 ms
α (I_p power)	0.19
β (nel power)	0.37
C_{1A}	0.35
C_{1B}	0.55
C_{1C}	0.49
C_{2A}	0.26
C_{2B}	0.51
C_{2C}	0.61

Table 17-5-1 Best-fit values for free parameters in reduced model for beam efficiency.

Using the database of L-H transitions and the corresponding L-mode discharges, a set of criteria was identified that excluded all L-mode points from the database while keeping as many H-mode discharges as possible:

- 1) $n_e > 1.25 \times 10^{19} \text{ m}^{-3}$
- 2) $V_{\text{surf}} < 1.15$
- 3) $|\text{dr}_{\text{sep}} - 0.2 \text{ cm}| < 0.6 \text{ cm}$
- 4) $O \text{ II} / D_\gamma < 1$

The first criteria sets a minimum density, the second criteria is that the surface voltage should be below 1.15 V, the third criteria is that the shape should be close to double null and the fourth criteria is that the oxygen content of the plasma should be below a threshold. The last criteria is a metric specific to NSTX-U, determined by taking the ratio of two filterscopes over a brief period near the beginning of a discharge. This ratio is typically around 0.2 following a boronization and rises throughout a campaign as the walls “decondition.”

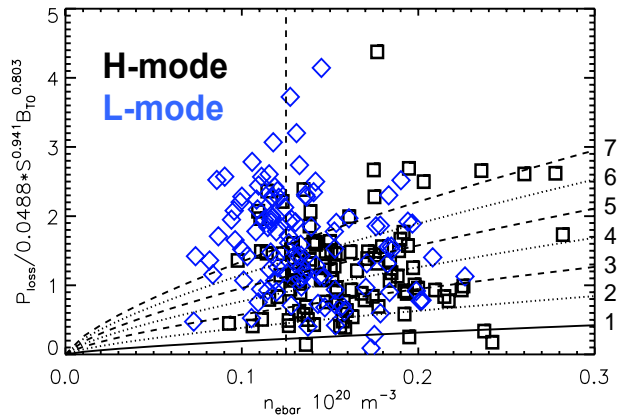


Figure 17-5-22 Loss power for L-H and L-mode points. The solid line shows the P_{loss} power threshold from the ITPA database. The dotted and dashed lines are integer multipliers of the ITPA threshold power

All 100 diverted L-mode time points chosen for the database are excluded by the criteria with two-thirds (67 entries) excluded by two or more of the criteria. About half (39 of the original 68) of the L-H transition entries satisfy all four criteria and most (63 out of 68) of the entries meet at least three of the four criteria. These results suggest it is unlikely to trigger an L-H transition with only two criteria met and very likely with all four provided $P_{\text{NBI}} \geq 3 \text{ MW}$.

The results from the database analysis provide guidance on the target conditions for triggering an L-H transition at the desired time. The requirement for good wall conditions and a shape near double null are decoupled from the other criteria. However, the primary actuator for the plasma density, neutral fueling, increases the surface voltage. Thus, the timing and location of the neutral fueling must be carefully tailored to meet the target density while achieving a low surface voltage at the desired timing. The introduction of a pause (lasting 20 – 50 ms) in the I_p ramp at the desired L-H timing was used in NSTX and NSTX-U to temporarily reduce V_{surf} to about 1 V. This result justifies including an I_p pause in the future development of H-mode scenarios.

Section R17-5-6: MHD stability limits during ramp up

The ramp-up phase in H-mode discharges that achieved the highest performance on NSTX-U were difficult to consistently reproduce. Often attempts to repeat the H-mode scenarios with $I_i \leq 0.55$ had a fast disruption within 100 ms after the L-H transition. Figure 17-5-23 presents one of the best H-mode discharges on NSTX-U (black) and three failed attempts to repeat the discharge (red, blue and green). The vertical lines show the times when the three discharges have an abrupt decrease in β_N and deviate from the target discharge.

One common feature of the discharges that had a fast disruption is that $I_i \leq 0.55$ at the time of maximum β_N (panel c). Another common feature is that dr_{sep} is less than zero (lower SN in the favorable ion grad-B drift direction) and at least 1 cm away from balanced DN. A feature shared by most of the discharges that disrupted was a period of low surface voltage (panel h). It was common for vertical oscillations during ramp-up (see section R17-5-5) to drive the oscillations in the surface voltage.

One hypothesis was that these discharges were difficult to repeat due to MHD activity. However, calculation of the ideal MHD stability found that the discharges operated well below the no-wall stability limit. Figure R17-5-24 shows a calculation using the DCON stability code [R17-5-2]

for discharge 204131 where the discharge is steadily moving away from the no-wall limit through the ramp-up phase. While the uncertainty in the q-profile without an MSE constraint could introduce significant errors in the ideal stability calculation, most discharges that ended during ramp-up followed the same trend toward becoming more stable following the L-H transition. Furthermore, typical metrics of stability, such as the pressure peaking factor (panel g) and the ratio β_N/I_i (panel f) were in the range of typical H-mode operation. Work planned FY18 will examine if the ideal stability limit can restrict operations in regimes not yet explored on NSTX-U, such as when operating with faster I_p ramp rates.

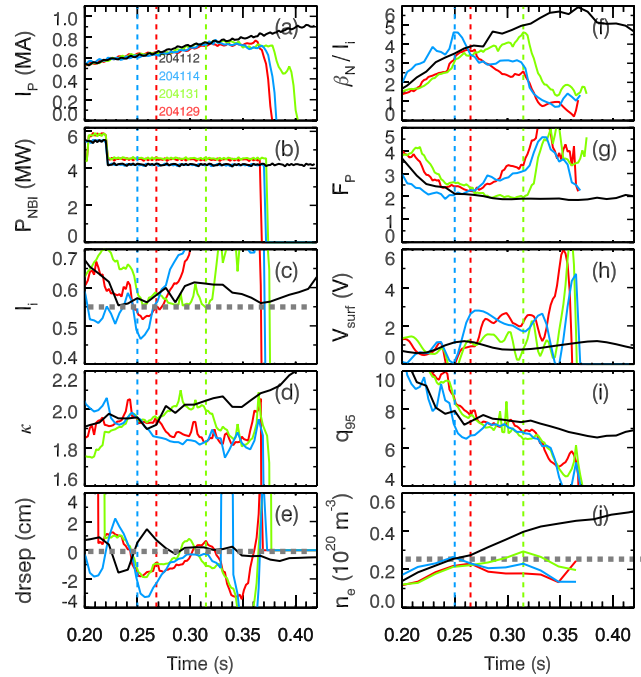


Figure 17-5-23 Comparison of a high-performance H-mode discharge (black) to three attempts to repeat the discharge that disrupts prior to the start of flattop

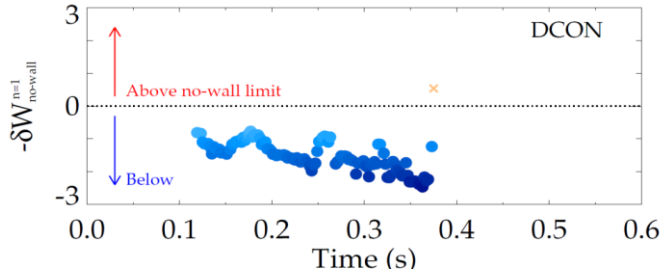


Figure 17-5-24 Discharge 204131 (green traces in 17-5-23) operates well below the no-wall stability limit prior to 0.32s.

The results of the MHD calculations prompted a reexamination of the low- I_i shots that ended during ramp-up. The large β_N drop is, in fact, an H-L back transition and independent of the MHD activity. The back transition is consistent with the dr_{sep} moving outside of 0.6cm and the $V_{surf} \sim 0$ being less conducive to triggering and sustaining the H-mode. The transient periods of large dr_{sep} and low surface voltage were due to the vertical oscillations after the time of the diverting (“the bobble”). Thus, mitigating the vertical oscillations and further increases of the heating power should provide an avenue for remaining in H-mode and achieving a reliable low- I_i scenario.

References

- [R17-5-1] Gates, D. *et al.* Progress towards steady state on NSTX. *Nucl. Fusion* **46**, S22–S28 (2006).
- [R17-5-2] Berkery, J. W., Sabbagh, S. A., Bell, R. E., Gerhardt, S. P. & LeBlanc, B. P. A reduced resistive wall mode kinetic stability model for disruption forecasting. *Phys. Plasmas* **24**, (2017).

Boundary Science Research Highlights

The Boundary Science group consists of three topical science groups (TSGs) including: pedestal physics and control, divertor and scrape-off layer physics, and materials and plasma facing components. Progress in each of these areas is described below.

A. Pedestal Structure and Control TSG Research Highlights

A central goal of the NSTX-U Pedestal Structure and Control TSG is to characterize H-mode access and L-H power threshold, characterize the pedestal structure, understand the turbulence in pedestal and identify common characteristics in phenomenology of different types of edge-localized modes (ELMs), and develop control approaches to improve the plasma performance. Below, we report on analysis of ELM stability in enhanced H-modes e.g. via lithium conditioning, and analysis of Enhanced Pedestal H-modes undertaken by this group.

1. ELM stability analysis with NIMROD, highlighting possible role of resistivity

Previous studies of edge stability in ELMy and lithiated discharges in NSTX indicated reference ELMy discharges with slowly growing modes that were completely stabilized by profile changes in lithiated discharges [BPR-PED-1, BPR-PED-2]. These same discharges were analyzed by the NIMROD code, which is an extended MHD model including finite-Larmor radius ion gyro-viscosity, two-fluid Hall, and electron diamagnetic drift effects [BPR-PED-3, BPR-PED-4]. A comparison of the single fluid and two-fluid calculations is shown in Figure BP-PED-1. In both cases, the growth rate of

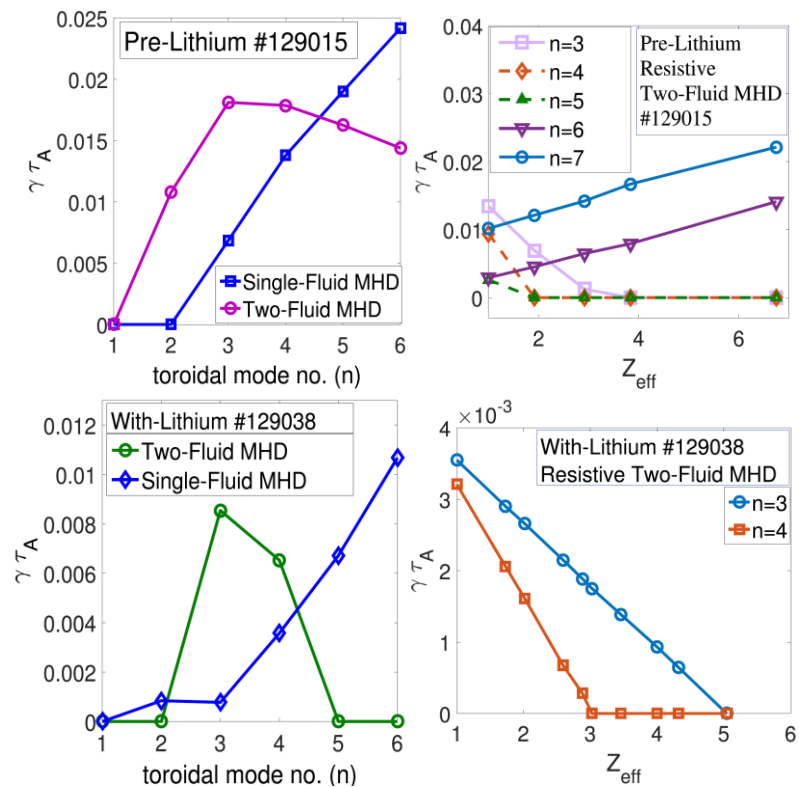


Figure BP-PED-1: Effect of two-fluid terms on low-n mode growth rates, and effect of resistivity on growth rates for n=3,4: top panels for pre-lithium ELMy reference, bottom panels for with-Li ELM-free discharges in NSTX [BPR-PED-2, BPR-PED-3].

intermediate n=3-4 modes was enhanced by the two-fluid effects, using a Spitzer resistivity model with $Z_{eff} = 1$. When the enhanced resistivity η due to the increase in Z_{eff} was included, these modes became fully stabilized with lithium but remained unstable without lithium. Thus, the

NIMROD results indicate that, in addition to the stabilizing effect of the profile modifications, the enhanced η plays a key role in explaining the mechanism behind the complete ELM suppression in lithium-conditioned H-mode discharges in NSTX. Access to the ELM stabilization may be accomplished through a ‘virtuous cycle’, in which initial profile changes contribute to reduced ELM frequency and increased impurity retention in the core, leading to higher Z_{eff} and improved or full stabilization.

2. Enhanced Pedestal H-mode studies

The Enhanced Pedestal (EP) H-mode [BPR-PED-5, BPR-PED-6, BPR-PED-7] describes a subset (~ 50 discharges) of NSTX H-modes where a region of enhanced carbon temperature (T_C) and rotation (v_ϕ) gradients exists that exceed the values of standard H-mode. A unique feature of EP H-mode discharges is that a bifurcation in the transport properties occurs following a large ELM. The increase in the confinement of the ion thermal energy is often accompanied by a reduction in the particle confinement. Consequently, EP H-mode is an attractive operating regime for NSTX-U and future devices since larger values energy confinement are realized ($H_{98} \sim 1.2 - 1.8$ is typical) while avoiding a concurrent increase in the particle confinement.

Previous analysis of an EP H-mode database established that the maximum local temperature gradient realized in EP H-mode scaled with plasma current (I_p) and the rotation frequency gradient (df_ϕ/dR) [BPR-PED-5]. However, it is possible to have H-mode discharges with large flow shear and not observe dT_C/dR gradients typical of EP H-mode.

Thus, recent analysis has considered additional criterion that must be met in order to trigger and/or sustain the transport bifurcation. One criterion that has been examined is the requirement that the ion collisionality be below a critical value. Analysis performed in FY17 established that this criterion is consistent with the EP H-mode dataset, provided the critical ion collisionality is treated as a profile versus ψ_N .

The requirement for sufficiently low ion collisionality is illustrated in Figure BP-PED-2. The dashed lines in all the plots are empirical boundaries for a database of standard H-mode discharges including some discharges thought to be close to the critical EP H-mode conditions. In figure BP-PED-2(a) and (c) the H-mode temperature gradients ($-dT_C/dR$) are below the dashed line while in figure BP-PED-2 (b) and (d) the ion collisionality is above the dashed line in H-mode. (Note that the criterion for inclusion in the EP H-mode database [BPR-

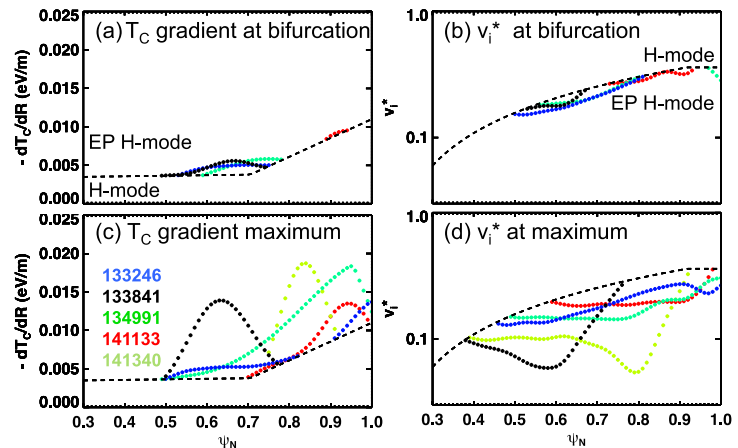


Figure BP-PED-2: (a) T_C gradient and (b) normalized ion collisionality at the EP H-mode bifurcation time and at the time with the maximum gradients (c – d).

PED-7] is $-dT_C/dR > 0.01$ eV/m). The colored points show regions where the temperature

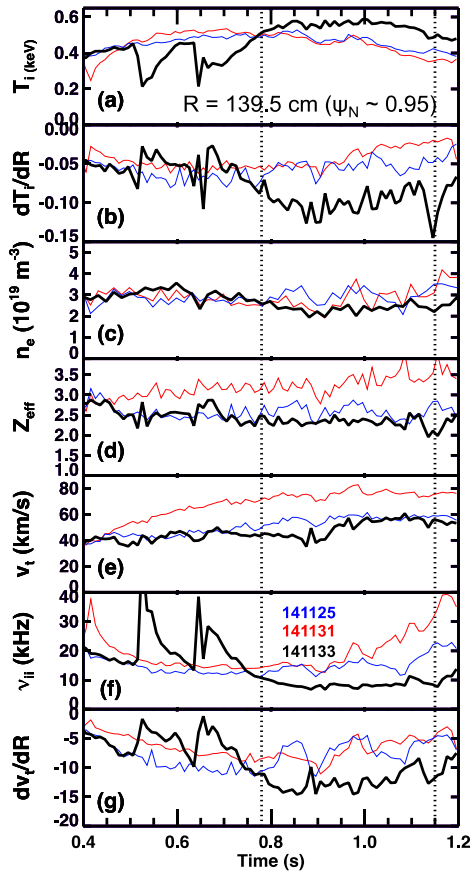


Figure BP-PED-3 Evolution of local parameters for two H-mode discharges (red and blue) compared to an EP H-mode discharge (black). All three discharges are similar except for the level of an applied $n=3$ magnetic perturbation.

lead to lower edge collisionality.

The role of a large ELM event in triggering EP H-mode is also consistent with the proposed dependence on ion collisionality. Figure BP-PED-3 shows local measurements from two H-mode discharges (red and blue) and one EP H-mode shot (black) at the location in the pedestal where the gradients in EP H-mode are a maximum. The red discharge has one ELM shortly after 0.4s, while the black discharges has two large ELMs; the blue discharge is ELM-free. The vertical dashed line indicates when the ion gradients appear to deviate from the H-mode discharge. The large ELMs reduces the edge Z_{eff} (figure BP-PED-3d) and leads to a brief moment during the ELM recovery where T_i exceeds the typical inter-ELM values. These effects drive the ion collision frequency (figure BP-PED-3f) to lower values compared to a similar discharge without an ELM (blue traces). The vertical dashed line reinforces that the larger T_C gradient is correlated with the realization of lower ion collisionality.

gradient and ion collisionality cross the empirical boundaries for different EP H-mode discharges. Figures BP-PED-2 (a) and (b) show the first measured profile when these boundaries are exceeded. The temperature gradient and collisionality boundaries are crossed concurrently and the locations in the profile where the boundaries are crossed are generally aligned. Figures BP-PED 2 (c) and (d) show the values at the time when the maximum $-dT_C/dR$ is realized. Again, the locations in the profile where the T_i gradients are larger than H-mode generally align with the regions of low collisionality.

This analysis supports the hypothesis that the local ion collisionality is a criterion for the bifurcation into EP H-mode. At sufficiently low collisionality, the ion energy transport is reduced (the reasons are under investigation), increasing the local ion temperature. This leads to a larger region of low collisionality, allowing the width of large gradient region to grow, analogous to the growth of the pedestal width after an L-H transition. Similarly, an increase in the momentum confinement drives an increase in the local rotation gradient, enabling the magnitude of the temperature gradient limit to increase. The role of ion collisionality is also supported by the database of EP H-mode discharges: EP H-mode is most often observed at low q_{95} and lower neutral fueling, which

Future efforts will examine the impact of ion collisionality on the neoclassical and turbulence mechanisms that govern the ion transport using simulations such as GTC-NEO and XGC. New capabilities on NSTX-U will advance the understanding of the access and sustainment criteria for EP H-mode. Namely, the new tangential beam lines provide a greater opportunity to control the local rotation shear. Access to higher fields will allow the exploration of low ion collisionality in an expanded range of regimes. Furthermore, expanded diagnostic capabilities will provide greater resolution of the kinetic profiles and turbulence characteristics during the triggering, growth and sustainment of EP H-mode.

References

- [BPR-PED-1] D. P. Boyle *et al.*, *Plasma Phys Control Fusion* **53** (2011) 105011.
- [BPR-PED-2] R. Maingi *et al.*, *Phys Rev Lett* **103** (2009) 075001.
- [BPR-PED-3] D. Banerjee, P. Zhu, and R. Maingi, *Nucl Fusion* **57** (2017) 076005.
- [BPR-PED-4] D. Banerjee, P. Zhu, and R. Maingi, *Phys Plasmas* **24** (2017) 054501.
- [BPR-PED-5] R. Maingi *et al.* *J. Nucl. Mater.* **390–391** (2009) 440.
- [BPR-PED-6] R. Maingi *et al.* *Phys. Rev. Lett.* **105** (2010) 135004.
- [BPR-PED-7] S.P. Gerhardt *et al.* *Nucl. Fusion* **54** (2014) 83021.

B. Divertor and Scrape-off Layer TSG Research Highlights

The NSTX-U divertor and SOL TSG encompasses a range of topics, including e.g. plasma-materials interactions (PMI). This group connects the pedestal TSG and the materials and PFCs TSG, and has some overlap in the areas of research. We have attempted to separate these for the annual report, but overlap is still evident. For organizational purposes, this section is divided into SOL physics, PMI and wall conditioning (including core impurity spectroscopy which falls in the responsibility of this group), and power exhaust. The latter section includes both inter-ELM and ELM heat flux, active management via radiative divertors, and the impact of 3-D fields. The associated topic of innovative divertor design is considered in the final sub-section.

1. SOL Turbulence and Transport

As discussed separately in this report, gas-puff imaging (GPI) observations made on NSTX [BPR-DSOL-1] have revealed two-point spatial correlation patterns in the plane perpendicular to the magnetic field. These correlations are relevant to the fundamental spatial structure of edge turbulence. A common feature is the occurrence of dipole-like patterns with significant regions of negative correlation. In recent work, Lodestar, in collaboration with S. Zweben [PPPL], has explored the possibility that these dipole patterns may be due to blob-hole pairs. Statistical methods were applied to determine the two-point spatial correlation that results from a model of blob-hole pair formation. It was shown that the model produces dipole correlation patterns that are qualitatively similar to the GPI data in many respects. Effects of the reference location (confined surfaces or scrape-off layer), a superimposed random background, hole velocity and lifetime, and background sheared flows have been explored. Results will be presented at an upcoming conference. [BPR-DSOL-2]

The parallel structure of filamentary instabilities in typical NSTX and MAST plasma shapes is also being studied using Lodestar's ArbiTER eigenvalue code [BPR-DSOL-3, BPR-DSOL-4]. The ArbiTER code allows the calculation of separatrix-spanning modes (i.e. including closed and open field lines) in realistic geometry. This work is exploring the 3-D structure of edge/SOL turbulence to determine the conditions under which filamentary turbulent structures can be expected to reach the divertor target in an ST geometry. For sufficiently collisional SOL plasmas, and field lines passing close to the X-point, parallel propagation is found to be impeded [BPR-DSOL-3]. Results are qualitatively consistent with the experimentally observed quiescent X-point region in MAST and with a reduction in divertor fluctuations near the separatrix and a loss of midplane correlation in NSTX [BPR-DSOL-5]. Penetration of filamentary structures to the divertor plate is important for assessing their effect on divertor plate damage and erosion as well as the turbulent coupling between the midplane SOL and divertor region, important for SOL heat flux width considerations.

GPI-related research results for NSTX-U in FY17

A new paper "Two-dimensional turbulence cross-correlation functions in the edge of NSTX" by S.J. Zweben, D.P. Stotler, F. Scotti, J.R. Myra was submitted to Physics of Plasmas in May 2017. The 2-D radial vs. poloidal cross-correlation functions of edge plasma turbulence were measured near the outer midplane using the gas puff imaging (GPI) diagnostic on NSTX. These correlation functions were evaluated at radii $r = 0$ cm, ± 3 cm, and ± 6 cm from the separatrix and poloidal locations $p = 0$ cm and ± 7.5 cm from the GPI poloidal center line for 20 different shots. The ellipticity and tilt angle ϕ of the positive cross-correlation regions, and the minimum negative cross-correlation "cmin" and total negative over positive values "neg/pos" were evaluated for each of these cases. The average results over this data set were $e = 2.2 \pm 0.9$, $\phi = 87 \pm 34^\circ$ (i.e. poloidally oriented), $c_{min} = -0.30 \pm 0.15$, and $neg/pos = 0.25 \pm 0.24$. Thus there was significant variation in these correlation results within this database, with dependences on the location within the image, the magnetic geometry, and the plasma parameters. Possible causes for this variation are discussed, including the misalignment of the GPI view with the local B field line, the magnetic shear of field lines in the edge, the poloidal flow shear of the turbulence, blob-hole correlations, and the neutral density 'shadowing' effect in GPI.

An invited review paper "Gas puff imaging diagnostics of edge plasma turbulence in magnetic fusion devices highlighted results of GPI from NSTX and Alcator C-Mod" has been published [BPR-DSOL-6]. Gas puff imaging (GPI) is a diagnostic of plasma turbulence which uses a puff of neutral gas at the plasma edge to increase the local visible light emission for improved space-time resolution of plasma fluctuations. This paper reviews gas puff imaging diagnostics of edge plasma turbulence in magnetic fusion research, with a focus on the instrumentation, diagnostic cross-checks, and interpretation issues. The gas puff imaging hardware, optics, and detectors are described for about 10 GPI systems implemented over the past 15 years. Comparison of GPI results with other edge turbulence diagnostic results is described, and many common features are observed. Several issues in the interpretation of GPI measurements are discussed, and potential improvements in hardware and modeling are suggested.

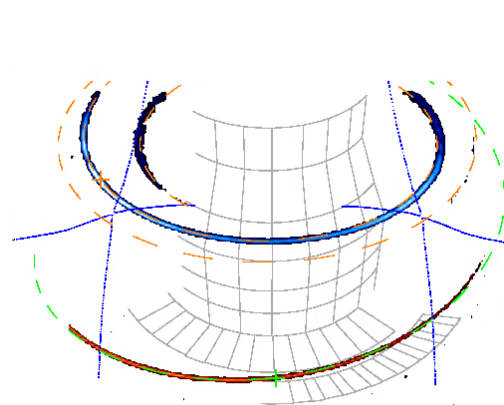
Synthetic Gas Puff Imaging Diagnostic for XGC1 Turbulence Code

The full-f edge gyrokinetic code XGC1 has been used recently to study problems of significant interest, such as the divertor heat flux width [BPR-DSOL-7] and the L-H transition [BPR-DSOL-8]. Moreover, XGC1 simulations of the heat flux width in ITER have different edge turbulence characteristics that lead to widths large relative to those based on empirical scalings. To be confident that this and other XGC1 predictions are accurate will require more detailed validation tests of the code against experimental data. One invaluable source of such data is the gas puff imaging (GPI) technique [BPR-DSOL-6], which measures edge plasma turbulence. We are in the process of extending the DEGAS 2 based synthetic diagnostic developed previously to analyze NSTX GPI experiments [BPR-DSOL-9] to use the time varying, 3-D plasma data produced by the XGC1 code. Single time step 3-D simulations have been performed; time dependent runs are planned for the near future. Once complete, the data produced by the synthetic diagnostic will be analyzed in exactly the same manner as the experimental data, allowing a direct comparison of simulated and observed turbulence characteristics, such as fluctuation amplitude, auto-correlation time, and correlation lengths.

Near-separatrix divertor fluctuations in NSTX-U L-mode discharges

Progress was made in the analysis of near-separatrix filaments observed on the divertor legs of NSTX-U L-mode discharges as described in the FY2016 NSTX-U Annual Report. Improvements in the spatial alignment via in-vessel metrology after the end of the experimental campaign and correlation with other fast imaging diagnostics enabled a better characterization of the observed divertor fluctuations. The analysis takes into consideration NBI-heated L-mode discharges in NSTX-U at low triangularity ($\delta \sim 0.45$), low elongation ($\kappa \sim 1.7$) and large X-point height with long divertor legs (0.3 and 0.55 m for the poloidal length of inner and outer legs, respectively).

In Figure BP-DSOL-1, cross correlations of a single pixel with the rest of the image are shown for an inner leg filament (blue) and an outer leg filament (red). Field lines from equilibrium reconstruction via EFIT02 are overlaid with dashed lines: in orange a field line located in the inner divertor leg private flux region, in green a field line located on the outer divertor separatrix. Field line overlay allowed for the radial localization of inner leg filaments to the private flux region.



Observed poloidal and parallel correlation lengths are 1-3 cm ($10\text{-}50 \rho_i$) and several meters, respectively. For the outer leg filaments, poloidal correlation lengths decrease along the divertor leg away from the strike point. Typical effective toroidal mode numbers are in the range of 10-20. Autocorrelation times for both inner and outer leg filaments are on the order of several 10s of microseconds. Inner and outer leg

Figure BP-DSOL-1: Cross correlation of a single pixel with the rest of the image for an inner leg filament (blue) and an outer leg filament (red). Field lines from EFIT02 equilibrium reconstruction are overlaid with dashed lines: inner divertor leg private flux region (orange), outer leg separatrix (green).

fluctuations show comparable probability density functions with near-Gaussian shapes and small positive skewness. Analysis is ongoing to correlate filament properties with plasma parameters for comparison with theory expectations for divertor-localized modes.

Divertor fluctuations were simultaneously imaged in C III and D- α emission using two fast cameras at different toroidal locations. Cross correlation between time series from inner leg fluctuations from the different cameras was up to 0.7, indicating that the measured emission fluctuations are mostly representative of n_e fluctuations. Cross correlation was performed between the divertor filaments and upstream turbulence as measured by passive D- α imaging via the GPI optics. No significant correlation was observed between divertor filaments and upstream turbulence.

Poloidal velocities are on the order of 1 km/s for both inner and outer leg filaments. Motion is generally upward (towards X-point) in both legs but opposite propagation has also been observed for inner leg filaments. No radial propagation is observed for outer leg filaments. UEDGE simulations with the inclusion of cross field drifts are in progress to understand the experimentally observed filament motion. The shape, dynamics and absence of correlation with upstream turbulence suggest that these fluctuations are generated and localized in the divertor region.

2. SOL Exhaust and 3D Perturbations

(a) SOL heat flux width in Double-Null Discharges

A scan of δ_r^{sep} was performed in 2010 on NSTX. The discharges had $I_p = 0.9$ MA, $\delta_{\text{bot}} \sim 0.8$ with $P_{\text{NBI}} = 4$ MW and utilized ~ 100 mg of lithium evaporation prior to each discharge. However, close to double-null, there was significant variation in both of δ_r^{sep} and δ_{bot} . Figure BP-DSOL-2 shows the peak heat flux on the lower divertor at the outer strike point measured using the dual-band IR camera system to account for emissivity changes due to the use of evaporative lithium coatings. The power passing through the last closed

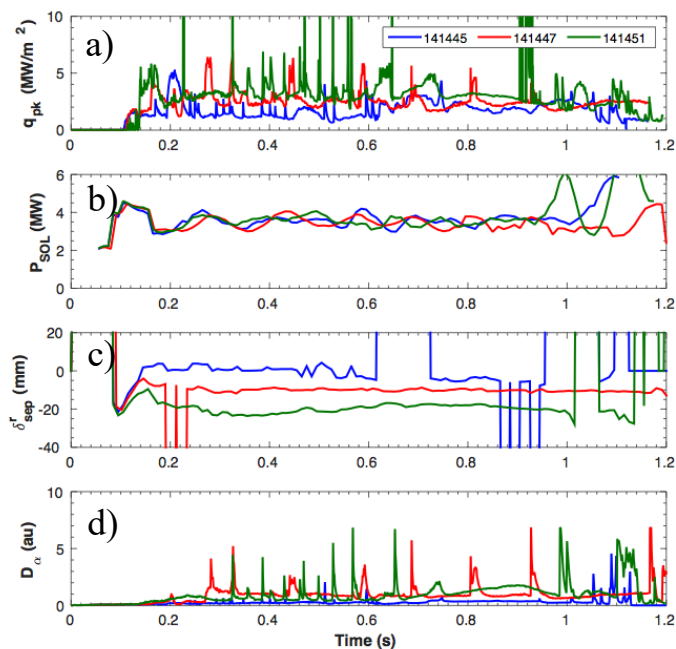


Figure BP-DSOL-2: NSTX data showing the variation in a) peak heat flux on the lower divertor at the outer strike point; b) P_{SOL} ; c) δ_r^{sep} and d) D_α in the lower divertor for shots 141451 ($\delta_r^{\text{sep}} = -20$ mm), 141447 ($\delta_r^{\text{sep}} = -10$ mm), and 141445 ($\delta_r^{\text{sep}} \sim 0$ mm).

flux surface into the SOL, P_{SOL} which is defined as $P_{\text{SOL}} = P_{\text{NBI}} + P_{\text{oh}} - \frac{dW}{dt} - P_{\text{rad}}^{\text{core}}$ is shown in

Fig. BP-DSOL-2b. P_{NBI} is the injected neutral beam power. P_{oh} is the ohmic power. dW/dt is the time rate of change of the plasma energy and $P_{\text{rad}}^{\text{core}}$ is the power radiated from the core plasma. Figure BP-DSOL-2c and 2d show the value of δ_r^{sep} derived from an EFIT02 magnetic equilibrium reconstruction and the lower divertor D_α respectively. Infrared coverage in NSTX was only available for the lower, outer strike point (LOSP) preventing a full accounting of the heat fluxes at each strike point. From Fig. BPR-DSOL-2a, it's clear that the inter-ELM divertor heat flux at the lower, outer strike point (LOSP) is reduced as δ_r^{sep} approaches double-null. Based on preliminary observations, its unclear if the ELM behavior in these discharge is similar to previous work [BPR-DSOL-10] that was performed under boronized conditions or whether the ELM behavior with respect to δ_r^{sep} has changed due to the addition of lithium.

Preliminary analysis shows that the deposited heat flux profiles, shown in Fig. BP-DSOL-3c, broaden as δ_r^{sep} approaches 0 mm. However, it's unclear if this is due only to the change in δ_r^{sep} or to other parameters changing such as triangularity or flux expansion in the SOL. This is resolved by calculating the parallel heat flux and mapping it to the outer midplane (OMP). Shown in Fig. BP-DSOL-3a and b are the ‘‘Eich’’ Diffusive-Gaussian fits [BPR-DSOL-11] of

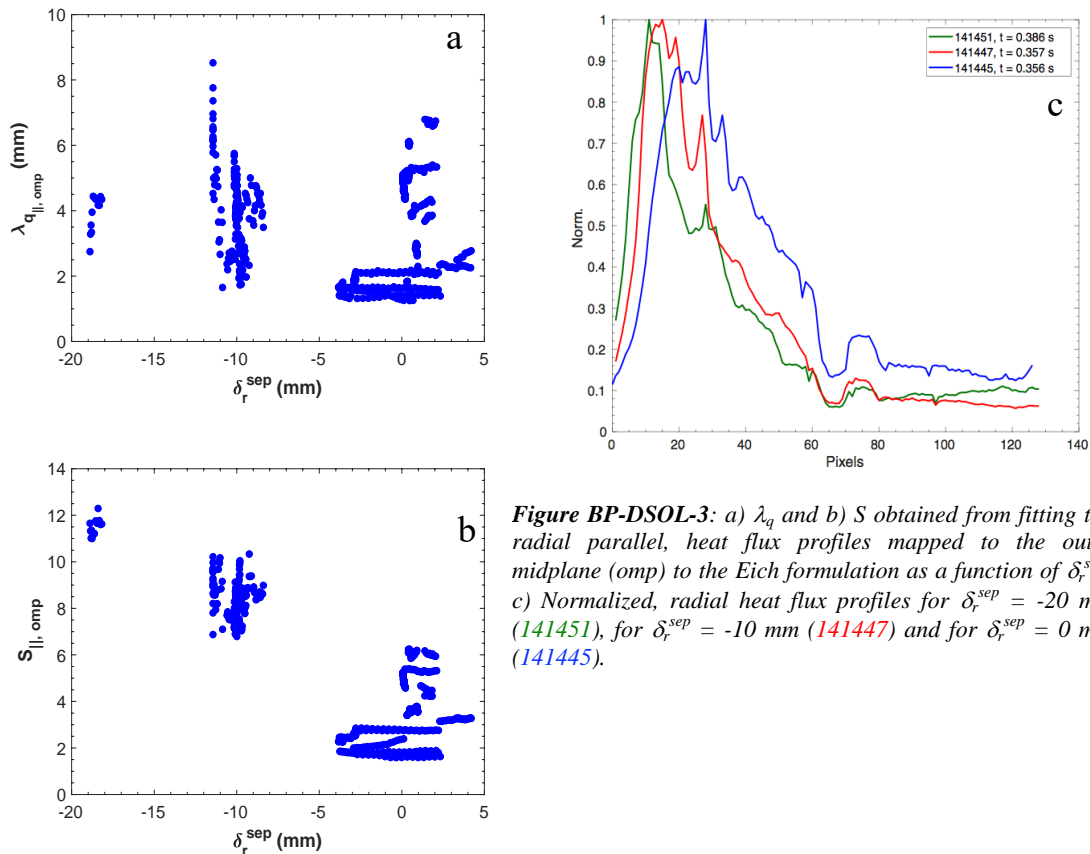


Figure BP-DSOL-3: a) λ_q and b) S obtained from fitting the radial parallel, heat flux profiles mapped to the outer midplane (omp) to the Eich formulation as a function of δ_r^{sep} ; c) Normalized, radial heat flux profiles for $\delta_r^{\text{sep}} = -20$ mm (141451), for $\delta_r^{\text{sep}} = -10$ mm (141447) and for $\delta_r^{\text{sep}} = 0$ mm (141445).

parallel heat flux data measured at the LOSP and mapped to the OMP of a) λ_q and b) S . The diffusive-gaussian fits were performed only on measurements from the LWIR band (6.5 – 10 μm). Because of the reduced divertor heat flux at DN, the signal in the individual IR bands is also reduced making the image registration process difficult and distorts the radial profile. The

same procedure was used for the discharges in LSN for consistency in fitting all the IR profiles. However, the magnitude of the divertor heat fluxes are taken from the dual-band measurements.

From Fig. BP-DSOL-3a, little change in $\lambda_{q||, OMP}$ is observed as a function of δ_r^{sep} . Meanwhile, $S_{||, OMP}$ is found to be systemically higher in LSN compared to DN discharges shown in Fig. BP-DSOL-3b. This is qualitatively consistent with measurements made in MAST inter-ELM H-mode discharges of λ_q and S

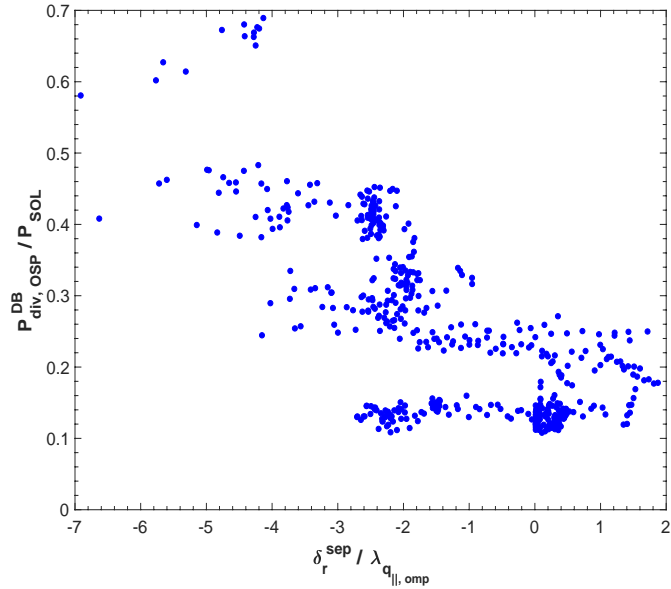


Figure BP-DSOL-4: Ratio of deposited power at the lower, outer strike point to P_{SOL} as a function of $\delta_r^{sep} / \lambda_{q||, omp}$.

[BPR-DSOL-12]. Assuming similar physics are setting the λ_q and S values in both NSTX and MAST, this suggests the SOL width in NSTX operating scenarios near DN will scale similar to the recent MAST scaling in near-DN plasmas [BPR-DSOL-13] of $\lambda_q = 1.84(10)^{-3} P_{sol}^{0.18} B_{pol, omp}^{-0.68}$ rather than the established, NSTX LSN inter-ELM H-mode scaling found previously [BPR-DSOL-14]. This is conjecture as there is currently insufficient data from both MAST and NSTX for a complete understanding of how the SOL width varies in STs between LSN and DN discharges. Future work on both MAST-U and NSTX-U will focus on understanding the differences in SOL transport between LSN and DN discharges and projecting to larger more powerful STs.

Power accounting in DN discharges in NSTX is complicated due to limited IR coverage of the inner strike points and the upper divertor in general. Figure BP-DSOL-4 shows the power deposited at the LOSP, as measured by the dual-band IR camera, normalized to P_{SOL} versus the ratio of $\delta_r^{sep} / \lambda_{q||, OMP}$. While P_{SOL} is shown to be constant between the discharges in Fig. BP-DSOL-2b, this normalization is done to account for changes in P_{rad}^{core} which has been shown to vary as discharge time progresses due to accumulation of carbon impurities in ELM-free NSTX discharges. The ratio of $\delta_r^{sep} / \lambda_{q||, OMP}$ is used as a dimensionless ordering parameter. From Fig. BP-DSOL-4, power to the LOSP is minimized for $\delta_r^{sep} / \lambda_{q||, OMP} \pm 2$. In this range, only 10 – 25% of P_{SOL} reaches the LOSP.

(b) Validating model of SOL flows with asymmetric fueling experiments at MAST

There is a need to have validated modeling of exhaust phenomena in spherical tokamaks to support ongoing efforts to model density control with 3D fields in future high performance NSTX-U discharges. Asymmetric fueling experiments carried out at MAST provide a unique laboratory for validation of codes and understanding of SOL exhaust. Neutral puffing from a single high field side location at MAST led to field aligned flows in the SOL which were measured using a Coherence Imaging Spectrometer (CIS) [BPR-DSOL-15]. Good agreement [BPR-DSOL-16] was found

between the CIS measurements and the EMC3-EIRENE simulations as shown in Figure BP-DSOL-5. Analysis showed that the neutrals drive a local spike in static plasma pressure, which in turn drives flows away from the site of neutral puffing.

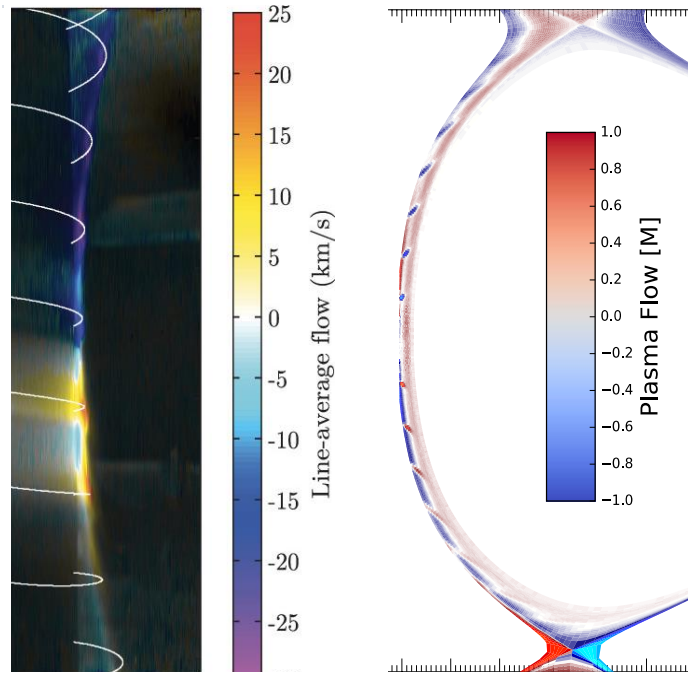


Figure BP-DSOL-5: Qualitative agreement shown between CIS flow measurements (left) and EMC3-EIRENE simulations (right) with asymmetric neutral fueling in the SOL [BPR-DSOL-16].

(c) Incorporating plasma response into 3D edge modeling for fueling and exhaust

A comprehensive set of experiments have been carried out at MAST to investigate the response of a plasma to the application of 3D fields [BPR-DSOL-17, BPR-DSOL-18]. These experiments showed that density pump-out can be achieved in both L-mode and H-mode configurations over a range of 3D field strengths and configurations. EMC3-EIRENE simulations have been carried out to further characterize this density pump-out and determine the relative roles of fueling and exhaust in the observed phenomena. To better simulate realistic impacts of 3D fields, the MARS-F magneto-hydrodynamic code was used to determine the total 3D perturbation from applied field coils and the plasma's response to this perturbation. These total (vacuum fields and plasma response fields) magnetic fields are then used to build EMC3-EIRENE models that more accurately represent the impact of 3D fields on the edge (as shown below in Figure BP-DSOL-6), which can then be used to analyze fueling and exhaust in steady state operation of high performance tokamaks. Experimental analysis is being enabled by a global, 0-D particle balance model [BPR-DSOL-19].

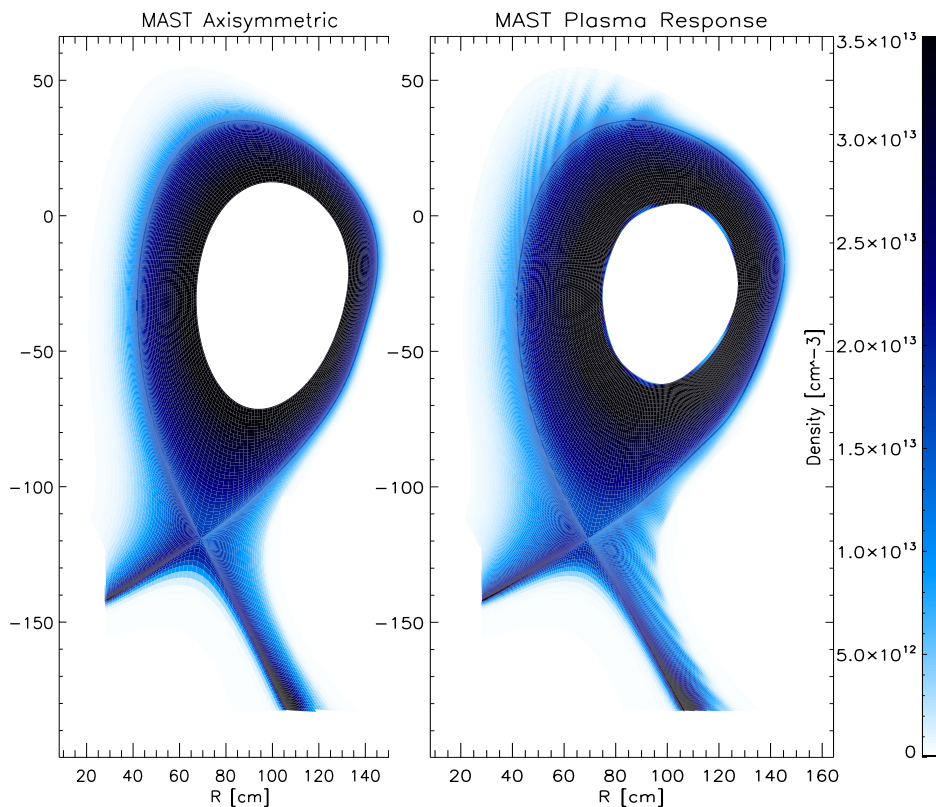


Figure BP-DSOL-6: Plasma density is shown for EMC3-EIRENE simulations of a MAST H-mode discharge for axisymmetric (left) and RMPs with plasma response (right) cases. The more realistic edge conditions accessed with the plasma response fields allow better analysis of fueling and exhaust with a multi-reservoir particle balance.

References

- [BPR-DSOL-1] S.J. Zweben *et al.*, “Two-dimensional turbulence cross-correlation functions in the edge of NSTX,” *Phys. Plasmas* (2017) submitted.
- [BPR_DSOL-2] J.R. Myra *et al.*, abstract submitted to the 59th Meeting of The American Physical Society, DPP, Milwaukee, Wisconsin, October 23 - 27, 2017.
- [BPR-DSOL-3] D. A. Baver *et al.*, “ArbiTER studies of filamentary structures in the SOL of spherical tokamaks,” Transport Task Force Workshop, Williamsburg, Virginia, April 25-28, 2017, B-18.
- [BPR-DSOL-4] D. A. Baver *et al.*, “Penetration of filamentary structures in the x-point region of spherical tokamaks,” abstract submitted to the 59th Meeting of The American Physical Society, DPP, Milwaukee, Wisconsin, October 23 - 27, 2017.
- [BPR-DSOL-5] F. Scotti *et al.*, “Characterization of intermittent divertor filaments in L-mode discharges in NSTX and NSTX-U,” 58th Annual Meeting of the APS Division of Plasma Physics, San Jose, Oct. 31 – Nov. 4, 2016, paper NP10.28.
- [BPR-DSOL-6] S. J. Zweben *et al.*, *Rev. Sci. Instrum.* **88** (2017) 041101.
- [BPR-DSOL-7] C.S. Chang *et al.*, *Nucl. Fusion* **57** (2017) 116023.
- [BPR-DSOL-8] C.S. Chang *et al.*, *Phys. Rev. Lett.* **118** (2017) 175001.
- [BPR-DSOL-9] B. Cao *et al.*, *Fusion Sci. Technol.* **64** (2013) 29.
- [BPR-DSOL-10] R Maingi, et al. *J. Nucl. Mater.* **337-339** (2005) 727-731
- [BPR-DSOL-11] T. Eich, et al. *Phys. Rev. Lett.* **107** (2011) 215001
- [BPR-DSOL-12] JR Harrison, et al. *J. Nucl. Mater.* **438** (2013) S375-S378
- [BPR-DSOL-13] A. Thornton, *Plasma Phys. Control. Fusion.* **56** (2014) 055008
- [BPR-DSOL-14] TK Gray, et al. *J. Nucl. Mater.* **415** (2011) S360-S364
- [BPR-DSOL-15] S.A. Silburn *et al.* *Rev. Sci. Instrum.* **85** (2014).
- [BPR-DSOL-16] I. Waters *et al.*, Proc. 44th EPS Conference on Plasma Physics, (2017).
- [BPR-DSOL-17] I.T. Chapman *et al.*, *Nucl. Fusion* **54** (2014) 123003.
- [BPR-DSOL-18] A Kirk *et al.*, *Plasma Phys. Control. Fusion* **53** (2011) 065011.
- [BPR-DSOL-19] G. Maddison *et al.*, *Plasma Phys. Control. Fusion* **48** (2006) 71.

C. Materials and Plasma-Facing Components TSG Research Highlights

The Materials and PFC (M&P) research program on the NSTX-U exists to perform the critical research needed to address the fundamental question of what materials are suitable to a fusion plasma experiment and, eventually, a fusion power plant. In the context of the NSTX-U program, this practically means gaining an understanding of the existing materials and wall-conditioning techniques (carbon plasma-facing components (PFCs) + boronization and lithiumization) in use in the machine so that incremental upgrades to reactor-relevant systems (e.g. high-Z tungsten/molybdenum and flowing liquid lithium) will provide the greatest knowledge gain and minimize the operational learning curves.

The research program in M&P has been divided into three main thrust areas: surface science to support long-pulse operation, tokamak induced material migration, and vapor-shielding physics. Each of these thrusts addresses needs of both solid and liquid PFCs with-respect to future power-producing reactors.

Materials and PFCs TSG is working to enable integrated models of the NSTX-U through the use of state-of-the-art computational capabilities. In plasma-material interaction research, this activity is complicated due to subtle material interactions and subtle plasma transport phenomena. The M&P TSG team members are working in a range of activities to develop codes, simulations, and experimentally validate the results of not just materials simulations, but whole device models. The sections below highlight research results in these areas made possible by advanced tokamak diagnostics such as the MAPP (J.P. Allain, U-Illinois)[BPR-MP-10], advanced computational capabilities such as quantum-classical molecular dynamics (P. Krstic, SUNY), and whole-device modeling such as can be done with the WallDYN code (J. Nichols, PPPL). This activity is inherently multi-disciplinary and requires broad expertise in experimental methods (ranging from laboratory scale to confinement devices) as well broad expertise in computational methods for materials and plasma transport.

This year, more immediate research is also needed to support the NSTX-U Recovery project. In particular, the PFC Requirements Working Group has been established to help define the requirements of the PFCs so that PPPL engineering can develop designs to accomplish the needs of the machine.

Some research contributions are included below in each of these areas of work ranging from surface-science activities, whole-machine device modelling, advanced PFC development, and PFC requirements activities.

1. Advanced computational atomistic simulations of NSTX-U materials (P. Krstic, SUNY at Stony Brook)

Our work [BPR-MP-1] involved the use of advanced computational atomistic simulations (CMD and QCMD) of the chemistry inside the irradiated surface, validated with MAPP XPS

measurements of low-energy deuterium irradiation of boron-treated graphite samples introduced in the NSTX-U divertor region. The subtle interplay of boron, carbon, oxygen and deuterium chemistry is explained by reactive molecular dynamics simulations, verified by quantum-classical molecular dynamics and successfully compared to the measured XPS data. Combining the atomistic simulations with the dynamic measurements of chemical states by MAPP is a great strength of this work as both cover different spatial and temporal scales that when combined elucidate key D retention mechanisms (Fig. BP-MP-1). The calculations deciphered the roles of oxygen and boron for the deuterium retention and predicted deuterium uptake into a boronized carbon surface close in value to previously predicted for a lithiated and oxidized carbon surface (Fig. BP-MP-2).

The implications of this combined theoretical and experimental work are far-reaching given for the first time NSTX-U ability to observe “in vacuo” the complex surface chemistry and physics induced by exposure of device walls to the extreme environment in tokamak plasma that combines three states of matter (i.e. the MAPP diagnostic). One significant contribution of this work is that for the first time the evolving, reconstituted surface exposed to a tokamak plasma in the first 4-8 nm is dynamically measured and the findings, in combination with computer simulation, elucidated the critical role played by oxygen in the condensed matter state. This aspect of plasma-facing surfaces and the critical role surface chemistry plays on hydrogen retention is beginning to bring a new understanding of how surface impurities and their balanced interaction with plasma chemistry could influence bulk plasma behavior.

Using the computational simulations we compare the deuterium retention probabilities of lithiated or boronized surfaces in various configurations. Though both boronized and lithiated surfaces show similar trends in retention of deuterium when composition of the material is varied, the former surfaces show somewhat higher degree of retention, less dependent on the oxygen content than in case of lithiated surfaces. The experimental data, done at UIUC by JP Allain group, and new theoretical data show a reasonable qualitative agreements for both lithiated and boronized surfaces [BPR-MP-4].

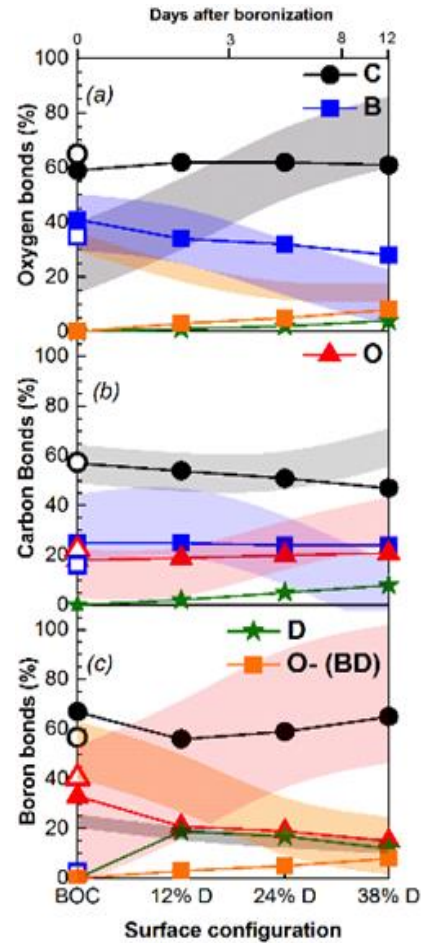


Figure BP-MP-1: Percentage of bonds of (a) O, (b) C, and (c) B to other constituents in the BCOD surface as a function of D concentration in the upper 7.5 Å of the computed sample. The shaded colored areas, bands, are \pm one standard deviation about the mean values measured by XPS of the corresponding bonding (color matched to the calculated values, grey is C, pink is O, light-blue is B, yellow is B-O-D), averaged over the 4 days of plasma exposure. [BPR-MP-1].

We also studied the effects of D retention in simultaneously boronized and lithiated, oxidized and deuterated carbon surfaces [BPR-MP-7]. We did analyses for different concentrations of B, C, and O in boronized surfaces as well as Li in lithiated surfaces (Fig. BP-MP-3). The effect of the mixture of Li-C-B-O surfaces is analyzed by considering different percentages of each constituent calculating the deuterium retention and the chemistry presented by the surface. Role of O and B in retaining D is about the same (mid point, LiBCO, in the graph BP-MP-3), the oxygen role increasing in comparison to B as B concentration decreases. Role of B is strongly dominant in comparison to O only in BCO mixture (without Li). Even small concentrations of Li help to increase a role of oxygen in the retention. However lithium plays smaller role in the retention chemistry for all studied concentrations of Li and B in the LiBCO mixture. This is similar to the previously studied and well known case of D retention in lithiated carbon, where oxygen is the main player in the retention chemistry of D.

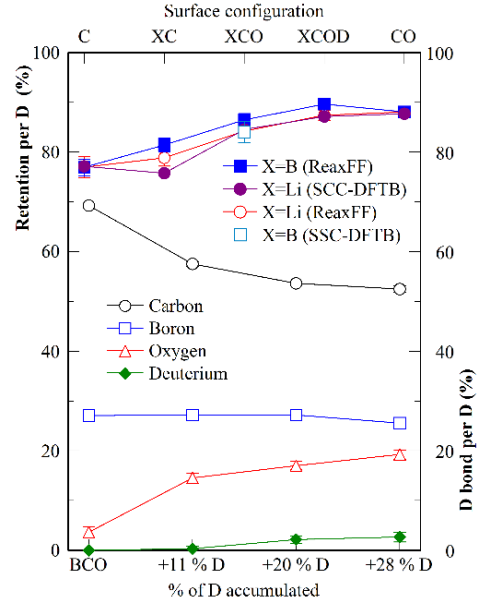


Figure BP-MP-2: Percentage of D bonds with constituents of the BCOD surface as function of the deuterium accumulated concentration (right axis). Left axis: Retention per impact of D for various configurations of C,B,Li,O, D. SCC-QCMD data are shown for the verification purposes [BPR-MP-1].

Chemical sputtering, unlike the retention probability, is strongly dependent on the impact energy. This energy dependence for the material matrices considered here is numerically intensive. We studied sputtering of lithiated and oxidized amorphous carbon surfaces by deuterium impact in energy range 5-30 eV [BPR-MP-3]. Using classical molecular dynamics with REAXFF potential and with Energy Equalization Method (EEM) and verification by QCMD, we obtained the sputtering yield, the mass and energy spectra, as well as the angular distribution of ejected atoms and molecules of the surfaces saturated by accumulated deuterium impacts. Our results are successfully compared with existing experimental and theoretical data for amorphous a-C:D surfaces. Presence of lithium reduces erosion of carbon, while presence of oxygen additionally reduces the erosion. The novel results in the paper are sputtering yields for various particles ejected from Li-C:D and Li-C-O:D surfaces. In absence of oxygen, we find that the total carbon erosion is suppressed in

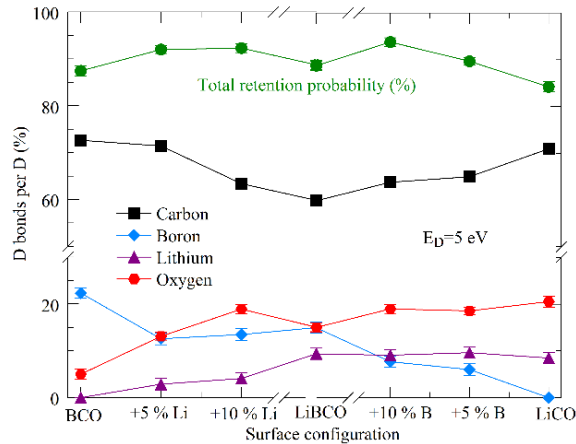


Figure BP-MP-3: Total retention probability per impact D for the LiBCO configuration, varying Li and B percentage content (green line). Lines for C, B, Li and O characterize the probability (in %) that impact D is bonded to these atoms in the mixture. LiBCO (mid configuration) contains 20% of B, Li and O each; BCO contains 20% B and O, while LiCO is made of 20% of Li and 20% of O [BPR-MP-7].

comparison to a-C:D by about factor 2. However, Li contributes almost equally to carbon to the total sputtering at 30 eV, while its contribution at lower energies dominates sputtering due to the weak bond of Li to C. In presence of oxygen, the carbon erosion (40% in atomic form) is reduced by factor 4 in comparison to a-C:D, while Li sputtering (of which 75% is in atomic form) is reduced by factor 4 in comparison to Li-C:D (Fig. BP-MP-4). The research shows also changes in molecular emission from the surfaces.

We also studied the chemical sputtering of boronized and oxidized amorphous carbon surfaces by deuterium irradiation in range of impact energies 5-30 eV [BPR-MP-2]. As in case of lithiated surface we report the sputtering yields as well as mass, energy and angular spectra of ejected atoms and molecules of both virgin and deuterium saturated BCO surfaces, and compare them with our data for a deuterated BC surface and existing theoretical and experimental results for amorphous C:D. Boron significantly (stronger than lithium) suppresses the erosion of carbon. This effect is further enhanced by presence of oxygen, with total carbon yields per D, made mainly of CD₃ and CD₂, staying in the range below 0.2%. While in case of the lithiated surfaces CD and LiD are dominating the sputtered material, potentially emitted into the plasma, CD and D₂O are dominating the emitted molecules from boronized surfaces, which becomes exclusively D₂O with increase of the D accumulation. OD and O are the dominant sputtered particles from BCO:D surface, with yields ranging from 0.5% to almost 2%. Sputtering yield of D₂O reaches 1% at lower energies, to be replaced with atomic oxygen at higher energies. Translational energy for ejected oxygen atoms and OD_x molecules of BCO:D surface are in the range 1-2 eV, which is higher than energy of sputtered CD_x molecules (around 1 eV).

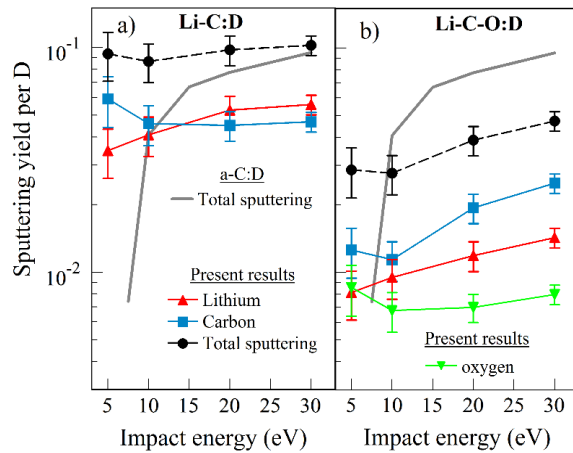


Figure BP-MP-3: Total sputtering yields (including molecules) for C and Li of Li-C:D, and b) for C, Li, and O from the Li-C-O:D surface. Presence of oxygen in the Li-C mixture reduces the sputtering of carbon and lithium. We compare our results with total sputtering yield of a-C:D surface [BPR-MP-3].

H retention in pure Li and Li₂O films was measured and calculated as a function of surface temperature under UHV conditions. It was shown that both pure Li and Li₂O are able to retain H. This suggests that low H recycling can be achieved if Li₂O is formed under fusion reactor conditions, since both Li and Li₂O are comparable in efficiency in trapping H. Our results also show that H retention drops with surface temperature in the range 90-520 K from 95% to by 2 to 3 times, due to loss of H with increasing temperature. The modeling results are consistent with experimental results in terms of both retention fraction and the trend of retention with temperature, for both H or D impact particles, and for both pure Li and Li₂O [BPR-MP-6].

2. Lithium coating chemical evolution and analysis (D. Donovan, UTK)

The University of Tennessee-Knoxville (UTK) has been working in collaboration with Oak Ridge National Laboratory (ORNL) and Princeton University on the LTX-Beta device at Princeton Plasma Physics Laboratory (PPPL) to investigate the surface characteristics and low recycling properties of lithium plasma facing components (PFCs). Previous operation of LTX has documented improved plasma performance when lithium coatings are applied to their high-Z PFCs, which is believed to be due to the low-recycling operating regime created by the presence of lithium. It was initially believed that the formation of lithium hydrides was responsible for the retention of hydrogen and the low recycling. However, in-vacuo measurements performed on the Materials Analysis Particle Probe (MAPP) indicated the presence of high levels of lithium oxide on the PFCs [DP Boyle, et al., PRL, 2017]. These observations have raised a series of questions regarding the nature of lithium oxide surfaces, whether the oxygen remains near the surface as an orderly lithium oxide coating or exists as an amorphous mixture of lithium and lithium oxide throughout the coating on the PFC, and to what extent the lithium oxide is capable of retaining hydrogen.

UTK graduate student, Anurag Maan, has been working with Dr. Robert Kaita (PPPL) to perform deuterium retention experiments on lithium coatings in the surface chemistry laboratory of Professor Bruce Koel (Princeton U.), with additional direction from Professor David Donovan (UTK), Dr. Theodore Biewer (ORNL), and Dr. Richard Majeski (PPPL). Deuterium exposures are able to be performed in this laboratory in a controlled and characterized environment using a compact electron cyclotron plasma source to simulate exposure conditions of PFCs in LTX. Characterization of bulk lithium samples have been performed using high resolution x-ray photoelectron spectroscopy (HR-XPS). Preliminary HR-XPS scans have identified lithium oxide on sputter cleaned lithium samples. The next step of the analysis, now being performed, is to transfer the samples in argon filled cases to an ion beam facility to perform Rutherford Backscatter Spectroscopy (RBS) and Nuclear Reaction Analysis (NRA). The NRA/RBS analysis will provide details regarding how deuterium is chemically bound and what kind of compositional changes are seen between D-exposed and unexposed lithium samples. These offline experiments will enhance the understanding of the surface chemistry team at LTX-Beta regarding the underlying mechanisms of lithium oxide formation and the effects on hydrogen retention, which then leads to more directed experiments to be performed on LTX-Beta. A new sample exposure stage is under development by PPPL and Princeton University that will allow samples to be exposed at the inner wall of LTX-Beta and subsequently retracted and removed in an argon case without disrupting the experiment vacuum or exposing the sample to atmosphere. UTK is contributing to the development of the vacuum suitcase and the development of Langmuir probes to be inserted at the same radius to characterize the plasma conditions to which the sample will be exposed. The combination of advanced fundamental understanding of surface chemistry through offline experiments, performing sample exposure and retrieval on LTX-Beta combined with ex-situ analysis, and characterization of the plasma exposure conditions will greatly advance the understanding of how lithium coatings on PFCs behave in the presence of the LTX-Beta plasma discharges.

3. Interaction of Lithium Coatings with D and He ions on Tungsten Substrates (A.L. Neff and J.P. Allain, UIUC)

At the University of Illinois at Urbana-Champaign, we have been investigating the chemical and physical behavior of thin film Li (100s of nm) on tungsten substrates under low flux ($10^{17} \text{ m}^{-1}\text{s}^{-1}$) and high flux ($10^{24} \text{ m}^{-1}\text{s}^{-1}$) hydrogen and helium ions. The low flux irradiations occurred in the facility IGNIS (Ion-Gas-Neutral Interactions with Surfaces) at UIUC and the high flux exposures were carried out in collaboration with DIFFER on Magnum-PSI. Specifically, we have analyzed the effect that He has on the retention of hydrogenic species in Li coatings and are investigating the interaction between nano-structured fuzz and Li layers.

Simultaneous irradiations with a variations in He flux (0, 1, 5, 10% He to D flux) have shown a qualitative reduction (decrease in the Li-O-D functionality peak in XPS [BPR-MP-8]) in the retention of D ions up to a flux ration between the He and D of 5%. When the He flux is at 10%, the retention increased again but is still less than the case of pure D (Figure BP-MP-5). Sequential irradiations of D and He are ongoing but are indicating that He does not appear to inhibit the formation of the Li-O-D functionality if the Li film is exposed to He ions before D ions. However, when He ions follow the D ions, then there is a reduction in the Li-O-D functionality that is converted back to Li_2O . Sequential exposures were also carried out a DIFFER with H and He. The analysis of *post-mortem* analysis is on going.

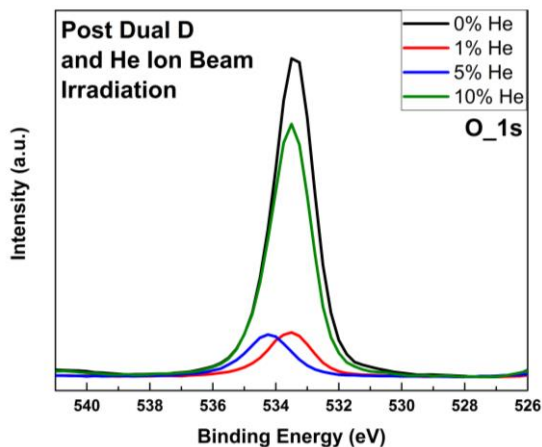


Figure BP-MP-4: O 1s region of XPS scans of lithiated W under dual beam irradiation with varying He flux concentrations showing the Li-O-D functionality peak at ~533.5 eV binding energy. The shift in the peak for the 5% He case is likely due to charging on the surface of the sample.

We have also analyzed sputter erosion mechanisms of nano-structured fuzz with and without Li coatings. We have developed a method to grow fuzz tendrils on W foil in a Helicon plasma with resistance heating of the foil. The coatings of Li were deposited both before and after the fuzz was formed and then exposed to 1 keV Ar and Kr ions to enhance the erosion. The tendrils show little reduction in the thickness of the layer but the individual tendril increase in thickness and become cone shaped. This change in tendril thickness is present for all of the tendrils but it more pronounced for the case when Li was present either during the formation of the fuzz or deposited after the fuzz was grown. We suspect that the Li is contributing to the thickening of the tendrils. TEM lift-out

samples have been prepared of these tendrils and are awaiting characterization with EELS (Electron Energy Loss Spectroscopy) to confirm this supposition.

4. Material Migration Modeling of the NSTX-U (J. Nichols and M.A. Jaworski, PPPL)

Significant progress has been made in developing a mixed material evolution model for NSTX-U, using the WallDYN code framework. WallDYN allows for the calculation of time- and poloidally-resolved surface concentrations and impurity erosion fluxes for a fully mixed C/Li/B/O/Mo environment. Unlike other modeling approaches that attempt to iteratively couple plasma transport and surface effects and run into computational hurdles due to the disparate time and length scales, WallDYN operates by parameterizing the outputs of plasma transport and surface sputtering codes into rate equations, which can be solved simultaneously without strenuous computing requirements. Recent development has focused on the B/C/O system present in the FY2016 NSTX-U campaign, with a focus on material evolution following boronization.

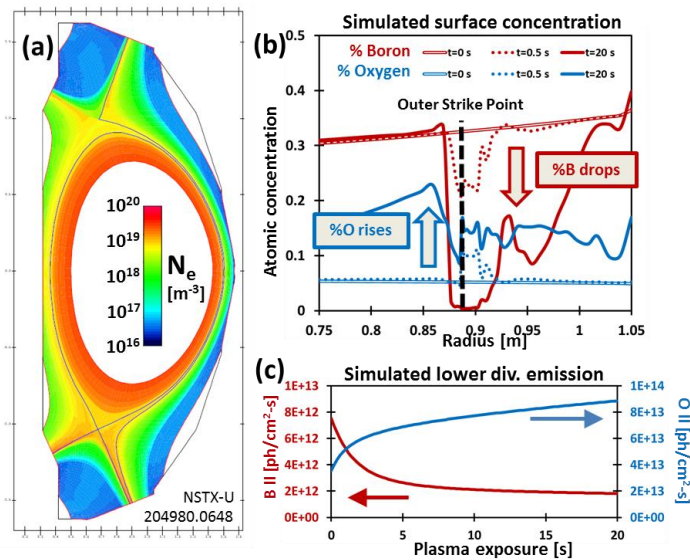


Figure BP-MP-5: WallDYN simulations of NSTX-U discharge 204980 following a 1/4 bottle boronization: (a) Background electron density. (b) Calculated surface atomic concentrations of boron and oxygen, at 3 time steps, near the lower outer strike point. (c) Calculated time evolution of reconstructed lower divertor spectroscopic signals for B II and O II.

campaign. A spatial distribution model for the films deposited during the dTMB boronization process on NSTX-U has also been developed. All of these advances have enabled first-of-their-kind WallDYN simulations of PFC evolution following conditioning. Figure BP-MP-5b shows the modeled atomic concentration of boron and oxygen on the lower divertor PFC surface (near the outer strike point at $R=88$ cm), following a so-called “mini-boronization” of 1/4 bottle dTMB. Simulations show erosion of boron initially from the strike point, followed by erosion from the rest of the outer divertor over the course of 20 seconds of plasma exposure (approximately a day of operations). Concurrently, the surface concentration of oxygen increases over the course of a day. Figure BP-MP-5c shows line-integrated photon emission of B II and O II for this simulation, matching the sightlines of the NSTX-U lower divertor filterscope system. Similar to the concentration evolution, the boron signal decreases and the oxygen signal increases with plasma exposure. Both of these results are qualitatively consistent with experimental results from MAPP XPS and filterscopes/filtered cameras (described elsewhere) that show a consistent suppression of

SOL plasma reconstructions of select discharges during the 2016 NSTX-U campaign have been calculated using the OSM fluid equation solver and EIRENE neutral particle code, utilizing experimental Langmuir probe profiles as boundary conditions. Novel computational grids extending all the way to the wall have been developed for NSTX-U, allowing for accurate modeling of particle fluxes to all surfaces and a better representation of far SOL transport. Figure BP-MP-5a shows the calculated electron density for discharge 204980, a low-triangularity 1 MW L-mode scenario commonly used in the

oxygen signals after boronizations, followed by a gradual increase in oxygen as the PFCs decondition.

Work is ongoing to make quantitative comparisons between observed PFC evolution rates and those calculated by WalldYN for the corresponding plasma scenario. This work is part of an ongoing effort to develop a deeper understanding of the interplay between plasma operations and PFC conditioning, beyond the ad hoc procedures currently used. A fully validated WalldYN model of conditioning would represent a significant step in whole-machine integrated modeling, and allow predictive simulations to be used to help optimize operations.

5. Pre-filled liquid metal target development (MA Jaworski, PPPL)

The NSTX-U research program had developed a staged pathway to eventually convert the PFCs to high-Z components as well as deploy liquid metal plasma-facing components. After development of the high-Z prototypes for row 2, pre-filled targets were proposed as a means of introducing a macroscopic quantity of lithium to the machine without the use of the LITER evaporators. These concepts are described in reference BPR-MP-9.

A significant technical challenge is to establish a design or procedure for maintaining lithium chemical composition during the NSTX-U bake-out. Bake-out, itself, maintains the NSTX-U vessel at 350C for periods of about 2 weeks. The PFC outgassing products, the temperature, and the time are all sufficient to completely react any lithium that might be present in the machine. In addition, previous methods for overcoming this problem when using limiter devices are not suitable to a divertor application.

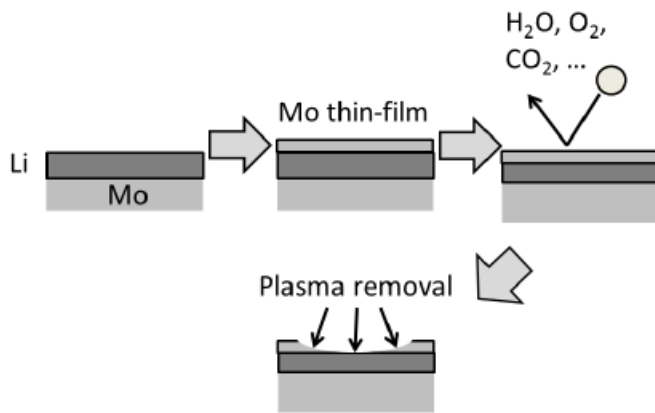


Figure BP-MP-6: Diagram of present scheme for mitigating contamination of a pre-filled lithium component. First, lithium is loaded onto a metallic substrate. A thin film of molybdenum is deposited on top of the lithium. This layer serves to avoid contamination of the lithium during bake-out. Finally, when ready to proceed with experiments, the protective thin-film is removed by plasma etching exposing the underlying lithium layer.

A novel, sacrificial metal layer was used to survive bake-out and was tested in collaboration with the University of Illinois at Urbana-Champaign. The essential steps are described in Figure BP-MP-6.

The samples were tested in a set of chambers at UIUC which were designed to mimic the NSTX-U bake-out conditions. Temperatures were duplicated and a partial pressure of CO₂ and water vapor was maintained such that the pressure-time product was identical to that experienced during a typical NSTX-U bake-out. The result was that the metal-coated sample gave indications

that higher lithium purity had been maintained in the sample as opposed to the bare lithium sample which had clearly reacted.

These tests indicate a path forward for pre-filled targets in the NSTX-U in future campaigns. These results were reported at the 2016 IAEA FEC.

6. Lithium vapor box testing and development (R. Goldston, PPPL)

We have continued to make progress on the concept for a lithium vapor box divertor. Eric Emdee has developed a version of the Sparta code that should provide an accurate description of the box performance. This Direct Simulation Monte Carlo code calculates fluid flow taking into account evaporation, condensation, and finite mean-free-path of vapor atoms. In relevant regimes it shows agreement in the density drop from box to box with Goldston's original multi-box model, but it allows exploration outside of these regimes. It appears that the original prediction that lithium efflux can be effectively contained is correct, and can be achieved in a range of configurations. Inclusion of an absorbing plasma beam even reduces the predicted efflux by a factor ~ 5 . So far calculations have been performed in the appropriate geometry for tests at DIFFER, but soon NSTX-U and reactor geometries will be explored.

An experimental test is being developed for validation of the essential physical processes predicted in the 0D and 1D modeling of the vapor box. PU graduate student, Jacob Schwartz, is developing an on-site experiment that will measure transport of lithium from one container to another to develop a path toward testing in a linear plasma device such as Magnum-PSI. Numerous technical advancements are being made to accomplish this test including experimental methodologies for measuring lithium mass transport, as well as calorimetric measurements. Both of these measurements need to be made at high temperatures ($\sim 600\text{C}$) and with sufficient accuracy to validate the simulations. Tests at PPPL are planned for the fall of 2017.

7. PFC Performance and Monitoring Requirements Working Group

In early 2017, the Recovery Project DVVR process identified a series of concerns related to the plasma facing components. Not only were existing PFC designs shown to be unable to meet combined halo current and heat flux loads in the NSTX-U General Requirements Document (GRD), but the GRD PFC power flux specifications did not accurately reflect planned high current and high power NSTX-U scenarios. The first Extent of Condition (EoC) review in March 2017 recognized changes to PFC designs as one of four high level programmatic decisions and suggested adding real-time PFC protection as an action to increase long-term reliability. As heat exhaust in tokamak plasmas is still an on-going research topic, the NSTX-U Research Director established a Working Group to provide input to the Recovery Project on these matters and established the [PFC Performance and Monitoring Requirements \(PFCR-WG\)](#) in late March 2017. Matthew Reinke (ORNL) was chosen to lead the WG and Michael Mardenfeld (PPPL) was chosen as deputy. The selection of an engineer as deputy emphasized the need to coordinate work between physics and engineering – and this was established as one of the charges. Others include 1) defining parameters to be included in an updated requirements document for NSTX-U

PFCs 2) the generation of updated requirements using reduced models and, ultimately, validated models and 3) to prepare instrumentation plans and operations guidance for integrating PFC monitoring into NSTX-U. Present membership, via an e-mail list, is 40 members, covering engineering, experiment and theory from PPPL, ORNL, LLNL, SNL, University of Wisconsin, University of Washington as well as contributions from MAST-U. Monthly meetings are held and (approximately) weekly update e-mails are distributed, and a portion of the WG is active on a team [Slack channel](#). Work is organized through maintaining a list of open and closed [action items](#) and contributions are generally provided through a series of memoranda, indexed by PFCR-MEMO-#.

The PFCR-WG has successfully provided input to the Recovery Project's PFC design and engineering team as well as coordinated with the NSTX-U TSGs to develop new PFC requirements that capture the science mission. Recommendations on shaping of tiles (PFCR-MEMO-002, PFCR-MEMO-005) and graphite temperature limits (PFCR-MEMO-003) provided important contributions to guide early designs of the inboard divertor horizontal and a new draft of the PFC Requirements document. A simple reduced model (PFCR-MEMO-004, PFCR-MEMO-007) was used along with TSG input to systematically document heat flux, angle of incidence and duration requirements for each region of the PFCs (PFCR-MEMO-008, PFCR-MEMO-009, PFCR-MEMO-010). This was used as input to the new PFC Requirements (NSTXU-RQMT-RD-002) and presented at the Conceptual Design Review in August 2017. This achievement demonstrates NSTX-U now has a traceable and maintainable physics basis for PFC heat fluxes, and ensures that the science mission and sponsor expectations remain linked to engineering requirements.

The WG will continue to support the Recovery Project PFC team through the final design process and into the commissioning phase. Future near-term work will include examining the impact of 3D plasma effects (e.g. error fields) and the impact of finite ion gyroradius on limitations on tile shaping. As the PFC designs mature, concepts for monitoring will be explored, coordinated by the PFCR-WG, building upon initial WG guidance submitted following the first EoC review (PFCR-MEMO-001).

References

- [BPR-MP-1] F. J. Domínguez-Gutiérrez *et al.*, *Nucl. Fusion* **57** (2017) 086060.
- [BPR-MP-2] F.J. Domínguez-Gutiérrez *et al.*, *Journal Applied Phys.* **121** (2017) 215302.
- [BPR-MP-3] F. J. Domínguez-Gutiérrez and P. S. Krstić, *J. Nucl. Mater.* **492** (2017) 56.
- [BPR-MP-4] F.J. Domínguez-Gutiérrez *et al.*, *Nucl. Mater. Energy* 2016, DOI: 10.1016/j.nme.2016.12.028.
- [BPR-MP-5] F.W. Meyer *et al.*, *Nucl. Mater. Energy* 2017, DOI: 10.1016/j.nme.2017.01.013).
- [BPR-MP-6] L. Buzi *et al.*, "Hydrogen retention in lithium and lithium oxide films", to be submitted to *J. Nucl. Mater.* (2017).

- [BPR-MP-7] F. J. Domínguez-Gutiérrez, P. S. Krstić, and Adri C. T. van Duin, "Deuterium uptake and sputtering of simultaneous lithiated, boronized and oxidated carbon surfaces irradiated by low-energy deuterium", to be submitted to *J. Nucl. Mater.* (2017).
- [BPR-MP-8] C.N. Taylor, B. Heim, and J.P. Allain, *J. Appl. Phys.* **109** (2011) 053306.
- [BPR-MP-9] M.A. Jaworski *et al.*, *Fusion Eng. Des.* **112** (2016) 93.
- [BPR-MP-10] F. Bedoya, "Plasma Facing Components Conditioning Techniques and their Correlation with Plasma Performance in the National Spherical Torus Experiment Upgrade (NSTX-U)," Ph. D. Thesis, Department of Nuclear, Plasma, and Radiological Engineering, University of Illinois at Urbana-Champaign

II. Core Science Research Highlights

The Core Science group consists of three topical science groups (TSGs) including: (a) macroscopic stability, (b) transport and turbulence, and (c) energetic particles. Each of these TSG areas is covered as a sub-section in the core science report below.

A. Macroscopic Stability TSG Research Highlights

Macroscopic stability research at NSTX-U in FY2017 was aimed at improving predictive and control capability of MHD and disruptive instabilities in NSTX-U, as well as developing and validating advanced physics simulations in various tokamak devices through collaborations. The DECAF code for disruption forecast was further expanded for MHD mode frequency tracking, sawtooth tracking, and disruption warning near the Greenwald density limit, as successfully tested in TCV and NSTX. A new fast electromagnetic disruption mitigation system is also being developed and well tested in NSTX-U. On disruption physics area, MS TSG led international efforts on halo current dynamics completing database across multiple devices, which indicates substantial halo current in low-frequency rotation possible for ITER. The unique center-stack halo current measurements revealed halo current fraction and toroidal peaking factor relevant for NSTX-U recovery project. MS TSG also led international efforts on error field correction for ITER and successfully conducted experiments in KSTAR, COMPASS, DIII-D, demonstrating a clear negative B_T scaling of error field threshold and also multi-mode characteristics of high-field-side error field. For general 3D physics, collaboration with KSTAR showed the first-time clear demonstration of co- I_p neoclassical offset rotation by electron NTV, implying a great future possibility of rotation shear control. Advanced 3D MHD spectroscopy based on Nyquist diagram has been successfully validated in DIII-D, extending the detecting capability of linear stability. Strong collaborations with General Atomics on classical and neoclassical tearing modes improved the method of NTM identification and analysis in NSTX-U, as well as fundamental tearing mode physics understanding through the verification and validation exercise using a newly developed code such as resistive DCON. See the following sections for each detail.

1. Progress on Disruption Event Characterization and Forecasting (DECAF) Code

The disruption event characterization and forecasting (DECAF) code provides quantitative statistical characterization of the chains of events, which most often lead to disruption of plasmas. DECAF was previously used to characterize a set of NSTX discharges with unstable resistive wall modes (RWM), where it was found that a simple threshold on low frequency poloidal magnetic sensors usually gave RWM timings near the disruption time unless there were minor disruptions and statistics on the disruption event chains provided insight into the typical sequences of NSTX disruptions. Additionally, a reduced kinetic model for RWM stability that calculates the projected growth rate was implemented in DECAF and tested on NSTX discharges [MS-1]. Finally, a DECAF module developed to identify existence of rotating MHD modes was previously reported. It is able to determine mode frequency with a fast Fourier transform (FFT), and to track characteristics that lead to disruption, such as rotation bifurcation and mode locking,

and has been used to analyze both NSTX and NSTX-U discharges. Several important expansions of the DECAF code, as well as further analysis of NSTX-U discharges, occurred in FY17.

(a) MHD Analysis and Expansion to TCV

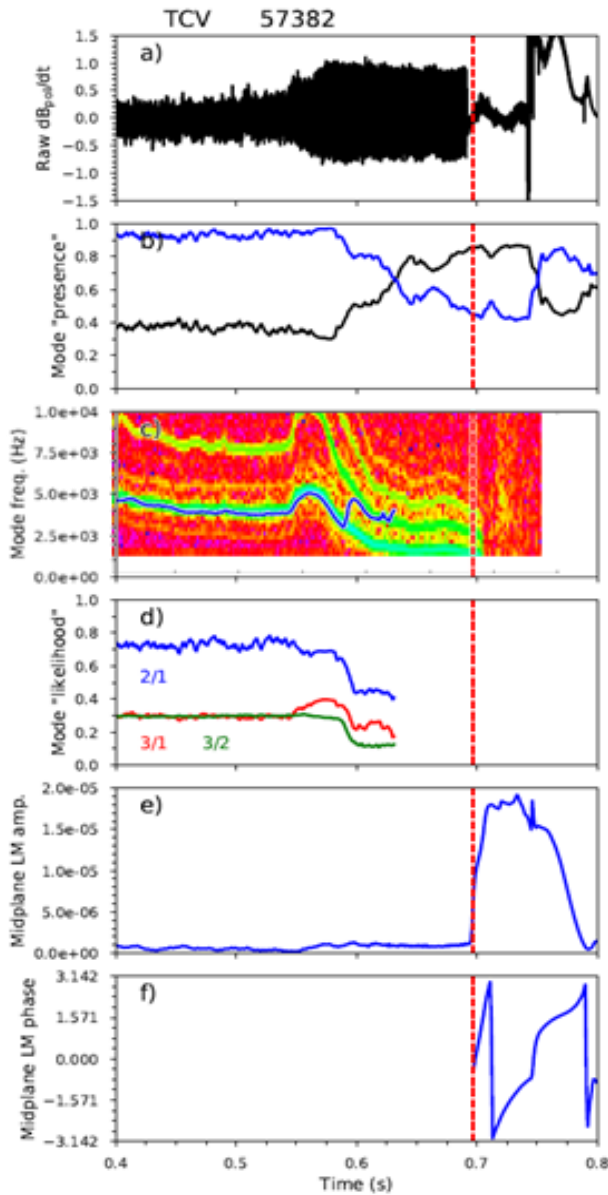


Figure MS-1: MHD analysis signals for TCV discharge 57382 including a) the raw Bdot signal, b) Black: singular value entropy (if it is high there is little phase coherence in the Mirnov signals). Blue: relative magnitude of the first principal axis of the SVD (Higher values indicate the presence of a first mode), c) Frequency of the first mode overlaid on a MHD spectrogram, d) Mode “likelihoods”, e) Midplane locked mode amplitude, and f) Midplane locked mode phase.

Capabilities for phase matching and singular value decomposition algorithms are presently being added to DECAF to automatically determine mode numbers and to track the strongest modes, similar to a real-time MHD analysis capability used in the FTU and TCV devices [MS-2~3]. These algorithms will be general, with the ability to process data from multiple machines.

The DECAF code is written to be flexible, so that in order to use on other machines changes only need to be made to the code control workbooks to specify where to read data from, to turn off certain tests if specific measurements are not available for that device, and to specify threshold levels and warning points which may need to be changed for a new device. The coding in a given physical event modules is not changed, although different modules may be added as appropriate for a given device.

The Tokamak à Configuration Variable (TCV) device is a relatively small tokamak with the major advantage of excellent real-time measurement and control capabilities. The DECAF code has now been used to analyze TCV data with the goal of helping to inform the real-time control approach for disruption avoidance and to develop and test new strategies, warning algorithms, and threshold levels offline.

This work will also benefit NSTX-U by testing MHD analysis techniques and setting them up in the code to operate smoothly when NSTX-U returns to plasma operation.

TCV has a real-time MHD analysis capability [MS-3]. Bandpass filtered fast magnetic signals from Mirnov coils are subjected, in real time, to a singular value decomposition. This is compared to signals from theoretical models of 2/1, 3/1, and 3/2 rotating modes. These are simple, linear screw models that depend only on the plasma z position in real time (theoretically the models could be improved and could depend on other real-time plasma signals). The outputs of the analysis are “presence markers”, “likelihood markers” (likelihood of a present mode being a 2/1 or 3/2, etc...), frequencies of any present modes, and standard odd-n and even-n amplitude signals. Additionally, locked mode amplitude and phase signals from “upper”, “lower”, or “midplane” arrays of 8 saddle loops each on the vessel wall are available. All of these signals have now been read in to DECAF, as shown in Fig. MS-1. The example shows that these signals can give a warning of the mode presence and what type of mode it is likely to be, both useful for disruption avoidance techniques. However, due to a low-pass filter in the algorithm, the frequency of the mode cannot be followed down close to zero to give a warning of impending mode locking. This is indicated in Fig. MS-1c by the frequency signal (blue) not following the post-processed spectrogram mode frequency as it decreases to the point of mode locking indicated by the dashed vertical red line (determined by the midplane locked mode amplitude signal). This limitation was discovered through this DECAF analysis, and plans for alleviating it are under way.

(b) Sawtooth Timing in NSTX-U

Sawtooth oscillations in tokamaks are MHD instabilities of internal kink modes when the safety factor on axis, q_0 , is close to unity. A module has been created in DECAF, which simply monitors the safety factor on axis and issues warnings when it crosses various user-defined levels to provide a warning of the onset of sawteeth. In the future, other tests monitoring the onset of sawtooth oscillations in the D_α signal and their frequency could also be employed.

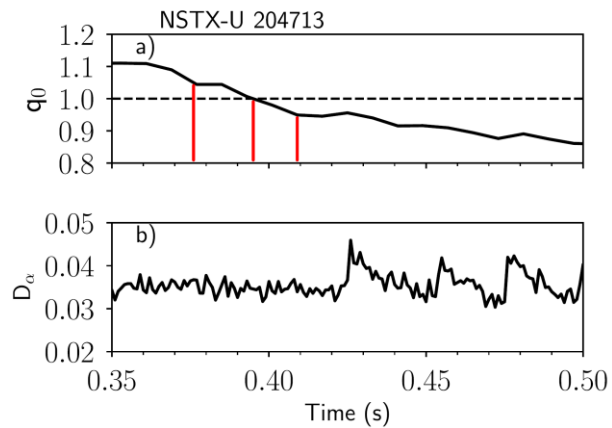


Figure MS-2: a) q_0 and b) D_α signals vs. time for NSTX-U discharge 204713, showing the times of q_0 crossing 1.05, 1.0, and 0.95, and the sawtooth oscillations shortly thereafter.

Reproducible sawtooth discharges that had not been available in NSTX were created in NSTX-U and proved useful to provide evidence that the q profile was being modified by the second, more tangential neutral beam in NSTX-U [MS-4]. Fig. MS-2 shows one such sawtooth discharge in NSTX-U along with the

times of DECAF warnings for levels of $q_0 = 1.05, 1.0,$ and 0.95 . The warnings occur a short time before the onset of the sawtooth oscillation.

A set of 13 NSTX-U discharges with sawteeth was then analyzed, with the timing of the three q_0 warning levels compared to the time of sawtooth onset as determined by manual observation of the $D\alpha$ signal. Fig. MS-3 shows a histogram of the results, indicating that, as expected, $q_0 = 1.05$ generally gave earlier warning, $q_0 = 1.0$ centered around the time of the onset, and $q_0 = 0.95$ was typically later (and in three of the discharges q_0 never reached 0.95). Unfortunately for the NSTX-U discharges analyzed here, only equilibrium reconstructions from magnetic signals were available. Reconstructions with partial kinetic profiles (density and temperature), or with motional Stark effect measurements which help constrain the q profile, were not available. These would almost certainly help to improve the accuracy of the results.

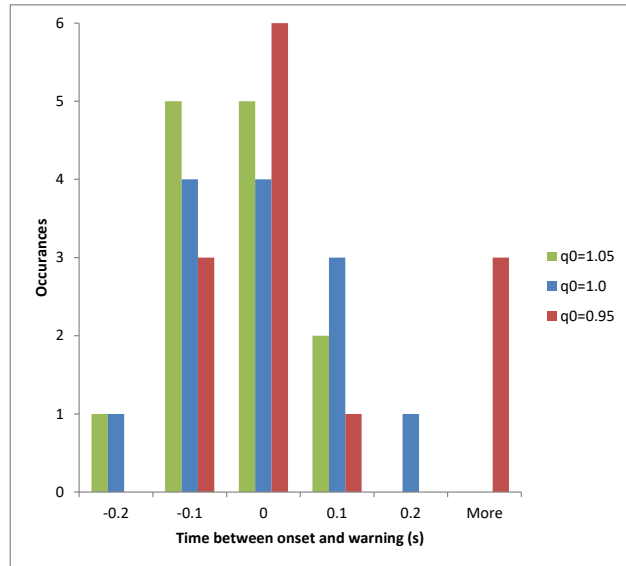


Figure MS-3: Histogram of time between onset of sawteeth and the DECAF warning with various q_0 levels listed. Negative time means the warning came before the actual onset, positive means after.

(c) Greenwald Limit

Threshold tests for the Greenwald density limit were previously implemented in DECAF but failed to capture any instances of the GWL event (at a level of $n_e/n_G = 0.99$, see table 1) in previous analysis of a database of RWM unstable shots (though NSTX has been known to reach densities near the Greenwald limit from its early days [MS-5]). Therefore the GWL event in DECAF has now been further tested with a few discharges from NSTX-U that were seen to experience stored energy collapses with rising densities. Two examples are shown in Fig. MS-4, where the levels of $n_e/n_G = 0.90, 0.95,$ and 0.99 are indicated.

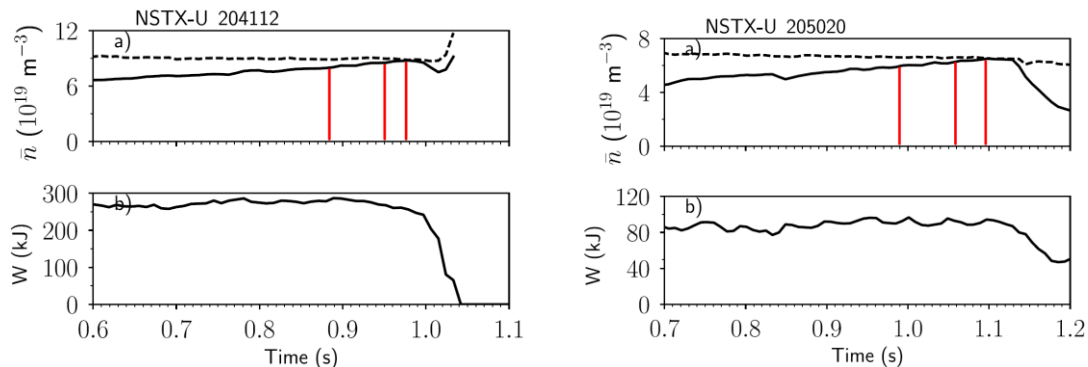


Figure MS-4: Two NSTX-U discharges which experience stored energy (W) collapses (b) following line average density rises (a) up to the Greenwald density (shown in the dashed line). Levels of $n_e/n_G = 0.90, 0.95,$ and 0.99 are indicated by the red lines.

(d) Portable MHD spectrogram analysis for mode discrimination in DECAF

Automated and portable identification of evolving MHD instabilities is a critical advancement in capability for DECAF to intelligently diagnose mode activity for large databases from NSTX/-U and other tokamaks that we have begun to analyze using the code. We have made significant progress in this area by producing a portable, general code to perform magnetic MHD spectrum analysis which can be used to identify and track instabilities. The code is written in the Python language (as is the DECAF code) and can easily be set up to process magnetic toroidal probe data from any desired tokamak. An example of a magnetic spectrogram generated by this code for an NSTX shot is shown in Fig. MS-5. The code uses singular value decomposition for noise rejection and discriminates toroidal mode numbers by magnetic signal phase matching. Present development of the DECAF code in using this new MHD analysis information includes MHD event identification including discrimination of separate modes and their evolution – whether they stabilize, or grow and evolve toward a rotation bifurcation point, mode locking and disruption. This completed task is a critical milestone that now allows automated analysis of large tokamak databases to characterize the disruptions events based on the MHD mode activity leading to disruption. This is also a required step for the validation of forecasting these dynamics with DECAF.

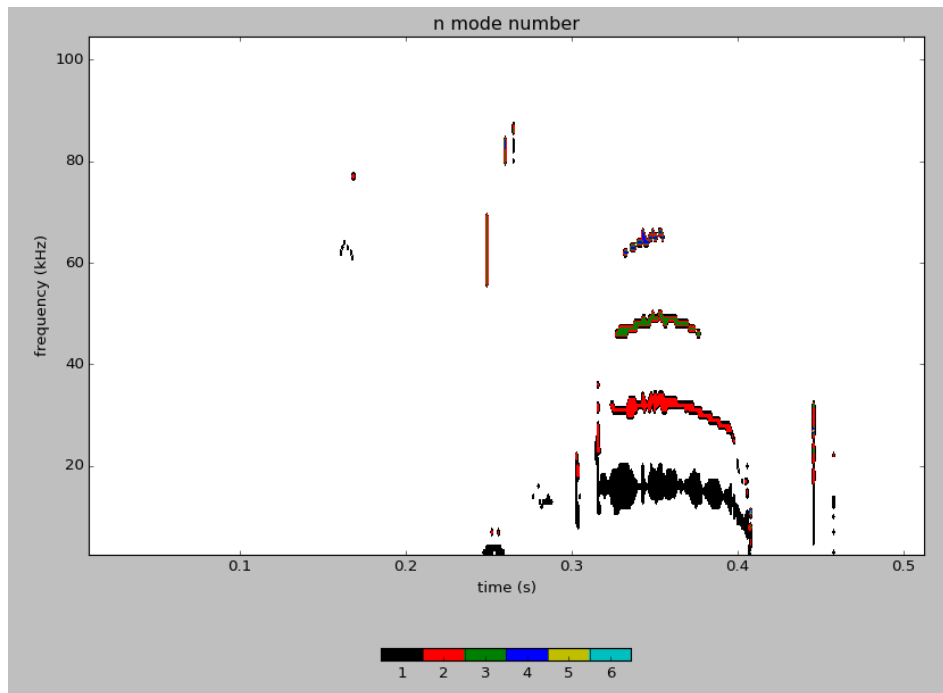


Figure MS-5: Toroidal mode number discrimination based on magnetic MHD spectrum analysis generated by a new, portable and automated module for the DECAF code.

2. Development of a Fast Time Response Electromagnetic DM System

The warning time for the onset of some disruptions in ITER and next step tokamak and ST based systems could be less than 10 ms. None of the currently planned disruption mitigation systems for ITER can respond on this short time scale because the radiative payload propulsion systems rely on the sound speed in gas which is limited to about 300 to 400m/s. Some other complex faster acting systems have been suggested, that rely on plasma for payload acceleration, and although these could respond on a fast time scale, the accelerating plasma needs to travel through long distance in intense magnetic fields, which would make the application of such systems for DMS applications questionable.

During 2016, we reported that much of the hardware to test a novel system, referred to as the Electromagnetic Particle Injector (EPI), that can address this critical need for ITER and future

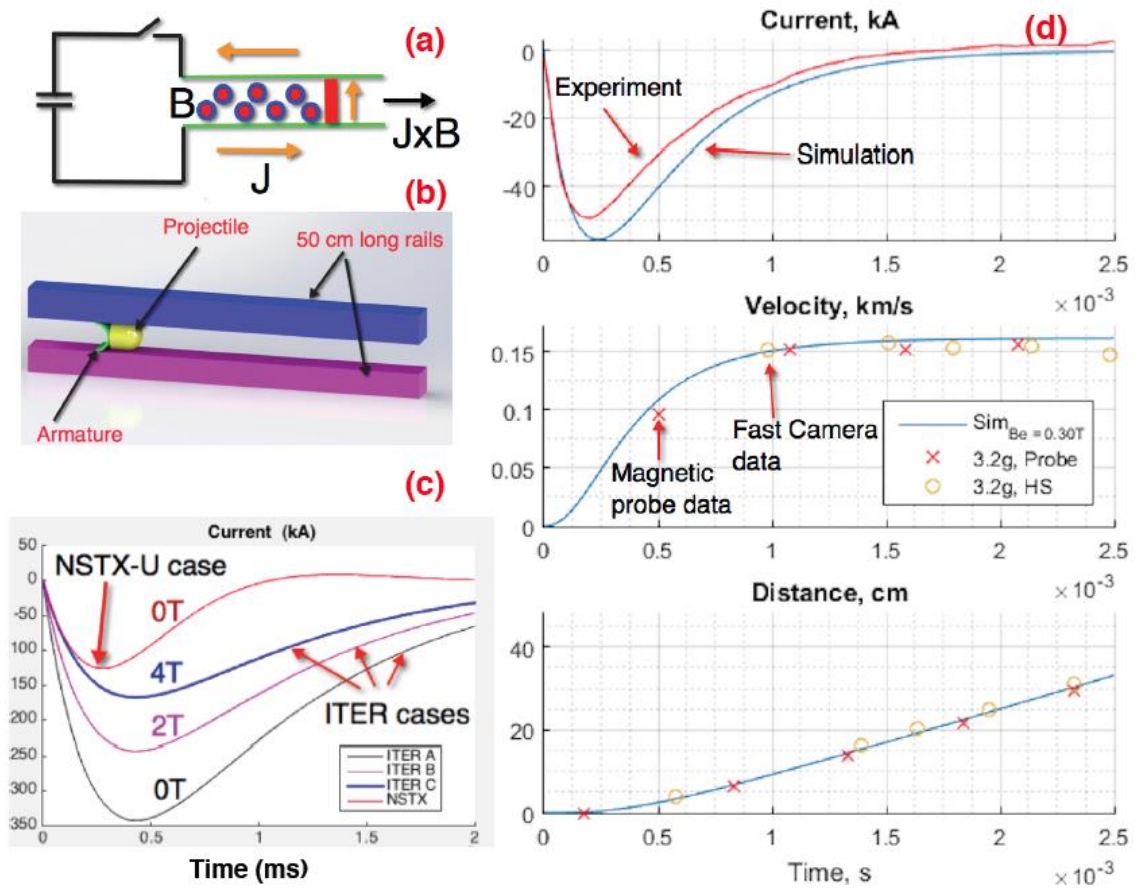


Figure MS-6: Shown are: (a) Cartoon showing rail gun operating principle, (b) physical arrangement of rails and armature. The armature (or the sabot) is captured, and the projectile, which consists of numerous small sized spheres of the payload, is injected in to the plasma. (c) Calculations for an ITER-scale injector showing the dramatic reduction in the accelerating current with increased external magnetic field augmentation. (d) Shown on the right are experimental results from a University of Washington off-line experiment showing attainment of 150m/s velocity for a 3.2g mass within 1.5ms after the system is energized, consistent with the calculated parameters.

Tokamak / ST based devices was in place at the University of Washington. What is important for DMS applications is whether a rail gun based system could be made small enough to accelerate 10g sized payloads, with a 2-3ms response time. We have now operated this NSTX-U scale system and have been able to verify the most important parameters; the system response time and the attained velocities. As shown in Fig. MS-6, both are consistent with the model calculations, giving confidence that larger systems can be built to attain the target goals.

The EPI system does not rely on any form of plasma for acceleration, so it is immune to external magnetic fields. In fact, close installation to a reactor actually takes advantage of the free external fields to increase the EPI system efficiency, and response time, as described in Reference [MS-6].

3. Progress on Halo Current Study

(a) ITPA analysis of non-axisymmetric and rotating halo currents (ITPA MDC WG-6)

Large halo currents are often driven in the metal components of a tokamak vessel when a disrupting plasma comes into contact with the first wall. Halo currents are known to exhibit non-axisymmetric and rotating features in several devices including JET, Alcator C-Mod, DIII-D, ASDEX Upgrade, and NSTX. Such non-axisymmetries are of great interest to ITER because they can increase mechanical stresses during a disruption, especially if the rotation resonates with the natural frequencies of the vessel. As such, the ITPA MHD, Disruption, and Control Topical Group has formed a working group to conduct a multi-machine analysis of these phenomena. This working group (ITPA MDC WG-6) is led by researchers on the NSTX-U team. In FY17, a collaborative visit to JET resulted in the addition of hundreds of JET discharges to the database. These encompass both carbon wall and metal ITER-like wall operations. With the addition of the JET data, the ITPA halo current rotation database now spans a wide range of spatial scales and toroidal field strengths and is considered to be complete. The data have been analyzed, and the results have been submitted for publication [MS-7].

Fig. MS-7 shows eight representative halo current measurements from the five devices in the ITPA halo current rotation database. These data are obtained from toroidally resolved arrays of halo current sensors that are comprised of either shunt tiles or segmented Rogowski coils. In each panel of the figure, the halo current amplitude, I_h , is plotted in color as a function of time and toroidal angle. The timebase is normalized to the characteristic minimum quench timescale for each device, τ_{CQ} . The black lines represent the toroidal phase of the rotating halo current lobe. It is clear that significant non-axisymmetries and rotation are observed in each device. Furthermore, a similar range normalized rotation frequencies are observed across devices.

The primary objective of this work is to use the ITPA halo current rotation database to understand how rotating halo currents are expected to behave in ITER. In particular, the question is whether the forces that the halo currents generate are likely to be dynamically amplified, which can occur if the halo currents complete 2–3 full rotations at the resonant frequencies of the major machine components. For ITER, the critical resonant frequencies are in the range of 3–8 Hz, though integrated system resonances can stretch into the 10–20 Hz band. It is therefore important to

develop scaling for the number of halo current rotation to expect at rotation frequencies below 20 Hz in ITER.

The parameters required to assess halo current rotation can be extracted by tracking the duration and rotation of the halo currents in each discharge in the ITPA halo current rotation database. The two most important parameters are the rotation duration, t_{rot} , and the number of rotations, N_{rot} . These two parameters can in turn be combined to give a third parameter of interest: the average rotation frequency, $\langle f_{\text{h}} \rangle = N_{\text{rot}}/t_{\text{rot}}$. The extracted parameters for the examples in Fig. MS-7 are listed in the top left of each panel. The database-wide results, on the other hand are collected in Figure MS-8.

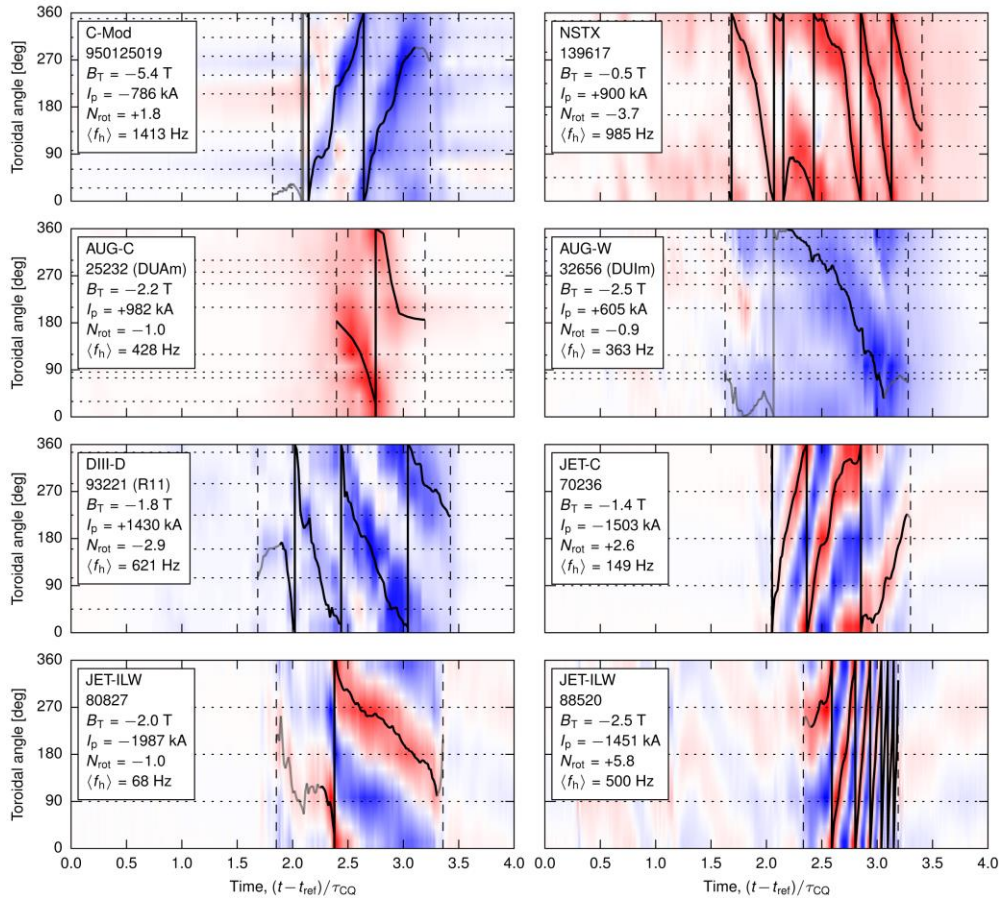


Figure MS-7: Toroidally resolved measurements of non-axisymmetric and rotating halo currents in five different devices. Color represents the halo current magnitude, while the black lines track the toroidal phase of the rotating halo current lobe. Time is referenced to an arbitrary time, t_{ref} and normalized to the characteristic fast quench time for each device, τ_{CQ} .

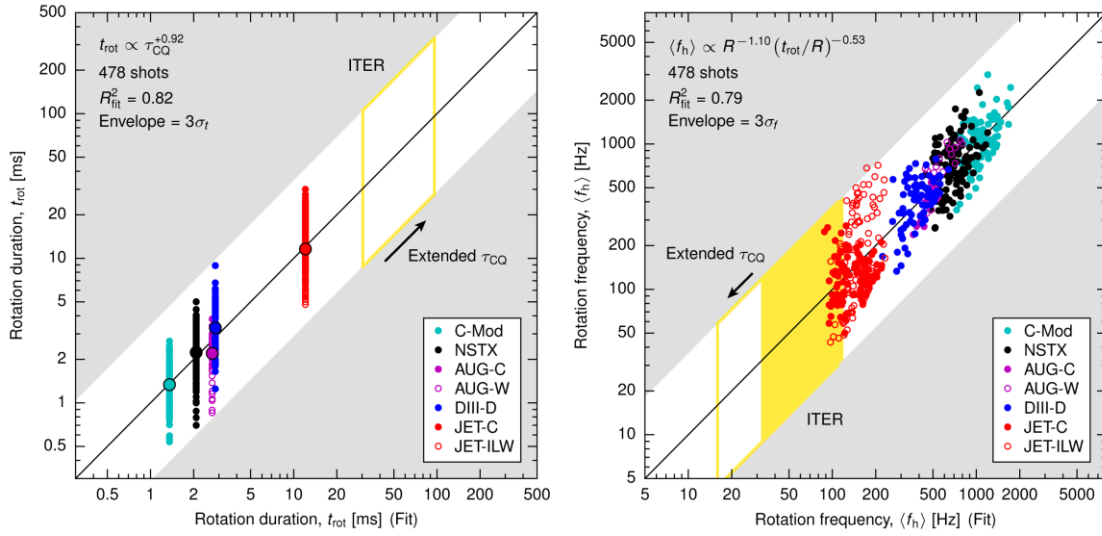


Figure MS-8: Scaling of the rotation duration, t_{rot} , and the average rotation frequency, $\langle f_h \rangle$, as determined from the ITPA halo current rotation database. The rotation duration scales nearly linearly with the minimum current quench time, τ_{CQ} , while the rotation frequency scales (to first order) with the inverse major radius. Both panels include ITER projections based on its major radius and expected fast current quench time.

The empirically determined halo current rotation scaling for two key parameters, the rotation duration, t_{rot} , and average rotation frequency, $\langle f_h \rangle$, are shown in Fig. MS-8. Here, t_{rot} is found to scale nearly proportionally the minimum quench time, τ_{CQ} . This minimum quench time is extrapolated using the ITPA current quench scaling of Wesley et al. [MS-8]. The rotation frequency, on the other hand, is found to scale to first order with the inverse major radius, R . The second factor in the scaling, t_{rot}/R , varies weakly from machine-to-machine. A rotation frequency that varies with R^{-1} implies a consistent rotation velocity from machine-to-machine. The fact that machines ranging in size from C-Mod to JET exhibit comparable rotation velocities is surprising and provides motivation for renewed theoretical and numerical work on the mechanisms that drive halo current rotation. An additional result is that the halo current rotation parameters do not change substantially from carbon to metal wall machines. This is a positive result for ITER given the propensity for long current quenches in metal wall machines.

The ITER projection on in the right-hand panel of Fig. MS-8 indicates that halo current rotation below 20 Hz is to be expected in some ITER disruptions. The remaining question, then, is whether the halo currents rotating below 20 Hz are likely to complete the 2–3 full rotations required to dynamically amplify the halo current forces. To answer this question, the N_{rot} versus t_{rot} parameter space for each machine in the database and for ITER are plotted in Fig. MS-9. The shaded parallelograms in the figure represented the projected halo current rotation parameters based on the scalings developed here, while the individual dots represent that data upon which the scalings are based. The resulting ITER projection (bottom right-hand panel) indicates that we cannot rule out the possibility of halo currents completing 2–3 rotations below 20 Hz. This is especially true if the minimum current quench time, τ_{CQ} , in ITER is found to be at the long end of its projected range.

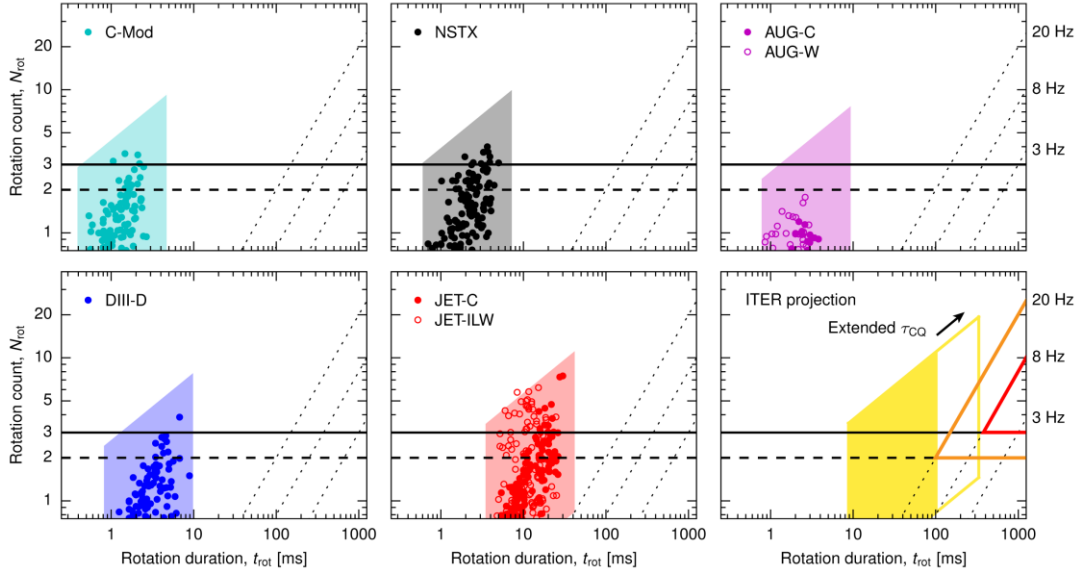


Figure MS-9: Halo current rotation in the N_{rot} versus t_{rot} parameter space. The parallelograms represent the projected halo current rotation parameters based on the scalings developed from the ITPA database, while the individual dots represent the data upon which the scalings are based. The ITER projection is shown in the bottom right-hand panel (see the text for further details).

(b) Halo current measurements in the NSTX-U center-stack

During the FY16 experimental campaign, NSTX-U acquired first-of-a-kind measurements of the halo currents that are driven in the center-stack of a spherical torus during a disruption. The diagnostics that collected these measurements are (1) an array of 18 shunt tiles mounted on the first wall of the center-stack casing; and (2) an array of ‘rotated’ mirnovs at the center-stack midplane that acts as a segmented rogowski coil to measure currents flowing vertically in the center-stack casing. Both of these halo current sensor arrays were instrument for the FY16 campaign, and halo current data from both the shunt tiles and the rotated Mirnovs was successfully acquired.

In FY17, the NSTX-U center-stack halo current data have been analyzed in support of the NSTX-U Recovery Project. More specifically, the data have been used to inform the halo current force specification for the center-stack first wall. As one example, Fig. MS-10 shows a comparison of the halo currents measured at the center-stack midplane (y -axis) with the currents flowing through the CHI bus at the bottom of the machine. This plot reveals the distinct signatures of three different types of disruptions: In upward-moving vertical displacement events (VDEs), for example, currents of the same sign circulate through both the CHI bus and the center-stack midplane as they complete a full poloidal transit of the vessel. In downward VDEs, on the other hand, outboard-to-inboard (negative) CHI bus currents are measured as the plasma drives into the bottom of the machine. Finally, in center-stack limited disruptions, strong midplane currents with very little corresponding CHI bus current are measured as the plasma drives laterally into the center-stack (see the diagram on the left in Fig. MS-10). These discharges produce circulating currents that enter and exit the center-stack casing and are therefore measured by the center-stack

shunt tiles (not shown).

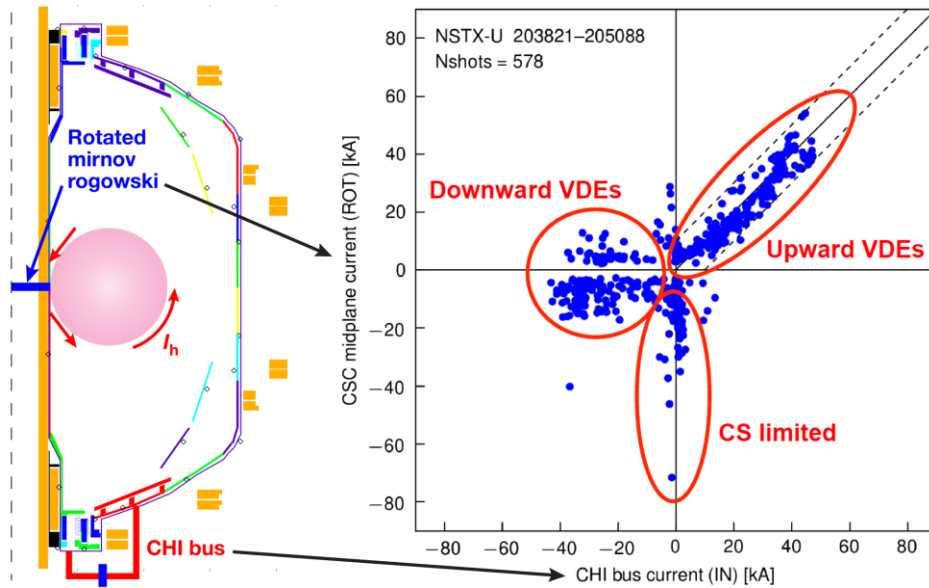


Figure MS-10: Comparison of halo current measurements from the center-stack midplane and the CHI bus in NSTX-U. Three different types of disruptions (labeled in red in the right-hand panel) produce different signatures (see the text for more detail).

The NSTX-U center-stack halo current measurements have been used to show that the halo current fraction, I_h/I_p , was limited to less than 10% in the FY16 campaign. Furthermore, these data indicate that the toroidal peaking factor, which quantifies the amount of toroidal asymmetry in the halo current pattern, was limited to $TPF < 2$ in disruptions that produce substantial halo current entering and exiting the center stack shunt tiles. These findings have been used to generate a halo current specification for the NSTX-U Recovery Project that provides guidance on the halo current forces at the full operating parameters of NSTX-U ($B_T = 1$ T and $I_p = 2$ MA).

4. Progress on error field correction and physics studies

(a) Error field threshold scaling across devices for ITER

The prediction of error field threshold is a critical issue for ITER to develop error field correction (EFC) strategies to avoid disruptive core MHD events during operation. Presently ITER is adopting two EFC criteria, one based on vacuum superposition (3-mode) [MS-9] and the other based on ideal plasma response (overlap) [MS-10]. In both, the goal is to compensate core resonant field that can penetrate and drive locked modes when large enough to hit a threshold. It has been a strategy for ITER to keep both and prepare EFC for whichever is lower in locking thresholds, but there was an increasing demand from the community to replace the misleading vacuum method by an alternative if needed. As ITER is expecting a finalized design of EFC coils in a few years, ITER organization requested the community a comprehensive physics review with 3 charge questions. This review was led by NSTX-U and PPPL, as a part of MDC-19 international activity in ITPA MHD group, answering the charge questions as well as identifying

new research area as follows. The complete document can be found in ITER IDM (ITER_D_UMLSUW) [MS-11].

Q1: Should ITER continue to use the “3-mode” and the “overlap” criteria?

The 3-mode metric must be retired. It is not based on a coordinate-independent quantity, and is not physically correct for layer dynamics or MHD equilibrium physics. Compared to the overlap metric, the 3-mode criterion can be highly misleading as is shown by EFC efforts and explicit compass scans in DIII-D and in phasing dependence scans in KSTAR [MS-12], EAST [MS-13], and MAST [MS-14]. No parametric correlation across devices has been successfully made for this misleading criterion.

Q2: Should ITER use only the “overlap” (resonant) criterion?

The overlap field is the best available metric for core resonant (CR) field minimization. The ideal CR overlap has applied and tested on many machines, and an updated parametric scaling was completed in 2012 [MS-15]. However, the reliability of various overlap metrics as well as alternative metrics must be investigated. The single-mode overlap metric has been widely successful in machines with low-field side EF sources for which the drive for each of the core rational surfaces is well coupled [MS-11,16,17]. Inboard EF sources, as highlighted by recent NSTX-U (See R17-3) and COMPASS research [MS-18] (See Sec. 4(b)), have the potential to decouple core rational surfaces. In this case, the component of the EF coupled to the 2/1 surface represents the preferred single mode “overlap” metric. The parametric scaling for field penetration is less reliable, and should be further developed over global locked-mode database (See Sec. 4(c) for new B_T scaling in DIII-D national campaign). The interplay among operating parameters should be understood, as exemplified by weak density correlations in EAST and KSTAR, by β scaling across the no-wall limit in NSTX and DIII-D, and by strong rotation scaling seen in multiple devices [MS-19] (See Sec. 4(b) for new KSTAR studies). Advanced modeling with GPEC, MARS, and M3D-C1 must also be tested to move beyond ideal MHD and develop a predictive capability. To facilitate these advances, it is critical to build an open toolkit and locked-mode database for efficient validation and verification efforts.

Q3: Are non-resonant $n=1$ error fields important for plasma performance (e.g. plasma rotation, L to H mode transition, energy confinement in H-mode), even if at present we have not numerical criterion? If so, should we keep capability of simultaneous reduction of resonant (“overlap”) and non-resonant $n=1$ error fields (e.g. error fields caused by misalignments of CS and TF coil inner legs having very small “overlap” amplitude)?

The residual EF with no CR includes edge resonance (ER) as well as non-resonant (NR) fields, which must be distinguished for each n . TBM mock-up experiments in DIII-D implied the $n=1$ CR overlap field was the only component of the EF with a significant impact on locking in Ohmic plasmas [MS-20], but experiments in KSTAR implied that higher- n residuals can change the $n=1$ locking threshold [MS-11]. The necessity of non-resonant $n=1$ EFC can be better concluded by new experiments, for example, in COMPASS with new high-field side (HFS) EF coils. In H-modes, DIII-D shows that the residual EF is highly NR and can only slightly degrade

rotation. The isolation of CR, ER, NR fields is difficult for $n=1$ but could be important to understand the diversity of impacts. KSTAR also shows that the pure $n=1$ NR fields would change only rotation but small ER can degrade particle and energy confinement, which may be predictable with the use of torque metrics (See Sec. 4(d)). ITER should consider higher $n>1$ EFC (See Sec. 4(c) for new $n=2$ scaling in DIII-D national campaign). Consider the $n=2$ field at minimum, which has been shown to behave similar to the $n=1$ component. In general, the residual EFC must be studied along with resonant magnetic perturbation (RMP) and neoclassical toroidal viscosity (NTV) physics studies. The EF can also change L-H transition thresholds as shown in KSTAR, but the impact of the residual EF without CR remains to be isolated.

Additional Q4): Is there any evidence indicating the utility of ITER EFC Top and Bottom coils?

As of yet, there is no evidence indicating that the ITER EFC top and bottom coils will have utility in correcting EFs to prevent locking and disruption. Compared to the midplane EFCM, the top and bottom EFCT/B coils are 10% as effective at EFC as measured by multiple overlap metric in average across 3 different ITER scenarios. The metrics include the standard dominant mode overlap as well as higher order SVD modes based on both core coupling and full coupling matrices for both $n=1$ and $n=2$. The inefficiency of EFCT/B can be also seen by vacuum superposition, when the proper geometric weighting is used rather than the 3-mode. The 2010 IPEC ITER report showed that EFCT/B + EFCM can reduce NTV more than EFCM alone, but not generally better than the small use of RMPU/L + EFCM. However, The assessment of CR/ER/NR correction capability by each of EFCT/M/B and RMPU/M/L must be revisited along with new research progress, and so the conclusion for this question will be deferred to then.

(b) Extended collaboration for $n=1$ error field in COMPASS and KSTAR

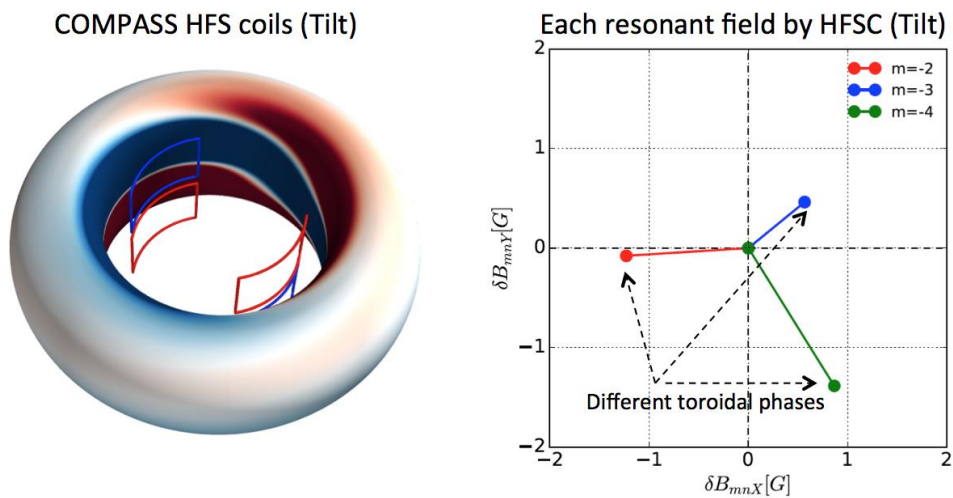


Figure MS-11. HFS tilt coil configuration in COMPASS tokamak and normal field on the boundary surface due to ideal plasma response (left). The field creates 2/1, 3/1, 4/1 resonant fields driving islands in all very different toroidal phases, similarly to what is shown by NSTX-U TF error fields (right).

Motivated by new MDC-19 review efforts and by NSTX-U TF error field studies, NSTX-U MS group collaborated with COMPASS research team to further understand and test error fields coming from the high field side (HFS) [MS-18]. COMPASS resumed HFS control coils to generate an $n=1$ “TF-tilt like” (Tilt) error field as well as “TF-shift like” (Displacement) error field. As predicted by IPEC overlap field criterion, there is no significant effect observed with the Displacement error field even with the maximum current 4kA. However, the standard IPEC overlap field based on the full resonant coupling matrix was not successful to predict the error field threshold by Tilt error field either, due to the strong decoupling between core and edge resonance. See Fig. MS-11 and different toroidal phases in each resonant field. This characteristic is similar to what’s seen from NSTX-U TF (See Fig. R17-3-14), indicating that the local resonant decoupling may be universal in HFS EFs. On the other hand, IPEC overlap field based on the core-only resonant coupling could predict locking thresholds successfully. One can see from Fig. MS-12 that the core-only coupling prediction by IPEC (black dots) becomes more consistent with the measured error field thresholds (red dash dots). IPEC tends to overestimate the threshold in higher density due to β_N scaling, which may or may not be relevant in Ohmic or L-mode plasmas. Recently COMPASS added more power supplies to operate LFS coils together with HFS coils, and so will explore the parametric scaling as well as the possibility of individual control of each resonance in more detail.

NSTX-U also collaborated with KSTAR research team to understand the mysteriously weak density correlation in KSTAR error field studies. As seen in other devices, rotation is found to be an important hidden physics parameter to change such an operating parametric dependence. Fig. MS-13 shows 3 different L-mode KSTAR discharges in the same level of density but with different rotation by beam modulation. One can see clearly see that the $n=1$ error field threshold increases when rotation is stronger with more injection torque. This NSTX-U and KSTAR collaboration on EFs also demonstrated the direct $n=2$ locking in KSTAR for the first time, as well as strong negative B_T scaling as is also found in DIII-D national campaign. All of these results will be combined into multi-device error field threshold scaling for $n=1$ and $n=2$ and will provide new EF physics bases for ITER.

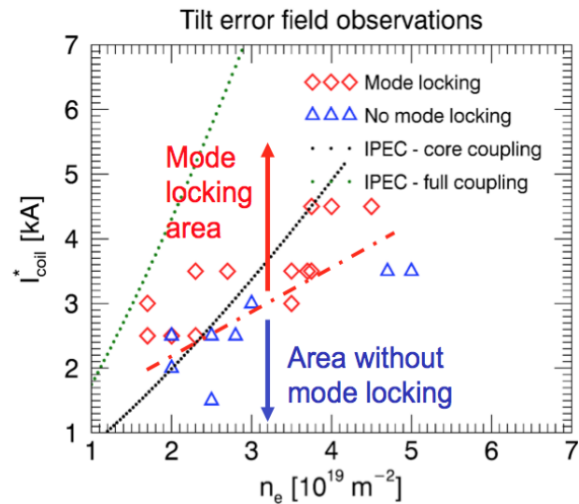


Figure MS-12: IPEC core and full coupling prediction vs. experiments on $n=1$ error field thresholds

(c) Toroidal field and spectrum dependence of the $n=2$ locking threshold in DIII-D

Collaborative experiments were conducted as part of the FY17 DIII-D National Campaign to explore the effect of the toroidal magnetic field and or the error field resonance spectrum on the $n=2$ locking threshold. These experiments are relevant to NSTX-U given that, as presented in the FY16 year-end report, evidence of a sizeable intrinsic $n=2$ error field was observed during the

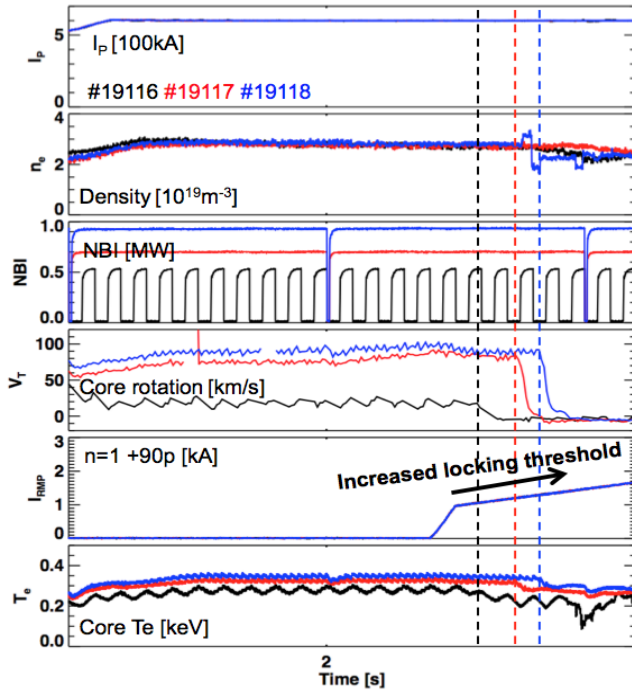


Figure MS-13. KSTAR 3 L-mode discharges and error field applications showing the increased threshold due to higher rotation.

FY16 commissioning campaign. An important question, then, is whether the outboard midplane coil array in NSTX-U is sufficient to correct this $n=2$ error field, or whether more capacity to tune the resonant spectrum of the applied fields is required. A broader application for the study of $n=2$ locking is to inform the error field correction (EFC) strategy for ITER. In particular, ITPA MDC-19 is a task force dedicated to understanding the EFC requirements for ITER. As indicated in a recent ITPA MDC-19 report to ITER, one of the open questions is whether ITER should consider $n=2$ EFC, which is not presently addressed with its planned EFC coil configuration [MS-11].

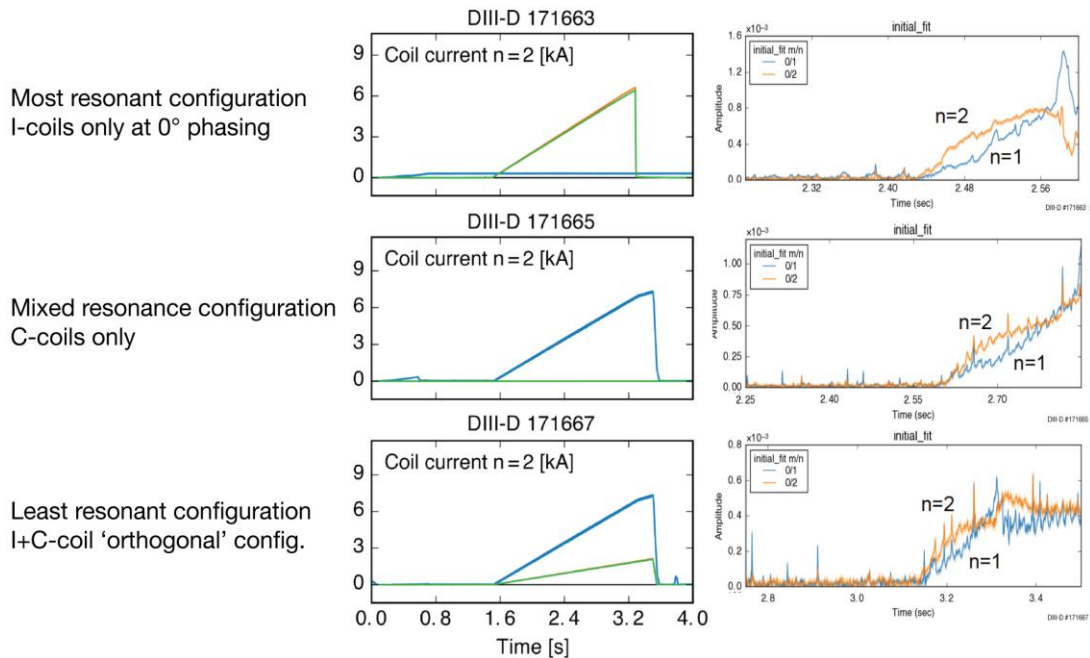


Figure MS-14: Evidence of $n=2$ locking events generated by externally applied $n=2$ fields from sources with three different field resonance spectra. In all three cases, the applied field ramp shown in the left-hand column eventually generates an $n=2$ -dominated locked mode shown in the right-hand column. Note that the locking time varies with the amount of applied resonant field, with the most resonant configuration locking first (2.43 sec vs. 2.61 sec vs. 3.14 sec).

The DIII-D National Campaign experiments first demonstrate that $n=2$ locking can be generated with three different applied field resonance spectra. As shown in Fig. MS-14, a clear $n=2$ -dominated locking signature (left panels) is generated as the $n=2$ applied field coil currents are ramped in time (left panel). The fact that the plasma can be locked in all three resonance configurations indicates that $n=2$ error fields can be corrected with a variety of resonance spectra. The locking time varies with the amount of applied resonant field, however, with the most resonant configuration locking first. Not shown in Fig. MS-14, however, is that substantial non-resonant braking was observed in the least resonant configuration, indicating that the resonance spectrum does generate second-order effects on the plasma performance.

A detailed scan of the $n=2$ locking threshold as a function of toroidal field strength was also conducted during the DIII-D National Campaign experiments (see Fig. MS-15). Here, four different scans of toroidal field strength were carried out, each with different applied field spectra or neutral beam injection parameters. In all cases, the normalized $n=2$ locking threshold declines rapidly with increasing toroidal field. Changes to the field resonance spectrum (C-coils versus I-coils) and the fast particle population (Ohmic versus L-mode) also show marked changes in the locking threshold, with the maximum resonant ohmic case (blue dots) locking the most easily and the mixed resonance L-mode case (magenta squares) locking the least easily. The conclusion that the locking threshold decreases with increasing B_T is similar to the understanding of the $n=1$ locking threshold [MS-11]. These results have implications for $n=2$ EFC in NSTX-U given that the toroidal field will be increased to $B_T=1T$ when operations resume. It also indicates that an $n=2$ EFC strategy should be considered for ITER given its similar behavior to $n=1$ fields.

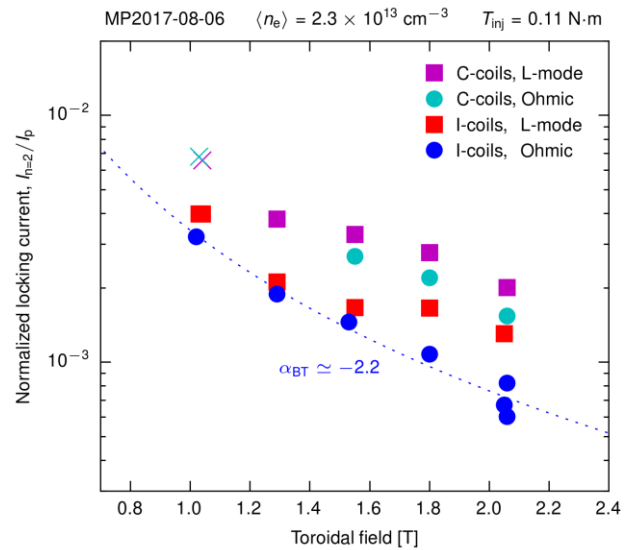


Figure MS-15: Toroidal field dependence of the $n=2$ locking threshold in DIII-D. As the toroidal field increases, the locking threshold sharply decreases. The plasma is easier to lock with the I-coils (most resonant), and a small amount of injected neutral beam power (100 kW) meaningfully shifts the locking threshold upward.

(d) Non-resonant error field effects in KSTAR

Error field correction to avoid core MHD often leaves substantial amount of residual fields. The residuals can not only degrade momentum confinement and modify rotation, but also can degrade particle and energy confinement. These fields could be totally non-resonant but also resonant with the plasma edge, as can be categorized roughly by core-resonance (CR), edge-resonance (ER), and non-resonance (NR). See the reference [MS-11] for their subtle differences. Generally it is difficult to decouple ER from CR or NR, particularly for $n=1$ due to strong Kink response. As described earlier, NSTX-U and COMPASS studies implied that HFS coils might provide better

chances to isolate each resonance in the future. It is still possible to achieve some degree of separation when the multiple rows of coils are available in LFS. This is a motivation to the off-midplane non-axisymmetric control coils (NCCs) in NSTX-U and to the strong collaboration with KSTAR to utilize their unique 3 rows of internal coils.

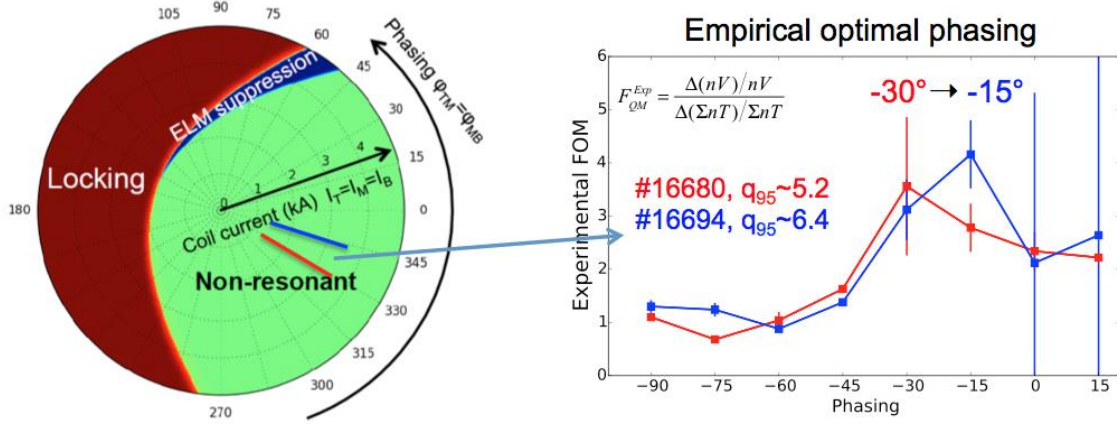


Figure MS-16: Stability and utility diagram in the KSTAR standard coil configuration space (left). The figure on the right shows the empirically determined figure of merit for quiescent magnetic braking, by measuring the ratio of momentum to energy degradation.

Recent KSTAR collaboration for $n=1$ field applications illustrated these challenges and opportunities. The diagram on the left in Fig. MS-16 shows the IPEC predicted utility of $n=1$ fields in KSTAR on a map of the coil current and phasing. Recent studies in KSTAR demonstrated a remarkable accuracy of this diagram's predictions [MS-21]. The red region delineates predicted CR locking thresholds, the blue region represents predicted ELM suppression using an empirical ER threshold, and the green region is for residual effects such as momentum or energy degradation. Again it is difficult to separate ER from CR with LFS coils, but there is narrow margin where the ER fields are large enough for ELM suppression while the CR fields are not enough to hit locking thresholds. Note also that the green region is not only purely NR but also may contain significant CR or ER components below their respective thresholds.

One possible way to quantify the residual effects, and to build non-resonant EFC criteria, is to relate a physical ER and NR metric (for example, $T_{j \times B}$ or T_{NTV}) to density and momentum confinement degradation through empirical scaling;

$$\Delta(nT) \propto f(\delta B_{m1}^{ER} \text{ or } T_{j \times B}^{ER})$$

$$\Delta(nV) \propto g(\delta B_{m1}^{All} \text{ or } T_{NTV}^{All})$$

The ratio of momentum degradation to energy degradation in experiments is a good figure of merit for purely NR braking, referred to as quiescent magnetic braking. The plot on the right of Fig. MS-16 shows the most non-resonant $n=1$ phasing for two different q_{95} targets, measured by this empirical figure of merit, $F_{QM}^{Exp} \propto \Delta(nV)/\Delta(nT)$. One can see that the two most non-resonant phasings are both located near the center of the green zone. They also qualitatively

agreed with a figure of merit based on the torque metric, $F_{QM}^{Model} \propto T_{NTV}^{All}/T_{j \times B}^{ER} \propto T_{NTV}^{All}/\delta B_{m1}^{ER^2}$. Still, these are only the initial results from one machine. Serious commitments are needed from the community if quantitative and robust ER or NR EFC criteria are desired to minimize any of the residual effects in ITER. There is great potential in this effort, as the subject of the residuals clearly has strong linkages to RMP ELM control and NTV physics.

5. Progress on general 3D physics studies

(a) Observation of the generalized neoclassical toroidal viscosity offset rotation in KSTAR

As part of our collaboration on neoclassical toroidal viscosity physics on the KSTAR device, we have observed for the first time the generalized neoclassical toroidal viscosity offset rotation profile in which plasma rotation was increased in the direction of I_p (co- I_p direction). Plasma rotation provides improved stability and confinement in contemporary tokamak plasmas utilizing unbalanced neutral beam injection. However, tokamak devices aiming to produce high fusion power output, including ITER, are expected to rotate much more slowly due to relatively small levels of momentum injection and larger plasma mass compared to present machines. Therefore methods of producing and altering plasma rotation on these devices are highly desired. Understanding how plasmas intrinsically rotate is of primary interest to confidently extrapolate this effect to ITER-scale plasmas as it may provide significant rotation. NTV physics also provides the potential for providing a form of intrinsic rotation in tokamaks such as ITER that can apply low-level non-axisymmetric fields to the plasma. This effect, typically referred to as the NTV “offset rotation” in the literature [MS-22,23] may supplement other forms of plasma intrinsic rotation, or potentially provide the main rotation. The effect also has the potential of providing significant rotation shear in the plasma, a profile characteristic that is generally stabilizing for MHD modes. An important advantage of this effect is that it is controllable by varying the strength of the non-axisymmetric field. If sufficiently strong, this rotation and its shear could provide stabilization and improved performance in ITER and future devices.

Research to date has identified this affect in the DIII-D tokamak [MS-24] with evidence of it also noted in experiments on TCV [MS-25], yet important questions remain. In the DIII-D study, the total injected NBI torque, T_{NBI} , was attempted to be kept low to measure the offset rotation by making best efforts to balance the torque of the injected sources, but it is not possible to do this exactly for the entire profile, even if the NBI is set up to provide zero global net input torque. Both the NBI and NTV torques have radial profiles (especially important to determine flow shear), so aiming to have global net input torque of zero is not sufficient to ensure zero NBI torque across the plasma radius. Since the local NBI torque at a given point along the plasma radius can be significantly larger than the torque due to the NTV offset rotation *profile*, T_0^{NTV} , measuring this profile in these conditions is subject to error. Such plasmas can also have significant intrinsic rotation, V_I , from other sources which must be handled in the analysis. Analysis has been conducted on DIII-D to best handle these significant sources of error in torque balance calculations of the intrinsic rotation. Non-NTV-induced intrinsic rotation is found to be equivalent to the rotation driven by one full power neutral beam source [MS-26]. Both experimental studies also introduce some element of modeling to describe an important

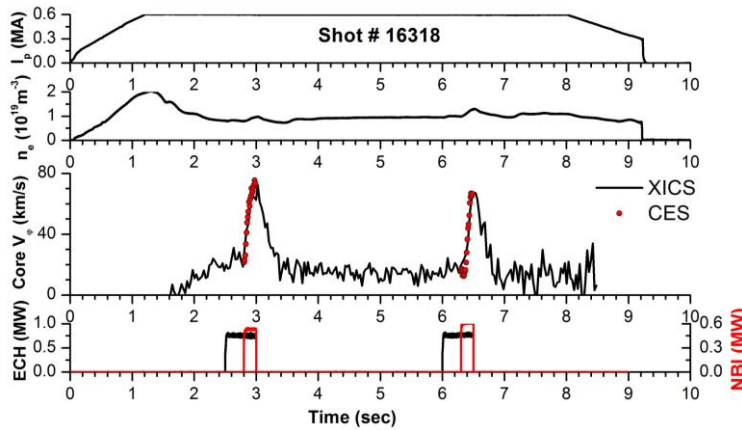


Figure MS-17: Target plasma experimental setup for measurement of the NTV offset rotation profile (3D field not applied).

V_0^{NTV} , being proportional to ∇T_i . However, more complete NTV theory allows for torques generated by both the ion and the electron channels, the balance of which yields the total V_0^{NTV} profile [MS-27]. Recent experiments conducted on the KSTAR superconducting tokamak aimed to directly measure the V_0^{NTV} profile in plasmas not utilizing NBI heating, doing so for the first time in plasmas expected to have V_0^{NTV} dominated by the electron channel to more fully examine the theory. The experiment to directly measure the V_0^{NTV} profile utilized a simple approach. Fig. MS-17 illustrates the plasma current and line-averaged density used. Long pulse plasmas (up to 8s I_p flat-top duration) allowed quasi-steady-state conditions to be produced, permitting two measurement times per plasma discharge. As discussed earlier, a prime objective of the experimental setup was to avoid the use of NBI to heat the plasma, as the co- I_p directed NBI system in KSTAR would also produce significant plasma rotation. Steady-state rotation speeds in an NBI heated plasma are expected to be approximately an order of magnitude larger than V_0^{NTV} , and so the use of NBI would obscure its measurement. Experiments were therefore conducted in plasmas heated ohmically, and also by the addition of up to 0.8 MW of 140 GHz second harmonic electron cyclotron heating (Fig. MS-17), as the strength of T_0^{NTV} theoretically depends strongly on plasma temperature. The plasma rotation profile was measured using charge exchange spectroscopy (CES) by utilizing a single NBI source running at somewhat derated voltages (50 – 60kV as opposed to normal operation at 90 – 95 kV) solely for the purpose of allowing plasma rotation and ion temperature profile measurement. Fig. MS-17 shows the relative timing of the ECH and NBI pulses, along with the core plasma rotation as measured by CES during NBI (in red). The measurement of V_0^{NTV} was made directly at the start of the NBI pulse, either using the earliest available measurement interval, or by making a small time extrapolation (~ 10 ms) back to the time at which NBI started (2.8s, 6.3s). An X-ray imaging crystal spectrometer (XICS) channel is shown along with the CES measurements in Fig. MS-17. Applied 3D fields were added to these plasmas to generate the NTV effect utilizing the KSTAR in-vessel control coils (IVCC) configured to deliver a predominantly $n = 2$ field. While measuring V_0^{NTV} , density feedback was utilized to maintain density control while 3D field strength was varied. To study its effect on V_0^{NTV} , variations to plasma temperature were also made by varying density at fixed applied 3D field strength.

component of the analysis, for instance, the NBI torque profile (which is not directly measured), or the solution of torque balance including both resonant and non-resonant magnetic braking. In addition, experimental research published to date has entirely focused on the ion channel providing the dominant drive for the NTV offset rotation, manifest by the models of the NTV offset rotation velocity,

The measurement of the V_0^{NTV} profile made here attempts to minimize error in the torque balance equation used to isolate it. Consider a simple and often-used torque balance equation $dL/dt = T_{NTV} + T_{NBI} + T_{ECH} + T_{Intrinsic} - L/\tau_{2D}$, where L is the plasma angular momentum, T_j terms are torques due to NTV, NBI, ECH, and a base “intrinsic” torque in an ohmic plasma, and τ_{2D} is the plasma momentum confinement time before the addition of the 3D field. We then consider a highly-simplified but often used expression for $T_{NTV} = C_I \delta B^2 (V_\phi - V_0^{NTV})$, where δB is the magnitude of the applied 3D field. The multiplicative term C_I is known to be a function of plasma parameters, especially temperature. Replacing L by $IV_\phi R$ where I is the plasma moment of inertia, and considering that the intrinsic plasma rotation be considered as generated by the combination of T_{ECH} and $T_{Intrinsic}$, *without* any applied 3D field, the torque balance equation in terms of velocities is:

$$C_I \delta B^2 (V_\phi - V_0^{NTV}) + \frac{I}{R_{-2D}} (V_\phi - V_I) = 0$$

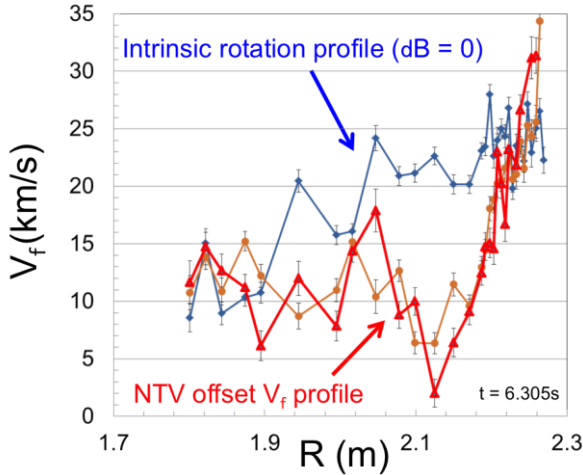


Figure MS-18: Measured intrinsic rotation profile V_f , and saturated V_0^{NTV} profile in an EC heated plasma.

An example is summarized in Fig. MS-18, which shows the measured V_I profile, and two profiles that saturate when the current, $I_{n=2}$, used to generate the applied $n = 2$ field reaches 3.2 kA/turn. Values of $I_{n=2}$ less than this value generated V_ϕ between these two profiles, which are omitted for clarity. The last two profiles in the scan of the applied 3D field are shown.

Several characteristics of the V_0^{NTV} profile for the plasma target in Fig. MS-18 are noteworthy theoretically and potentially important for future devices. First, the V_0^{NTV} is in the co- I_p , rather than the counter- I_p direction found in past work and thought to be the sole direction for V_0^{NTV} . However, the present result is expected when NTV theory is considered more generally, as the direction depends on the balance of the electron and ion non-ambipolar fluxes. Being EC heated, the core plasma in Fig. MS-18 has (T_e/T_i) greater than 4, and the electron to ion NTV torque which scales as $(m_i/m_e)^{0.5} (T_e/T_i)^{3.5}$ indicates that the electron channel should be dominant, consistent with the co- I_p direction of V_0^{NTV} . Also, while the rotation in the plasma edge region, which equates to more than 12 krad/s, is not large compared to core V_ϕ values generated by NBI, it is quite significant compared to projections for ITER, which for a range of conditions are

approximately 2 krad/s in the pedestal region [MS-28]. Finally, the rotation shear that is generated in V_0^{NTV} is quite large – 15 times greater than the shear measured for the V_I profile shown.

Plasma conditions were varied to compare V_ϕ profiles under different heating conditions and to examine the effect of plasma temperature on the V_0^{NTV} profile. First, Fig. MS-19 shows a progression of V_ϕ profiles in ohmic plasmas, and an ECH plasma producing a V_0^{NTV} profile. First, the V_I profile (no applied 3D field) shown under ohmic conditions has V_ϕ near zero in the core region, increasing to about 7 km/s in the outer plasma. When the $n = 2$ applied field is added, (at somewhat smaller than the level needed to saturate the V_ϕ profile at V_0^{NTV}), the V_ϕ in the outer region approximately doubles to 15 km/s. This shows that this rise is due to the application of the 3D field, and not simply due to a mechanism of the ECH. However, when ECH is added, the heating in the outer region apparently leads to a strong increase of V_ϕ , again more than doubling it to 35 km/s. This profile has increased $I_{n=2}$ to levels that saturate the rotation profile, producing the V_0^{NTV} profile. In this case, while the characteristic strong co- I_p rotation is found in the outer region, the core region now shows rotation in the counter- I_p direction as is expected if the NTV torque is dominated by the ion flux. This may be due to a higher density and somewhat lower (T_e/T_i) ratio in the core.

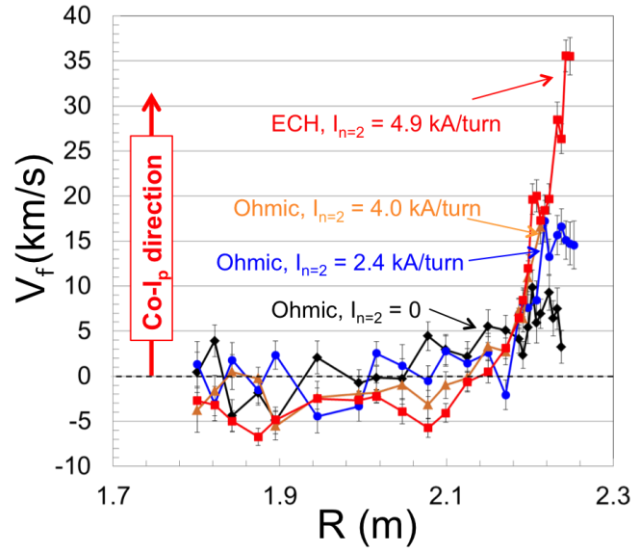


Figure MS-19: Comparison of plasma rotation profiles in ohmic and ECH plasmas at varied 3D field levels.

A comparison of V_0^{NTV} profiles is shown for various plasma temperatures and constant $I_{n=2}$ in

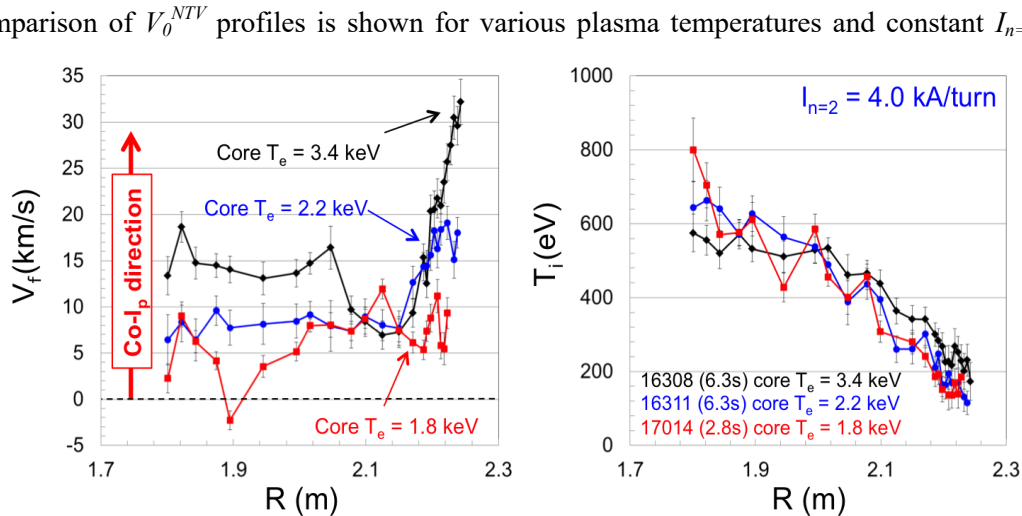


Figure MS-20: (a) V_0^{NTV} profiles at different plasma temperatures, and (b) T_i profiles for these variations.

Fig. MS-20. The temperature variations were created by changing plasma density. The highest temperature plasma (the lowest density) yields a V_0^{NTV} profile in the co- I_p direction in both the core and outer region, with strong rotation shear in the outer region. The middle temperature produced with a line-averaged density feedback setting of $1.5 \times 10^{19}/\text{m}^3$ has decreased rotation in the core and outer regions. The lowest temperature had density set to $2.0 \times 10^{19}/\text{m}^3$ and V_ϕ in the outer region has dropped to levels found in the lowest rotation ohmic plasma in Fig. MS-19.

Separate from the measurement of V_0^{NTV} , an observation of the toroidal rotation profile evolution during the period of NBI heating in Fig. MS-17 shows that the effects observed are not caused by the heating systems alone, and have NTV characteristics. Most striking is the behavior of the plasma rotation when both the ion temperature and applied 3D field are sufficiently high. In plasmas where no 3D field is applied, once the NBI is turned on, the plasma expectedly spins up in the direction that the beam is injected. This is obvious and is completely intuitive. However, as seen in Fig. MS-21, at $I_{n=2} = 4$ kA/turn, the evolution of the V_ϕ profile away from the V_0^{NTV} profile is in the direction *counter* to the injected beam. Other examples at slightly lower $I_{n=2}$ show that the V_ϕ profile first increases in the direction of the injected beam, and later *reverses* direction and moves in the direction *counter* to the injected beam as the plasma ion temperature increases. Note that no MHD modes are observed, and there is no evidence of conventional mode locking in this case. This unintuitive result can be understood by a change in the T_{NTV} which typically increases with ion temperature, or a change in the V_0^{NTV} profile itself due to the temperature change.

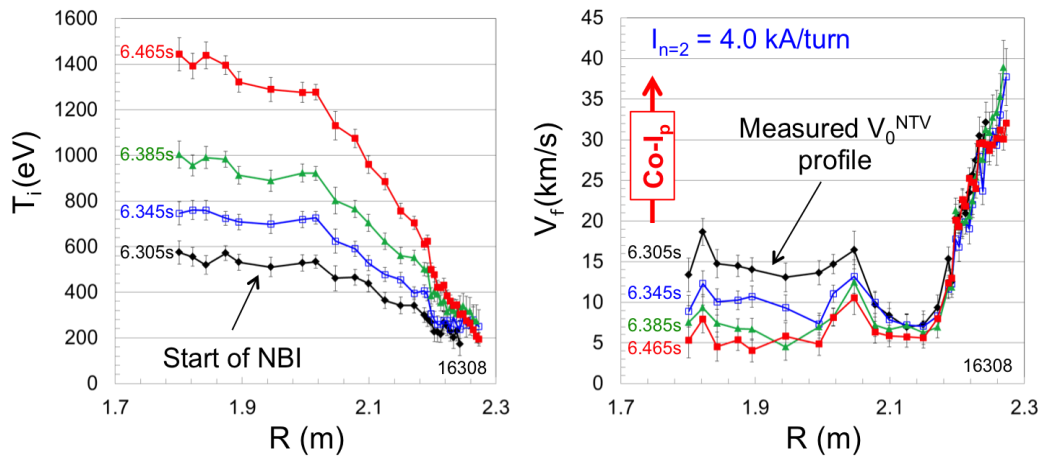


Figure MS-21: Unintuitive observation of the plasma rotation profile moving in the direction opposite of an injected neutral beam when the plasma has sufficient temperature and applied 3D field strength.

(b) 3D MHD Spectroscopy to extract multi-mode plasma transfer function

The complex damping rate (eigenvalue) of MHD modes determine their proximity to instability and their level of (stable) response to driving external fields. Having experimental methods to determine the stability of these modes would prove valuable for disruption prediction and avoidance in advance tokamak operation such as NSTX-U, DIII-D, ITER and future reactors. The new developed 3D MHD spectroscopy method has been proposed and tested to extract multi-mode plasma transfer function in DIII-D experiments. The method uses upper and lower internal

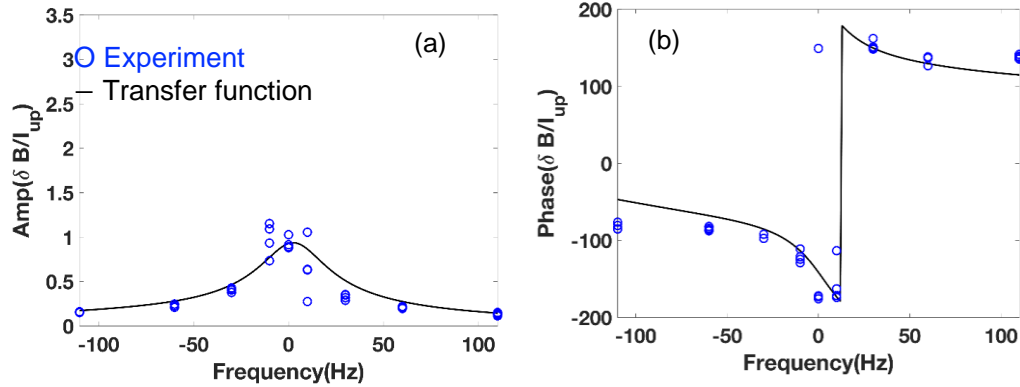


Figure MS-22: Amplitude (a) and phase (b) of magnetic response measured at ISLD1A sensor are plotted as the function of coil frequency. The transfer function (solid line) is compared with the experimental measurement ('o').

coils to perform scans of frequency and phasing with the new coil power supply module (SSPA). The corresponding $n=1$ magnetic response is measured on multiple arrays of 3D magnetic sensors. The multi-mode transfer function, depending on coil phasing and frequency, is extracted, based on Padé approximation, by fitting the measured signals on different sensors simultaneously. In the transfer function, the damping rate of least stable mode, $-17.8+2.62i$ (1/s), is extracted for the first time and infers the plasma stability qualitatively. In Fig. MS-22, the extracted transfer function is extrapolated and compared with the measured signal in a separated experiment performing the frequency scan using only upper I-coils. The good agreement demonstrates the linear property of plasma response in the experiments and the validation of

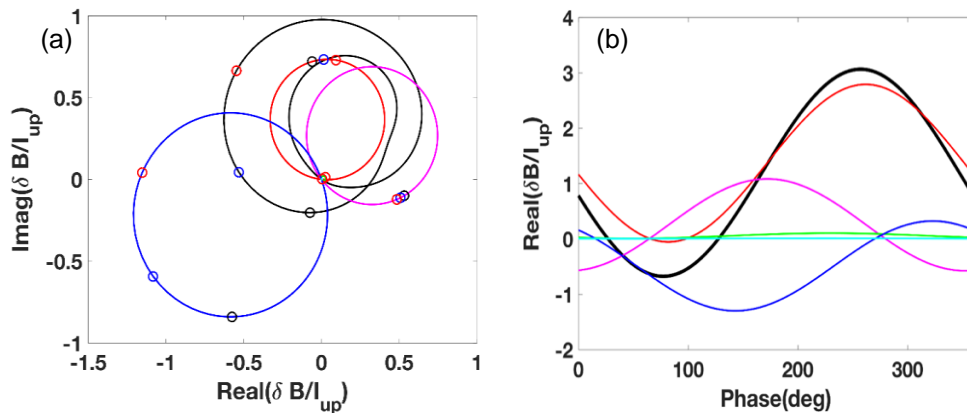


Figure MS-23: Nyquist plot (a) with upper-lower phase difference of 100 deg and (b) an upper-lower phase scan of magnetic response with DC fields at MPID sensor are presented, where full transfer function is in black. The least, secondary and third stable modes are plotted in blue, red, magenta color respectively. Two modes in green and cyan color are fourth and fifth modes with little contribution to the response.

transfer function approach.

The experimental transfer function not only points out the multi-mode plasma response but also indicates the number of dominant modes and the contribution of each mode to the plasma response, as shown by Nyquist plot in Fig. MS-23 (a). Using the transfer function, Fig. MS-23 (b) reveals the variation of each dominant mode with respect to DC phasing scan, where the

secondary mode is dominant the plasma response around 280 deg. The extracted function will be further compared with MARS simulation to explore more physics of DIII-D plasma response.

The success of validating 3D MHD spectroscopy in DIII-D experiment suggests the importance of installing NSTX-U NCC. The new technique will greatly help NSTX-U and other advance tokamaks to better understand underlying 3D MHD physics and the role of each eigenmode in RMP-ELM suppression. The further effort will be made to optimize this method which has the potential to be applied as a reliable real-time plasma stability monitor and predictor in future fusion reactor.

6. Progress on classical and neoclassical tearing mode physics

(a) Core MHD mode structural identification and stability analysis

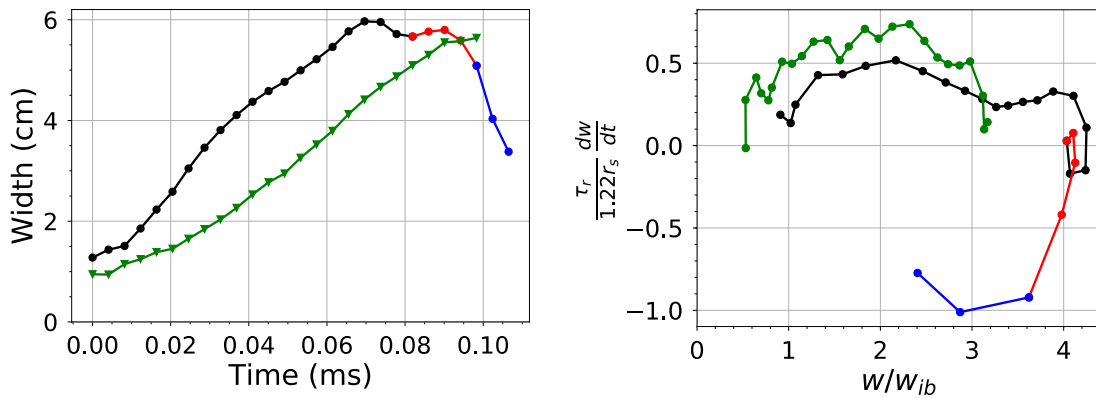


Figure MS-24: (a) Comparison of NSTX-U shot 204112 (green) magnetic island width (versus time since mode onset) against shot NSTX shot 134020 (black/red/blue). The green points are followed until the plasma shuts down. The black points correspond to the initial mode growth and saturation. At the black/red transition the NBI power was reduced by one-third, causing the mode amplitude to decay (red and blue points). (b) The growth rate normalized to resistive time as a function of the island width normalized to the ion banana width for the same dataset.

Saturated core MHD instabilities such as (neoclassical) tearing modes (NTMs) are observed to degrade core confinement or to brake plasma rotation, leading to disruptions. The increase of plasma aspect ratio due to the expansion of the center-stack during the upgrade of NSTX is predicted to reduce the strength of the Glasser-Green-Johnson effect [MS-29], in which favorable magnetic field line curvature helps stabilize tearing-type modes.

To test this prediction, we have compared discharges in NSTX and NSTX-U with unstable $n = 1$ modes with predominant $m = 2$ poloidal

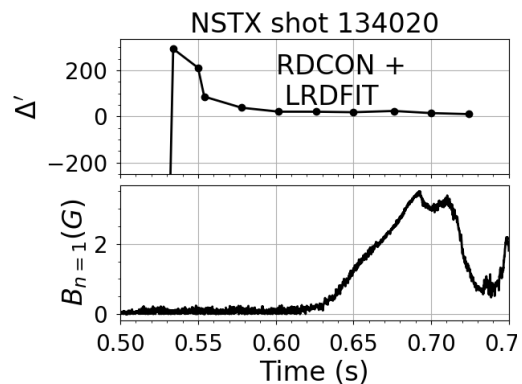


Figure MS-25: (Upper) Stability index calculated from RDCON, indicating a destabilizing classical tearing mode drive term. (Lower) Magnetic fluctuation time history.

structure which are thought to be NTM-type instabilities. Both have $\beta_N \approx 4$, $\beta_N/l_i \approx 6$ and $q_{95} \approx 8$. Fig. MS-24(a) shows the magnetic island width (proportional to the square root of the measured $n = 1$ magnetic fluctuations) while 24(b) shows the growth rate as a function of width in normalized units. The longer time to saturation in 1a in NSTX-U is likely due to the higher BT, higher T_e (at $q=2$) and thus longer resistive time. The peak normalized growth rate in 24(b) is larger for the NSTX-U case while the similar saturated island in 24(a) is smaller when normalized in 24(b) due in large measure to the assumed higher T_i and thus larger ion banana width.

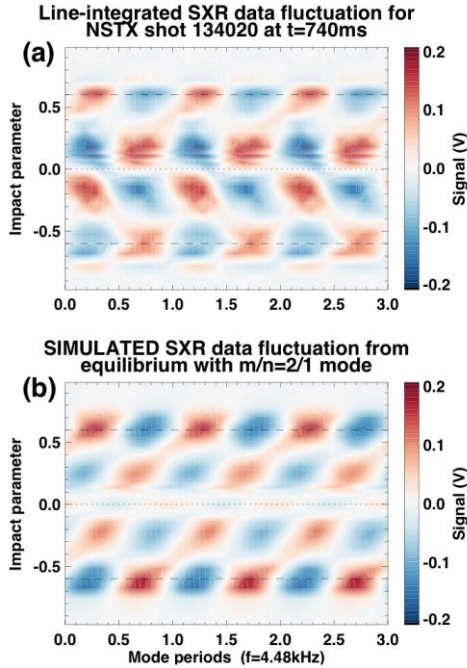


Figure MS-26: Comparison of (a) measured and (b) modeled soft X-ray brightness fluctuations versus SXR chord line-of-sight impact parameter assuming an $m/n=2/1$ tearing mode resonant at $\rho_s = 0.6$.

Linear MHD stability calculations using M3D-C1 and RDCON have been conducted to compare with the observed mode structure and onset time. Linear M3D-C1 simulations based on EFIT reconstructions of NSTX shot 134020 near the onset time, and including measured toroidal rotation shear, indicate that a resistive edge-localized mode may be unstable, depending on the details of the edge rotation profile. This supports the observation that the core mode may have been triggered by an edge instability. RDCON calculations (Fig. MS-25) based on a time-series of LRDFIT [MS-30] equilibrium reconstructions for the same shot show a slightly destabilizing (positive) classical tearing drive term (Δ') for the $m/n = 2/1$ mode. The constancy of Δ' around the mode onset time indicates that the classical drive is not the trigger for the mode onset. Addition of the curvature effect is likely to result in a net stable contribution from classical effects, which would confirm the importance of the neoclassical drive in these cases. Similar analysis is underway for the NSTX-U discharge 204112.

Progress has been made in discriminating tearing-type modes from other core instabilities using internal optical & beam diagnostics. The SXR FIT code, which reconstructs a mode using the soft X-ray emission diagnostics, has been modified to incorporate electron temperature measurements from Thomson Scattering. Other modifications include improvements to the fitting algorithm and data pre-processing methods, methods for reading M3D-C1 eigenmodes, and preliminary efforts to account for the centrifugally-induced radial asymmetry in heavy impurity species. Fig. MS-26 shows an example fit to the soft X-ray fluctuations. The parity of the fluctuations across $\rho = 0$ suggests an odd- m component to the mode structure, *in addition to* the modeled $m = 2$ tearing. Efforts to generalize the model to non-single-helicity are on-going. Similar analysis is underway for the NSTX-U discharge 204112.

(b) Validation of Resistive DCON with theory and PEST3

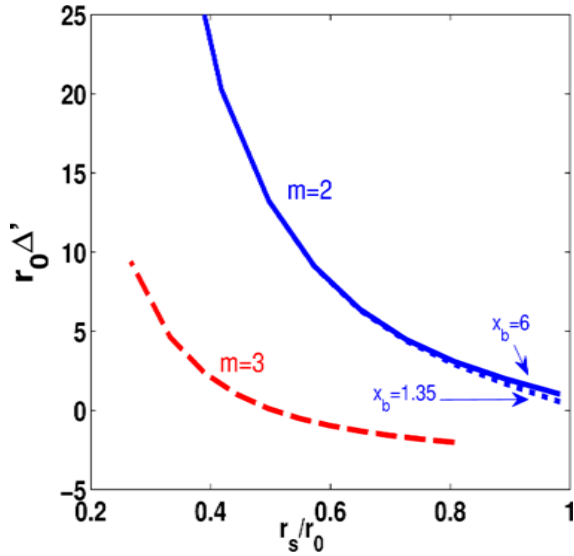


Figure MS-27: Δ' , solved by RDCON, is plotted as the function of singular surface location r_s . r_0 , as the normalization factor and x_b , as the wall location, are defined in [MS-29]. The values of (2,1) and (3,1) Δ' are marked in blue and red respectively.

In FY16, resistive DCON (RDCON) has been applied to study tearing instability in NSTX-U experiments by solving the outer region Δ' . RDCON indicates $n=1$ tearing mode can be unstable in Shot 204718, where an unstable $n=1$ mode is observed in this ohmic plasma experiment. The success of RDCON application is very helpful to study Δ' variation in future NSTX-U experiments. To confirm the reliability of Δ' solved by RDCON, the code is applied to compare the results in [MS-31] and to qualitatively compare with Δ' solved by PEST3 code. Presently, only RDCON and PEST3 codes have the capability to solve Δ' in full toroidal geometry in tokamaks. Since analytical results of Fig. 1 in Ref. [MS-31] is based on zero β assumption and cylindrical geometry, a series of large aspect ratio equilibria, which

has the similar current profile and small pressure, has been generated as close as possible to that defined in [MS-31]. Fig. MS-27 shows Δ' solved by RDCON for $n=1$ mode. The values of Δ' are plotted as the function location of singular surface. The results show RDCON can well reproduce Δ' behavior at $q=2$ and 3 surfaces in Fig. 1 in Ref. [MS-31].

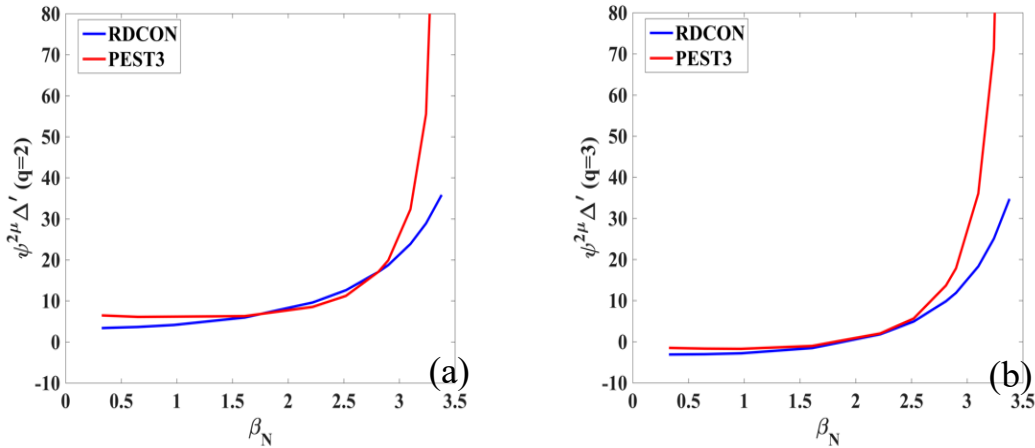


Figure MS-28: Δ' values, at $q=2$ (a) and $q=3$ (b) surfaces are plotted as the function of β_N , where Δ' values solved by RDCON are in blue and PEST3 results are in red.

In the benchmark between RDCON and PEST3, a series of DIII-D equilibrium, based on shot 137559, is generated to perform β_N scan towards ideal wall limit $\beta_N^{no\ wall} \sim 3.5$. In this work, the factor, $\psi^{2\mu}$, has been figured out to convert Δ' calculated by RDCON to PEST3's Δ' dimension.

Here ψ is the normalized poloidal flux at the singular surface. $\mu = \sqrt{-D_i}$, where D_i is the Mercier index. This factor greatly helps the first qualitative benchmark between the two codes. Δ' values, solved by RDCON and PEST3, are compared in Fig. MS-28 for $q=2$ and 3 surfaces. Two codes show very good agreement when β_N is small and not close to $\beta_N^{no\ wall}$. When β_N approaches to idea wall limit, the discrepancy of Δ' between two codes is significant because PEST3 keeps only up to first order term in power series solution [MS-32] and RDCON keeps arbitrary high order terms. Theoretically, while increasing pressure and μ , high order terms are required to make Δ' converge. This benchmark effort confirms RDCON and PEST3 can solve Δ' in full toroidal geometry. With this achievement, the work implementing RDCON into TRANSP to provide Δ' for NTM simulation is undergoing. In particular, the capability of RDCON solving the converged Δ' in high pressure plasma is very important to NSTX-U since spherical tokamak is featured to operate in high β region.

References

- [MS-1] J. W. Berkery et al., *Physics of Plasmas* **24**, 056103 (2017)
- [MS-2] C. Galperti et al., *Plasma Physics and Controlled Fusion* **56**, 114012 (2014)
- [MS-3] C. Galperti et al., *IEEE Transactions on Nuclear Science* **64**, 1446 (2017)
- [MS-4] J. E. Menard et al., *Nuclear Fusion* **57**, 102006 (2017)
- [MS-5] S. A. Sabbagh et al., *Nuclear Fusion* **41**, 1601 (2001)
- [MS-6] R. Raman, et al., *Fusion Science and Technology* **68**, 797 (2015)
- [MS-7] C. E. Myers et al. “A multi-machine scaling of halo current rotation”, submitted to *Nucl. Fusion* (2017)
- [MS-8] Wesley et al., “Disruption characterization and database activities for ITER”, *Proceeding of the 21st IAEA Fusion Energy Conference*, IT/P1-21 (2006)
- [MS-9] V. Amoskov et al., “Statistical analysis of expected error fields in tokamaks and their correction”, *Plasma Devices and Operations* **13**, 87 (2005)
- [MS-10] Y. Gribov et al., “Error field expected in ITER and their correction”, *Proceeding of the 24th IAEA Fusion Energy Conference*, ITR/P5-29 (2012)
- [MS-11] J.-K. Park et al., “Assessment of error field correction crieteria for ITER”, *ITPA MHD MDC-19 Report* (2017).
- [MS-12] Y. In et al., *Nuclear Fusion* **55**, 043004 (2015)
- [MS-13] H. Wang et al., *Nuclear Fusion* **56**, 066022 (2016)
- [MS-14] A. Kirk et al., *Plasma Physics and Controlled Fusion* **56**, 104003 (2014)
- [MS-15] J.-K. Park et al., “WG9 update on locking scaling database and DIII-D proxy error field experiments”, *March ITPA MHD Meeting* (2012)
- [MS-16] J.-K. Park et al., *Nuclear Fusion* **51**, 023003 (2011)
- [MS-17] C. Paz-Soldan et al., *Physics of Plasmas* **21**, 072503 (2014)
- [MS-18] T. Markovic et al., “Effects of controlled $n=1$ HFS error fields on H- and L-mode plasmas on COMPASS”, *March ITPA MHD Meeting* (2017)
- [MS-19] J.-K. Park et al., *Nuclear Fusion* **52**, 023004 (2012)
- [MS-20] M. J. Lanctot et al., *Nuclear Fusion* **57**, 036004 (2017)
- [MS-21] J.-K. Park et al., “Optimizing 3D magnetic fields for control of MHD instabilities in tokamak plasmas”, submitted to *Nature Physics* (2017)

- [MS-22] K.C. Shaing, Phys. Plasmas **10** (2003) 1443.
- [MS-23] Y. Sun et al., Nucl. Fusion **52** (2012) 083007
- [MS-24] A.M. Garofalo et al., Phys. Rev. Lett. **101** (2008) 195005
- [MS-25] S. Nowak et al., Journal of Physics Conference Series **401**, 012017 (2012)
- [MS-26] W.M. Solomon et al., Phys. Plasmas **17** (2010) 056108
- [MS-27] K.C. Shaing et al., Nucl. Fusion **55** (2015) 125001
- [MS-28] A.R. Polevoi et al., Nucl. Fusion **45** (2005) 1451
- [MS-29] A. H. Glasser et al., Physics of Fluids, **18**, 875 (1975)
- [MS-30] J. Menard et al., Phys. Rev. Lett. **97**, 095002 (2006).
- [MS-31] H.P. Furth et al., Physics of Fluids, **16** 1054 (1973)
- [MS-32] A. Pletzer et al., Journal of Computational Physics **115**, 530-549 (1994)

B. Transport and Turbulence TSG Research Highlights

Transport and turbulence research in FY17 proceeded on multiple fronts. Additional analysis and simulation work was performed for initial NSTX-U experiments as well as continued for previous NSTX data. Development of electromagnetic gyrokinetic code capability has also progressed. Finally, collaborative efforts with DIII-D were established while those from previous MAST momentum transport experiments were completed.

1. NSTX-U analysis and modeling

Additional modeling has been performed for NSTX-U L-mode discharges that were developed to validate gyrokinetic predictions at low beta and low aspect ratio [TT-1]. Linear gyrokinetic stability analysis performed for two of these discharges (Fig. TT-1) show that electrostatic ITG modes are unstable at ion scales ($k_{\theta}\rho_i < 1$) as is commonly found at conventional aspect ratio. However, the $E \times B$ shearing rates can be larger than the linear growth rates over some regions ($\rho \sim 0.6$), consistent with the TRANSP analysis showing that ion thermal transport is near neoclassical and electron transport dominates thermal losses [TT-2]. Fluctuation amplitudes measured at ion scales from beam emission spectroscopy (BES) increase in amplitude at increasing radii, consistent with the relative increase in γ_{ITG}/γ_E , suggesting ITG turbulence may be more important in regions further out. In addition to ITG, the electromagnetic microtearing mode (MTM) is also unstable at ion scales. This is in contrast to what is commonly found at conventional aspect ratio due to the larger beta values ($\beta_N = 2.0$ & 1.7 for 204551 & 204963, respectively) and the high collisionality of these plasmas chosen to avoid L/H transitions. The change in the relative strength of ITG and MTM in the different discharges can be related back to the profile changes due to different NBI power, plasma current and density. For example, 204963 had lower injected NBI power (and torque) and density. Consequently, ITG growth rates are larger due to reduced T_i/T_e (since $R/L_{Ti,crit-ITG} \sim 1 + T_i/T_e$), while $E \times B$ shearing rates are reduced. On the other hand, MTM growth rates are reduced due to lower beta. The larger values of γ_{ITG}/γ_E in 204963 suggest ITG turbulence should be more important at ion scales, and measured BES fluctuation amplitude are indeed larger for this case.

The ITG and MTM instabilities propagate in different directions, with phase velocities in the plasma frame of $V_{ph,ITG,sim} = +(0.5-1)$ km/s (ion direction) and $V_{ph,MTM,sim} = -(2-3)$ km/s (electron direction). Measurements of density fluctuations using the upgraded

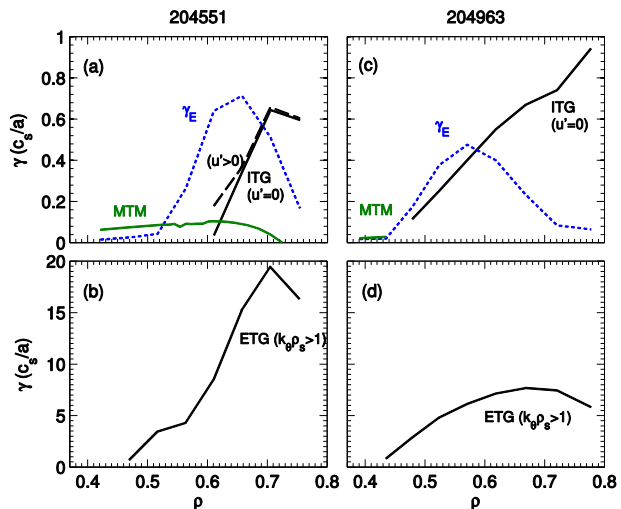


Fig. TT-1. Radial profile of (a,c) ITG and MTM growth rates and (b,d) ETG growth rates for shots 204551 (left) and 204963 (right). $E \times B$ shearing rate is shown by the dashed blue line. The simulations with finite parallel velocity gradient ($u > 0$) are shown by the dashed black line in (a).

2D BES diagnostic also show bimodal turbulence propagation [TT-3]. Figure TT-2 shows the coherence and cross-phase between two poloidally-separated BES channels on the midplane at $\rho \sim 0.7$. The coherence is statistically significant over 0–200 kHz, but dips around 50 kHz. The cross-phase, whose sign gives the lab-frame turbulence propagation direction, is negative below 50 kHz but reverses above 50 kHz. This data implies there is a low-frequency mode propagating in the electron diamagnetic direction at 7 km/s and a high-frequency mode propagating in the ion diamagnetic direction at 14 km/s, which could qualitatively be consistent with having two distinct micro-instabilities. However, using rotation data from the CHERS diagnostic to transform these velocities into the plasma frame shows that the electron mode has near zero velocity. Furthermore, correlation analysis of this mode shows zero phase-shift for radially separated channels. So it is likely that this feature is a result of common-mode beam fluctuations due to edge shadowing. In contrast, the ion mode propagates at approximately the ion diamagnetic velocity, remaining consistent with the presence of ITG instability.

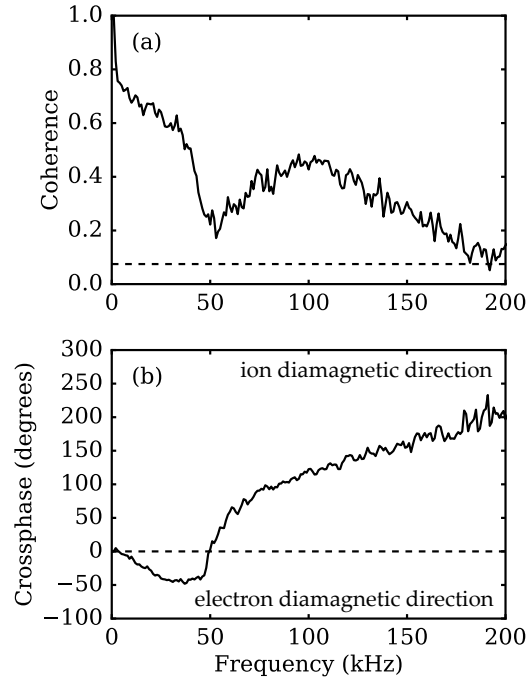


Figure TT-2. (a) Coherence and (b) cross-phase between two poloidally-separated BES channels ($\Delta Z = 3$ cm) at $r/a = 0.73$ in shot 204551. Dashed lines represent (a) the minimum statistically significant coherence and (b) a zero-phase reference line.

In the region of $\rho = 0.6$ the $E \times B$ shear is sufficiently strong to expect complete suppression of ion scale turbulence in the *local* limit. In this region the ETG instability has relatively large growth rates (Fig. TT-1). Under these conditions it is straightforward to run nonlinear electron scale simulations (i.e. no multi-scale effects) to predict electron heat flux contributions from ETG turbulence. Fig. TT-3a shows the predicted ETG electron heat flux from nonlinear GYRO simulations varies between 0.7–1.7 MW, spanning the experimental value, $Q_{e,\text{exp}} = 1.2 \pm 0.5$ MW illustrating it plays a significant role in the anomalous electron heat losses [TT-4]. The gyrobohm-normalized heat flux spectra (Fig. TT-3b) show that the peak in ETG transport is predicted to occur around $k_{\theta} \rho_s = 10$. The contributions at smaller wavenumbers at $\rho = [0.56, 0.66]$ falls off by an order of magnitude, consistent with the strong $E \times B$ shear suppressing ion scale turbulence in this region. At $\rho = 0.75$, the low $k_{\theta} \rho_s$ contributions do not fall off as significantly, due partially to increase in relative linear ETG drive. In this region the ITG growth rates are larger than $E \times B$ shearing rates. Under such conditions, recent real-mass multi-scale simulations have shown the multi-scale effects can change the total transport and relative contribution between ion and electron heat flux in non-intuitive ways [TT-5]. It may be necessary to consider similar multi-scale simulations to account for transport in these discharges.

It may also be necessary to consider global simulations in these plasmas as the ion scale growth rates and $E \times B$ shearing rates are predicted to vary significantly over a narrow width, $\sim 30 \rho_i$ ($\rho = 0.5-0.75$) due to the relatively large values of $\rho_* = \rho_i/a \sim 1/150$ in these plasmas. While global, multi-scale simulations are typically prohibitive for conventional aspect ratio at low ρ_* , the relatively large ρ_* values in the ST plasmas make it slightly more tractable to consider (global, multi-scale simulations which have been attempted in other large ρ_* plasmas (e.g. [TT-6]).

2. NSTX analysis and modeling

ETG simulations and high-k synthetic diagnostic

In collaboration with MIT (graduate student J. Ruiz-Ruiz and Professor A. White) a synthetic diagnostic for the high-k scattering systems is nearing completion for the validation of electron scale simulations against experiment. Two equivalent approaches have been pursued that are applicable to general plasma scattering measurements including both original and new NSTX/NSTX-U high-k scattering systems and also Doppler backscattering diagnostics. The first implementation is based on the traditional filtering in wavenumber space following initial investigations reported previously [TT-7,8]. Fig. TT-4 shows a comparison of the measured high-k scattering signal for NSTX discharge 141767 as well as the synthetic spectra calculated using a nonlinear GYRO ETG simulation [TT-9] coupled with wavenumber filtering. The Doppler shifted turbulent spectra centered at -1 MHz is apparent in both cases with similar spectral width. (The $f \sim 0$ peak in the measurement is due to spurious radiation.) A comparison of amplitudes is not possible as the measured power spectrum is not calibrated.

The second, equivalent, implementation of the synthetic diagnostic is based on filtering in real space (see Fig. TT-5) which is in fact the more natural approach as it stems directly from the general expression of the scattered power from an ensemble of electrons. It is also easier to implement and is more directly applicable to all codes since it only requires plotting fluctuations in real space to apply a common filter algorithm. Applying the wavenumber filter is more arduous to perform since it requires a detailed mapping of wavenumbers depending on the coordinate system particular to each code. On the other hand, the real space filter is more computationally intensive (3-5 \times) than the wavenumber filter approach, although this expense is minor compared to the expense of the nonlinear gyrokinetic simulations.

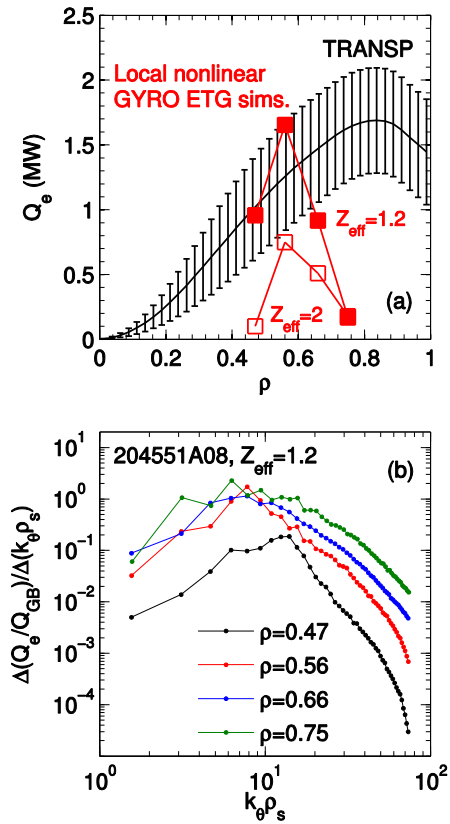


Fig. TT-3. (a) Predicted electron heat flux from nonlinear ETG simulations using two different values of Z_{eff} compared with experimentally inferred electron heat flux from TRANSP. (b) Normalized electron heat flux spectra simulated at four radii using $Z_{\text{eff}}=1.2$.

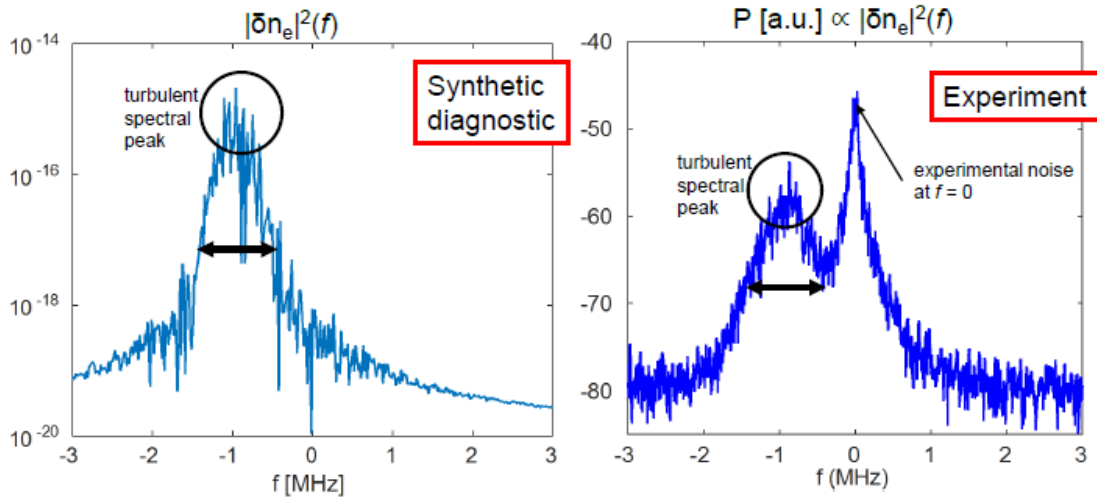


Fig. TT-4. (left) Synthetic high- k power spectra calculated using results from a nonlinear GYRO simulation coupled with the wavenumber filtering method. (right) Scattered power P measured from channel 1 of the NSTX high- k scattering system for shot 141767. The measured and predicted power spectra both show the same turbulent spectral peak around -1 MHz.

Considerable effort has been invested to verify the equivalence of both approaches. The proof-of-principle for both methods was first verified using a 1D toy model. The equivalence of both methods was then demonstrated using nonlinear GYRO simulations of the community standard benchmark Cyclone Base Case which is a new contribution [TT-10] that has not been reported before. In order to compare the synthetic diagnostic to experiment and apply it to the more realistic simulations relevant for the high- k scattering diagnostic, additional “big box” electron scale simulations are required which are presently being queued on the systems at NERSC.

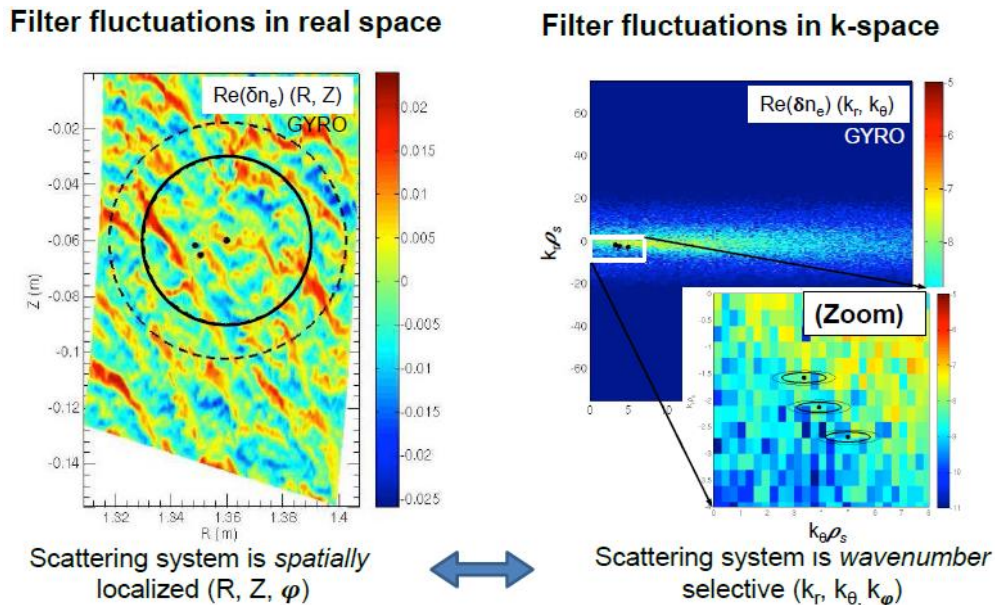


Fig. TT-5. (left) Color contours of ETG normalized density fluctuations (dn/n_0) from nonlinear GYRO simulations. Black lines show the e^{-1} and e^{-2} Gaussian beam widths of the high- k scattering probe volume. (right) 2D wavenumber spectra of ETG simulations. Black lines show the e^{-1} and e^{-2} spectral width of the high- k scattering.

Thermal transport due to Alfvén eigenmodes

Analysis done in FY16 presented initial results of a parametric investigation of CAE and GAE stability and their role in core energy transport over large range of parameter using a database [TT-11] of NSTX beam-heated discharges. New analysis since then has led to several interesting results [TT-12]. CAE and GAE mode amplitude (δB) is found to scale with absorbed beam power as $\delta B \sim P_{\text{abs}}^{2.5}$, which is roughly consistent with the expectation from recent theory simulations $\delta B \sim P^2$ [TT-13]. The strong correlation between normalized frequency (ω/ω_{ci}) and toroidal mode number ($n/R \cdot v_{b||}/\omega_{ci}$) reported in FY16 has also been found to depend on density profile shape. In particular, the constant of proportionality between frequency and wavenumber changes significantly with density profile flatness (Fig. TT-6). Finally, electron energy confinement time and peak electron temperature in the core is found to correlate with normalized frequency and mode number of the modes (Fig. TT-6). This correlation is consistent with the hypothesis that CAEs and GAEs influence electron thermal transport. However, these calculations were done using TRANSP assuming no fast ion anomalous transport, so further investigation is needed to understand the change in NBI power deposition.

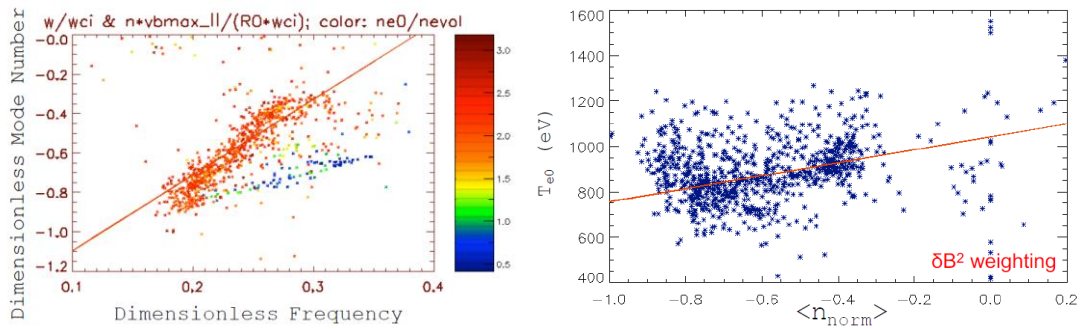
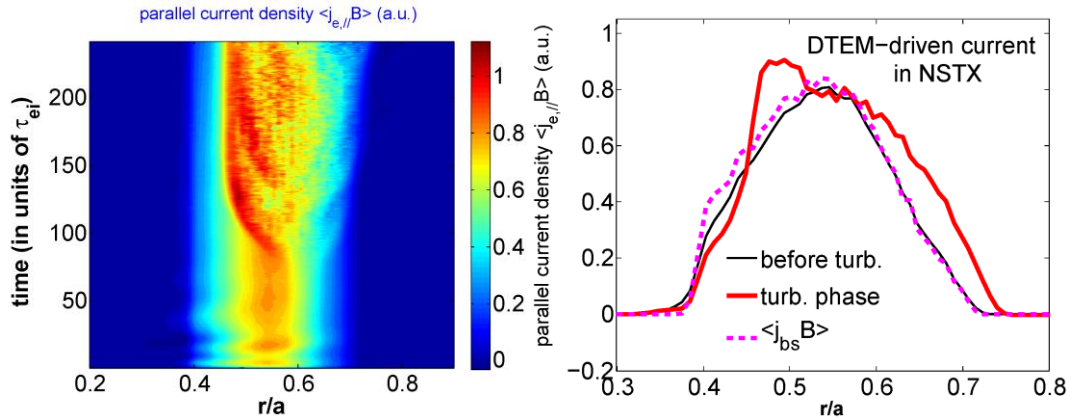


Fig. TT-6. (left) Dimensionless measured GAE/CAE toroidal mode number ($n/R \cdot v_{b||}/\omega_{ci}$) vs. normalized frequency (w/w_{ci}). The colormap represents the ratio of density peaking, $n_{e0}/(n_e)$. (right) Central electron temperature, T_{e0} , vs. density peaking.

Non-inductive current generation in NSTX plasmas with turbulence

Plasma self-generated non-inductive current (e.g., the bootstrap current) not only contributes to the generation of poloidal magnetic field for plasma confinement, but also strongly affects key MHD instabilities such as neoclassical tearing mode (NTM) and edge localized mode (ELM). For spherical tokamak experiments, it is of great interest to explore fully non-inductive current operation with high bootstrap current fraction. This critical research interest provides a strong motivation for us to investigate turbulent effects on plasma current self-generation in ST devices. Our simulation study employs a global gyrokinetic model coupling self-consistent neoclassical and turbulent dynamics. Recently, it was found from global gyrokinetic simulations that long wavelength dissipative trapped electron mode (DTEM) destabilized in NSTX collisionality regime by large electron density and temperature gradients achieved in H-mode plasmas may provide an important source of turbulence responsible for plasma transport and confinement in the presence of strong ExB flow shear [TT-14,15]. The present simulation study focuses on electron current generation in the DTEM dominated turbulence regime. More specifically, nonlinear global GTS simulations including self-consistent turbulent and neoclassical dynamics

are applied to simulating an NSTX H-mode discharge where the density gradient driven DTEM turbulence is shown to produce experimentally relevant plasma transport in multiple channels.



TT-7. (Spatio-temporal evolution of electron current density (left) and simulated stationary current density profile in neoclassical phase and fully developed turbulence phase (right). The GTS simulation was carried out for NSTX discharge #140620@536.

Distinct phases in electron current generation are illustrated in these initial value simulations (Fig. TT-7). In the early phase before turbulence develops, the electron bootstrap current is established in a time scale of ten electron collision times, which closely agrees with the neoclassical prediction. The second phase follows when DTEM turbulence begins to saturate, during which turbulent fluctuations are found to strongly affect mean electron current. The profile structure, amplitude and phase space structure of electron current density are all significantly modified relative to the neoclassical bootstrap current by the presence of DTEM turbulence. Both electron parallel acceleration and parallel residual stress drive are shown to play important roles in turbulence-induced current generation. The former changes the total (volume-integrated) plasma self-generated current though turbulence-induced momentum exchange between electrons and ions, and the latter merely modifies the current density profile while keeping the total current unchanged. The simulation study of current generation with turbulence will be extended to different turbulence and collisionality regimes relevant to NSTX-U experiment

3. Theory and computational developments

Development of electromagnetic GTS capability

Progress has been made on updating the Startsev-Lee scheme to include toroidal electromagnetic effects in the GTS code (EM-GTS) which will enable simulating tearing modes, microtearing modes (MTM) and the transition between ITG and kinetic ballooning mode (KBM) instabilities in tokamaks. Most of the benchmarked results so far have been for circular flux-surface tokamaks. As an example, Fig.TT-8 shows the odd-parity electrostatic potential perturbation from a linear MTM simulation in a circular cross section tokamak.

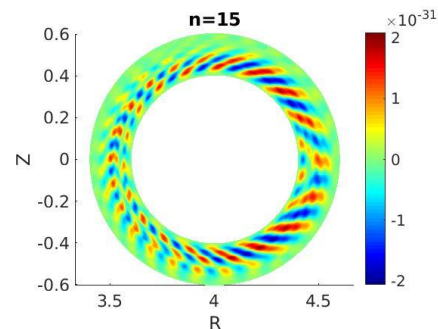


Fig.TT-8. Electrostatic potential ϕ plotted in the poloidal plane of a circular flux-surface tokamak with aspect ratio $R/a=4$ and electron beta $\beta_e=4\%$. The odd-parity of the potential around rational surfaces associated with microtearing modes is apparent.

Additional progress has been made to update EM-GTS to handle general geometry which is important for spherical tokamaks. Two distinct schemes were tested initially (including schemes by Mishichenko's group in Germany and Z. Lin's group at UC Irvine) that have shown promise in circular flux-surface geometry, but may have problems handling MTM and the ITG-KBM transition. The third EM scheme that is being developed by PPPL-Theory is a simplified version of the Startsev-Lee scheme that has been reformulated for general geometry which shows promise for simulating MTM in NSTX. An example of a preliminary beta scan is shown in Fig. TT-9. As beta increases the predicted global instability evolves from MTM peaking on the high field side, to MTM peaking on the LFS, to ultimately a KBM. This promising initial result demonstrates the code can operate in NSTX geometry and can simulate electromagnetic modes with both ballooning and tearing parity. Near term work will be to compare all three schemes for the NSTX geometry so that the optimal scheme can be identified for continued development.

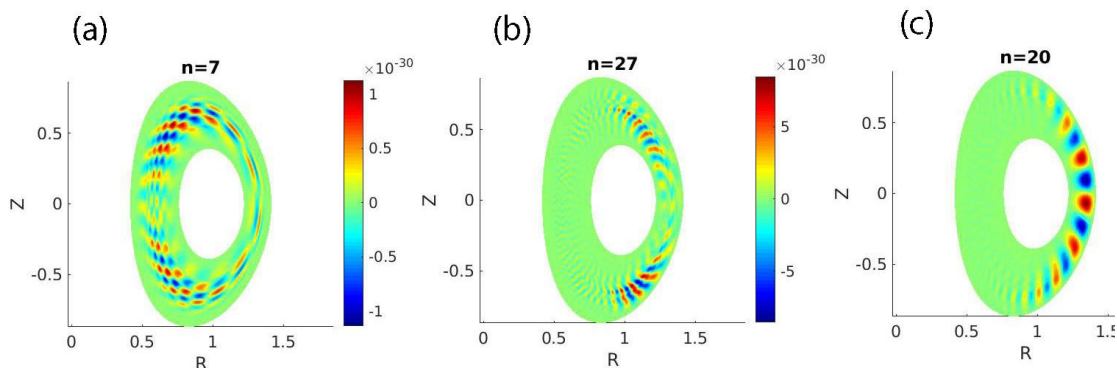


Fig.TT-9. Electrostatic potential ϕ plotted in the poloidal plane of NSTX with increasing electron beta: (a) $\beta_e=0.5\%$, (a) $\beta_e=1.6\%$, (a) $\beta_e=3.2\%$. As beta increases the unstable low-n micro-tearing mode (MTM) (a) which has its maximum on high-field side switches to high-n MTM (b) on low-field side. As beta is increased further, the kinetic ballooning mode (KBM) is destabilized in low field side of NSTX (c).

Progress of electromagnetic simulations using XGC1 for NSTX and NSTX-U plasmas

The XGC1 gyrokinetic code is beginning to study electromagnetic modes for NSTX and NSTX-U plasmas. The goal is to explore the global, multiscale EM physics effects (including micro-turbulence, MHD-like modes, neoclassical physics, neutral particles) on transport and stability in a strongly-toroidal, tight-aspect ratio plasma, while other gyrokinetic codes study the local micro-turbulence effect only. 3D magnetic perturbation physics is also a part of the EM study in XGC1.

At present there are three different XGC1 EM versions that will eventually be combined. The first version uses hybrid gyrokinetic ions and fluid electrons while keeping the kinetic electron density zero [TT-16]. This version studies the EM modes at a much faster speed than the other versions by excluding trapped electron and micro-tearing modes. Gyrokinetic peeling-ballooning modes, resistive tearing modes, kinetic-ballooning modes, ITG, and neoclassical physics are among the important research objectives using this approach. It is expected that the ELM physics will rely mostly on these modes. Kinetic electrons will be turned on at a later time. The second version uses drift-kinetic electrons that can study not only the fluid/MHD type instabilities [TT-17], but also the neoclassical tearing modes, micro-tearing modes, trapped electron modes, kinetic ballooning modes and all other important ion-scale instabilities and turbulence in a toroidal

geometry. ETG modes are being studied only in the electrostatic limit at the present time. Both codes use either explicit or implicit time stepping, with the explicit time stepping being more limited in the physics capability (such as the high Lundquist number plasma in NSTX/NSTX-U). The third EM version is for the 3D RMP magnetic perturbation physics in which the RMP penetration and the plasma transport evolution are calculated self-consistently.

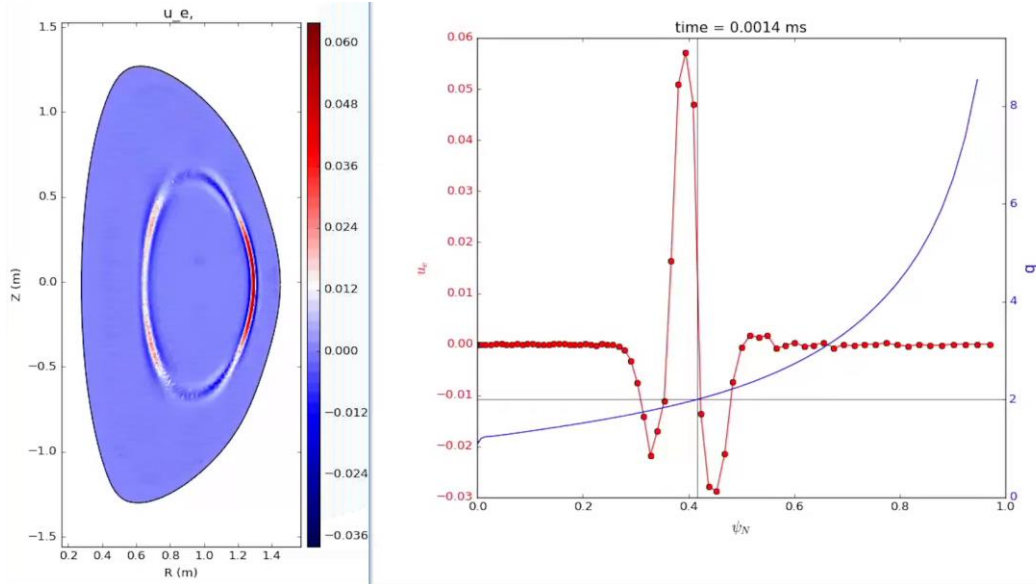


Fig. TT-10. The (2, 1)-type resistive tearing mode from XGC1 around $q=2$ surface in the linear growth stage in the NSTX discharge #139047. The Lundquist number is lowered to $S=2.3 \times 10^5$ for numerical stability in the explicit time stepping taken here. Distortion of the (2,1) tearing mode structure from the high toroidicity of NSTX can be seen.

As examples, Figure TT-10 shows the ($m=2$, $n=1$) resistive tearing parity mode in the NSTX discharge #139047, using the hybrid version with explicit time marching. A lower Lundquist number $S=2.3 \times 10^5$ is used for numerical stability in the explicit time marching. An implicit time marching can improve the Lundquist number to realistic value at a reasonable time-step size [TT-16].

It can be seen that the electron current perturbation from the (2,1) resistive tearing mode is not highly in-out asymmetric as in a cylinder or a large aspect ratio plasma. The mode structure is distorted from the strong toroidicity effect at low aspect ratio. Figure TT-11 depicts the KBM onset study of the same NSTX plasma #139047 using the hybrid XGC1 version spanning in the outer region of the plasma ($0.5 < \Psi_N < 0.9$) showing that the KBM onset occurs for electron beta $\sim 2.5 \times$ larger than the experimental electron beta value $\beta_{e,\text{exp}}$. Local linear GYRO simulations also predicted the onset of KBM in this region to occur for $2-2.5 \times \beta_{e,\text{exp}}$ providing confidence in the ability of both codes to predict KBM thresholds. More comprehensive XGC1 study of global EM physics for NSTX and NSTX-U plasmas is in

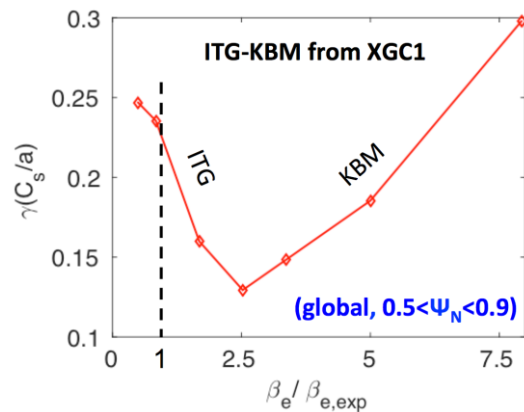


Fig. TT-11. Global XGC1 simulation of the ITG to KBM transition behavior ($0.5 < \Psi_N < 0.9$) of the NSTX discharge 139047, showing that the KBM onset is at $\sim 2.5 \times$ of the experimental electron beta value $\beta_{e,\text{exp}}$ [J. Lang, et al].

progress, which also includes the micro-tearing modes, the edge localized modes, RMP penetration and transport, and others.

4. Collaborations

Two transport experiments lead by NSTX-U team members were chosen to run as part of the DIII-D “NSTX-U Campaign” that was established following the unplanned NSTX-U outage in FY17. These experiments were conducted in July, 2017 and have already provided a number of interesting early results.

DIII-D “NSTX-U campaign” experiment: Study of collisionality dependence of ion- and electron-scale turbulence in advanced inductive hybrid scenario with ST-relevant q_{95} on DIII-D

The strong inverse collisionality dependence of normalized energy confinement time ($B\tau_E \propto \nu_e^{*-1}$) observed in NSTX [TT-18] and MAST [TT-19] is a unique feature of spherical tokamak plasmas and is determined by electron thermal transport [TT-18]. We emphasize that this energy confinement scaling is the primary motivation for NSTX-U. In addition, energy confinement of conventional tokamaks may also have a collisionality dependence. We note that although the present ITER confinement scaling shows weak dependence on collisionality, an analysis of a DIII-D H-mode data set has shown a stronger collisionality dependence, i.e. $B\tau_E \propto \nu_e^{*-0.5}$ [TT-20]. However, the mechanisms underlying the above observed collisionality dependence have not been understood. In order to investigate this important physics problem, an experiment entitled “study of collisionality dependence of ion- and electron-scale turbulence in advanced inductive

hybrid scenario with ST-relevant q_{95} on DIII-D” was carried out on DIII-D as a part of the DIII-D/NSTX-U national campaign. The experiment aims to measure ion- and electron-scale turbulence in a well-controlled dimensionless electron collisionality scan in DIII-D advanced inductive hybrid scenario with a ST-relevant q_{95} and with other dimensionless quantities (e.g. ρ^* , β , T_e/T_i , q) kept approximately constant, leveraging DIII-D’s the well-established experimental procedure of collisionality scan, excellent plasma control system and extensive turbulence diagnostics. The collisionality scan was achieved experimentally by varying B_T and I_p together with B_T/I_p and plasma

density kept constant (with fixed plasma shape), and with electron temperature, T_e , varied as $T_e \propto B^2$ by changing heating power (NBI and ECH), which leads to $\nu_e^* \propto T_e^{-2} \propto B^{-4}$.

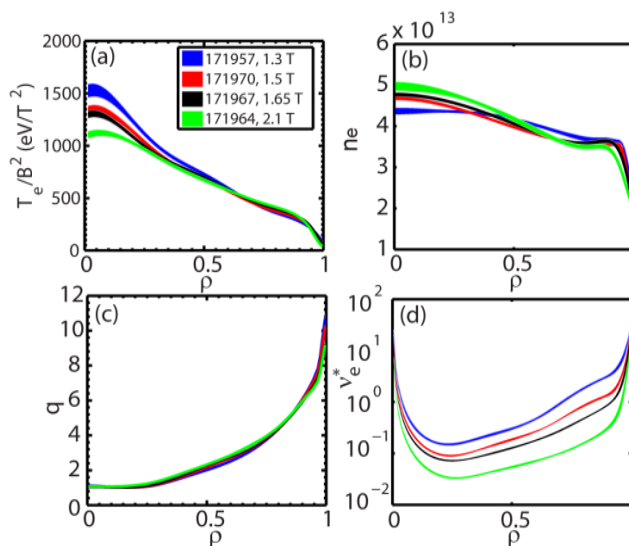


Fig. TT-12. Experimental profiles of some relevant dimensional and dimensionless quantities: (a) normalized electron temperature, T_e/B^2 ; (b) electron density; (c) safety factor, q ; (d) electron collisionality. The experimental profiles are averaged over $t=3$ to 4 s, and widths of the shaded region denote the standard deviation of the time variation between $t=3$ and 4.4 s.

Here we present some initial results from this experiment. Since matching different plasma profiles is essential to the success of this dimensionless collisionality scan, in Fig. TT-12 we show the experimental profiles of some relevant dimensional and dimensionless quantities for discharges with different B_T values (and different electron collisionality). It is clear that the normalized electron temperature, T_e/B^2 , [Fig. TT-12(a)] is well matched among the discharges at $\rho \gtrsim 0.4$, while the matching is worse near the magnetic axis. The matching for the electron density, n_e , seen in Fig. TT-12(b), is similar to that of T_e/B^2 , i.e. good match at $\rho \gtrsim 0.4$ and worse near magnetic axis. On the other hand, q profile [Fig. TT-12(c)] is better matched near magnetic axis than around mid-radius. To quantify the profile matching, we define a matching parameter, $M = (p_1 - p_2)/p_2$, where p is any physics quantity, the subscript denotes different discharges and by definition $p_1 > p_2$. We can then compute M for any two of the four discharges show in Fig. TT-12 as a function of ρ , and we use the maximum of M s computed with any two discharges of the four discharges to represent how well the profiles are matched. For T_e/B^2 , M is less than 9% from $\rho = 0.5$ to 0.7 and is about 30% at $\rho = 0.1$. The matching of n_e is much better across the whole radius, i.e. about 11% for M at $\rho = 0.1$ and less than 6% for M from $\rho = 0.5$ to 0.7. As we have pointed out, the safety factor, q , is much better matched near magnetic axis with an M value of about 4%, while less matched with $M \lesssim 15\%$ from $\rho = 0.5$ to 0.7. The variation of the electron collisionality, ν_e^* , achieved in the experiment can be seen in Fig. TT-12(d) with ν_e^* varied by a factor of about 5.6 at $\rho = 0.5$ and by a factor of about 9.2 at $\rho = 0.7$.

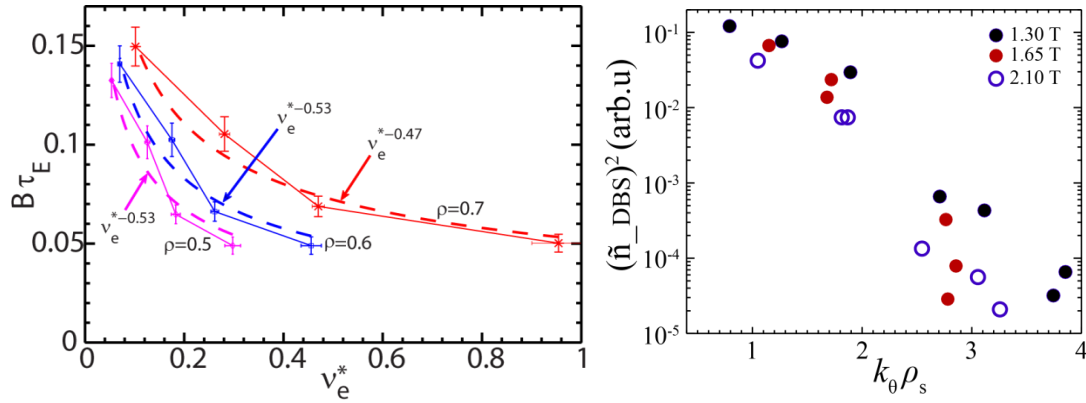


Fig. TT-13. (left) normalized energy confinement time, $B\tau_E$, as a function of ν_e^* at three different radial locations: $\rho = 0.5$ (magenta), $\rho = 0.6$ (blue) and $\rho = 0.7$ (red). The symbols denote experimental values. Note that both τ_E and ν_e^* are functions of ρ . Also note that the four data points in each of the three curves are from the same four discharges with different B_T values (and different collisionality). The energy confinement time, τ_E , is calculated through transport analysis using TRANSP code. The dashed lines are power law fittings to the experimental data with corresponding power law expressions shown in the figure. The error bars denote the standard deviation of the time variation between $t=3$ and 4 s. (right) density fluctuation wavenumber spectra measured by the DBS system at $\rho \sim 0.55 - 0.65$, averaged between $t=3750$ and 4000 ms for different B_T s (and different collisionality) discharges: 1.3 T (black), 1.65 T (red), 2.1 T (purple).

The collisionality dependence of normalized energy confinement time, $B\tau_E$, is shown in the left panel of Fig. TT-13. Since both τ_E and ν_e^* are functions of ρ , three curves corresponding to $\rho = 0.5, 0.6$ and 0.7 are shown. The best power law fittings to these three curves are also shown, where scalings, i.e. $B\tau_E \propto \nu_e^{*-0.53}$, $B\tau_E \propto \nu_e^{*-0.53}$ and $B\tau_E \propto \nu_e^{*-0.47}$, are found for $\rho = 0.5, 0.6$

and 0.7, respectively. The fact that all three power law fittings have an exponent of about -0.5 supports the validity of the power-law fittings. We note that confinement scalings shown in the figure are consistent with what was found for DIII-D H-mode plasmas, i.e. $B\tau_E \propto \nu_e^{*-0.5}$ [TT-20]. In the right panel of Fig. TT-13, we show the density fluctuation wavenumber spectra measured by a Doppler Back Scattering (DBS) system on DIII-D [TT-21]. The measurements were made at $\rho \sim 0.55-0.65$ (averaged between $t=3.75$ and 4 s) and cover a wavenumber range of $k_\theta \rho_s \sim 0.8 - 4$. It can be seen that the measured spectral power clearly decreases at lower wavenumbers, i.e. $k_\theta \rho_s \lesssim 2$, as B_T increases (collisionality decreases), consistent with the improved confinement at lower collisionality shown in the left panel Fig. TT-13. At higher wavenumbers, i.e. $k_\theta \rho_s \gtrsim 2$, the dependence on collisionality is less clear. While the 1.3 T case clearly shows larger spectral power, the difference between the 1.65 T and 2.1 T cases may be small. Further analysis is ongoing to understand the observed confinement scaling and turbulence variation with collisionality.

DIII-D “NSTX-U campaign” experiment: Validating electromagnetic effects in high performance plasmas

Identifying and validating the transport mechanisms responsible for setting confinement scaling in NSTX-U at high beta is a top priority of the NSTX-U Five Year Plan. Measuring internal magnetic field fluctuations associated with these EM effects, and using them to validate directly the gyrokinetic predictions, is a key priority to distinguishing which mechanisms are the most important, depending on operational regime. The UCLA diagnostic group currently is funded to implement in NSTX-U a cross-polarization scattering (CPS) measurement that is sensitive to local, internal δB perturbations. A CPS system has recently been installed on DIII-D and already acquired initial data [TT-22,23], offering the possibility of using this measurement now in dedicated core transport validation studies. This was the main motivation for this DIII-D “NSTX-U campaign” MP.

The MP utilized low-density QH-modes as these allow for deep core access ($\rho \sim 0.3$) of DBS and CPS scattering measurement. Previous validation studies also demonstrated that the inclusion of electromagnetic fluctuations in nonlinear GYRO simulations provides significant stabilization of ITG/TEM turbulence, critical to achieving quantitative agreement with experimental fluxes and DBS measurements [TT-24,25]. This effect has been predicted in other machines like JET and ASDEX-UG and is likely important to include to correctly project fusion gain for ITER. The strong EM effects occur as the deep-core profiles are within $\sim 10\%$ of the KBM threshold

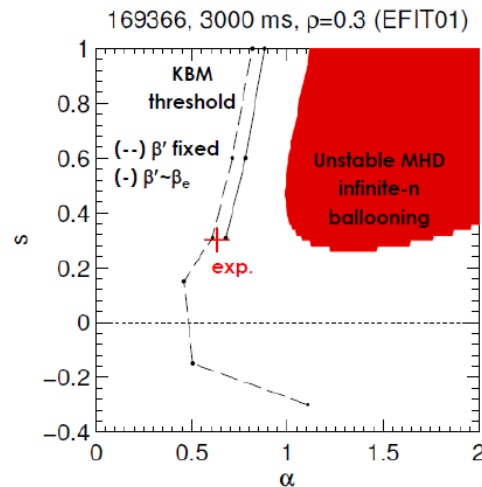


Fig. TT-14. Stability threshold of ideal MHD infinite- n ballooning modes vs. total normalized pressure gradient (α) and magnetic shear (s) at $\rho=0.3$ for a target DIII-D QH-mode. Solid lines show the KBM threshold calculated by linear GYRO. The experimental value of (α, s) is shown by the red + to be very close to the KBM threshold.

($\alpha/\alpha_{\text{crit}} \approx 0.9$, where $\alpha = -q^2 R \nabla P \cdot 2\mu_0 / B^2$ is the relevant normalized pressure gradient and α_{crit} is the KBM threshold). Linear ideal-MHD infinite-n ballooning mode and linear GYRO simulations of KBM were used to verify the target shot was similarly close to the KBM limit (Fig. TT-14), and strong EM coupling is therefore expected. Additional scoping simulations were performed to predict how the KBM threshold varies with T_i/T_e and $\eta_i = L_n/L_{Ti}$ to identify how $\alpha/\alpha_{\text{crit}}$ and the expected strength of EM stabilization can be varied experimentally [TT-26].

Figure TT-15 shows density profiles obtained from the run day for two discharges obtained as part of a beta scan ($\beta_N = 1.5$ to 2.3). Time slices were chosen to best match the DBS/CPS scattering locations in the two different shots as predicted by GENRAY calculations, shown by the circle symbols. The square symbols show where additional DBS measurements were obtained from the higher-frequency W-band DBS system on loan from the UCLA/NSTX-U collaboration. Fig. TT-16 shows DBS and CPS power spectra for the same density profiles in Fig. TT-15 at $\rho \sim 0.5$. There are a few observations to note. First, the DBS signal is centered at ~ 2000 kHz due to the Doppler shift ($k_\theta \cdot V_{E \times B}$) at relatively high k_θ of the scattering geometry for this configuration ($k_\theta \gg k_r$ for DBS). The signal at $f \sim 0$ is from spurious radiation and is slightly dimmed for clarity. On the other hand, the CPS signal is centered at around $f \sim 0$ as $k_\theta \ll k_r$ for the CPS geometry so little Doppler shift expected. [Part of the run day was spent trying to optimize vertical position of the plasma to measure more favorable wavenumbers. Unfortunately a power supply current limit in one of the shaping F-coils limited the available shift.] The CPS measurement was performed by injecting X-mode waves from one antenna while receiving O-mode waves from a separate antenna. Tests using X-mode collection show the collected signal drops considerably,

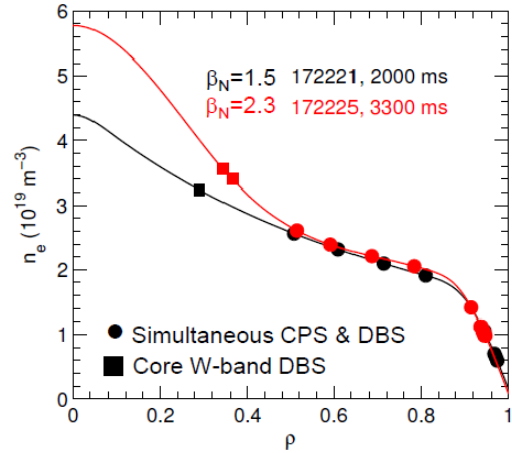


Fig. TT-15. Density profiles from two discharges as part of the beta scan ($\beta_N = 1.5, 2.3$ respectively). The circle symbols indicate locations of simultaneous DBS and CPS measurements. The square symbols indicate locations of the higher frequency (W-band) DBS system on loan from NSTX-U.

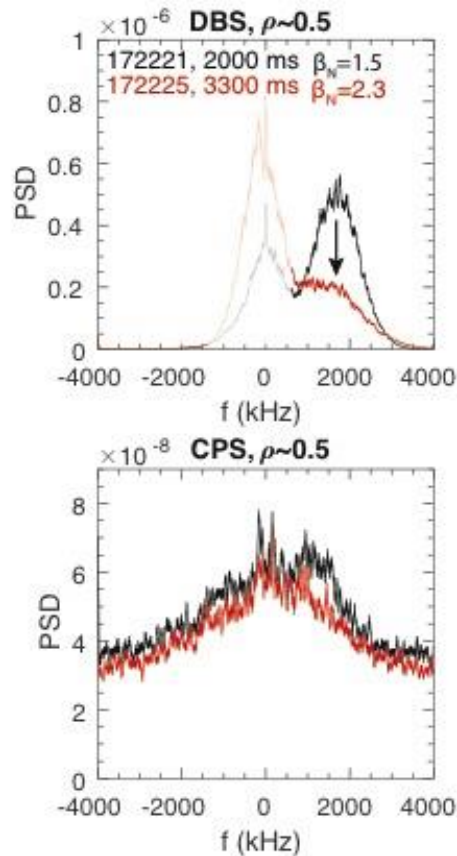


Fig. TT-16. Power spectra measured from (top) DBS and (bottom) CPS at $\rho \sim 0.5$ for the two discharges shown in Fig. TT-15 at two different values of β_N .

providing initial confidence that the signal is in fact due to δB fluctuations and not from contamination due to scattering or reflection of the launched X-mode. As beta is increased from shot-to-shot (by increasing NBI power), the measured DBS power drops significantly while the CPS amplitude remains largely unchanged. Naively, one might expect the CPS amplitude to increase at higher beta if it is in fact proportional to δB . However, the relative change in DBS and CPS amplitudes suggests the ratio of $\delta B/\delta n$ has increased, which is what is expected at increasing beta, although this interpretation is very preliminary. Considerable analysis, including full wave simulations along with gyrokinetic predictions coupled to synthetic diagnostics, are now being pursued to help clarify the interpretation of the CPS measurements.

MAST perturbative momentum transport

The perturbative momentum transport experiment performed in MAST to investigate momentum pinch in L-mode [TT-27] has been recently been published [TT-28]. This work showed that a very weak momentum pinch is predicted in spherical tokamak L-mode experiments. Although there is large uncertainty in the time-dependent data, the experimental measurements overlap with the predictions. As part of this work, additional physical mechanisms that can influence the rotation profile were considered. As an example, up-down flux surface asymmetry can also lead to a residual stress momentum flux, $\hat{\Pi}_\phi = \hat{\chi}_\phi \left[u' + (RV_\phi / \chi_\phi) u + \hat{C}_{ud} / \hat{\chi}_\phi \right]$ which may be expected to contribute in the MAST experiment given the strong lower-biased equilibrium used (Fig. TT-17). In addition to predicting Pr and RV_ϕ / χ_ϕ , the quasi-linear gyrokinetic simulations were also used to predict C_{ud} / χ_ϕ . Fig. TT-17 shows the comparison of the diffusive component (u'), convective component ($RV_\phi / \chi_\phi \cdot u$) and the residual stress component ($\hat{C}_{UD} / \hat{\chi}_\phi$) in the MAST L-mode. The residual stress is inward directed over most of the radius, but relative to

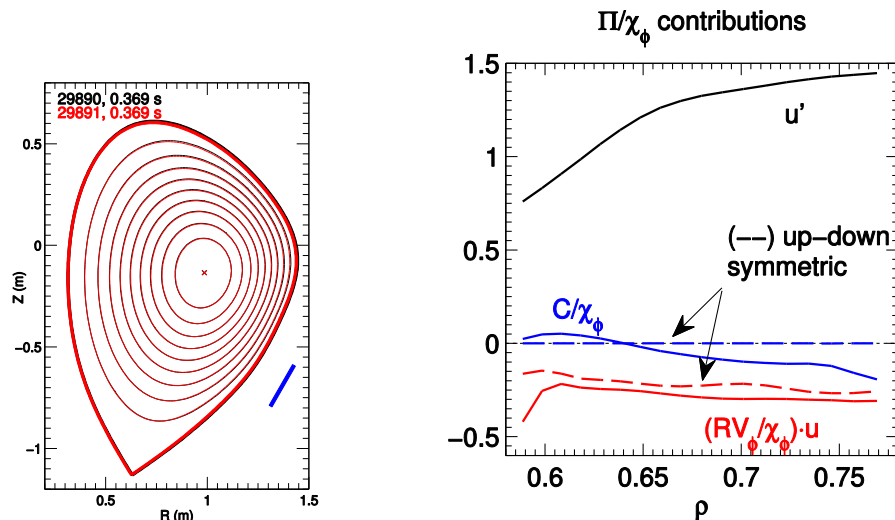


Fig. TT-17. (left) Flux surfaces from MSE-constrained EFIT++ (axisymmetric) reconstructions for two MAST-L-mode discharges used in the perturbative momentum transport experiment. The straight blue line indicates the position of the lower 12 coils used to generate the $n=3$ field. (right) Predicted contributions to the normalized momentum flux from local, quasi-linear gyrokinetic simulations. Solid lines use the EFIT++ equilibrium surface as represented by a Fourier expansion. The dashed lines represent the same surfaces but with the up-down asymmetric Fourier components set to zero.

diffusion is even smaller than the already weak pinch. To verify this residual stress is in fact due to the up-down asymmetry, additional simulations were run removing the up-down asymmetry of the flux surfaces [48]. The resulting predictions give zero residual stress and a very similar pinch contribution (dashed lines in Fig. TT-17).

References

- [TT-1] W. Guttenfelder et al., APS-DPP oral, San Jose (2016).
- [TT-2] S.M. Kaye et al., APS-DPP, San Jose (2016).
- [TT-3] D.M. Kriete et al., APS-DPP, San Jose (2016).
- [TT-4] W. Guttenfelder et al., Nucl. Fusion (in review).
- [TT-5] N.T. Howard et al., Nucl. Fusion **56**, 014004 (2016).
- [TT-6] F. Jenko et al., Nucl. Fusion **53**, 073003 (2013).
- [TT-7] F.M. Poli et al., Phys. Plasmas **17**, 112514 (2010).
- [TT-8] F.M. Poli et al., APS-DPP, Chicago (2010).
- [TT-9] J. Ruiz-Ruiz et al., Phys. Plasmas **22**, 122501 (2015).
- [TT-10] J. Ruiz-Ruiz et al., to be presented at APS-DPP, Milwaukee (2017).
- [TT-11] E.D. Fredrickson et al., Nucl. Fusion **55**, 013012 (2015).
- [TT-12] S. Tang et al., US/EU-TTF plenary talk, Williamsburg (2017).
- [TT-13] E.V. Belova et al., Phys. Plasmas **24**, 042505 (2017).
- [TT-14] W.X. Wang et al., Nucl. Fusion **55**, 122001 (2015).
- [TT-15] W.X. Wang et al., Phys. Plasmas **22**, 102509 (2015).
- [TT-16] R. Hager et al., Phys. Plasmas **24**, 054508 (2017)
- [TT-17] S. Ku et al., APS-DPP, San Jose (2016).
- [TT-18] S. M. Kaye, et al., Phys. Rev. Lett. **98**, 175002 (2007)
- [TT-19] M. Valovic, et al., Nucl. Fusion **51**, 073045 (2011)
- [TT-20] T. Luce, et al., Plasma Phys. Controlled Fusion, **50**, 043001 (2008)
- [TT-21] T.L. Rhodes et al., Rev. Sci. Instrum., **81**, 10D912 (2010)
- [TT-22] T.L. Rhodes et al., Rev. Sci. Instrum. (2014); Rev. Sci. Instrum. (2016).
- [TT-23] K. Barada et al., RSI (2016).
- [TT-24] W. Guttenfelder et al., APS-DPP, Savannah (2015).
- [TT-25] D.R. Ernst et al., Phys. Plasmas **23**, 056112 (2016).
- [TT-26] W. Guttenfelder et al., to be presented at APS-DPP, Milwaukee (2017).
- [TT-27] W. Guttenfelder et al., IAEA-FEC, Kyoto (2016).
- [TT-28] W. Guttenfelder et al., Nucl. Fusion **57**, 056022 (2017).

C. Energetic Particles TSG Research Highlights

Energetic particle research in FY-17 has focused on improving numerical tools for analysis, simulation and prediction of energetic particle driven instabilities and for interpretation of experimental data.

New data collected during the initial NSTX-U operation in FY-16 have contributed to EP-TSG achievements in FY-17. In particular, first results obtained with the 2nd, more tangential NB line have expanded the parameter range previously achievable on NSTX. The enhanced flexibility in controlling the fast ion distribution parameters from NBI have revealed new physics for Alfvénic instabilities, as discussed more in detail below and in the Summary of Research Milestone R17-4. Several research activities by the Energetic Particle TSG have been conducted in collaboration with other institutions and facilities. Specific collaborations will be discussed throughout the following Sections.

1. Improve simulation and analysis tools for EP-driven instabilities

Considerable progress has been made in FY-17 towards the development and validation of numerical tools. One of the main lines of research is the development of reduced models to account for the effects of instabilities on the energetic particle population.

In the past years, the so-called “kick model” has been implemented in the NUBEAM module of the TRANSP code. More recently, coupled TRANSP + kick model simulations have been successfully used to interpret experiments from NSTX and DIII-D scenarios [EP-1][EP-2][EP-3][EP-4]. Work in FY-17 has built upon the “interpretive” use of the reduced model to explore the possibility of “predictive” runs, from which linear stability and saturation amplitude of the instabilities can be inferred. In essence, the kick model probability function in TRANSP simulations provide an estimate of the power exchanged between fast ions and each specific set of instabilities used in the simulation. The computed power represents the “drive” term (if positive) for the instabilities. By knowing the damping rates, e.g. from the NOVA-K code, one can estimate the mode amplitude for which drive and damping compensate each other – that amplitude represents the “saturation amplitude”. Initial tests for a well-diagnosed NSTX discharge show that TRANSP + kick model predictions are consistent with experimental data on fluctuation amplitude from the UCLA reflectometers [EP-5], see Fig. EP-1. The same procedure has been applied to a NSTX-U discharge with tangential injection from the 2nd NBI line. Quite surprisingly, after an initial phase with unstable co-propagating TAE modes, the off-axis NBI results in the destabilization of *counter*-propagating TAEs with low toroidal mode number, $|n|=1-2$. Time-dependent analysis through TRANSP and kick model reveals the basic mechanisms that lead to unstable counter-TAEs, namely the formation of a hollow fast ion density profile [EP-6]. Overall, TRANSP modeling successfully reproduces the main features observed in the experiment, such as the transition from co- to counter-propagating unstable TAEs (Fig. EP-2).

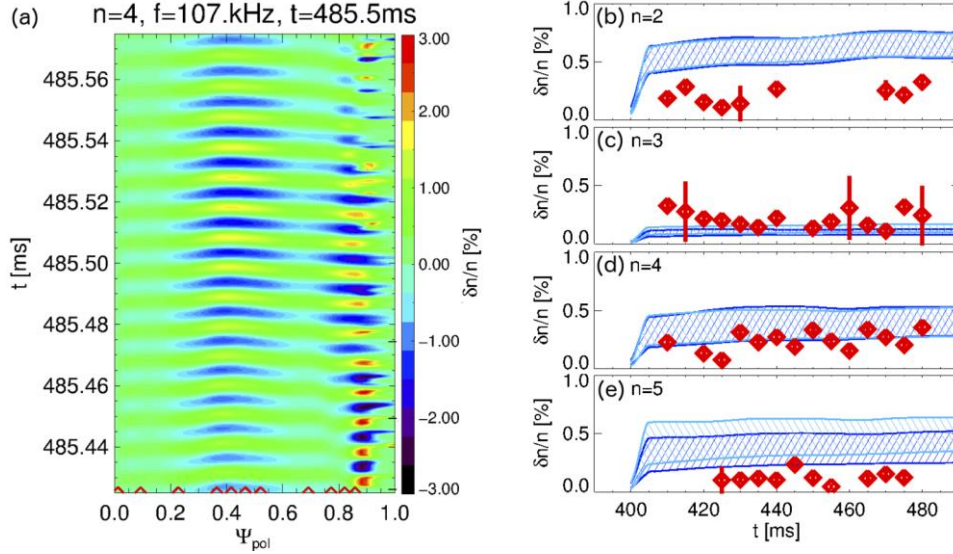


Figure EP-1: (a) Reconstructed time evolution of radial density perturbations from UCLA reflectometer data. Measurement locations are indicated by the red diamonds. (b-e) Comparison between measured (symbols) and predicted (hashed regions) density fluctuations. Kick model results from two sets of modes are shown with light/dark blue. For each set, amplitude is computed assuming damping rates from NOVA-K and for a constant value $\gamma_{damp}/\omega = 1\%$.

It should be noted that the new approach through the time-dependent kick model has also highlighted the high sensitivity of the results on the values of damping rate, as pointed out in previous work using the ORBIT code [EP-7]. This conclusion is further confirmed by initial tests on a DIII-D discharge.

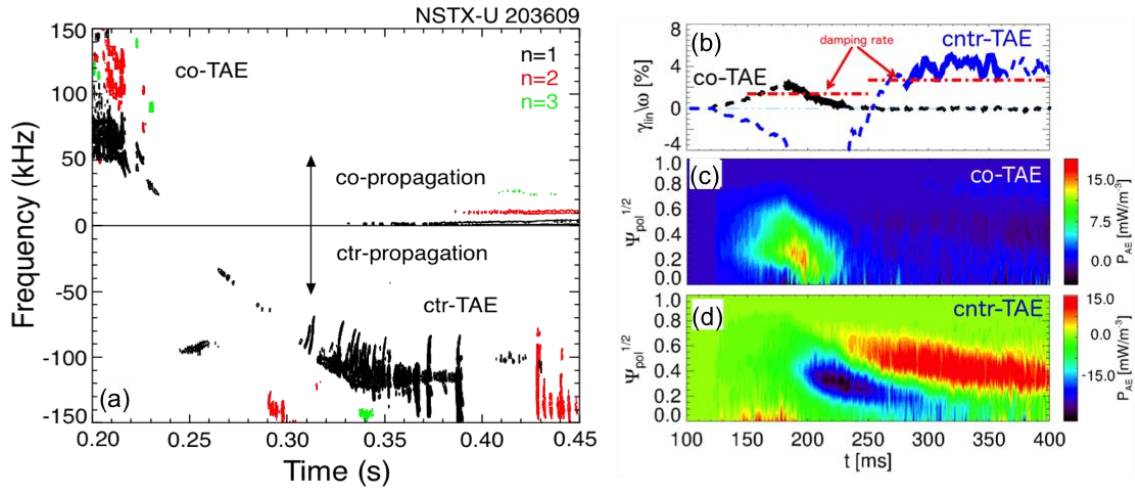


Figure EP-2: (a) Fluctuation spectrum from Mirnov coils showing the transition from co- to counter-propagating TAEs with $|n|=1$. (b) Computed linear growth rate from kick model. Solid lines indicate the range of confidence for the kick model analysis. Dot-dashed lines represent the damping rate from NOVA-K. (c-d) Radial profile vs time of the power transferred from fast ions to the modes (NUBEAM/TRANSP simulation), showing the complex balance of stabilizing/destabilizing regions when a hollow fast ion profiles develops after $t \sim 250$ ms.

In parallel with the validation work of the “kick model” in TRANSP, a second approach for the development of reduced EP transport models has been pursued. This approach is based on the quasi-linear theory for fast ion transport by Alfvén eigenmodes, originally proposed by Berk and co-workers [EP-8]. Recent developments in collaboration with the University of Sao Paulo (Brazil) have included the effect of resonance broadening on the wave-particle interaction processes, leading to the formulation of the so-called RBQ-1D model [EP-9]. At present, the

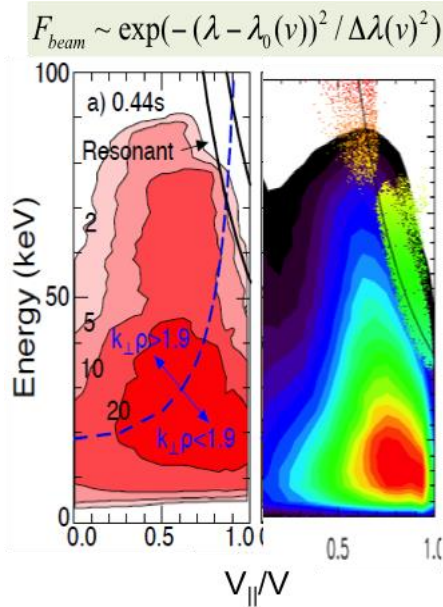


Figure EP-3: (a) TRANSP fast-ion distribution for $t=0.44$, resonant line for $n=-11$ GAE; (b) HYM fast-ion distribution from $n=-10$ GAE simulations. Dots show resonant particles.

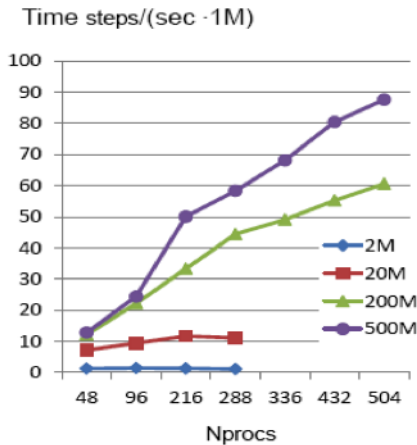


Figure EP-4: Parallel scaling of the HYM code for different number of simulation particles, from 2M up to 500M.

The improved capabilities that are being developed and implemented as part of the NUBEAM/TRANSP framework are the starting point the development of a energetic particle

model assumes that (i) fast ion transport by instabilities such as TAEs and RSAEs mostly occurs in the canonical angular momentum variable (hence, the “1D” tag in the code’s acronym), and (ii) modes achieve a saturated state (that is, no bursting character). So far, the development and validation of the RBQ-1D model has been conducted under the PPPL/DIII-D collaboration and details on initial results will be reported elsewhere. Initial validation for DIII-D scenarios with quasi-stationary TAEs/RSAEs is in progress. To validate the model, the same infrastructure implemented in NUBEAM/TRANSP is used. Namely, a post-processor for the RBQ-1D has been implemented in the NOVA-K code to provide the “transport probability matrices” that describe energetic particle transport in NUBEAM, similarly to what is done for the kick model. The NSTX-U EP-TSG is also expected to provide additional validation scenarios to explore the applicability of the RBQ model to instabilities that present intermittent, bursting behavior.

Predictions from both kick and RBQ-1D models benefit from additional information on the expected character of the instabilities that cause fast ion transport. The work reported from FY-16 on the development of an improved criterion for predicting the nature of Alfvénic instabilities – quasi-stationary vs. bursting/chirping – has made further progress with improved comparison between predictions and experiments [EP-10]. As for the RBQ model development, this activity is also part of an ongoing collaboration with the University of Sao Paulo (Brazil).

transport module for integrated simulations. This task fits within an ambitious, multi-year project recently funded by DoE (ISEP/SciDAC grant 2017).

Activities for the development and validation of reduced models mostly target instabilities in the TAE range of frequency. Characterization and simulation of higher-frequency instabilities near the ion cyclotron frequency, such as CAE and GAE modes, require a different approach. Progress in this area, related to Research Milestone R17-4, is discussed in a separate Section. Only the main achievements are summarized here below:

- NSTX-U operation in FY-16 with a 2nd, more tangential NB line has considerably expanded the parameter range for studies of sub-cyclotron frequency Alfvénic instabilities.
- Experimental results show GAE suppression by tangential NBI.
- Stability predictions through the HYM code compare well with experimental results.
- Parameter scans with the HYM code predicts relevant modifications of GAE properties caused by energetic particles with respect to ideal MHD predictions.
- The eigenmode solver CAE3B is being validated to complement HYM simulations for the assessment of CAE properties against experimental data.
- A database has been compiled to assess high-frequency AE properties vs experimental plasma and NBI parameters.

To achieve those results, the HYM code has been improved in two important areas. A more realistic representation for the equilibrium beam ion distribution function, $F_{\text{beam}}(\lambda)$, has been implemented in the code, leading to a better fit to the NUBEAM/TRANSP data. In particular, the pitch-angle parameter distribution now allows for energy dependent peak value and width in $F_{\text{beam}}(\lambda)$, see Fig. EP-3. The new model allows for multiple beams with different parameters to be included in the simulation. The modified distribution function has been used to study the stability of counter-propagating GAEs in NSTX-U experiments [EP-11]. Linear simulations demonstrate an improved agreement of the calculated growth rates with the experimental estimates.

The parallel scaling in the HYM numerical model has also been improved to enable the use of a larger number of processors, and faster execution time [EP-12] (Fig. EP-4). The domain decomposition in the HYM code has been modified to allow more efficient mapping between the particle grid and field grid, and use up to 500 processors for a moderate size computation grid. The new version of the code can use up to 500M simulation particles, and will allow simulations using full kinetic description of the thermal ions, which is essential for simulations of KAW and ICE in NSTX and NSTX-U.

In addition to development and validation of numerical codes, analysis of experimental data has also made progress in FY-17. New results have been submitted to the journal Nuclear Fusion showing measurements of the internal amplitude and structure of CAE and GAE density perturbations in NSTX. These measurements are being compared with the CAEs and GAEs from simulations by the Hybrid MHD code (HYM) and the results will be presented in an invited talk at the 15th IAEA Technical Meeting on Energetic Particles in Magnetic Confinement Systems in (Princeton - NJ, Sep. 2017).

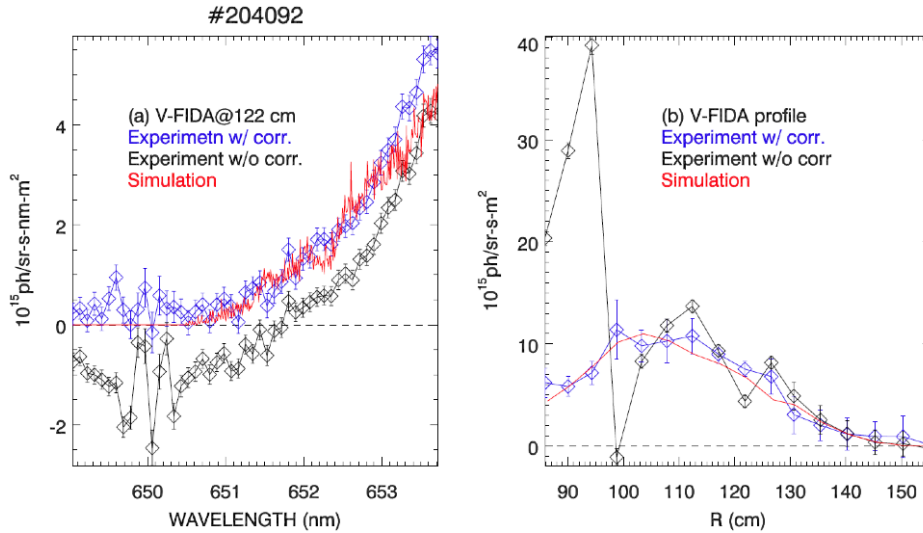


Figure EP-5: Comparison of (a) FIDA spectra and (b) FIDA spatial profile from measurements with (blue) and without (black) scattering correction and FIDASIM simulations (red).

Analysis of Fast-ion D-alpha (FIDA) data on NSTX-U shows that the cold D_α line can significantly contaminate the baseline of FIDA spectra, which make it challenge to extract the net FIDA signal. A scattering correction approach based on the singular value decomposition (SVD) has been developed in the FIDA data analysis. After scattering correction, a much better agreement is achieved between both FIDA spectra and spatial profiles and predictions from the FIDASIM code, see Figure EP-5. This scattering method works reasonably well for most fibers, but fails in a few innermost fibers in some cases because those active and passive views intercept the divertor at different radii. A paper entitled with “On the scattering correction of fast-ion D-alpha signal on NSTX-U” has been submitted to Rev. Sci. Inst. [EP-13].

Recent analysis of Fast-ion D-alpha (FIDA) data on NSTX-U shows that, owing to the large fast-ion gyro-radius, passive FIDA signal is relatively large and it can be comparable with active FIDA signal. Here, *active* FIDA means active D-alpha emission from reactions between fast ions and beam neutrals, while *passive* FIDA denotes the radiation emitted by the reactions between fast ions and background neutrals. Figure EP-6 shows the temporal evolution of measured and simulated FIDA signals during a “beam-blip” discharge from a vertical-FIDA (v-FIDA) channel and tangential FIDA (t-FIDA) channel with $R=117\text{cm}$. In the first beam blip with source 1C, the measured FIDA signal is the combination of active and passive FIDA signals since the sightline of both v-FIDA and t-FIDA systems intersects with the beam 1A footprint. In the second beam blip with source 2A, the measured FIDA signal is purely passive FIDA signals because FIDA sightlines do not intersect with the footprint of 2A. The experimental data clearly shows that the passive FIDA signal can be comparable with active FIDA signal. It also shows the passive-FIDA light has the expected dependence on beam injection geometry. For v-FIDA, the passive light is largest when the more perpendicular source (1C) is injected. For t-FIDA, the signal is equally large when the more tangential source (2A) injects. A paper entitled “Measurement of the passive fast-ion D-alpha emission on the NSTX-U tokamak” is in preparation [EP-14].

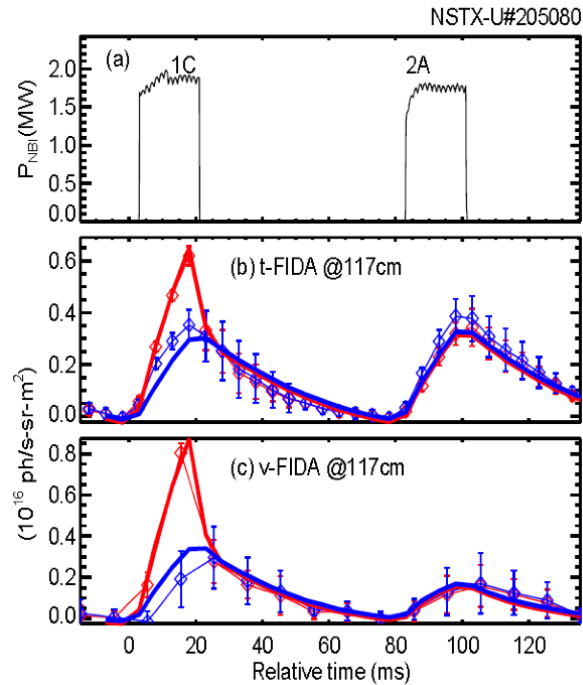


Figure EP-6: Time evolution of (a) beam power, (b) a tangential-FIDA signal and (c) a vertical FIDA signal in NSTX-U. The red data points are from active views, while the blue points are from reference views. The curves are FIDASIM predictions of the passive light (blue) and the active + passive light (red). The passive FIDA signal is comparable in magnitude to the active FIDA signal.

References

- [EP-1] Podestà, M. et al., Phys. Plasmas 23, 056106 (2016)
- [EP-2] Podestà, M. et al., Nucl. Fusion 56, 112005 (2016)
- [EP-3] Collins, C. C. et al., Nucl. Fusion 57, 086005 (2017)
- [EP-4] Heidbrink, W. W. et al., Phys. Plasmas 24, 056109 (2017)
- [EP-5] Podestà, M. et al., Plasma Phys. Control. Fusion 59, 084005 (2017)
- [EP-6] Podestà, M. et al., Phys. Rev. Lett. (submitted 2017)
- [EP-7] White, R. B. et al., Plasma Phys. Control. Fusion 58, 115007 (2016)
- [EP-8] Berk, H. et al., Nucl. Fusion 35, 1661 (1995)
- [EP-9] Ganthous, K. et al., Phys. Plasmas 21, 032119 (2014)
- [EP-10] Duarte, V. et al., Nucl. Fusion 57, 054001 (2017)
- [EP-11] Fredrickson, E. D. et al, Phys. Rev. Lett. 118, 265001 (2017).
- [EP-12] Belova, E. V., EPR Workshop, Vancouver Canada (2017)
- [EP-13] Hao, G. et al., Rev. Sci. Instrum. (submitted 2017)
- [EP-14] Hao, G. et al., Plasma Phys. Control. Fusion (in preparation 2017)

III. Integrated Scenarios Research Highlights

The integrated scenarios group is tasked with understand the following elements within the NSTX-U program:

- ST startup & ramp-up,
- HHFW heating and current drive,
- neutral beam current drive,
- axisymmetric plasma control,
- fully non-inductive plasma scenarios, including non-inductive ramp-up, and
- integration of the above elements amongst themselves, and with the scientific understanding achieved in the other science groups.

As in FY-16, the science group is led by Stefan Gerhardt (PPPL), with Roger Raman (U. of Washington) as the deputy. The science group is divided into three topical science groups (TSGs), as follows in the list below. This leadership is the same as in FY-16.

- A. The **Solenoid Free Plasma Startup** (SFPS) TSG is tasked with understanding solenoid free startup-up and ramp-up. The TSG leader is Dennis Mueller (PPPL) with Roger Raman as the deputy. Fatima Ebrahimi (Princeton University) acts as the theory and modeling representative.
- B. The **Wave Heating and Current Drive** (WHCD) TSG is tasked with understanding the physics and technology of HHFW, ECH, and potentially EBW, in the unique plasma conditions and geometry of the ST. The group is led by Rory Perkins (PPPL), with Joel Hosea (PPPL) as the deputy. Nicola Berteli (PPPL) is the theory and modeling representative, and Paul Benoli (MIT) is the university representative.
- C. The **Advanced Scenarios and Control** (ASC) TSG is tasked with understanding axisymmetric plasma control, scenarios with very high non-inductive current fraction or very long pulse, and discharge scenario development in general. The TSG leader is Devon Battaglia (PPPL), with Stefan Gerhardt as the deputy. Francesca Poli (PPPL) is the theory/modeling representative, and Prof. Egemen Kolemen (Princeton University) is the University representative.

A. Solenoid-Free Start-up and Ramp-up TSG Research Highlights

A.1 CHI and ECCD on QUEST

During the past year, we were able to fully commission the newly installed transient CHI system on QUEST. This was completed in two parts. First, during March 2016, University of Washington personnel traveled to Kyushu University to test and commission the CHI capacitor bank, CHI gas injection systems and the hi-voltage snubber systems in a laboratory located near the QUEST ST. The control system to operate these from the QUEST Control Room was also tested, and some hardware improvements for the capacitor bank and control system were identified. Between April and November the additional needed hardware was built. QUEST personnel also moved the capacitor bank to the QUEST Test Cell (Fig. IS-SFSU-1), built a protective cage around the capacitor bank, and connected the capacitor bank to the three CHI current feed locations on QUEST. QUEST personnel also installed the two gas injection systems and installed three high voltage snubber assemblies to the current feed locations on QUEST.

Then during December 2016, University of Washington personnel traveled to QUEST to fully commission the CHI system. The goals were to establish reliable gas breakdown and measure toroidal current generated by CHI.

QUEST is the largest ST in Japan

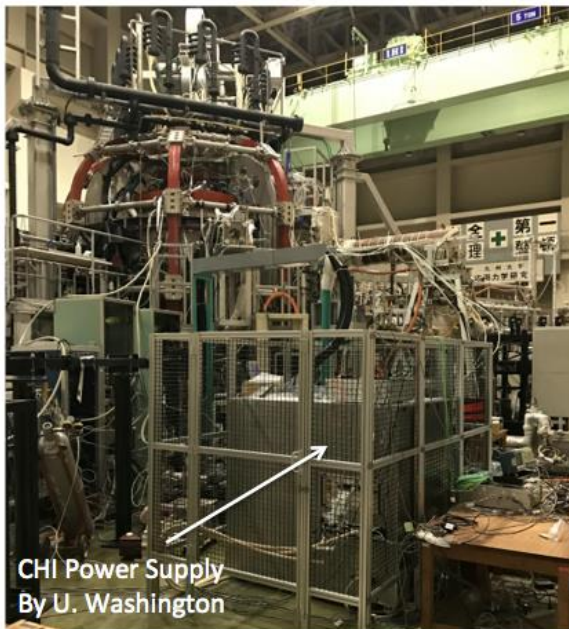


Figure IS-SFSU-1: QUEST ST will test ECH heating of CHI in an all-metal configuration using a new CHI electrode configuration.

The first week was spent commissioning the CHI capacitor bank and the two fast CHI gas injection systems, both of which were now attached to the QUEST machine. During these non-plasma tests remote control operation of both systems was tested, and the QUEST vessel was subjected to 600V for the first time. During the second week, reliable plasma breakdown was demonstrated for the first time in the new ST-FNSF relevant CHI electrode configuration used on QUEST. During these tests, the QUEST vessel was subjected to the full 2kV CHI voltage potential. This was followed by operation with increased capacitor bank energy using two switching ignitrons to generate at least 18 kA of toroidal current. A slow visible camera showed plasmas detaching from the CHI electrode and drifting up. The magnitude of the toroidal current is similar to that

achieved on NSTX during first CHI commissioning tests on NSTX. A journal paper summarizing these first experimental results was published.

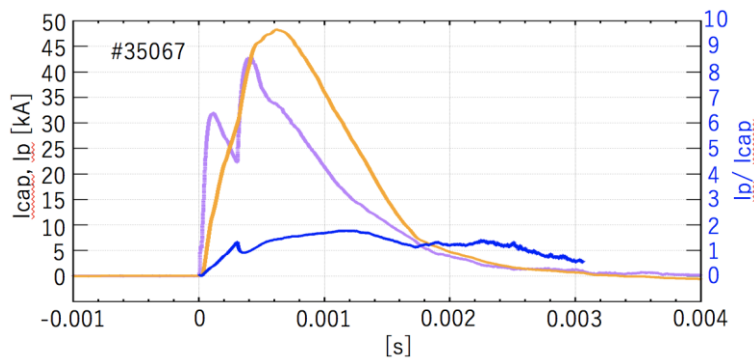


Figure IS-SFSU-2: Traces from a transient CHI discharge on QUEST showing the attainment of 48kA of CHI generated toroidal current and attainment of current multiplication factors of 9, with a peak injector current of 42kA.

also commissioned during CHI plasma discharges. This was followed by quickly re-establishing discharges conducted during the December, 2016 campaign. During the second week, significant progress was made in four areas. First, the CHI produced toroidal current was increased from 29kA (achieved in December 2016) to 48kA. Second, the current multiplication ratio at peak injected current was increased from 0.75 to over 1.5. Third, during the design phase of the new biased electrode system for QUEST, it was believed that this configuration might be more prone to absorber arcs. During this run, improved camera measurements of the lower divertor region identified the occurrence of absorber arcs. However, through proper programming of the poloidal field coils, and gas injection conditions, these arcs could be readily controlled. Fourth, the absorber arc control allowed us to initiate a new discharge configuration in a narrower injector flux footprint configuration, with the use of higher vertical fields, to conduct useful scans of the vertical field, the applied CHI voltage, and the impact of operating with a single gas valve. During these two weeks of CHI experiments, the CHI engineering systems operated with 100% reliability with no issues. An example of a high-current discharge obtained during this campaign is shown in Figure IS-SFSU-2.

CHI on QUEST is lead by the University of Washington. These tests represent the effort of over three years of activities by the University of Washington, PPPL and Kyushu University groups to design, implement and test a new-design (much more reactor relevant) CHI configuration on QUEST. Successful gas breakdown and toroidal current generation, in this new configuration, are major accomplishments for the Transient CHI effort to test solenoid-free plasma current generation in an electrode configuration in which the CHI insulator is not part of the vessel vacuum boundary, as on HIT-II and NSTX devices. [Re: R. Raman, T. Brown, L.A. El-Guebaly, T.R. Jarboe, B.A. Nelson, J.E. Menard, Design Description for a Coaxial Helicity Injection Plasma Start-up System for a ST-FNSF, Fusion Science and Technology **68**, 674 (2015)]. Consequently, the injector current needs to be fed to the electrodes using a custom-design vacuum feedthrough that can withstand large $J \times B$ forces. During over 150 CHI pulses on QUEST; the CHI engineering systems operated with 100% reliability with no issues either to the CHI system or to the QUEST system.

Then during a second campaign in May, the first week was spent on improving the voltage monitoring system on the capacitor bank, re-testing the CHI capacitor bank and improving two fast CHI gas injection systems by using smaller gas injection plenums and increasing the operating pressure from 0.4 to 0.8 MPa. A new fast mid-plane camera system was

The CHI capacitor bank, the large primary CHI insulators, the gas injection system, and the high-voltage snubber systems, and fast voltage monitors were built at the University of Washington and shipped to QUEST, and are “in-kind” USA contributions to CHI effort on QUEST. Unlike other systems that attach to an ST or tokamak on ports that have gate valves to isolate these systems, CHI is an integral part of the ST. High voltages are directly applied to the vessel components. Thus we are especially pleased that our design and engineering was sound and that transient CHI capability, in a new un-tested configuration, was successfully enabled on QUEST without any issues. QUEST CHI activities are now in a position to actively support CHI studies in support of NSTX-U and a ST-FNSF.

The QUEST ST is located in Kyushu University in Japan. It has a major/minor radius of 0.68/0.4 m, the estimated plasma volume is about 4.5 m³. Features present on QUEST, that are absent on HIT-II and NSTX are: 1) It is an all metal system, an aspect which is very desirable for the CHI method as low-Z impurities could be reduced, 2) It is equipped with a high power Electron Cyclotron Resonance (ECH) heating system that will increase the electron temperature of CHI generated discharges, thereby further improving their confinement properties, and provide early data on ECH heating of CHI plasmas in support of NSTX-U experiments, 3) Improvements to the CHI installation concept would allow QUEST to explore CHI in a configuration similar to that which would be more suitable in an ST-FNSF.

ECCD: NSTX-U has a long-term plan to use 28 GHz heating to start-up the plasma current non-inductively, either with electron cyclotron current drive (ECCD) or electron Bernstein wave current drive (EBWCD) [F. M. Poli, et al., Nucl. Fusion **55**, 123011 (2015)]. The goal of the QUEST spherical tokamak program at Kyushu University in Japan is to generate steady-state fully non-inductive plasmas with 8.2, 8.56 and 28 GHz heating and a total of 3 MW of microwave power. NSTX-U researchers began a collaboration with QUEST research in 2017 to develop ECCD and EBWCD plasma current ramp-up. Initial QUEST 28 GHz ECCD plasma current ramp-up experiments had previously used an open-ended waveguide launcher to generate up to 66 kA of non-inductive current with 270 kW of 28 GHz power [H. Idei, et al., “Fully non-inductive second harmonic electron cyclotron plasma ramp-up in the QUEST spherical tokamak”, to be published in Nuclear Fusion (2017)]. This year, a new 28 GHz transmission line with a quasi-optical polarization rotator and focusing mirror launcher was commissioned in July 2017. These experiments generated 85 kA with 230 kW of 28 GHz power. There were however sudden drops in the ECCD that limited the rise in current. These drops were often associated with bursts of Oxygen II emission and will be investigated in future QUEST experiments.

TSC Simulations: We conducted a number of detailed TSC simulations to study the impact of the toroidal field, injector flux, applied voltage, and electron temperature in the NSTX-U CHI configuration. Below, we briefly describe one set of simulations that were conducted in support of a NSTX-U decision point to assess the benefits of the PF1BL coil on NSTX-U.

For Transient CHI the primary parameter that determines the maximum closed flux current that can be generated in a ST is the magnitude of the injector flux. By knowing how much magnetic flux connects the positive and negative electrode, one can place an upper limit on the maximum possible closed flux current that can be generated in a device.

The magnitude of the injector flux available from PF1CL is about 200 mWb. PF1BL provides an additional ~75 mWb. Simulations with TSC show that if PF1BL is used (in addition to PF1CL), the current generated by CHI could be increased from ~400 kA to over 600 kA (Fig. IS-SFSU-3).

It is important to note that for Transient CHI on NSTX-U, PF1CL is the primary coil, PF1BL is not essential; however PF1B is a very important coil for the reasons described below.

- 1) Non-inductive current ramp-up: The present NSTX-U plan is to generate 400 kA of closed flux current using Transient CHI, and then to ramp-up this current to ~0.8 to 1 MA. If the initial target current that can be generated on NSTX-U could be increased to ~600 kA, then requirements on current ramp-up are much easier.
- 2) ST-FNSF designs: The divertor coils on a ST-FNSF would be located much farther away from the plasma than on NSTX-U. On NSTX-U, the PF1CL coil is ideally located near the injector gap, and PF1BL is located much farther away from the gap. Thus, experiments that study the current generation potential using only PF1CL, only PF1BL, and with both coils (all on the same machine) contribute to the understanding of divertor coil positions in future devices.

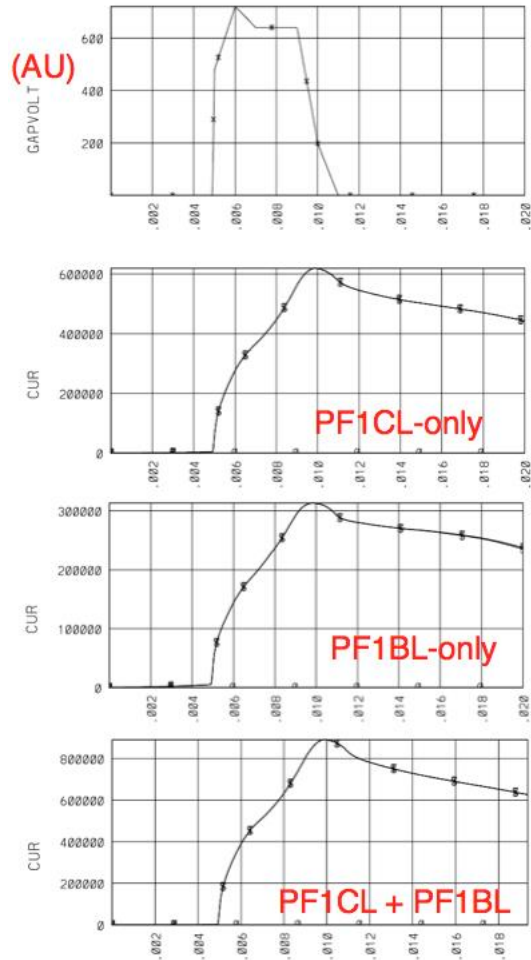


Figure IS-SFSU-3: Top: Voltage programming in these TSC simulations for all configurations is the same. Time axis is in seconds. Comparison of toroidal current generation potential for operation with PF1CL-only (16kA – 20 turns), PF1BL-only (13kA – 24 turns – with the top of the coil lowered by 5 cm from its present position), and with both coils.

- 3) Snowflake and Super X-divertor configurations: These configurations are well suited for transient CHI, because these configurations require a number of divertor coils to control the divertor flux pattern. These coils can also be used to generate the CHI injector flux. Understanding the PF1BL/PF1CL synergism on NSTX-U would again allow us to better predict CHI capability in these advanced divertor configuration devices.
- 4) Touch base with NSTX results: The present PF1B coil is located in approximately the same location as the PF1BL on NSTX, so it allows for a direct comparison of the NSTX results, and also as the electrode configurations on NSTX-U are changed (metal divertor and divertor cryo pumping).

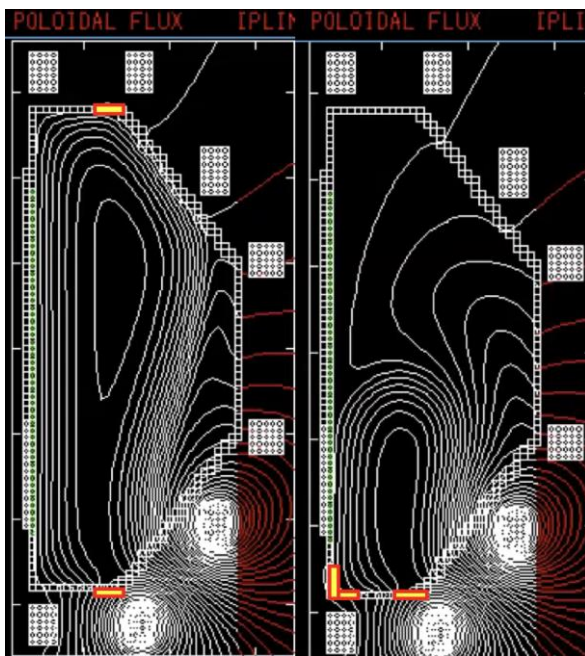


Figure IS-SFSU-4: Preliminary poloidal flux evolution in TSC simulations that compare the discharge evolution as the CHI insulator geometry is changed from NSTX-like (left) to QUEST-like (right).

Because of these reasons, it is desirable to retain some PF1BL capability on NSTX-U; for example, by reducing the physical size of the present PF1BL coil.

Dr. Kengoh Kuroda, who is a Post Doctoral fellow at Kyushu University visited NSTX-U to learn to develop a TSC model of CHI start-up on QUEST. Dr. Kuroda built TSC models that ranged from a simple vessel configuration to one that contained more detailed elements of the QUEST vessel. The code was successfully run with the simplified geometry in which the insulator positions were arranged to be like on NSTX and like the ones on QUEST. Comparative studies in both these configurations are in progress and will be reported in upcoming conferences, and in a NSTX-U FY18 milestone document. Preliminary simulations of the poloidal flux evolution for the two cases in which different insulator arrangements were used in

shown in Figure IS-SFSU-4.

Three-dimensional MHD simulations of Coaxial Helicity Injection:

Plasma initiation without reliance on the central solenoid would simplify steady-state operation of a reactor. In a low-aspect-ratio Spherical Torus (ST) and ST-based fusion reactor, ST-FNSF, due to the restricted space for a central solenoid, elimination of the central solenoid, and thus non-inductive current-drive techniques, is necessary. These methods could also simplify the tokamak design by eliminating a large component not needed during steady-state operations. Transient Coaxial Helicity Injection (CHI), a form of electrostatic helicity injection, is a leading candidate

method for solenoid-free plasma initiation in the ST configuration and has already demonstrated 100-200kA of closed-flux plasma current generation in present STs. In this technique, plasma current is generated by injecting open poloidal flux into the vacuum vessel. As helicity and flux is injected, the process of magnetic reconnection is instrumental for flux closure and generation of closed flux equilibrium. Through series of papers, [F. Ebrahimi, et al. Phys. Plasmas **20**, 090702 (2013) & F. Ebrahimi, et al. Phys. Plasmas **21**, 056109 (2014) & F. Ebrahimi, R. Raman, Physical Review Letters **114**, 205003 (2015)] we have investigated the process of magnetic reconnection using resistive MHD NIMROD simulations. In particular, our earlier axisymmetric MHD simulations have shown to produce large-volume flux closure [F. Ebrahimi, R. Raman,

Nuclear Fusion Letters **56**, 044002 (2016)].

Our simulations also suggest that plasmoid-mediated reconnection may be the leading mechanism for fast flux closure observed during the experiments.

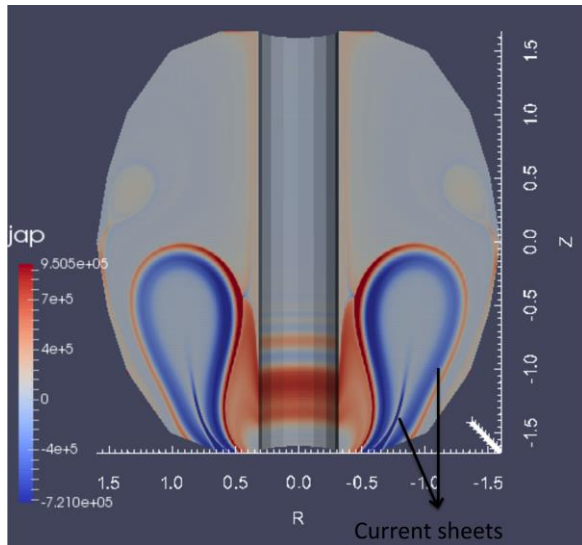


Figure IS-SFSU-5: Poloidal R-Z cuts toroidal current density. Edge current sheet formed during the nonlinear evolution causes the non-axisymmetric modes to grow.

Here, we report our new results of the formation of flux closure during transient CHI during full three-dimensional MHD simulations. Our 3-D MHD simulations have now, for the first time, been able to show large fraction conversion of injected open flux to closed flux in the NSTX-U geometry (to be submitted for publication). Regardless of i) axisymmetric current-carrying plasmoid formations during injection phase or ii) non-axisymmetric 3-D edge perturbations, large volume flux closure is formed in transient CHI. It has

been shown that nearly all of the CHI-generated current is closed-flux current. Simulations show 3-D nonaxisymmetric perturbations arising from edge current sheets (see Fig. IS-SFSU-5)

instabilities can push the open field lines near the injection region and cause flux closure. This process can be recognized as a trigger mechanism for reconnection or 2-D plasmoid formation. It is therefore found that even in the presence of 3-D perturbations, reconnection could occur at every stage of the helicity injection. As these perturbations enhance local Lundquist number via local magnetic field amplification [F. Ebrahimi, Phys. Plasmas **23**, 120705 (2016) & Invited talk by F. Ebrahimi at the 58th APS-

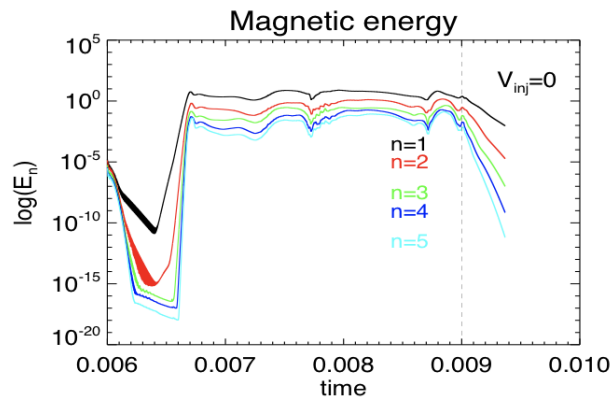


Figure IS-SFSU-6: 3-D nonlinear simulations during CHI. Total magnetic energies of different toroidal mode numbers vs. time (sec). (unpublished)

We performed full 3-D simulations with 43 toroidal modes in NSTX-U geometry with toroidal field of $B_T = 1.23\text{T}$. As seen from the magnetic energy in Fig. IS-SFSU-6, low- n current-driven edge localized peeling modes [PoP 2016 & F. Ebrahimi, Phys. Plasmas 24, 056119 (2017).] are linearly triggered. Only $n=1 - 2$ are linearly unstable. As the instabilities are localized current-sheet instabilities, they grow fast, close to the poloidal Alfvén time scales. The local Lundquist number for reconnection is $S = LV_A / \eta \sim 1.2 \times 10^5$ (peak reconnecting poloidal field around the edge current layers, $B_z \sim 0.087\text{T}$ is used). Other low- n modes are nonlinearly driven to grow fast. These low- n modes saturate at $t = 6.7\text{ms}$, and exhibit relaxation cycles in the nonlinear phase. The modes saturate by modifying and breaking the axisymmetric edge current density layer (Fig. IS-SFSU-5). Modes with higher n grow to much lower amplitudes.

The flux closure is examined during both the injection and the decay phases during CHI. The Poincaré plots, the intersections of a field line with a poloidal plane, at two times are shown in Fig. IS-SFSU-7. At $t=9\text{ms}$ during the injection phase, some open field lines near the injection region have been closed and several islands (five plasmoids) have been formed due to plasmoid instability.

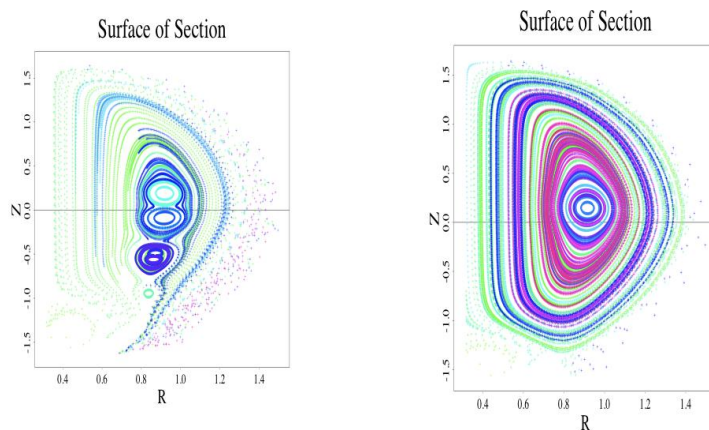


Figure IS-SFSU-7: Poincaré plots during nonlinear 3-D simulations. Left: at $t=9\text{ms}$ during the injection phase. Right: at $t=9.37\text{ms}$ during the decay phase ($V_{inj}=0$). (unpublished)

The presence of nonaxisymmetric fluctuations can be identified through a stochastic region near the edge of open field lines. In transient CHI, to force all the remaining injected open field lines to close and form a large volume flux closure, the injector voltage will be turned off. During the decay phase at $t=9.37\text{ms}$, most of the open field lines are closed and a large volume of closed flux surfaces are formed as seen in 3-D Poincaré plot. (Fig. IS-SFSU-7.b) During the decay phase, as the plasma current on the open field lines starts to decay, the amplitudes of nonaxisymmetric modes also start to decay. We have calculated the total plasma current in the closed flux region, and found a maximum of 228 kA closed flux current. Nearly all of the CHI-generated current is closed-flux current.

A.2 Time-Dependent Simulations of Fast-Wave Heated High-Non-Inductive-Fraction H-Mode Plasmas in NSTX-U

30 MHz fast-wave heating on NSTX-U may be able to ramp the plasma current non-inductively to 300 - 400 kA, a level suitable for neutral beam injection [IS-SFSU-1]. Earlier experiments on NSTX used 30 MHz fast-wave heating to increase $T_e(0)$ from 200 eV to 2 keV in 30 ms, resulting

in the generation of a H-mode discharge with a non-inductive fraction, $f_{\text{NI}} = 0.7 \pm 0.2$ during an inductively-initiated $I_p = 300$ kA plasma (shot #138506) [IS-SFSU-2]. The NSTX-U fast-wave heating system will couple up to 4 MW of 30 MHz RF power (P_{RF}), and NSTX-U will operate with a maximum toroidal field at the magnetic axis, $B_T(0)$ of 1 T, almost twice the $B_T(0)$ achieved in NSTX.

Predictive TRANSP free-boundary transport simulations [IS-SFSU-3] were used to study the dependence of f_{NI} on $B_T(0)$ and P_{RF} in $I_p \leq 300$ kA NSTX-U discharges. The TRANSP simulations used the TORIC full wave spectral code [IS-SFSU-4] to calculate the fast-wave heating and current drive. Simulations were run with a launched $k_{\parallel} = 8 \text{ m}^{-1}$, the current drive antenna phasing used during NSTX shot #138506, with $P_{\text{RF}} \leq 4$ MW coupled into plasmas with $0.5 \text{ T} \leq B_T(0) \leq 1 \text{ T}$. Predictive TRANSP simulations using the multimode MMM7.1 transport model [IS-SFSU-5] were run for NSTX-U plasmas with $I_p = 200$ and 300 kA. An NSTX-U simulation using the MMM7.1 transport model, $B_T(0) = 0.5 \text{ T}$, $P_{\text{RF}} = 1.4 \text{ MW}$ and $n_e(0) = 1.15 \times 10^{19} \text{ m}^{-3}$, similar to NSTX shot# 138506, predicted plasma parameters (eg. f_{NI} , $T_e(0)$ and plasma pressure) similar to those obtained experimentally during NSTX shot #138506, validating the use of the MMM7.1 transport model [the point with error bars in Figure IS-SFSU-8]. f_{NI} is predicted to increase significantly with $B_T(0)$ and P_{RF} . $f_{\text{NI}} = 1.7$ is predicted for an $I_p = 300$ kA NSTX-U plasma with $P_{\text{RF}} = 4$ MW at $B_T(0) = 1 \text{ T}$ (see Figure IS-SFSU-1) and $f_{\text{NI}} = 2.7$ is predicted for an $I_p = 200$ kA NSTX-U plasma with $P_{\text{RF}} = 4$ MW at $B_T(0) = 1 \text{ T}$ (see Figure IS-SFSU-9).

References

- [IS-SFSU-1] F. M. Poli, et al., Nucl. Fusion **55**, 123011 (2015)
 [IS-SFSU-2] G. Taylor, et al., Phys. Plasmas **19**, 042501 (2012)

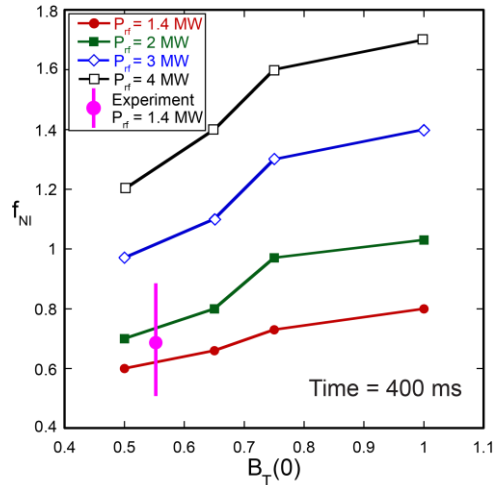


Figure IS-SFSU-8: Dependence of f_{NI} versus $B_T(0)$ predicted by TRANSP for an $I_p = 300$ kA NSTX-U plasma. Good agreement was found with the experimental f_{NI} obtained during NSTX shot# 138506, validating use of the MMM7.1 transport model.

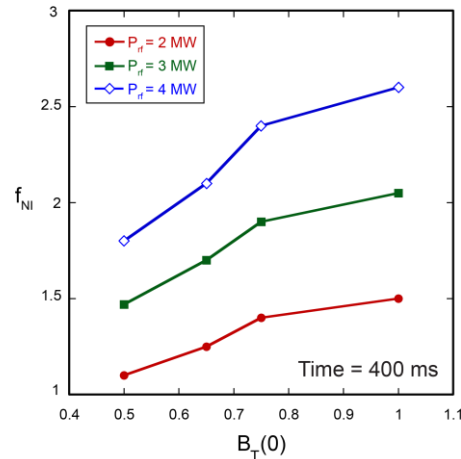


Figure IS-SFSU-9: Dependence of f_{NI} versus $B_T(0)$ predicted by TRANSP for an $I_p = 200$ kA NSTX-U plasma.

[IS-SFSU-3] R. Andrei, Bull. Am. Phys. Soc. **57**, 12 (2012)

[IS-SFSU-4] M. Brambilla, Plasma Phys. Control. Fusion **44**, 2423 (2002)

[IS-SFSU-5] T. Rafiq, et al., Phys. Plasmas **20**, 032506 (2013)

B. Wave Heating and Current Drive TSG Research Highlights

B.1: Status of HHFW System and Diagnostics

Over the past year, the RF group has repaired and refurbished the HHFW diagnostics in the NSTX-U test cell. The diagnostics measure and archive HHFW antenna voltages, currents and phase. Power supplies were refurbished, drifting components replaced, input signal levels optimized, obsolete optical links replaced, offsets readjusted and internal calibrations performed. Deteriorated AC power wiring was updated and made more serviceable. The diagnostic units will be returned to the NSTX Test Cell around the end of FY17. An electrical installation package for new RF Divertor Probe arrays, to measure RF fields in the outer divertor regions, was completed, as were installation packages for an infrared camera looking at the HHFW antenna. Work to complete installation of these diagnostics has begun.

B.2: Modeling the impact of non-Maxwellian distribution functions on full-wave simulations of HHFW heating regimes in NSTX plasma

At the power levels required for significant heating and current drive in magnetically-confined toroidal plasma, modification of the particle distribution function from a Maxwellian shape is likely [IS-WHCD-1], with consequent changes in wave propagation and in the location and amount of absorption. To study these effects computationally, both the finite-Larmor-radius and the high-harmonic fast wave (HHFW) versions of the full-wave, hot-plasma toroidal simulation code TORIC [IS-WHCD-2, IS-WHCD-3], have been extended to allow the prescription of arbitrary velocity distributions. The wave-field and power absorption are evaluated with the full wave solver, with the ion-distribution function provided by either a Monte-Carlo particle or Fokker-Planck code. Besides the capability to deal with numerical distribution functions obtained from the Fokker-Planck code CQL3D [IS-WHCD-4] for IC minority heating regime, the extension of TORIC to use directly the particle lists generated by the Monte-Carlo particle code NUBEAM [IS-WHCD-5, IS-WHCD-6] is particularly important for the study of the interaction between fast waves and energetic particles, such as fast ions generated by NBI as in NSTX.

The coupling of a particle-based code (NUBEAM) with a continuum code (TORIC) is handled by the P2F code [IS-WHCD-7, IS-WHCD-8], which converts a discrete particle list to a 4-D continuum distribution function. To test our implementation we first checked the Maxwellian distribution case by making use of the P2F code. First, we have artificially generated a particle list representing a Maxwellian distribution in an NSTX plasma geometry with analytical temperature and density profiles given by analytical kinetic profiles for electron and fast ion population. Second, we have run P2F by using the Maxwellian particles list to obtain a continuum distribution function. Third, we have numerically evaluated the dielectric tensor and we have run TORIC. Finally, we have compared the results with the reference case. Figure IS-WHCD-1a shows indeed the results of this comparison. In particular, in figure IS-WHCD-1a the black curve indicates the reference case. In addition, there are other four cases which are obtained assuming a

particles list with 2×10^3 (red curve), 10^4 (green), 10^5 (magenta curve), and 10^6 (cyan curve) particles.

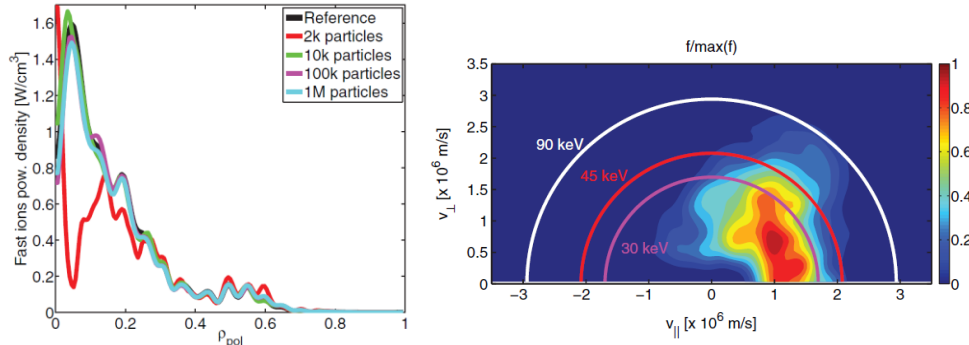


Figure IS-WHCD-1. (a) RF power deposition on fast ions from TORIC using P2F distributions as a function of ρ_{pol} . Black curve represents the reference case whereas the color curves indicate different particle number adopted in the calculations as shown in the legend. (b) Fast ion distribution function at $R = 1 \text{ m}$ and $z = 0 \text{ m}$ obtained from the P2F code starting from a NUBEAM particles list for an NSTX plasma without HHFW (shot 141711 at time = 0.47 s).

Figure IS-WHCD-1b shows the fast ion distribution function at $R = 1 \text{ m}$ and $z = 0 \text{ m}$ obtained from the P2F code starting from a NUBEAM particles list for a NSTX shot 141711 at time = 0.47 s without HHFW. The number of particles used for this case in NUBEAM are 53115. For reference, the 90 keV beam injection energy is represented by the white curve while the half (45 keV) and third energy (30 keV) components are represented by red and magenta curves, respectively. As done for the minority heating regimes, power flow to the different species is shown in Table IS-WHCD-1. As expected, a larger power flow to fast ions is found when a realistic distribution is considered with respect to the equivalent Maxwellian case. It is worth noting that the relatively small differences in the power flow to fast ions between equivalent Maxwellian and the realistic case shown in Table IS-WHCD-1, are due to the fact that the distribution function in the case considered here is not affected by RF therefore the distribution function does not have a large RF tail to higher energies. Furthermore, Table IS-WHCD-1 shows the power flow to the fast ions for an anisotropic Maxwellian distribution with the same energy content in the parallel and perpendicular directions as the actual distribution shown in figure IS-WHCD-1b. Additional details and results are published in [IS-WHCD-9].

Abs. fraction	Maxw.	Non-Maxw.	bi-Maxw.
D	4.26%	3.89%	10.27%
D-NBI	53.94%	58.12%	55.55%
Electrons	41.80%	37.99%	34.18%

Table IS-WHCD-1. Power flow to each species. The Maxw. case corresponds to an equivalent Maxwellian temperature for the fast ions population, the Non-Maxw. case corresponds to the numerical non-Maxwellian distribution obtained by P2F starting from a NUBEAM particles list. Finally, the bi-Maxw. case corresponds to the anisotropic Maxwellian with the same energy content in the parallel and perpendicular directions as the actual distribution.

B.3: Full wave simulation of helicon waves in DIII-D and ITER

Helicon waves have been recently proposed as an off-axis current drive actuator for DIII-D, FNSF, and DEMO tokamaks. Previous ray tracing modeling [IS-10] using GENRAY [IS-11] predicts strong single pass absorption and current drive in the mid-radius on DIII-D in high beta tokamaks. The full wave code AORSA [IS-WHCD-12], which is valid to all order of Larmor radius and can resolve arbitrary ion cyclotron harmonic, has been recently used to validate the ray tracing technique. If the scrape-off-layer (SOL) is ignored in the modeling, AORSA agrees with GENRAY in both the amplitude and location of driven current for DIII-D and ITER cases. These models also show that helicon current drive can possibly be an efficient current drive actuator for ITER. Previous GENRAY analysis did not include the SOL. AORSA has also been used to extend the simulations include the SOL, so as to estimate possible power losses of helicon waves in the SOL that would reduce the current drive efficiency in the core. AORSA calculations show that there is another mode in the SOL that can cause significant SOL losses. This mode leads to significant SOL losses at high SOL densities. At low SOL densities, the helicon wave is evanescent, also leading to significant SOL losses. It is shown that there is an optimal SOL density to minimize helicon power losses in the SOL, similar to previous modeling results for mid and high harmonic fast wave on DIII-D and NSTX [IS-WHCD-13, IS-WHCD-14].

B.4: Initial and preliminary EC/EBW simulations on QUEST

Graduate student Ryota Yoneda from Kyushu University visited to PPPL as part of the collaboration between NSTX-U and QUEST. The main purpose of his visit was to work on EC/EBW modelling for QUEST plasmas employing ray tracing and Fokker-Planck codes. This work was done in collaboration with the PPPL hosts, N. Bertelli and M. Ono. Ray tracing simulations were performed (i) for 28 GHz EC system in QUEST plasma and (ii) for 8.2 GHz EC high field side launcher for possible future X-B experiments.

We also started to investigate high energy electrons by mean of the Fokker-Planck code CQL3D coupled to the ray tracing code GENRAY. The preliminary results show that the driven current goes into runaway regime and the energy hits 100keV. However, it is important to mention that in these first runs we have assumed the presence of a small Ohmic field ($V_{DC} = 0.25$ V) and the energy grid up to 100 keV. Further studies will be performed in collaboration in FY18. This work is done in collaboration with R. W. Harvey, M. Ono and QUEST team.

B.5: Full-wave simulations of HHFW propagation in the scrape-off layer of NSTX plasma

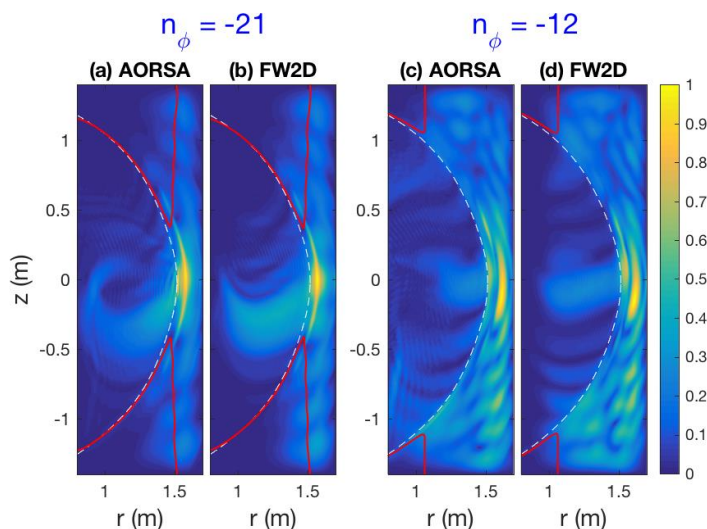


Figure IS-WHCD-2. Two-dimensional simulation results of the total electric field amplitude using the AORSA and FW2D codes for (a-b) $n_\phi = -21$ and (c-d) $n_\phi = -12$ for $N_{ant} = 1.5 \times 10^{18} \text{ m}^{-3}$. Each electric field amplitude has been normalized to its maximum value. White and red solid lines are LCFS and FW cut-off, respectively.

The SOL losses of HHFW power observed in NSTX [IS-WHCD-15] may be partially captured by full-wave simulations using the AORSA code. However, AORSA uses a rectangular vessel boundary, which differs substantially from the actual vessel. To overcome this limitation, we have adapted the flexible two-dimensional full-wave (FW2D) code [IS-WHCD-16] to tokamak geometry and have used it to examine radio frequency (RF) waves in the SOL of NSTX. We find that the vessel boundary significantly affects the FW propagation in the SOL, and it is definitely necessary to adopt a realistic boundary shape of tokamak to investigate RF wave propagation.

The validity of FW2D for this application was demonstrated in a benchmark against AORSA for a rectangular boundary case [IS-WHCD-13]. Figure IS-WHCD-2 shows the electric-field amplitude (normalized to its maximum value) calculated by AORSA (Figs. a and c) and FW2D (Figs. b and d) for a single toroidal mode $n_\phi = -21$ (Figs. a and b) and $n_\phi = -12$ (Figs. c and d) for NSTX shot 130608. The wave frequency is $f = 30 \text{ MHz}$ and the antenna is located at $r = 1.575 \text{ m}$. The density profile is exponentially decaying as Refs. [IS-WHCD-13, IS-WHCD-14] and the density at the antenna is taken to be $N_{ant} = 1.5 \times 10^{18} \text{ m}^{-3}$ in an electron-deuterium plasma. In Figure IS-WHCD-2, AORSA and FW2D simulations show excellent agreement in the SOL and also in the core plasmas where warm plasma effects, included in AORSA but not FW2D, start to play a role.

Upon adapting FW2D to more realistic vessel boundary (similar to that used in Ref. [IS-WHCD-17]), the standing waves observed for AORSA are still present but have different properties than when computed with a rectangular boundary. The results are summarized in Figure IS-WHCD-3 for both FW2D with a realistic geometry and AORSA with a rectangular boundary, each for three different densities at the antenna. As previously observed, for N_{ant} small enough that the FW cut-off is ‘closed’ in front of the antenna, the FW fields are strongly localized in front of antenna. On the other hand, for $N_{\text{ant}} = 2.0 \times 10^{18} \text{ m}^{-3}$ and $4.0 \times 10^{18} \text{ m}^{-3}$, the FW cut-off ‘opens’ in front of the antenna, and standing waves clearly appear in the SOL. The FW2D simulation shows that the maximum amplitude of the wave electric field for $N_{\text{ant}} = 4.0 \times 10^{18} \text{ m}^{-3}$ seems to be stronger than for $N_{\text{ant}} = 2.0 \times 10^{18} \text{ m}^{-3}$. On the other hand the AORSA shows the maximum amplitude of standing wave modes occur for $N_{\text{ant}} = 2.0 \times 10^{18} \text{ m}^{-3}$ and the peak of the wave electric field in the SOL for the AORSA simulation occurs outside region of the limiter boundary. In addition, for $N_{\text{ant}} = 4.0 \times 10^{18} \text{ m}^{-3}$, the standing wave amplitude for $z > 0$ is stronger than for $z < 0$, which is different with respect to the AORSA showing stronger wave electric field appear at $z < 0$. These preliminary results clearly show that the boundary shape can significantly affect the FW propagation in the SOL.

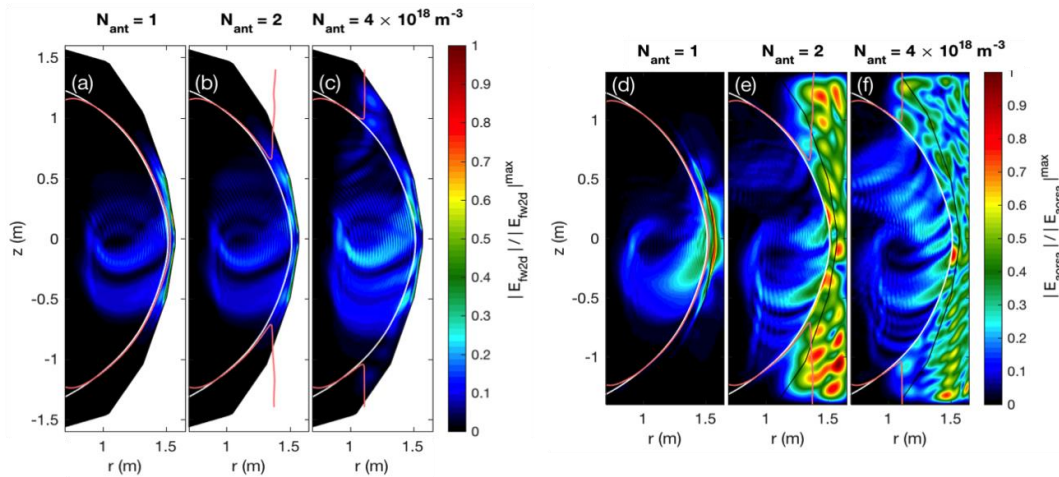


Figure IS-WHCD-3. Two-dimensional electric field amplitude from (a-c) the FW2D simulation with a realistic vessel boundary and (d-f) AORSA simulation assuming a rectangular boundary for $N_{\text{ant}} = 1, 2,$ and $4 \times 10^{18} \text{ m}^{-3}$, respectively. In this figure, white, black and light red solid lines are the LCFS, the limiter boundary, and the FW cut-off, respectively.

B.6: RF SciDAC proposal submitted and awarded

In 2017, N. Bertelli served as the PPPL co-PI of the RF-SciDAC project. In particular, he worked with the RF SciDAC team to prepare a proposal for the competition that was recently awarded for 5 years starting from 1st September 2017. A collaboration with MIT and RF SciDAC team on the use of the finite element code MFEM (for the edge plasma) coupled to the TORIC code (for the core plasma) has started. This collaboration will continue also in FY18.

B.7: Research Supporting Non-Inductive Plasma Current Start-Up and Ramp-Up in NSTX-U

NSTX-U has a long-term plan to use a combination of 30 MHz fast wave heating (FWH) and 28 GHz electron cyclotron heating (ECH) or electron Bernstein wave heating (EBWH) to start-up and ramp-up the plasma current to 300 - 400 kA, a level suitable for neutral beam injection [IS-WHCD-18]. Recent TRANSP free-boundary transport simulations [IS-WHCD-19] predict the non-inductive fraction, f_{NI} , will increase significantly with axial toroidal field, $B_T(0)$, and FWH power, P_{rf} . TRANSP simulations predict that, at the maximum $B_T(0)$ on NSTX-U of 1 T, 4 MW of FWH power can non-inductively ramp-up the plasma current to 400 - 500 kA.

A collaboration has begun with the QUEST spherical tokamak program at Kyushu University in Japan to generate steady-state fully non-inductive plasmas with a combination 8.2, 8.56 and 28 GHz ECH and EBWH. Initial QUEST 28 GHz ECH plasma current ramp-up experiments with an open-ended waveguide launcher generated up to 66 kA of non-inductive current with 270 kW of 28 GHz ECH power [IS-WHCD-20]. A new 28 GHz transmission line, that included a quasi-optical polarization rotator and focusing mirror launcher was commissioned in July 2017 and generated 85 kA with 230 kW of 28 GHz ECH power.

B.8: Annulus-Resonant Modes and SOL Losses of HHFW Power

Using a cylindrical cold-plasma model of HHFW propagation in NSTX, a special class of modes, dubbed “annulus resonances” was identified as a potential explanation for the anomalously high amount of HHFW power lost to the SOL of NSTX [IS-WHCD-21]. As shown in Fig. IS-WHCD-4a and b, these modes have a half-wavelength structure in the combined edge region of the plasma, have a large loading resistance, and propagate a large portion of their wave power in the edge. We have evaluated the impact of annulus resonant modes on the three-dimensional wave-field reconstructions [IS-WHCD-22]. When plotted in wave-momentum space, the AR modes define a trajectory that depends on parameters such as edge density and magnetic field and can thus be moved relative to the antenna spectral peak, as shown in Fig. IS-WHCD-4c and d. Figure IS-WHCD-4c shows a simulation using current drive phasing where there is strong excitation of AR modes relative to non-AR modes located at the antenna spectrum peak. Over half of the total wave power is trapped in the edge in this case. Figure IS-WHCD-4d shows a case of heating phasing, in which the AR trajectory intercept weaker high-order sideband of the antenna spectrum, and there is a relatively weaker contribution from AR modes, and less power is trapped in the edge. In the case of dipole phasing, this leads to the results that the fraction of power coupled to the core improves with edge density, in contradiction to experiments and full-wave computations, and we conjecture that magnetic pitch could play an important role. Experimental investigation into the existence and significance of these modes awaits operation on NSTX-U or work at the Large Plasma Device (see below).

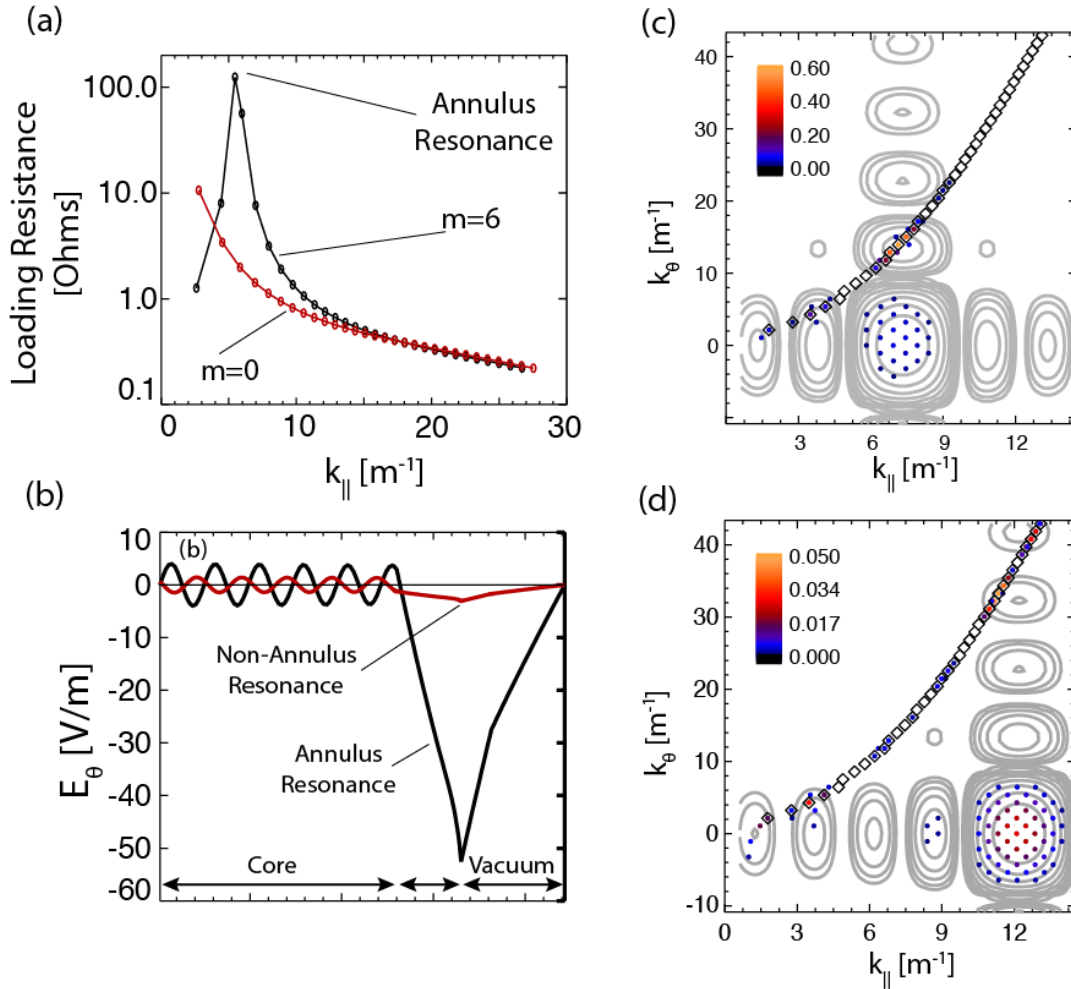


Figure IS-WHCD-4. (a) Annulus resonant modes can be identified as a peak in loading resistance, as seen in the $m=6$ modes (black), with m denoting azimuthal mode number. The $m=0$ (red) modes do not have an annulus resonance, and their loading resistances decrease monotonically with k_{\parallel} . (b) Radial E_{θ} profiles for the annulus resonance in (a) and a neighboring non-annulus resonant mode. The difference in field amplitude in the edge region is clear. (c) Contour lines denote the antenna spectral power in k -space for current-drive phasing. Colored dots indicate the largest modes of the system, with the color bar denoting loading resistance. Diamonds indicate annulus resonant modes; diamonds filled with a dot indicate an annulus resonance that is one of the largest mode. In this case, the power spectrum is dominated by annulus resonances. (d) As in (c), but for dipole antenna phasing. The wave power is more evenly split between non-annulus resonances at the antenna spectral peak and annulus resonances modes on weaker side lobes.

B.9: Exploration of fundamental ICRF/HHFW physics on the LAPD

RF rectification is a sheath phenomenon known to modifying the DC current and/or the DC sheath potential. The distinction between rectified currents and voltages is not emphasized in the existing literature, but rectified currents are suspected to play a significant role in the prompt loss of HHFW power to the divertor along SOL field lines [IS-WHCD-23]. Experiments aimed at studying the fundamental properties rectification and its detection were conducted on the Large Plasma Device (LAPD) [IS-WHCD-24] at the University of California Los Angeles, where a

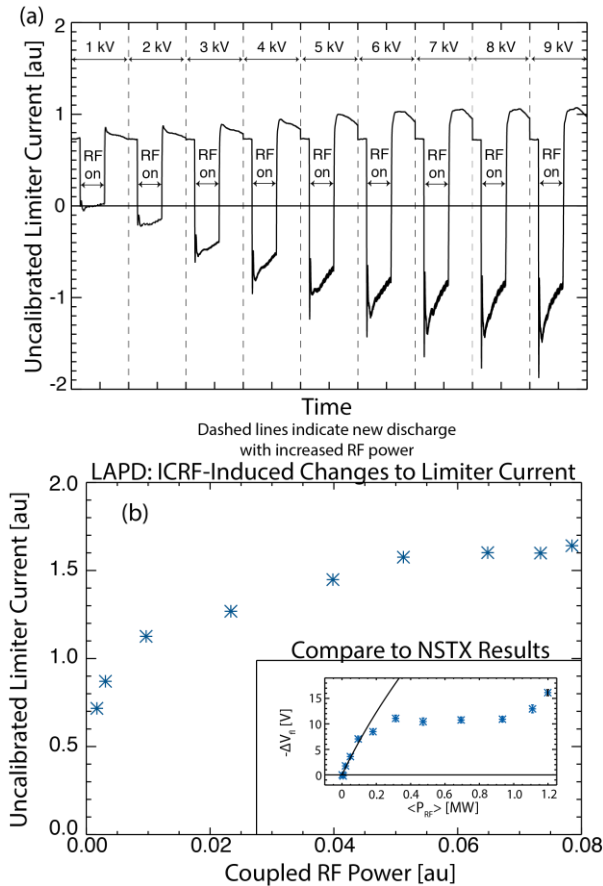


Fig. IS-WHCD-5. Preliminary results from LAPD in support of HHFW research on NSTX. (a) A concatenation of time series of DC (rectified) current collected by the LAPD limiter. Without RF, the limiter collects ion current (positive signal), but RF rectification, but RF rectification drives electron current into the limiter. (b) From the data in (a), plots the change in collected current against the amount of injected RF power. (c) Data from a divertor probe in NSTX [IS-WHCD-23], showing the change in probe floating potential, a quantity related to the amount of current drawn by the surrounding tiles, against the applied RF power. A similar saturation effect appears to be present in both sets of data.

high-power RF source and single strap antenna were recently installed to explore the physics of RF rectification [IS-WHCD-25]. HHFW collaborators from ORNL (J. B. Caughman, C. Lau, and E. H. Martin) participated and provided a retarding field analyzer, a helium-spectroscopy diagnostic, RF-phase resolved fast-camera, a double probe, and COMSOL simulations. The experiments included imposing different boundary conditions by floating the limiters, power scans were conducted during which the current and/or voltages were measured, retraction of the antenna while taking millimeter-resolved data, and tilting the antenna. Figure IS-WHCD-5a shows the DC current collected by the limiter for different RF power levels; the limiter collects electron current without RF but collects electron current during RF. Figure IS-WHCD-5b shows the change in DC current as a function of coupled RF power; this change in current appears to saturate with RF power, similar to measurements made in the divertor of NSTX (inset of Fig. IS-WHCD-5b). Analysis of the data from these experiments is ongoing.

B.10: ICRF collaboration with EAST: ICRF interactions with the SOL

An important aspect of the NSTX HHFW program is to compare results against conventional ICRF heating in conventional aspect-ratio tokamaks. EAST provides such an opportunity for collaboration, as it has 12 MW of ICRF power but unusually low coupling and heating efficiency, perhaps due in part to SOL losses as seen in NSTX [IS-WHCD-26]. In December 2016, a PPPL-submitted experimental proposal “Interactions of Fast Waves with the Scrape Off Layer Plasma” was granted run time to study the influence of ICRF on the SOL by separating the two antenna pulses in time and also by modulating the ICRF power waveforms. The results are currently

being analyzed. Figure IS-WHCD-6a shows the radial profiles of floating potential on the lower divertor (mapped back to the midplane) for a decreasing outer gap, showing that large increases in floating potential are observed only for probe connecting to the antenna, and a smaller negative decrease for probe between the antenna and separatrix. The latter is consistent with results from divertor probes in NSTX during HHFW [IS-WHCD-15]. Figure IS-WHCD-6b shows the currents delivered to upper and lower probes during ICRF are not equal, suggesting that cross-field diffusion is playing a role. Figure IS-WHCD-6c shows the effect of gas puffing, which seems to suppress the change in floating potential observed in the divertor on triple probes. Ongoing analysis will highlight the similarities and differences between HHFW heating on NSTX against conventional ICRF heating on EAST and may help determine if SOL losses are

impacting the EAST ICRF program.

References

- [IS-WHCD-1] Stix, *Nucl. Fusion* **15** (1975) 737.
 [IS-WHCD-2] Brambilla M., *Plasma Phys. Control. Fusion* **41** (1999) 1.
 [IS-WHCD-3] Brambilla M., *Plasma Phys. Control. Fusion* **44** (2002) 2423.
 [IS-WHCD-4] Petrov Y.V. and Harvey R.W., *Plasma Phys. Control. Fusion* **58** (2016) 115001.

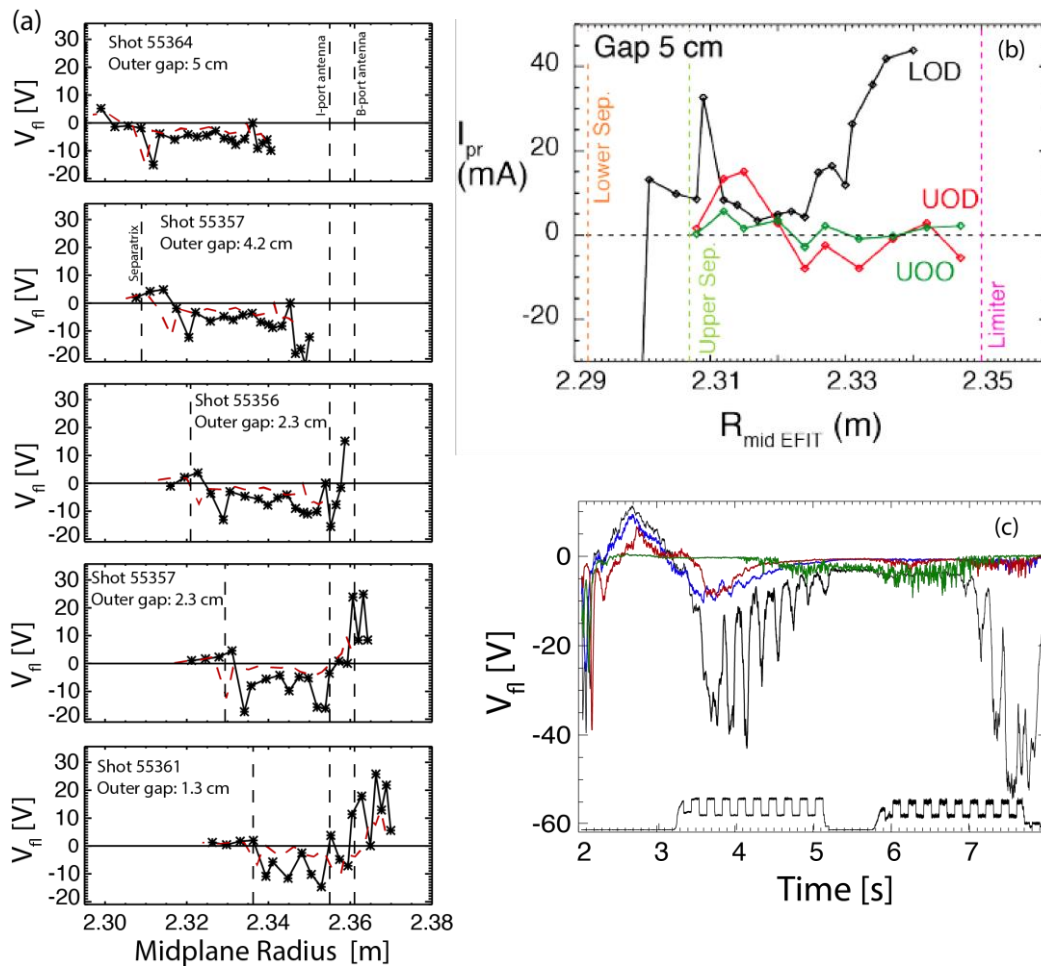


Fig. IS-WHCD-6. (a) Radial profile of divertor Langmuir probe floating potential, measured in the lower divertor, for different values of the outer gap. Probe positions have been mapped to the midplane for reference to antenna positions. Black curves indicate the profile during ICRF heating, while the red curves indicate the profiles before ICRF. Large increases in floating potential, predicted by RF rectification, are only observed for probes that connect to the antennas. (b) Current collected by a probe at zero bias (ground potential) for both the lower array (LOD) and upper arrays at Bay D (UOD) and Bay O (UOO). The currents are clearly greater for the lower divertor case, indicating that the rectified current path does not close from upper to lower divertor as that cross-field diffusion is playing a role. (c) Time series of floating potential measurement for a single probe for different levels of gas puffing at the Bay B antenna. The gas puff suppresses the large ICRF-induced change in floating potential.

- [IS-WHCD-5] Goldston R.J. *et al*, *J. Comput. Phys.* **43** (1981) 61.
- [IS-WHCD-6] Pankin A. *et al*, *Comput. Phys. Commun.* **159** (2004) 157.
- [IS-WHCD-7] Green D.L. *et al*, *J. Phys.: Conf. Ser.* **180** (2009) 012058.
- [IS-WHCD-8] Green D.L. *et al*, *AIP Conf. Proc.* **1187** (2009) 569.
- [IS-WHCD-9] Bertelli N. *et al.*, *Nucl. Fusion* **57** (2017) 056035.
- [IS-WHCD-10] Prater R. *et al.*, *Nucl. Fusion* **54** (2014) 083024.
- [IS-WHCD-11] Smirnov A.P. *et al.*, *Bull. Am. Phys. Soc.*, **39** (1994).
- [IS-WHCD-12] Jaeger, E. F. *et al.*, *Physics of Plasmas*, **8** (2001) 1573.
- [IS-WHCD-13] Bertelli N. *et al.*, *Nucl. Fusion* **54** (2014) 083004.
- [IS-WHCD-14] Bertelli N. *et al.*, *Nucl. Fusion* **56** (2016) 016019.
- [IS-WHCD-15] Perkins R. J. *et al.*, *Phys. Rev. Lett.* **109** (2012) 045001.
- [IS-WHCD-16] Kim, E.-H. *et al*, *Geophys. Res. Lett.* **42** (2015) 5147.
- [IS-WHCD-17] Green D. L. *et al.*, *Phys. Rev. Lett.* **107** (2011) 145001.
- [IS-WHCD-18] Poli F. M. *et al.*, *Nucl. Fusion* **55**, 123011 (2015).
- [IS-WHCD-19] Andrei R., *Bull. Am. Phys. Soc.* **57**, 12 (2012).
- [IS-WHCD-20] Idei H. *et al.*, to be published (2017).
- [IS-WHCD-21] Perkins R. J. *et al.*, *Phys. Plasmas* **23**, 070702 (2016).
- [IS-WHCD-22] Perkins R. J. *et al.*, *Nucl. Fusion*, accepted.
- [IS-WHCD-23] Perkins R. J. *et al.*, *Nuclear Materials and Energy*, in press.
- [IS-WHCD-24] Gekelman W. *et al*, *Rev. Sci. Instrum* **87** (2016) 025105.
- [IS-WHCD-25] M. J. Martin, thesis, 2017.
- [IS-WHCD-26] Hosea J. C. *et al.*, *Bull. Am. Phys. Soc.* **60** (2015).

C. Advanced Scenarios and Control TSG Research Highlights

C.1 Summary of Milestone R17-5

The milestone R17-5 is titled “Analysis and modelling of current ramp-up dynamics in NSTX and NSTX-U”. The report associated with the completion of this milestone details much of the relevant ASC work for this fiscal year, and the interested reader is referred to that report. Key highlights include the following.

- Target H-mode scenarios for NSTX-U are enabled by achieving large elongation and an L-H transition early in the ramp up phase.
- A database of NSTX and NSTX-U discharges demonstrates that the elongation versus I_i operation space for the two devices is similar for $I_i \geq 0.8$.
- A corresponding database was created of vertical disruption events (VDEs) on NSTX and NSTX-U using an automated VDE search algorithm. This identified that the limit to the elongation by VDEs was more restrictive on NSTX-U than NSTX. Thus, NSTX-U achieved a similar elongation to NSTX by operating closer to the VDE stability boundary.
- Calculation of the open-loop VDE growth rate found that NSTX-U achieved stable operation at larger VDE open-loop growth rates compared to NSTX due to improvements to the active vertical position controller. This is consistent with achieving stable operation closer to a stability limit.
- The elongation at the time of diverting was limited in NSTX-U operations by the occurrence of vertical oscillations (“bobble”) as the discharge transitioned to a diverted shape.
- Potential sources of the initial vertical motion are a mismatch at the time of transitioning between control algorithms, and a poor convergence of rtEFIT. An overshoot in the size of the inner gap exacerbates vertical position oscillations by increasing the vertical growth rate.
- Operational and scenario development improvements were identified that would reduce the probability of the deleterious oscillations. These include the removal of an algorithm transition within ISOFLUX at the time of diverting, improved rtEFIT reconstructions using multi-threading of the real-time calculation, an inner gap control algorithm that reduces overshoot and diverting with finite δ_{rsep} .
- A database of L-H transitions was created with a corresponding database of L-mode and dithering discharges with $P_{\text{NBI}} > 3$ MW. A set of four criteria for the database was developed that excluded all of the L-mode times from the database. The criterion informs the target conditions for triggering the L-H transition during ramp-up.
- The lowest I_i discharges ($I_i < 0.6$) on NSTX-U were susceptible to fast disruptions after the L-H transition. MHD stability calculations for the ramp-up phase indicate the discharges were ideally stable and moving away from the no-wall stability boundary at the time of the disruption. Subsequent analysis indicated that the fast disruption was initiated by an H-L transition that was most likely driven by changes to the equilibrium due to vertical position oscillations.

C.2 Development of TokSys Modeling Framework for Control Design and Simulation

A modeling framework based upon the TokSys toolbox [IS-ASC-1] is currently under-development and will enable model-based design and high-fidelity closed-loop simulations of the axisymmetric plasma shape control system on NSTX-U. The TokSys tools are now being used to design multi-input-multi-output plasma shape controllers that are required to enable advanced magnetic configurations such as the snowflake divertor (SFD). These modeling tools will be used in the coming years to perform critical tasks such as analyzing vertical stability limits during the current ramp-up and optimizing vertical position and plasma shape controllers during this phase of the plasma discharge.

The TokSys framework is implemented within the MATLAB/Simulink environment. The primary deliverables of the modeling process are models of the time-dynamics of electric currents within the primary axisymmetric conductors – poloidal-field (PF) coils and vacuum vessel – coupled to (linear or nonlinear) models of the plasma equilibrium evolution and auxiliary systems such as power supplies and diagnostic filters. The models generally assume the linear form,

$$\begin{aligned}\dot{x} &= AI + Bv + Fw, \\ y &= CI + Dv + Hw,\end{aligned}$$

where I represents the toroidal electric currents in all conductors, v represents the voltages applied to the PF coils, and w represents system disturbances such as changes in β_p , l_i , or noise. The entries of the matrices A , B , and F are computed using conductor resistances as well as mutual inductances that have been modified to incorporate effects due to plasma motion. The entries of matrices C , D , and F are composed mainly of plasma-modified inductances and describe how changes in PF coil currents map to changes in various model outputs such as magnetic diagnostic signals and shape parameters (gaps, plasma boundary and X-point locations, snowflake configuration, etc.).

Throughout the model development process, efforts have been made to validate the various

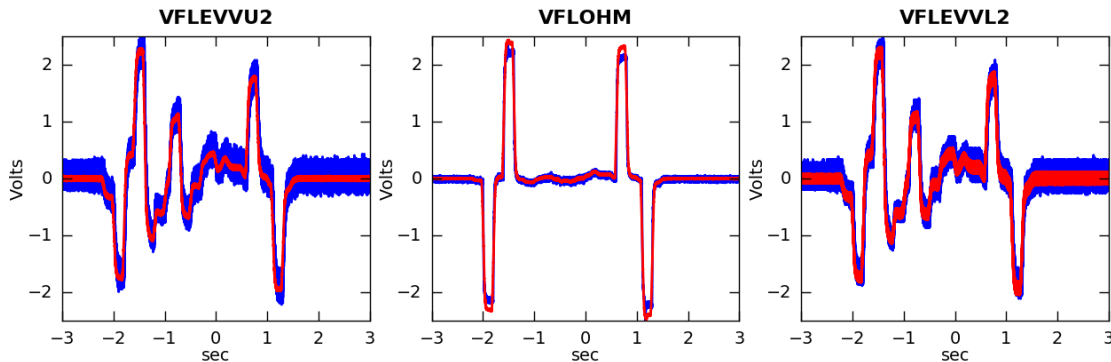


Figure IS-ASC-1: Comparison of simulated (red) and experimental (blue) magnetic diagnostic signals for NSTX-U shot 204735.

components of the model such as the vacuum vessel and plasma responses to applied axisymmetric fields. Figure IS-ASC-1 depicts a subset of results from one such validation procedure in which the responses of various magnetic sensors to feedforward PF current pulses were simulated and found to be in good agreement with measured magnetics signals from NSTX-U shot 204735. Simulations such as these are used as a proxy for the accuracy of the model describing the currents within the NSTX-U vacuum vessel.

Additional modeling work includes implementation of the nonlinear GSEVOLVE code (Anders Welanders, General Atomics) for simulating Grad-Shafranov equilibrium coupled to reduced models of toroidal current profile evolution. Progress has also been made toward linking the TokSys models within the Simulink environment to the real-time plasma control system to enable closed-loop predictive simulations.

C.3 Startup and rampup collaboration with MAST-U

A collaboration on Scenario and Control development between MAST-U and NSTX-U was initiated in FY17. Both devices require the development of robust and flexible discharge startup scenarios that maintain broad current profiles (i.e. low- I_i) and minimize the flux consumption (see R17-5 milestone). The goal of the collaboration is to develop common tools and metrics for optimizing the startup and rampup scenarios on the two MA-class ST devices. This increases the efficiency in sharing knowledge and encourages the joint development of control and analysis tools.

The activities performed toward this collaboration in FY17 focused on the development of “direct induction” (DI) startup scenarios on MAST-U. MAST relied primarily on “merge-compression” startup where the plasma discharge was initiated as two rings of plasma near outboard poloidal field coils, then merged into a single current channel. However, MAST-U will use DI startup, where a poloidal field null is created near the inboard center column to facilitate the acceleration of electrons by a toroidal electric field. This is the standard startup method on NSTX-U, thus the initial collaborative activities leveraged the experience of the NSTX-U team toward preparing for the initial operations of MAST-U.

Target startup scenarios were developed prior to NSTX-U operations using the LRDFIT code (see FY16 annual report). LRDFIT is a popular analysis tool at PPPL for computing vacuum fields and Grad-

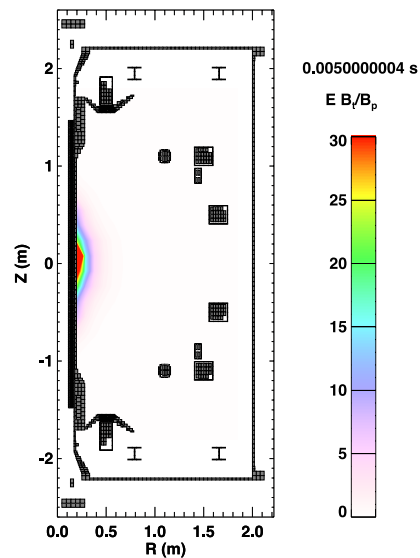


Figure IS-ASC-2 Calculations of null formation on MAST using LRDFIT (discharge 17418). The color contours show the Lloyd parameter in kV/m averaged over 1 ms around $t = 5ms$.

Shafranov equilibrium and it was the primary analysis tool used to confirm the magnetic calibrations and refine the axisymmetric model of the conducting structures on NSTX [IS-ASC-2] and NSTX-U. These activities improve the fidelity of EFIT calculations and provide an avenue for optimizing the magnetic field null required for inductive startup. LRDFIT was identified as tool that could be applied to similar tasks in preparation for MAST-U operations. Part of this effort includes comparing the calculations to MAST vacuum field discharges to provide confidence in the model and develop the routines required for loading and saving data within the CCFE system.

Adapting LRDFIT for MAST and MAST-U required three significant efforts in FY17. The first was porting the code over to the CCFE computer system, the second was developing the code I/O for the MAST data and the third was constructing the device description files for the MAST and MAST-U device. The device description files in LRDFIT provides the R,Z location of coils, conducting structures and magnetics, and a description of the power supplies.

Following these activities, the model calculations were compared to vacuum field discharges on MAST, as well as a subset of discharges that explored DI startup on MAST in preparation for MAST-U operations. Comparisons between the calculations and measurements for vacuum (no plasma) shots on MAST drove the refinement of the device description, and ultimately provided confidence in applying the calculations for predictive calculations.

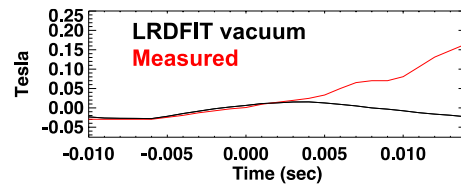


Figure IS-ASC-3 Comparison of the LRDFIT vacuum field calculation (black) to the measured signal (red) for a Mirnov measuring B_z at the inboard midplane. The model is in good agreement with the measurement until breakdown and the appearance of plasma current (17418).

LRDFIT was also used to examine a small subset of discharges on MAST that used DI startup in order to provide insight into DI startup on MAST-U. Figure IS-ASC-2 presents representative output from LRDFIT from the calculations for a DI discharge (17418). The figure shows the spatial distribution of the Lloyd parameter ($E_t B_t/B_p$) in kV/m at the time when this parameter is a maximum (5 ms) [IS-ASC-3]. The Lloyd parameter provides an estimate for the electric field along a helical field line where larger values indicate a greater probability of breakdown of the neutral gas. The magnitude and distribution of this breakdown metric at its maximum is comparable to NSTX and NSTX-U calculations. The most significant result is that the time predicted to be most likely to result in the formation of current channel (5 ms) is in good agreement with the first appearance of measurable plasma current. Figure IS-ASC-3 compares the predicted signal on a Mirnov coil at the inboard midplane (black) to the measured signal (red). The model is good agreement with the measurement until approximately $t = 4$ ms. The vacuum calculation does not include the fields generated by the plasma, thus the disagreement is due to field generate by plasma current. The timing of the field null is sensitive to the eddy currents in the conducting structures, therefore the agreement between the vacuum fields prior to 5ms and the observed time for breakdown provides confidence that the model is adequately capturing the dynamics of the induced current. Predictive calculations for startup scenarios for the first operation of MAST-U are ongoing and will continue into FY18.

C.4 Control of rotation and stored energy on DIII-D using variable beam voltage and perveance

As part of the DIII-D/NSTX-U National Campaign experiments, a new feedback algorithm was implemented in the DIII-D PCS that uses the recently added variable beam voltage and perveance capabilities of the neutral beam injectors [IS-ASC-4] for power, torque, energy, and rotation control. Building off of the control design approach developed for feedback control of non-inductive scenarios in NSTX-U [IS-ASC-5], a constrained real-time optimization-based control algorithm was developed for this application (depicted in Figure IS-ASC-4).

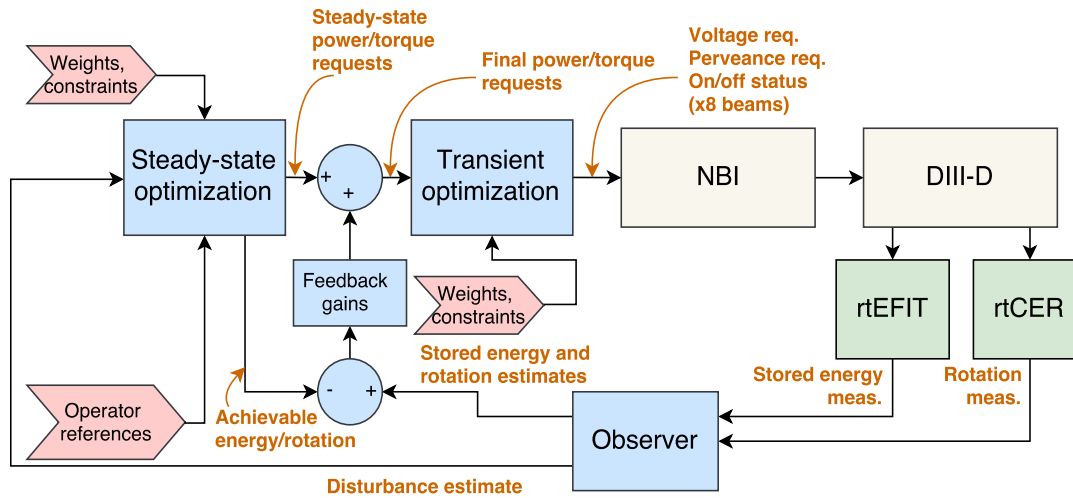


Figure IS-ASC-4 Schematic of control algorithm used for combined power, torque, energy and rotation control

In the design, an observer is used to reduce noise and produce estimates of modeling errors in real-time. These errors are then used to correct a model used by a real-time optimization algorithm to minimize a cost function that weights the steady-state tracking error and the use of each of the actuators according to operator inputs. This step determines the voltage, perveance, and duty cycle required at steady state to maintain the optimal stored energy and rotation values, accounting for the limits on the allowed range of voltage and perveance put in place to maintain beam reliability.

The time response of the outputs to these actuator values would be set by the energy and momentum confinement times and would be further slowed by the slow response of the beam voltage to requested changes, which are a result of bending magnet power supply limitations. To overcome this, the new algorithm includes an additional optimization step that compensates the slow response of the voltage, which is a result of bending magnet power supply limitations, by fast adjustments of the perveance and/or duty cycle to more quickly track the required power and torque, and augments the power and torque requests with a feedback term to improve energy and rotation target tracking.

The algorithm was tested during a half-day experiment during which the ability to track requested values while compensating for changes in confinement and pre-programmed ramps in the voltage of selected beams was demonstrated. Figure IS-ASC-5 shows an shot in which the algorithm was configured to track a target stored energy and rotation using voltage and perveance as actuators. Voltage from the counter-injection beams was reduced while the voltage of the co-injection beams was increased to track the targets. While the voltage was changed slowly due to slew rate limitations, the requested perveance varied more rapidly, often saturating in an attempt to compensate for large, sudden changes in confinement, like those visible in the stored energy around $t=3$ s. The results of the experiment were promising and motivate expanding the capability

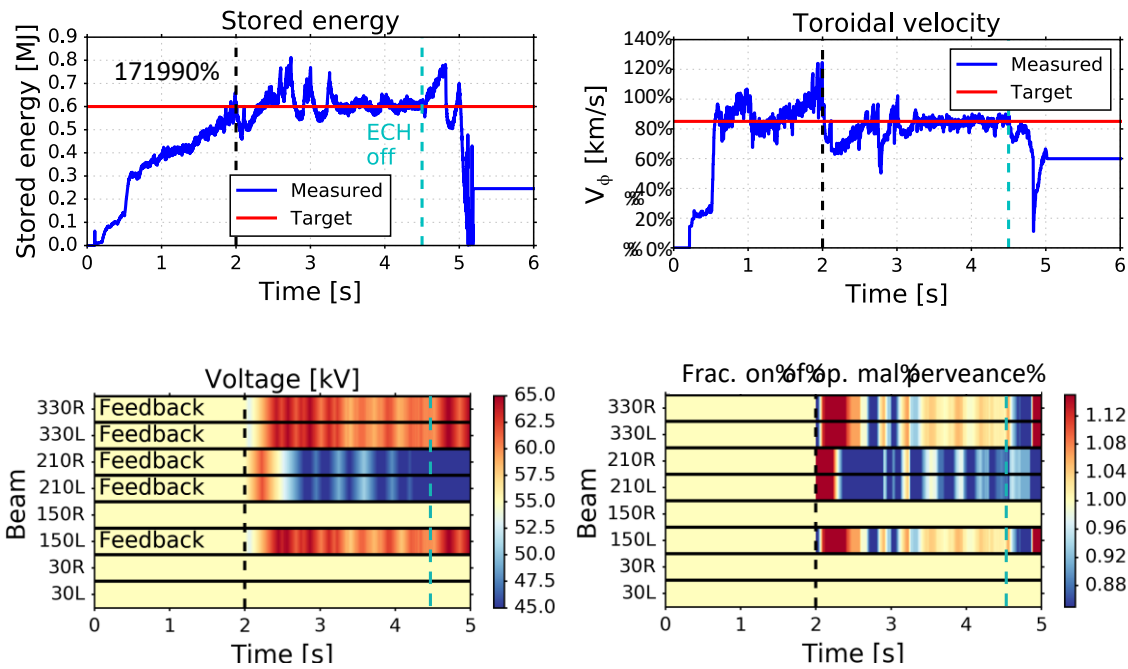


Figure IS-ASC-5: Stored energy, rotation, voltage requests, and perveance requests during DIII-D shot 171990 showing target tracking with voltage and perveance changes.

of the algorithm to control rotation shear, or to use the new actuation techniques for rotation and current profile control.

References

- [IS-ASC-1] D.A. Humphreys, et al., Nuclear Fusion, 47, n 8, Aug. 2007, p 943-51.
- [IS-ASC-2] D.A. Gates, et al., Rev. Sci. Instrum. 75, 5090–5093 (2004).
- [IS-ASC-3] Lloyd, B. et al. Nucl. Fusion 31, 2031–2053 (1991).
- [IS-ASC-4] D.C. Pace, et al., Nuclear Fusion 57, 014001 (2017).
- [IS-ASC-5] M.D. Boyer, et al., Nuclear Fusion 57, Number 6 (2017).

Papers Published by NSTX-U Researchers (Oct. 2016 - Sept. 2017)

1. MENARD JE, Brown T, El-Guebaly L, et al.,
Fusion Nuclear Science Facilities and Pilot Plants Based on the Spherical Tokamak
NUCLEAR FUSION **56** 106023 (October 2016)
2. HOOPER EB and Sovinec CR
A current-driven resistive instability and its nonlinear effects in simulations of coaxial helicity injection in a tokamak
PHYS. PLASMAS **23** 102502 (October 2016)
3. BERRY LA, Jaeger EF, Phillips CK, et al.,
A generalized plasma dispersion function for electron damping in tokamak plasmas
PHYS PLASMAS **23** 102504 (October 2016)
4. DAVIS WM, Tchilinguian GJ, Carroll T, et al.,
Control and data acquisition upgrades for NSTX-U
FUSION ENG. AND DESIGN **112** 932 (October 2016)
5. vanEDEN GG, Reinke ML, Peterson BJ, et al.,
Design and characterization of a prototype divertor viewing infrared video bolometer for NSTX-U
REV. SCI. INST. **87** 11D402 (November 2016)
6. BEDOYA F, Allain JP, Kaita R, et al.,
Unraveling wall conditioning effects on plasma facing components in NSTX-U with the Materials Analysis Particle Probe (MAPP)
REV. SCI. INST. **87** 11D403 (November 2016)
7. PETERSON BJ, Sano R, Reinke ML et al.,
Preliminary design of a tangentially viewing imaging bolometer for NSTX-U
REV. SCI. INST. **87** 11D410 (November 2016)
8. SCOTTI F, Soukhanovskii VA, Weller M,
Diagnostics for molybdenum and tungsten erosion and transport in NSTX-U
REV. SCI. INST. **87**, 11D445 (November 2016)
9. WANG Z, Liu Q, Waganaar, W, et al.,
Four-dimensional (4D) tracking of high-temperature microparticles
REV. SCI. INST. **87** 11D601 (November 2016)
10. SOUKHANOVSKII V et al.,
Real-time radiative divertor feedback control development for the NSTX-U tokamak using a vacuum ultraviolet spectrometer
REV. SCI. INST. **87** 11D605 (November 2016)
11. LIU D, Heidbrink WW, Tritz K, et al.
Compact and multi-view solid state neutral particle analyzer arrays on National Spherical

- Torus Experiment-Upgrade
REV. SCI. INST. **87** 11D803 (November 2016)
12. VANN R, Brunner KK, Ellis R, et al.,
Preliminary measurements of the edge magnetic field pitch from 2-D Doppler backscattering in MAST and NSTX-U
REV. SCI. INST. **87** 11D902 (November 2016)
 13. SCOTT E, et al.,
FIRETIP design and installation for NSTX-U
REV. SCI. INST. **87** 11E114 (November 2016)
 14. BRUNNER KJ, Chorley JC, Dipper NA, et al.
Modifications to the synthetic aperture microwave imaging diagnostic
REV. SCI. INST. **87** 11E129 (November 2016)
 15. WELLER M, Beiersdorfer P, Soukhanovskii VA, et al.,
Three new extreme ultraviolet spectrometers on NSTX-U for impurity monitoring
REV. SCI. INST. **87**, 11E324 (November 2016)
 16. MUNOZ BURGOS JM, Barubui T, Schmitz O, et al.,
Time dependent analysis of visible helium line-ratios for electron temperature and density diagnostic using synthetic simulations on NSTX-U
REV. SCI. INST. **87** 11E502 (November 2016)
 17. FLESCH K, Kremeyer T, Schmitz O, et al.,
Development of miniaturized, spectroscopically assisted Penning gauges for fractional helium and hydrogen neutral pressure measurements
REV. SCI. INST. **87**, 11E529 (November 2016)
 18. JAWORSKI MA, Brooks R, Kaita R, et al.
Upgrades toward high-heat flux, liquid lithium plasma-facing components in the NSTX-U
FUSION ENG. AND DESIGN **112** 93 (November 2016)
 19. RAMAN R, Pluckett G, Lay W-S
Massive Gas Injection Valve Development for NSTX-U
IEEE Transactions on Plasma Science (2016)
 20. PETROV YV and Harvey RW
A fully-neoclassical finite-orbit-width version of the CQL3D Fokker-Planck code
PLASMA PHYS. AND CONT FUSION **58** 115001 (November 2016)
 21. WHITE R, Gorelenkov N, Gorelenkova M,
Saturation of Alfvén modes in tokamaks
PLASMA PHYS. AND CONT FUSION **58** 115007 (November 2016)
 22. PODESTA M, Gorelenkova M, Fredrickson ED, et al.,
Effects of energetic particle phase space modifications by instabilities on integrated modeling
NUCLEAR FUSION **56** 112005 (November 2016)

23. MYRA JR, Russell DA and Zweben SJ,
Theory based scaling of edge turbulence and implications for the scrape-off layer width
PHYS PLASMAS **23**, 112502 (November 2016)
24. LUNSFORD R, Bortolon A, Roquemore AL, et al.,
Lithium granule ablation and penetration during ELM pacing experiments at DIII-D
FUSION ENG. AND DESIGN **112** 621 (November 2016)
25. ZHOU M and White R,
Collisional dependence of Alfvén mode saturation in tokamaks
PLASMA PHYS. AND CONT FUSION **58** 125006 (December 2016)
26. PODESTA M and Bell RE
Initial operation of the NSTX-Upgrade real-time velocity diagnostic
PLASMA PHYS. AND CONT FUSION **58** 125016 (December 2016)
27. SOUKHANOVSKII V, Allen SL, Fenstermacher ME, et al.,
Developing snowflake divertor physics basis in the DIII-D, NSTX and NSTX-U tokamaks aimed at the divertor power exhaust solution
IEEE TRANS ON PLASMA SCI **44** 12 (December 2016)
28. Ebrahimi F
Dynamo-driven plasmoid formation from a current-sheet instability
PHYS. PLASMAS **23**, 120705 (December 2016)
29. STOTLER DP, et al.,
Kinetic neoclassical calculations of impurity radiation profiles
J. NUCL. MAT. AND ENERGY (published on line December 2016)
30. WANG F, Fu GY and Shen W
Nonlinear Fishbone Dynamics in Spherical Tokamaks
NUCLEAR FUSION **57** 016034 (January 2017)
31. HVASTA MH, Kolemen E and Fisher A,
An IR-camera based particle-tracking technique to measure free-surface velocity in liquid metal systems
REV. SCI. INST. **88** 013501 (January 2017)
32. PARK J-K, Logan N,
Self-consistent perturbed equilibrium with neoclassical toroidal torque in plasma
PHYS. PLASMAS **24** 032505 (March 2017)
33. SMITH HM and Fredrickson E,
Compressional Alfvén eigenmodes in rotating spherical tokamak plasmas
PLASMA PHYS. CONTROLLED FUSION **59** 035007 (March 2017)
34. IZACARD O
Generalized fluid theory including non-Maxwellian kinetic effects
JOURNAL OF PLASMA PHYSICS **83** 595830201 (March 2017)

35. ONO M, Jaworski MA, Kaita R, et al.,
Liquid lithium applications for solving challenging fusion reactor issues and NSTX-U contributions
FUSION ENG. DESIGN **117** 124 (April 2017)
36. KAITA R, Lucia M, Allain JP, et al.,
Hydrogen retention in lithium on metallic walls from "in vacuo" analysis in LTX and implications for high-Z plasma facing components in NSTX-U
FUSION ENG. DESIGN **117** 135 (April 2017)
37. HIROOKA Y, Bi H, Shimada M, and et al.,
Hydrogen and helium recycling from a JxB-force convected liquid metal GA67IN20.5Sn12.5 under steady state plasma bombardment
FUSION ENG. DESIGN **117** 140 (April 2017)
38. MAINGI R, Canik JM, Bell RE, et al.,
Effect of progressively increasing lithium conditioning on edge transport and stability in high triangularity NSTX H-modes
FUSION ENG. DESIGN **117** 150 (April 2017)
39. ZWEBEN SJ, Terry JL, Stotler DP, et al.,
Gas puff imaging diagnostics of edge plasma turbulence in magnetic fusion devices
REV. SCI. INST. **88**, 041101 (April 2017)
40. BELOVA EV, Gorelenkov NN, Crocker NA, et al.,
Nonlinear simulations of beam-driven Compressional Alfvén Eigenmodes in NSTX
PHYS PLASMAS **24** 042505 (April 2017)
41. GOUMIRI IR, Rowley CW, Sabbagh SA, et al.,
Simultaneous feedback control of plasma rotation and stored energy on NSTX-U using neoclassical toroidal viscosity and neutral beam injection
PHYS PLASMAS **24** 056101 (May 2017)
42. EBRAHIMI F
Nonlinear reconnecting edge localized modes in current-carrying plasmas
PHYS PLASMAS **24** 056119 (May 2017)
43. BERKERY, JW, Sabbagh SA, Bell, R, et al.,
A reduced resistive wall mode kinetic stability model for disruption forecasting
PHYS PLASMAS **24** 056103 (May 2017)
44. DUARTE VN, Berk HL, Gorelenkov NN, et al.,
Prediction of nonlinear evolution character of energetic-particle-driven instabilities
NUCLEAR FUSION **57** 054001 (May 2017)
45. GUTTENFELDER W, Field AR, Lupelli, I, et al.,
Perturbative momentum transport in MAST L-mode plasmas
NUCLEAR FUSION **57** 056022 (May 2017)
46. BERTELLI N, Valeo EJ, Green DI, et al.,
Full-wave simulations of ICRF and HHFW heating regimes in toroidal plasma with non-

- Maxwellian distribution functions
NUCLEAR FUSION **57** 056035 (May 2017)
47. FIL A, Kolemen E, Ferraro N, et al.,
Modeling of lithium granule injection in NSTX using M3D-C1
NUCLEAR FUSION **57** 056040 (May 2017)
48. FREDRICKSON ED, Belova E, Battaglia D, et al.,
Suppression of Alfvén modes through additional beam heating
PHYS. REV. LETT. **118** 265001 (June 2017)
49. SOUKHANOVSKII VA
A review of radiative detachment studies in tokamak advanced magnetic divertor configurations
PLASMA PHYS. CONTROLLED FUSION **59** 064005 (June 2017)
50. KARIYA T, Imai T, Minami R, et al.,
Development of over-MW gyrotrons for fusion at 14 GHz to sub-THz frequencies
NUCLEAR FUSION **57** 066001 (June 2017)
51. BOYER MD, Andre R, Gates DA, et al.,
Feedback control design for non-inductively sustained scenarios in NSTX-U using TRANSP
NUCLEAR FUSION **57** 066017 (June 2017)
52. DIALLO A, Banerjee S, Zweben SJ, et al.,
Energy exchange dynamics across L-H transitions in NSTX
NUCLEAR FUSION **57** 066050 (June 2017)
53. REN Y, Belova E, Gorelenkov N, et al.,
Recent progress in understanding electron thermal transport in NSTX
NUCLEAR FUSION **57** 072002 (July 2017)
54. BANERJEE D, Zhu P, Maingi R,
Stabilizing effect of resistivity towards ELM-free H-mode discharge in lithium-conditioned NSTX
NUCLEAR FUSION **57** 076005 (July 2017)
55. CANAL JM, Ferraro NM, Evans TE, et al.,
M3D-C1 simulations of the plasma response to non-axisymmetric magnetic perturbations in the NSTX-U snowflake divertor
NUCLEAR FUSION **57** 076007 (July 2017)
56. LUNSFORD R, Bortolon A, et al.,
Multi-species impurity granule injection and mass deposition projections in NSTX-U discharges
NUCLEAR FUSION **57** 076008 (July 2017)
57. STOTLER DP, Lang J, Chang CS, et al.,
Neutral recycling effects on ITG turbulence
NUCLEAR FUSION **57** 086028 (August 2017)

58. AHN J-W, Briesmester AR, Kobayashi M, et al.,
Effect of 3-D magnetic perturbations on divertor conditions and detachment in tokamak and stellerator
PLASMA PHYS. CONTROLLED FUSION **59** 084005 (August 2017)
59. DOMINGUEZ-GUTIERREZ FJ, Bedoya F, Krstic P, et al.,
Unraveling the plasma-material interface with real time diagnosis of dynamic boron conditioning in extreme tokamak plasmas
NUCLEAR FUSION **57** 086050 (August 2017)
60. PODESTA M, Gorelenkova M, Gorelenkov N, et al.,
Computation of Alfvén Eigenmode stability and saturation through a reduced fast ion transport model in the TRANSP tokamak transport code
PLASMA PHYS. CONTROLLED FUSION **59** 095006 (September 2017)
61. STAGNER L AND Heidbrink WW,
Action-angle formulation of generalized, orbit-based, fast-ion diagnostic weight functions
PHYSICS OF PLASMAS **24** 092505 (September 2017)

Forthcoming Papers (as of 10/1/17)

62. MENARD J, Raman R, Battaglia D, et al.
Overview of NSTX Upgrade initial results and modelling highlights
NUCLEAR FUSION **57** 102006 (October 2017)
63. ONO M, Majeski R, Jaworski MA, et al.,
Liquid lithium loop system to solve challenging technology issues for fusion power plant
NUCLEAR FUSION **57** 116056 (November 2017)
64. KURODA K, Raman R, Hanada K, et al.
Current start-up using the new CHI system
PLASMA AND FUSION RESEARCH **12** 1202020 (December 2017)
65. SKINNER CH, Bedoya F, Scotti F, et al.,
Advances in boronization on NSTX-Upgrade
Published online in NUCL. MAT. and ENERGY (2017)
66. MAINGI R, Kaita R, Scotti F, et al.,
Elimination of Inter-discharge Helium Glow Discharge Cleaning with Lithium Evaporation in NSTX
Published online in NUCL. MAT. and ENERGY (2017)
67. PERKINS RJ, Hosea JC, Jaworski MA, et al.,
The Role of Far-Field RF Sheaths in SOL Losses of HHFW Power on NSTX, and Implications for Near-Field Studies of ICRF Antennae
Published online in NUCL. MAT. and ENERGY (2017)

68. SCOTTI F, Soukhanovskii VA, Ahn J-W, et al.,
Toroidal asymmetries in impurity influxes in NSTX
 Published online in NUCL. MAT. and ENERGY (2017)
69. NICHOLS JH, Jaworski MA and Schmid K
Sensitivity of WalldYN material migration modeling to uncertainties in mixed-material surface binding energies
 Published online in NUCL. MAT. and ENERGY (2017)
70. FIL A, Kolemen E, Bortolon A, et al.,
Modeling of lithium granule injection in NSTX with M3D-C1
 Published online in NUCL. MAT. and ENERGY (2017)
71. BEDOYA F, Allain JP, Kaita R, et al.,
Initial studies of plasma facing component surface conditioning in the national spherical tokamak experiment upgrade with the materials analysis particle probe
 Published online in NUCL. MAT. and ENERGY (2017)
72. STOTLER DP, Battaglia DJ, Hager R, et al.,
Kinetic neoclassical calculations of impurity radiation profiles
 Published online in NUCL. MAT. and ENERGY (2017)

Papers Recently Accepted for Publication

73. BERTELLI N, Gorelenkova M, Podesta M, et al.,
 Self-consistent calculation of the effects of RF injection in the HHFW heating regimes on the evolution of fast ions in toroidal plasmas
 Accepted for Publication in EUROPEAN PHYSICAL JOURNAL Web of Conferences (2017)
74. LEE J, Wright J, Bertelli N, et al.,
 A new quasilinear formulation for ICRF plasmas in a toroidal geometry
 Accepted for Publication in EUROPEAN PHYSICAL JOURNAL Web of Conferences (2017)
75. HOSEA J, et al.,
 Development of slow and fast wave heating from the C-Stellarator to NSTX
 Accepted for Publication in EUROPEAN PHYSICAL JOURNAL Web of Conferences (2017)
76. Kim, E.-H., N. Bertelli, E. Valeo, and J. Hoseas (2017) 2D full-wave simulation of waves in space and tokamak plasmas
77. ZWEBEN SJ, Stotler DP, Scotti F, et al.,
 Two-dimensional turbulence cross-correlation functions in the edge of NSTX
 Accepted for publication in PHYS. PLASMAS (2017)

Papers Submitted for Publication

78. SCOTTI F, et al.,
Characterization of intrinsic impurity sources and edge transport in NSTX discharges with lithium wall conditioning
Submitted to NUCLEAR FUSION (2016)
79. MYERS CE, Gerhardt SP, Eidietis NW, et al.,
A multi-machine scaling of halo current duration and rotation
Submitted to NUCLEAR FUSION (2017)
80. BOYER MD, et al.,
Plasma boundary shape control and real-time equilibrium reconstruction on NSTX-U
Submitted to NUCLEAR FUSION (2017)
81. PETRELLA J, Zatz I, Gerhardt S, et al.,
Forensic analysis of faulted NSTX-U inner poloidal field coil
Submitted to IERR SOFE TPS (2017)
82. DEN HARTOG DJ, Borchardt MT, Holly DJ, et al.,
A pulse-burst laser system for Thomson scattering on NSTX-U
Submitted to JOURNAL of INSTRUMENTATION (2017)
83. LESTZ JB, Belova EV, Gorelenkov NN
Energetic-particle-modified global Alfvén eigenmodes
Submitted to PHYS. PLASMAS (2017)
84. IZACARD O, Umansky MV
Gingred, a general grid generator for 2D edge plasma modeling
Submitted to COMP. PHYS. COMM. (2017)
85. HAO G, et al.,
On the scattering correction of fast-ion D-alpha signal on NSTX-U
Submitted to REV. SCI. INST. (2017)
86. HAO G, Heidbrink WW, Liu D, et al.,
Measurement of the passive fast-ion D-alpha emission on the NSTX-U tokamak
Submitted to PLASMA PHYS. CONTROLLED FUSION (2017)
87. WANG Z, et al.,
Drift kinetic effects on the plasma response in high beta spherical tokamak experiments
Submitted to NUCLEAR FUSION (2017)
88. PERKINS R, et al.,
Edge loss of high-harmonic fast-wave heating power in NSTX: a cylindrical model
Submitted to NUCLEAR FUSION (2017)
89. PHILION J, et al.,
Deuterium neutral beam orbits in NSTX-U nonaxisymmetric vacuum magnetic fields
Submitted to PLASMA PHYS. CONTROLLED FUSION (2017)
90. PODESTA M, et al.,
Destabilization of counter-propagating Alfvénic instabilities by off-axis, co-current neutral

beam injection
Submitted to PHYS. REV. LETT. (2017)

91. LOPEZ N, Poli F, et al.,
Feasibility study of O1-mode ECRH in NSTX-U startup plasma
Submitted to NUCLEAR FUSION (2017)
92. HAMMOND K, et al.,
Application of Townsend avalanche theory to tokamak startup by coaxial helicity injection
Submitted to NUCLEAR FUSION (2017)
93. GUTTENFELDER W, et al.,
NSTX-U L-mode plasma in support of transport and turbulence validation
Submitted to NUCLEAR FUSION (2017)
94. GLASSER A, et al.,
Fast numerical solution of the plasma response matrix for real-time ideal MHD control
Submitted to NUCLEAR FUSION (2017)
95. GAN K, et al.,
ELM-free and inter-ELM divertor heat flux broadening induced by Edge Harmonic
Oscillations in NSTX
Submitted to NUCLEAR FUSION (2017)
96. CROCKER N, et al.,
Density perturbation mode structure of high frequency compressional and global Alfvén
eigenmodes in the National Spherical Torus Experiment using a novel reflectometer analysis
technique
Submitted to PLASMA PHYS. CONTROLLED FUSION (2017)
97. REUSCH LM, et al.,
Model validation for quantitative X-ray measurements
Submitted to FUSION SCIENCE AND TECHNOLOGY (2017)

Invited / Oral Talks at Scientific Conferences (Oct. 2016 - Sept. 2017)

ICEF (Innovation for Cool Earth Forum), October 5 – 6, 2016 in Tokyo, Japan

1. M. Ono (PPPL) “Spherical Tokamak for Economical Fusion Energy Development”

1st International “All-about-Divertor” Symposium on Oct. 14 – 15, 2016 in Kyoto Japan

2. M. Ono (PPPL) “Advantages and challenges of liquid lithium based divertor”
3. E. Kolemen (Princeton University) “Fast flowing liquid metal development for fusion reactors”
4. J. Menard (PPPL) “Long-leg and liquid metal divertors for ST-based fusion facilities”

26th IAEA Fusion Energy Conference on Oct. 16-22, 2016 in Kyoto, Japan

5. J. Menard (PPPL), “Overview of First Results from NSTX-U and Analysis Highlights from NSTX”
6. M. Ono (PPPL). “Liquid Lithium Loop System to Solve Challenging Technology Issues for Fusion Power Plant”
7. A. Diallo (PPPL), “Energy Exchange Dynamics across L-H Transitions in NSTX”

58th APS Division of Plasma Physics Meeting on Oct. 31-Nov. 2, 2016 in San Jose, CA

8. I. Guomiri (Princeton U.), “A plasma rotation control scheme for NSTX and NSTX-U”
9. F. Ebrahimi (PPPL). “Plasmoids formation in a laboratory and large-volume flux closure during simulations of Coaxial Helicity Injection in NSTX-U ”
10. J. Menard (PPPL), “Impact of physics and technology innovations on compact tokamak fusion power plants”
11. J. Berkery (Columbia U.) “Resistive wall mode stability forecasting in NSTX and NSTX-U”

2016 Japan-U.S. Workshop on Heat Removal and Plasma Material Interactions for Fusion, Fusion High Power Density Components and Systems and IEA Workshop on Solid Surface Plasma Facing Components on Nov. 7, 2016 at the University of California, Berkeley

12. R. Kaita (PPPL), “Suppressed gross erosion of high-temperature lithium via rapid deuterium implantation”

21st MHD Stability and Control Workshop on Nov. 7-9, 2016 in San Diego, CA

13. S. Sabbagh (Columbia U.), “Disruption event characterization and forecasting in tokamaks”
14. J. Berkery (Columbia U.), “Resistive wall mode stability physics and forecasting in NSTX and NSTX-U”

2016 Annual Meeting of Sigma Xi, The Scientific Research Society on Nov. 11, 2016 in Atlanta, GA

15. R. Kaita (PPPL), “Student research opportunities at National Laboratories”

Max-Planck/Princeton Center for Plasma Physics, Dec. 5-8, 2016, Princeton, NJ

16. J. Menard (PPPL), “Tearing and kink physics in NSTX and NSTX-U”
17. C. Meyers (PPPL), “A multi-machine scaling of halo current duration and rotation”
18. D. Pfefferle (PPPL), “Vertical displacement events and reconnection”
19. T. Stoltzfus-Dueck (PPPL), “Parallel electron force balance and the L-H transition”
20. F. Ebrahimi (PPPL), “3D plasmoid reconnection during CHI”

Fusion Power Associates Meeting, Dec. 13, 2016, Washington DC

21. J. Menard (PPPL), “Progress and plans on NSTX-U”

IAEA Technical Meeting on Uncertainty Assessment and Benchmark Experiments for Atomic and Molecular Data for Fusion Applications”, December 19–21, 2016 (Vienna, Austria)

22. D.P. Stotler (PPPL), "Sensitivity of Tokamak Transport Modeling to Atomic Physics Data: Some Examples"

5th Kyushu Workshop on Solenoid-Free RF-Only ST Plasmas, Feb. 2-31 2017, Kyushu University, Kasuga, Japan

23. M. Ono (PPPL) “An Overview and Motivation for the NSTX-U Start-up Research Program”
24. N. Bertelli (PPPL),”PPPL Code Capabilities for ECH and EBW
25. G. Taylor (PPPL), “Non-Inductive Plasma Current Start-up, Ramp-up and Sustainment in NSTX-U”

ITER Disruption Mitigation Workshop, March 8-10, 2017, Cadarache, France

26. R. Raman (U. Washington), “Electromagnetic Particle Injection Concept” [remote participation]

44th Institute of Physics (IOP) Plasma Physics Conference and the MAST Upgrade Research Forum, April 3-5, 2017, Oxford UK

27. J. Menard (PPPL), “Physics and technology innovations for compact tokamak fusion power plants”
28. J. Menard (PPPL), “Progress and plans for research on NSTX Upgrade”

11th West Lake International Symposium on Energetic Particle Physics and Microturbulence, Hangzhou China, 24-26 April 2017

29. E. Belova, PPPL, "Nonlinear simulations of beam-driven compressional Alfvén eigenmodes in NSTX"

U.S. Transport Task Force Meeting, April 25-28, 2017, Williamsburg, VA

30. D. Battaglia (PPPL), “Bifurcation to Enhanced Pedestal H-mode on NSTX-U”
31. V. Duarte (Princeton U.), “Quasilinear relaxation formalism for energetic particle interactions with Alfvénic modes”
32. S. Tang (UCLA), “Parametric investigation of compressional and global Alfvén Eigenmode instability and effect on thermal confinement in NSTX-U”

- 33. F. Poli (PPPL), “The role of integrated modeling in the development of more robust control algorithms”
- 34. F. Scotti (LLNL), “Scrape-off layer and near-separatrix intermittent filaments in the NSTX and NSTX-U divertor”

EUROfusion Liquid Metal Strategy Meeting, May 10-11, 2017 [remote participation]

- 35. M. Jaworski (PPPL), “Experience and development of lithium and liquid metal experiments on the NSTX and NSTX-U devices”

2nd IAEA Technical Meeting on Fusion Data Processing, Validation and Analysis, May 30 - June 2, 2017, Cambridge, Massachusetts

- 36. J. Berkery (Columbia U.), “Disruption event characterization and forecasting of global and tearing mode stability for tokamaks”
- 37. D. Smith (U. Wisconsin), “Identification of ELM evolution patterns with unsupervised clustering of time-series similarity metrics”

22nd Topical Conference on Radiofrequency Power in Plasmas, May 30-June 2, 2017, Aix-en-Provence, France

- 38. J. Hosea (PPPL), “An overview of some of the main experimental results and challenges in the development of slow and fast wave heating from the C-stellarator to NSTX-U”
- 39. E.-H. Kim (PPPL), “2D full-wave simulations of waves in space and tokamak plasmas”

Workshop on ICRH scenarios for ITER, June 6-8, 2017, Cadarache, France

- 40. N. Bertelli (PPPL), “Self-consistent simulations of ITER plasmas using the TORIC-CQL3D coupling”
- 41. F. Poli (PPPL), “use of ICRF during the ITER half-field operation”

27th IEEE Symposium on Fusion Engineering (SOFE), June 2017, Shanghai, China

- 42. R. Maingi (PPPL), “Overview of NSTX-U Progress”
- 43. C. Neumeyer (PPPL), “Extent of condition review of the NSTX-U project”
- 44. R. Kaita (PPPL), “Synergies in liquid metal technology development for divertor applications”

SOFE Mini-Courses on Diagnostics for Fusion Plasmas and also on Plasma-Surface Interactions, June 2017, Shanghai, China

- 45. R. Kaita (PPPL), “Overview of diagnostics for fusion plasmas”
- 46. A. Diallo (PPPL), “Thomson scattering for direct and localized measurement of electron properties”
- 47. M. Podesta (PPPL), “Plasma confinement diagnostics to determine fusion device performance: ion temperature, density and plasma rotation”
- 48. K. Tritz (Johns Hopkins U.), “X-ray diagnostics for plasma macrostability research”
- 49. R. Ellis (PPPL), “Engineering issues for diagnostic implementation”
- 50. R. Maingi (PPPL), “Fundamentals of PMI and Plasma Edge Physics in Fusion Devices”

FESAC TEC PMI, June 2017, Chicago, IL

51. M. Jaworski (PPPL), “Slowly flowing and high temperature liquid metals as plasma-facing materials”

Theory & Simulation of Disruptions Workshop, July 17-19, 2017, Princeton, NJ

52. C. Myers (PPPL), “A multi-machine scaling of halo current rotation”

FESAC Transformative Enabling Capabilities Workshop, July 19–21, 2017 (Princeton, New Jersey)

53. D.P. Stotler (PPPL), "Plasma-Material Interface Modeling”

US Magnetic Fusion Research Strategic Directions Workshop, July 24-28, 2017, Madison, WI

54. J. Menard (PPPL), “Overview of goals and organization of the workshop
55. J. Menard (PPPL), “Increase Emphasis on Physics and Technology Innovations for Compact Tokamak Fusion
56. S. Sabbagh (Columbia U.), “Accelerated fusion development and predictive capability utilizing spherical tokamaks + Initiative on disruption elimination”
57. M. Jaworski (PPPL), “An applied energy program to achieve economical fusion energy”

15th IAEA Tech. Mtg on Energetic Particles (Sept. 5-8, 2017, PPPL)

58. N. A. Crocker (UCLA), “Local compressional and global Alfvén eigenmode structure on NSTX and their effect on core energy transport”
59. S. Tang (UCLA), “Experimental investigation of stability, frequency and toroidal mode number of compressional Alfvén eigenmodes in DIII-D” (Results from an experiment in the 2017 NSTX-U/DIII-D Collaborative Research National Campaign.)
60. E. Belova (PPPL) "Numerical simulations of GAE stabilization in NSTX-U"
61. E. Fredrickson, “Suppression of Alfvénic modes through modifications of the fast ion distribution”

1st Asia-Pacific Conference on Plasma Physics, Sept. 18-23, 2017, Chengdu, China

62. W. Guttenfelder, “Validating gyrokinetic predictions using NSTX and NSTX-U plasmas”
63. Y. Ren, “Exploring the regime of validity of global gyrokinetic simulation with spherical tokamak plasmas”
64. F. Poli, “EC power management for NTM control in ITER: the path from the commissioning phase to demonstration discharges”

19th International Spherical Torus Workshop (ISTW 2017), Seoul National University, 19-22 September 2017

65. E. Belova, "Numerical simulations of stabilization of Global Alfvén Eigenmodes (GAEs) in NSTX-U"
66. J. Menard, “Next-step low-aspect-ratio tokamaks using high-temperature superconductors and liquid metal plasma facing components”

67. J. Menard, "Menard - Overview of NSTX Upgrade initial results and modeling highlights"
68. S.-H. Ku, "Gyrokinetic heat-flux footprint in NSTX and NSTX-U plasmas"
69. W. Guttenfelder, "Validating gyrokinetic predictions using NSTX-U plasmas"
70. M. Reinke, "Requirements, designs and plans for NSTX-U high heat flux plasma facing components"
71. M. Ono, "Facility and diagnostic commissioning for initial operation of the NSTX-U facility"
72. D. Mueller, "NSTX-U plasma commissioning and scenario development"
73. J.-K. Park, "Non-axisymmetry at the center of NSTX – Lessons to optimize 3D tokamaks"
74. R. Raman, "Transient CHI Research on STs"
75. N. Bertelli, "The effects of the HHFW wave-field on the evolution of fast ion / beam ion populations in NSTX plasma"
76. D. Pfefferlé, "NSTX vertical displacement event 3D nonlinear modeling with M3D-C1"

Seminars and Colloquia by NSTX-U Researchers

1. M. Ono (PPPL) presented “ST Fusion Development Path and NSTX/NSTX-U Overview” at the University of Tokyo on October 7, 2016 in Tokyo, Japan
2. J. Menard (PPPL) presented “Progress and plans for NSTX Upgrade prospects for next-step spherical tori” on Nov. 7, 2016 to the student branch of the American Nuclear Society in the Dept. of Nuclear Engineering of the University of California, Berkeley
3. J. Menard (PPPL) presented “Progress and plans for research on NSTX-Upgrade” on Dec. 9, 2016 at the MIT Plasma Science and Fusion Center
4. J. Menard (PPPL) presented “Motivations for Spherical Torus research and initial results from NSTX-Upgrade” on Jan. 11, 2017 at the PPPL Colloquium, Princeton NJ
5. Jon Menard presented “Progress and Plans on NSTX-U” in Dec. 2016 at the Fusion Power Associates meeting, Washington DC.
6. M. Ono (PPPL) presented a laboratory seminar “Initial Results from NSTX Upgrade and Possible Areas of Scientific Collaboration with JT-60SA” at Naka, Gifu, Japan
7. W. Guttenfelder (PPPL) presented “NSTX-U first results, and progress in transport research” on Feb. 7, 2017 at the University of Washington, Seattle, WA
8. S. Sabbagh (Columbia U.) presented “Kinetic resistive wall mode stabilization in tokamaks and initial results from NSTX-U” on Feb. 9, 2017 at the KTH Royal Institute of Technology in Stockholm, Sweden
9. J.-K. Park presented “Plasma response analysis on resonant field coupling by HFS coils in COMPASS” in Feb. 2017 to the ITER Organization and the COMPASS Research Teams
10. F. Poli (PPPL) presented “The role of integrated modeling in discharge analysis, prediction, and for the development of more robust control algorithms” on March 13-14, 2017 at the University of York, UK
11. J. Menard (PPPL) presented “Motivations for advanced divertor system and materials research in next-step fusion facilities and NSTX Upgrade” on March 16, 2017 at Los Alamos National Laboratory, Los Alamos, NM
12. R. Kaita (PPPL) presented Synergies in Liquid Metal Technology Development for Divertor Applications” on July 18, 2017 in the Department of Nuclear, Plasma, and Radiological Engineering at the University of Illinois at Urbana-Champaign
13. M. Ono (PPPL) presented a laboratory seminar “NSTX-U Initial Operations and Liquid-Metal-Based Divertor R&D in the US” on May 25, 2017 as National Institute for Fusion Science, Toki, Japan.
14. Y. Ren (PPPL) presented a seminar “Recent Progress in Understanding Electron Thermal Transport in NSTX and NSTX-U” on November 22, 2016 at Southwestern Institute of Physics in Chengdu, China
15. D. Battaglia (PPPL) presented “Research at the National Spherical Torus Experiment Upgrade (NSTX-U) aimed at the development of fusion energy” on April 14, 2017 in the Department of Mechanical Engineering and Mechanics at Lehigh University, Bethlehem, PA.
16. D. Battaglia (PPPL) presented “Breakdown Studies in NSTX-U and MAST-U” at the MAST-U Session Leader Training on August 22, 2017 in Culham, UK
17. R.J. Goldston (PPPL) presented “New Scaling for Detachment and Implications for Tokamak Power Plant Design” at the ASDEX-Upgrade Seminar, May 11, 2017, on Garching Germany

18. R.J. Goldston (PPPL) presented “New Scaling for Detachment and Implications for Tokamak Power Plant Design” at the NSTX-U physics meeting, April 24, 2017, in Princeton, NJ
19. R.J. Goldston (PPPL) presented “New Scaling for Detachment and Implications for Tokamak Power Plant Design” at the IAEA Steady-State Operation meeting. March 23, 2017, in Vienna, Austria
20. R.J. Goldston (PPPL) presented “Technical Aspects of the Iran Deal” at the ANS Student Conference, April 7, 2017, in Pittsburgh, PA
21. R.J. Goldston (PPPL) presented “Breakout and Timely Verification at Large-Scale Gas Centrifuge Enrichment Plants” as a Union of Concerned Scientists Webinar, June 15, 2017, on line

Major Awards by NSTX-U Researchers

1. Stefan Gerhardt received the Fusion Power Associates 2016 Excellence in Fusion Engineering Award
2. Michael Jaworski was named a DOE Oppenheimer Science and Energy Leadership Program Fellow
3. Stanley Kaye was named by the International OP as one of the Outstanding Reviewer Award winners for 2016, in recognition of the high quality and timeliness of his publication peer reviews for Plasma Physics and Controlled Fusion
4. Olivier Izacard was named by the International OP as one of the Outstanding Reviewer Award winners for 2016, in recognition of the high quality and timeliness of his publication peer reviews for Plasma Physics and Controlled Fusion
5. C.S. Chang won the use of 269.9 million supercomputer hours to complete an extreme-scale study of the complex edge region of fusion plasmas.

Hosted / Organized Meetings and Workshops

NSTX-U researchers organized or co-organized the following meetings:

1. TRANSP User's Group Meetings (APS-DPP 2016, PPPL May 4-5, 2017)
2. ITPA T&C Meeting (May 1-3, 2017, PPPL)
3. IAEA Tech. Mtg on Energetic Particles (Sept. 5-8, 2017, PPPL)
4. ITPA EP (Sept. 11-12, 2017, PPPL)
5. Fusion Facilities Coordinating Comm. meetings (Nov. 2016, Dec. 2016)
6. ITPA Pedestal TG Meetings (April, Sept. 2017)
7. NSTX-U Program Advisory Committee Meetings (Jan. 2017)
8. Mini-Course on Diagnostics for Fusion Plasmas at the SOFE Conference (June 2017)
9. FESAC TEC PMI panel (June 2017)
10. US Magnetic Fusion Research Strategic Directions Workshop (July 2017)
11. Plasma Surface Interaction Meeting (June 2017)

NSTX-U Engineering organized:

1. Design Validation and Verification Reviews (Jan. – March 2017)
2. Extent of Condition Reviews (March 2017, May 2017)
3. NSTX-U Recovery Conceptual Design Review (August 2017)
4. NSTX-U Recovery Cost and Schedule Review (Sept. 2017)

PPPL Theory organized:

1. Disruption Workshop (July 2017)
2. Max-Planck Workshop (Dec. 2016)

NSTX-U PPPL Employee FY17 Leadership in Venues Outside of PPPL

1. Bertelli, N., PPPL PI of the RF SciDAC project
2. Darrow, D., Chair, ITPA Diagnostics, Fusion Products Working Group
3. Gerhardt, S. Leader, ITPA MDC WG-6
4. Gorelenkov, N., Leader, USBPO Energetic Particles Topical Group
5. Guttenfelder, W., Deputy Leader, U.S. BPO Transport & Confinement Topical Group
6. Hosea, J., Co-chair, US-Japan RF Physics Workshop
7. Kaye, S., PI of TRANSP funding grant by DOE
8. Kaye, S., Coordinator, International H-mode Database Update Task (ITPA)
9. Kaye, S., Panel Member, National Academy of Sciences Burning Plasma Study
10. Kolemen, E., PSI Conference Local Organizer
11. Maingi, R., Chair, ITPA Pedestal and Edge Physics Topical Group
12. Maingi, R., Chair, FESAC Transformative Enabling Capabilities (TEC) panel
13. Maingi, R., Chair of the 23rd International Conference on Plasma Wall Interactions, Princeton, NJ, 18-22 June 2018, and member of the Program Committee
14. Menard, J., Chair, Program Committee for 19th International Spherical Torus Workshop
15. Menard, J., Co-chair, International Advisory Committee for China Fusion Engineering Test Reactor (CFETR)
16. Menard, J., Chair, U.S. DOE FES Fusion Facility Coordinating Committee
17. Menard, J., Co-chair, U.S. Magnetic Fusion Research Strategic Directions organization/workshops
18. Park, J-K, MDC-19 Leader, ITPA MHD, Disruption and Control Topical Group
19. Park, J-K, Deputy Leader, MS Topical Science Group, NSTX-U Team
20. Park, J-K, Deputy Leader, 3D Task Force Group, KSTAR Team
21. Poli, F., Leader, BPO Topical Group on Integrated Scenarios
22. Poli, F., PI of ITER Task Agreement on EC modeling and applications
23. Poli, F., ITER Scientist Fellow
24. Skinner, C., Chair, Local Organizing Committee, 23rd International Conference on Plasma Wall Interactions, Princeton, NJ, 18-22 June 2018.
25. Stratton, B., Deputy Group Leader, USBPO Diagnostics
26. Wang, W. X., Secretary/Treasurer, Executive Committee of Sherwood Conference

NSTX-U PPPL Employee Membership and Participation in Scientific Groups and Meetings Outside of PPPL

1. Bell, R., Expert, ITPA Diagnostics Topical Group
2. Bortolon, A., Expert, ITPA Pedestal and Edge Physics Topical Group
3. Darrow, D., Expert, ITPA Diagnostics Topical Group
4. Diallo, A., Expert, ITPA Pedestal and Edge Physics Topical Group
5. Ferraro, N., Expert, ITPA Pedestal and Edge Physics Topical Group
6. Ferraro, N., Treasurer, Sherwood Fusion Theory Conference Executive Committee
7. Fredrickson, E., Member, ITPA Energetic Particle Physics Topical Group
8. Gates, D.A. IAEA-US and International Paper Section Committee (2016)

9. Gerhardt, S., Member, ITPA Integrated Operating Scenarios Group
10. Gorelenkov, N., Member, ITPA Energetic Particle Physics Topical Group
11. Guttenfelder, W., Member, ITPA Transport and Confinement Topical Group
12. Guttenfelder, W., TTF Executive Committee 2017
13. Hosea, J., Member, US ITER IO Red Team Review Panel to prepare for DOE's determination of the Project's readiness for Critical Decision 2 and 3, Approval of Performance Baseline and Approval of Start of Construction
14. Jaworski, M., Member, ITPA scrape-Off-Layer and Divertor Topical Group
15. Kaye, S., Expert, ITPA Transport and Confinement Topical Group
16. Kaye, S., Member, U.S. Transport Task Force Steering Committee
17. Kaye, S., Member, U.S. Burning Plasma Organization Research Council
18. Kaye, S., Invited participant in the ITER Research Plan Workshop, Feb. 2017, March 2017
19. Kaye, S., Member, Culham Centre for Fusion Energy Advisory Committee
20. Kolemen, E., Member, ITER Plasma Control System design review committee
21. Lunsford, R., Expert, ITPA Pedestal and Edge Physics Topical Group
22. Maingi, R., Expert, ITPA Diagnostics Topical Group
23. Maingi, R., Expert, ITPA Divertor and SOL Topical Group
24. Maingi, R., Member, ITPA Coordinating Committee
25. Maingi, R., Member, FESAC
26. Maingi, R., Member, Proto-MPEX Program Advisory Committee
27. Maingi, R., Technical Program Committee Member, of the H-mode Workshop
28. Maingi, R., Invited participant in the ITER Research Plan Workshop, July 25-29, 2016
29. Menard, J., Member, Executive Committee of IEA Implementing Agreement for Cooperation on Spherical Tori
30. Menard, J., Member, Culham Centre for Fusion Energy Advisory Committee
31. Menard, J., Member, MAST Upgrade project review committee
32. Menard, J., Member, Research Councils UK Fusion Advisory Board
33. Menard, J., Expert, ITPA MHD, Disruptions and Control Topical Group
34. Menard, J. Member, ITER Plasma Control System design review committee
35. Ono, M., Program Committee Member for the International Symposium of Liquid Metal
36. Ono, M., Program Committee Member for the 19th International Spherical Workshop
37. Ono, M., Associate Editor, Journal of Fusion Energy
38. Ono, M., International Visiting Professor, Kyushu University
39. Park, J-K, Committee Member, Workshop on MHD Stability Control
40. Park, J.K., Lecturer, Princeton University
41. Podesta, M., Member, ITPA Energetic Particle Physics Topical Group
42. Podesta, M., Member, TTF Executive Committee 2015
43. Podesta, M., Member of the Editorial Advisory Board of Review of Scientific Instruments
44. Poli, F., Member, US ITPA-IOS
45. Poli, F. Member, TTF Executive committee
46. Ren, Y., Expert, ITPA Transport and Confinement Topical Group
47. Skinner, C., Expert, ITPA Diagnostics Topical Group

48. Stotler, D., Member, IAEA Technical Committee on Uncertainty Assessment and Benchmark Experiments for Atomic and Molecular Data for Fusion Applications
49. Stratton, B., Member, ITPA Diagnostics Topical Group
50. Taylor, G., Expert, ITPA Diagnostics Topical Group

NSTX-U Collaborator Institutions

Number	Institution	Country
1	College of William and Mary	USA
2	Columbia University	USA
3	CompX	USA
4	Florida International University	USA
5	General Atomics	USA
6	Idaho National Laboratory	USA
7	Johns Hopkins University	USA
8	Lawrence Livermore National Laboratory	USA
9	Lehigh University	USA
10	Lodestar Research Corporation	USA
11	Los Alamos National Laboratory	USA
12	Massachusetts Institute of Technology	USA
13	Nova Photonics, Inc	USA
14	Oak Ridge National Laboratory	USA
15	Old Dominion University	USA
16	Princeton University	USA
17	Purdue University	USA
18	Sandia National Laboratory	USA
19	Tech-X Corporation	USA
20	University of California - Davis	USA
21	University of California - Irvine	USA
22	University of California - Los Angeles	USA
23	University of California - San Diego	USA
24	University of California, Space Sciences Laboratory	USA
25	University of Colorado	USA
26	University of Illinois	USA
27	University of Maryland	USA
28	University of Rochester	USA
29	University of Tennessee	USA
30	University of Texas	USA
31	University of Washington	USA
32	University of Wisconsin	USA
33	University of Costa Rica	Costa Rica
34	Institute of Plasma Physics-Czech Republic	Czech Republic
35	Hiroshima University	Japan
36	Japan Atomic Energy Agency	Japan
37	Kyoto University	Japan
38	Kyushu University	Japan
39	NIFS National Institute for Fusion Science	Japan
40	Niigata University	Japan
41	University of Hyogo	Japan
42	University of Tokyo	Japan
43	FOM Institute DIFFER	Netherlands
44	ASIPP - Institute of Plasma Physics - Chinese Academy Of Sciences	P.R. China
45	Ioffe Physical-Technical Institute	Russia
46	TRINITI - Troitskii Institute of Innovative & Thermonuclear Research	Russia
47	KAIST - Korea Advanced Institute of Science and Technology	South Korea
48	NFRI - National Fusion Research Institute	South Korea
49	Seoul National University	South Korea
50	Ulsan Science Institute of Science & Technology	South Korea
51	Institute for Nuclear Research-National Academy of Science	Ukraine
52	Culham Centre for Fusion Energy	United Kingdom
53	Tokamak Energy	United Kingdom
54	University of York	United Kingdom